OPTIMIZED OPTOELECTRONIC PROPERTIES OF ELECTRON TRANSPORT MATERIALS FOR DYE-SENSITIZED SOLAR CELLS

BENJAMIN KIPCHIRCHIR KORIR

A Thesis Submitted to the Graduate School in Partial Fulfillment of the Requirements for the Degree of Master of Science in Chemistry of Egerton University

EGERTON UNIVERSITY

OCTOBER 2025

DECLARATION AND RECOMMENDATION

Declaration

This thesis is my original work and has not been presented in this university or any other for the award of a degree.

Signature…… 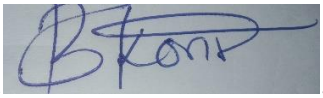 ……. .. Date……29/09/2025…….

Benjamin Kipchirchir Korir

SM11/13674/19

Recommendation

This thesis has been submitted with our approval as university supervisors.

Signature..... ..... Date..... 30/09/2025.....

Prof. Joshua K. Kibet, PhD.

Department of Chemistry,

Egerton University.

Signature.....  ..... Date..... 30/09/2025.....

Prof. Mwaniki Silas Ngari, PhD.

Department of Chemistry,

Egerton University.

COPYRIGHT

DEDICATION

This thesis is dedicated to my parents, Mr. William K. Ngetich and Rebecca Jebet, and friends who have played a key role in pursuing this. This thesis is also dedicated to my wife, Babra, and my son, Dalton, for their unconditional love and support.

ACKNOWLEDGEMENTS

First and foremost, I express deep gratitude to Almighty God for unwavering love and divine guidance, and boundless mercy throughout this academic journey. God has been the source of hope, strength, and perseverance to overcome obstacles throughout this academic journey. Secondly, I would like to express my sincere gratitude to my supervisors, Professor Joshua K. Kibet and Professor Mwaniki Silas Ngari of Egerton University, Department of Chemistry, for their patience, great advice, and contributions to my study. Their lectures, guidance, steadfast support, and expertise in chemistry immensely contributed to the success of this study. Their insightful feedback and encouragement throughout the research process shaped the direction of this study. Thirdly, I would like to sincerely thank the Egerton University Department of Chemistry and the Faculty of Science members for the support and resources that enriched this project. I would also like to thank Professor Kibet's research group, led by Dr Nicholas Rono, for creating and maintaining a collaborative scientific environment. Special thanks to Dr Nicholas Rono, who trained me to use a one-dimensional solar cell simulator capacitor. His support and motivation made the research a fulfilling and enjoyable one. I would like to acknowledge my friends Peter Mwangi Irungu and Den Skipper for their moral support during my postgraduate studies. Lastly, I also thank my classmates, including David M. Muthama and Albert O. Morang'a, for their collaboration and assistance in my research. God bless you all.

ABSTRACT

The past decade has witnessed significant progress in dye-sensitized solar cells (DSSCs) due to attractive power conversion efficiencies (PCEs), low toxicity, roll-to-roll compatibility, and versatility. As a result, significant strides have been made in developing high-performance DSSCs for the Internet of Things (IoT), highly integrated microelectronics, light-emitting diodes, and portable power supplies, among other emerging applications. Concurrently, fundamental studies have been conducted to elucidate the underlying electronic, chemical, and physical properties of isolated components of DSSCs from both theoretical and experimental perspectives. In this roadmap, this study optimized electron transport materials using density functional theory (DFT) formalism and numerical simulation methods to investigate the optoelectronic and photovoltaic characteristics of simulated solar cell models. One-dimensional solar cell capacitance simulator (SCAPS-1D) and Gaussian 09w SCAPS-1D program were used to study the solar cell configuration FTO/ZnOS/N719 dye/CuSCN/Au, while Gaussian 09w was used to analyze ground state properties, optimized geometries, and bandgap energies. FTO/ZnOS/N719 dye/CuSCN/Au achieves an outstanding performance of power conversion efficiency (PCE) of 10.87%, short circuit current (J_{sc}) of 20.32897 mA/cm^2, fill factor (FF) of 68.56% and open circuit voltage (V_{OC}) of 0.7800 V. For the HTL-free configuration, the architecture FTO/ZnOS/N719 dye/Au yielded an optimal power conversion efficiency (PCE) of 11.54%, 18.50 mAcm^{-2} as the short circuit current (J_{sc}), 62.71% as the fill factor (FF), and an open-circuit voltage (V_{OC}) of 0.99 V, while FTO/TiO_2/N719 dye/Au gave an optimal photovoltaic performance of 10.22% as the PCE, a J_{sc} of 16.50 mAcm^{-2}, and 63.58% as the FF. The computational studies of reduced density gradient (RDG) and molecular electrostatic potential (MEP) agree with earlier studies in statistical physics, which suggest that the N719 dye chemically bonds with photoelectrodes via the two carboxylic groups in a bidentate bridging configuration. This theoretical investigation demonstrates that SnO_2 and ZnOS are alternative photoelectrodes to conventional TiO_2 in harnessing visible light. Nonetheless, ZnOS stands out as a top ETL contender owing to its high J_{sc} and PCE, which enhance its light-harvesting capabilities.

TABLE OF CONTENTS

LIST OF TABLES

LIST OF FIGURES

LIST OF ABBREVIATIONS AND ACRONYMS

B3LYP	Becke 3-Parameter (Exchange), Lee, Yang, and Parr
CB	Conduction band
DSSCs	Dye-sensitized solar cells
DFT	Density functional theory
ELIS	Electronics and Information Systems
ETL	Electron transport layer
FTO	Fluorine-doped tin oxide
HOMO	Highest occupied molecular orbital
HTL	Hole transport layer
IPCE	Incident power conversion efficiency
LH	Light-harvesting
LUMO	Lowest unoccupied molecular orbital
MLCT	Metal-to-ligand charge transfer
NHE	Normal hydrogen electrode
PCE	Power conversion efficiency
PSCs	Perovskite solar cells
PV	Photovoltaic
QE	Quantum efficiency
RDG	Reduced density gradient
SCAPS-1D	One-dimensional solar cell capacitance simulator
SCPs	Solid conductive polymers
SDGs	Sustainable development goals
ssDSSCs	Solid-state dye-sensitized solar cells
S-Q	Shockley-Queisser
TCO	Transparent conductive oxide
T-D DFT	Time-dependent density functional theory
VB	Valence band

CHAPTER ONE
INTRODUCTION

1.1 Background information

For many years, fossil fuels have been the primary energy source worldwide for domestic and commercial applications (Halkos & Gkampoura, 2020). However, at the onset of industrialization in the 19th century, these finite fossil fuels were depleted at a higher rate, emitting pollutants to the environment, especially carbon dioxide (CO_2) and other greenhouse gases (Sati & Verma, 2021). The outflow of CO_2 is projected to increase by 85% by 2040 due to the continuous use of non-renewable energy sources (Sohag et al., 2020). The current worrying trends in global warming and the climate crisis, caused by conventional fossil fuels, have motivated the scientific community to explore modern and secure renewable energy alternatives (Chen et al., 2019). Most of these renewable sources are clean and include solar, hydropower, biomass, wind, geothermal, and biofuel. Developing countries require a sustainable, non-polluting energy sources to compete with developed countries for a low-carbon transition roadmap during energy production and use (Mills et al., 2021). Of all the possible renewable energy alternatives, solar technologies and biofuels are considered as credible economic alternatives that contribute mainly to achieving Sustainable Development Goals (SDGs) number seven (affordable and clean modern energy) and number 13 (climate action) (Nazari et al., 2021). Solar technologies are versatile and environmentally benign, capable of harnessing clean energy, with a broad potential to fulfill global energy demands in a pollution-free atmosphere (Mehrabian & Dalir, 2018).

Dye-sensitized solar cells, perovskites, organic, multi-linked tandem, and quantum-dot technologies belong to the third-generation solar cell systems (Rono et al., 2021a). They possess robust features, such as ease of fabrication and lower cost compared to conventional silicon solar cells, as well as high power conversion efficiency (PCE) under low-light illumination (Amin et al., 2012). Solid-state dye-sensitized solar cell (ssDSSC) consists of a photosensitive layer (dye) sandwiched between two charge-selective contacts –electron transport layers (ETL) and hole transport layers (HTL), electron and hole conductive materials, respectively. The photoanode (ETL) is a crucial component of solar cells, influencing the photovoltaic performance of DSSCs by controlling carrier concentration (MaríSoucase et al., 2016). The presence of ETLs in DSSCs

is critical in achieving a higher fill factor (FF), high open-circuit voltage (V_{OC}), good absorption of photon light, and better transport of directional charges (Snaith, 2010). The criteria for selecting the photoanode (ETL) are that it should possess fundamental properties: (i) long diffusion length, (ii) high electron mobility to minimize interfacial electron recombination, (iii) high internal surface area for maximum dye anchorage, (iv) energy levels that match other solar cell components (Zhang et al., 2018). Previous theoretical and experimental results have been reported, exploring new interfacial materials in third-generation thin-film solar cells (Rono et al., 2021b; Shao & Loi, 2020). Due to the complexities of solar cell structures, numerical simulation approaches have been employed to elucidate the electrical, optical, and mechanical properties of microscopic parameters in solar cells.

Computational modelling of isolated DSSC components (redox shuttles, semiconductor nanoparticles, and dyes) has successfully complemented experimental work by providing insights into the physical and chemical processes governing their operations (Tsipis, 2014). The hybrid density functional Becke 3-Parameter (Exchange), Lee, Yang, and Parr (B3LYP) level of theory has been identified as a reliable method for predicting properties, electronic structure, and geometry of conjugated materials (Aulakh et al., 2015). Various computer-based numerical simulation programs have been developed to theoretically assess solar cell performance prior to device fabrication (Kowsar et al., 2019). There are one-dimensional simulation tools such as solar cell capacitance simulator (SCAPS), one-dimensional analysis of microelectronic photonic structures (AMPS-1D), and one-dimensional personal computer simulation (PC-1D). Nevertheless, these simulators differ in the graphical interface, features, speed, effectiveness, and user accessibility (Kowsar et al., 2019). Of all the available numerical software for solar cell simulation, SCAPS-1D presents advantages such as easy-to-learn and intuitive control capabilities (Burgelman et al., 2013), the capability of simulating up to seven different layers with non-routine measurements, and the output results are also easy to interpret (Basak & Singh, 2021; Kim et al., 2017). Investigating various models with recombination mechanisms, interface defect-level, and batch calculations with bulk designs is also easier. Furthermore, SCAPS-1D simulation results have demonstrated good agreement with experimental studies and have been widely utilized in various types of solar cells (Rono et al., 2021a).

Whereas previous studies reported the theoretical power conversion efficiency of DSSCs to be approximately 20% (Snaith, 2010), today, the efficiency of DSSCs is just over 12.5% based on Ru(II) dyes by optimizing structural and material properties (Shabir et al., 2022). Nevertheless, these efficiencies are still lower than Si-based and thin-film solar cells, which post approximate efficiencies of 20-30% (Sharma et al., 2018). Consequently, this study seeks to develop a novel ssDSSC configuration by optimizing the material layer properties. In the proposed research, SCAPS-1D will perform modelling and numerical simulation calculations of the cell configuration: FTO/ETL/N719 dye/CuSCN/Au. Herein, FTO, ETL, N719 dye, CuSCN, and Au are the fluorine-doped tin oxide, ETL (SnO_2, TiO_2, and ZnOS) is the electron conductive layer, di-tetrabutylammonium *cis*-bis(isothiocyanato)bis (2,2′-bipyridyl-4,4 dicarboxylato) ruthenium (II) (absorber layer), CuSCN is the p-type layer, and gold (Au) back contact, respectively. Current-voltage and heterojunction characteristics, the effect of working temperature on cell performance, defect densities, electric losses due to shunt and series resistance, HOMO and LUMO energy levels, band gap energies, and quantum efficiency curves will be analyzed using SCAPS-1D, Gaussian 09w, and Chemissian computational tools.

1.2 Statement of the problem

Arguably, the simplest solution to reducing net carbon emissions is to generate power from renewable energy resources such as the sun. Solar energy is the most abundant resource with attractive potential for new energy advancements. Harnessing solar energy could become the most sustainable energy alternative, particularly due to its widespread abundance in most parts of the world. Nevertheless, there is a need to identify affordable and easily processable optoelectronic materials for efficient and large-scale production compared to conventional silicon semiconductors. The PCE of practical ssDSSCs remains very low compared to Shockley-Queisser (S-Q) limits due to fundamental losses stemming from shunt and series resistances, optical losses at the interfacial layers, reflection losses, and recombination due to defects. The current record of DSSC efficiency stands at 13.6%, with its fabrication designed to achieve low energy losses at excited states compared to the widely deployed single-crystalline silicon devices, which consist of positive–negative junctions (Si p-n), and have reached a maximum efficiency of approximately 25%. In order to optimize solar cell performance, the generation of electron-hole pairs must be

maximized, and the kinetics of charge recombination must be minimized. Recombination of charge lowers the open-circuit voltage (V_{OC}) and reduces short-circuit current (J_{sc}). There is a need for quality interfaces between the absorber layer and the charge-selective contacts. This indicates that interfacial optimization at the ETL/N719 interface is critical in electron transport and charge separation. Interface quality and stability may be enhanced by controlling the defects of the photosensitive and interfacial layers, using feasible contact layers to enhance charge carrier generation and collection, and minimizing the kinetics of recombinations. This research endeavours to probe the ground-state properties, geometry, HOMO and LUMO energies, band gap, and optoelectronic behaviour of various ETLs and CuSCN using SCAPS-1D, Gaussian 09w, and Chemissian software. In addition, the photovoltaic performance of the proposed DSSCs models will be evaluated by varying interface defect densities and ETLs, with optimization carried out under various operational conditions. Herein, the purpose of the computational simulation is to enhance and widen our understanding of the key parameters and novel ETLs to focus on in improving the photovoltaic performance of dye-sensitized solar cells towards the S-Q limits.

1.3 Objectives

1.3.1 General objective

To investigate optimized optoelectronic properties of various electron transport materials for solar cell applications using a solar cell capacitance simulator.

1.3.2 Specific objectives

i. To design a high-power conversion efficient solar cell configuration by optimizing the optoelectronic properties of TiO_2, SnO_2, and ZnOS electron transport materials.
ii. To determine the effect of varying critical device parameters on photovoltaic performance of the model solid-state dye-sensitized solar cell models.
iii. To simulate ssDSSCs models that yield optimal current-voltage characteristics.
iv. To determine the quantum efficiency curves of the proposed solid-state dye-sensitized solar cell configurations.

1.4 Research questions

i. How will optimization of the model ssDSSC configuration give a highly efficient solar cell configuration?
ii. Will the photovoltaic performance of the model ssDSSCs vary significantly when critical device parameters are varied?
iii. How can simulation of ssDSSC models be used to achieve optimal current-voltage characteristics?
iv. Is it possible to simulate ssDSSC based on a one-dimensional solar cell simulator that gives characteristic photovoltaic quantum efficiency?

1.5 Justification

To address the current global energy and environmental issues linked to the unabated consumption of fossil fuels, it is essential to explore sustainable energy alternatives, such as renewable solar energy. Third-generation thin-film PV devices, in particular, solid-state dye-sensitized solar cells, are versatile, emerging prospective candidates for meeting SDG number 13 (climate action), United Nations (UN) climate change act goals, enhance access to clean and modern energy in accordance with SDG number seven, SDG number one on poverty reduction, and SDG number nine that promotes industry and innovation. Moreover, as the Government of Kenya (GoK) strives to achieve food security and nutrition under the Big Four Agenda, post-harvest management of perishable foodstuffs has been noted as one of the most enduring challenges. The process requires financial and technological innovations to overcome the limitations associated with electricity supply, installation, and maintenance of conventional cooling systems. Conveniently, the advancement of solar energy technologies has been pivotal in mechanical refrigeration and temperature control in food storage systems. Solar-powered cooling systems have been associated with notable economic benefits, such as reducing energy costs, preventing root crops from decay, and improving nutrition due to the availability of adequate, high-quality food. This cold storage technology, which relies on solar panels, can be installed in food storage centers to extend the freshness of onions and other perishable foodstuffs. It is crucial to design and manufacture low-cost photovoltaic devices for effective solar energy harvesting. Despite recent developments in PV devices, there are still fundamental limits in converting sunlight to electricity, which is a steady

and valuable energy source. Therefore, this study focuses on the numerical simulation of the physical parameters of solid-state dye-sensitized solar cell models through a comprehensive analysis of their absorber layers, back contacts, and interfacial layers to develop new and cost-effective charge transport materials (ETL and HTL), counter electrodes (CE), and photoanodes for enhanced efficiencies and stabilities. The device performance is significant in meeting the large industrial demand for secure electricity and simultaneously meeting the UN climate development goals, besides enhancing food security and nutrition, as detailed in Kenya's Big Four Agenda. Nevertheless, capitalizing on the "tune-ability" of material properties is an important action with huge potential for the industrial production of PVs. Thus, the better alternative is DSSCs in terms of fabrication cost and is also a non-pollutant; however, its efficiency has not achieved the theoretical limits of ~ 33%. Therefore, there is much more to be explored since almost infinite combinations and modifications of potential materials can improve solar performance.

CHAPTER TWO
LITERATURE REVIEW
A REVIEW ON THE CURRENT STATUS OF DYE-SENSITIZED SOLAR CELLS: TOWARDS SUSTAINABLE ENERGY

Abstract

Dye-sensitized solar cells (DSSCs) represent an attractive third-generation photovoltaic technology, characterized by their adaptability, roll-to-roll compatibility, low toxicity, lightweight nature, and favourable power conversion efficiencies (PCEs). However, their transition from laboratory to industrial scale has been slow because of their inability to compete with silicon-based cells in terms of stability and efficiency. For decades, research has been conducted on dye-sensitized solar cells (DSSCs) to improve the efficiency and cost-effectiveness of photovoltaics; however, these efforts have been insufficient. In order to improve efficiency and commercialization, their chemical and physical properties must be optimized. This article provides a concise overview of the most recent developments in the field of dye-sensitized solar cells (DSSCs), including the development of molecular engineering techniques, the pursuit of improved electrodes, effective sensitizers, and enhanced carrier transport materials (CTMs). This study compiles data regarding the historical development of DSSCs, as well as contemporary advancements such as surface morphology control, doping techniques, modelling and simulation, characterization, and recent pioneering research in photovoltaic studies. This review investigates the practical applications of dye-sensitized solar cells (DSSCs) in the Internet of Things (IoT) and portable electronics, as well as the use of nanostructured materials as photoelectrodes. The objective is to identify potential issues and future advancements. The primary goal of this work is to provide a concise summary of solar energy harvesting materials and optimization techniques for various components of DSSCs.

2.1 Introduction

Presently, the global population is increasing rapidly in tandem with energy consumption, with the possibility of energy demand surpassing population growth (Zeren & Akkuş, 2020). Essentially, nuclear, bioenergy, and fossil fuels are the primary sources of energy. The unabated use of nuclear

and fossil fuels like coal, natural gas, and liquefied petroleum gas (LPG) has resulted in the emission of greenhouse gases (GHGs) like methane (CH_4), nitrogen oxides (NO_X), and oxides of carbon (CO_X) has resulted and radioactive wastes including Technetium-99 (^{99}Tc) isotopes (Temba et al., 2016). These have had a significant impact on global climate patterns and degraded the natural ecosystem. To address the ever-increasing demand for energy and mitigate the adverse effects of conventional fossil fuels and nuclear energy resources on human and environmental health, many countries have transitioned to highly environmentally desirable alternative forms of energy that are considered renewable and ecologically friendly (Moustakas et al., 2020). An energy source that is affordable, secure, reliable, and with minimal ecological and environmental hazards is essential to the quality of life (Nadimi et al., 2017).

The most attractive option for producing heat and electricity is solar energy, which is recognized as a sustainable and eco-friendly source (Rono et al., 2021b). Various industries employ the heat and electricity generated by solar energy. Solar thermal energy is employed in the textile industry, chemical processing, space heating, and food processing. Conversely, electricity generated by solar has been utilized in telecommunications, agriculture, construction, transportation, and water treatment (Hassanien et al., 2016). The earth receives 1.20×10^7 watts of energy from the sun in a single day, which is enough to power the world for two decades (Crabtree & Lewis, 2007). In 1.5 days, the solar system produces approximately 1.7×10^{22} Joules of power (Crabtree & Lewis, 2007). This energy is equivalent to the amount of energy generated by the 3 trillion barrels of oil reserves on earth (Hayat et al., 2019). In view of this, the sun can be the most accessible source of energy, provided that the necessary solar infrastructure and technology are well-developed (Hayat et al., 2019). The sun is estimated to produce 4.6×10^{20} Joules in a single hour, which is equivalent to the global energy demand for one year (Crabtree & Lewis, 2007). In terms of industrial scope and technology, solar energy development is presently in its inception (Bella et al., 2015). Nevertheless, ongoing research is being conducted to improve the efficiency of harnessing the inexhaustible solar energy by rationally designing, characterizing, and fabricating material components, technologies, and processes.

When a photon with energy hv that exceeds the band gap energy, E_g, strikes and excites an electron from the valence band (VB) to the conduction band (CB) of a semiconductor during solar harvesting, generating an electron-hole pair. The excess energy, $hv - E_g$, is rapidly shed off as the

heated hole and electron thermalize to the band edge. The fundamental limitations in enhancing the light-to-electricity conversion of dye-sensitized solar cells (DSSCs) toward the Shockley-Queisser (S-Q) limits of ~ 33% are attributed to this energy loss (Fujisawa & Hanaya, 2018). However, these devices also suffer limitations related to intrinsic and extrinsic stabilities, energy losses in dye regeneration kinetics, and interfacial recombination loss kinetics (Godin & Durrant, 2021; Yadav et al., 2017). DSSCs have demonstrated record efficiencies of approximately 14.2% under a one sun illumination (1000 W/m^2 Air Mass Global (AM 1.5 G) (Yildiz et al., 2021). Numerous novel electron and hole acceptors have been proposed in recent research, garnering significant attention for their potential to reduce energy losses through the optimization of charge transfer kinetics (Nabil et al., 2021). Additionally, considerable research has been undertaken to enhance the efficiency of device architectures towards S-Q limits by optimizing and controlling the nanoscale morphology and interfacial engineering (Lunt et al., 2011). Furthermore, a growing body of photovoltaic research suggests that solid-state hole-transporting layers (HTLs) are ideal replacements for liquid electrolytes, which are not only volatile and toxic but also corrosive to cell components (Jang et al., 2019). Hole-transporting layers (HTLs) are essential for stabilizing solar cells, preventing internal charge recombination, and enhancing hole migration. Various HTLs, such as conducting polymers, small molecule hole conductors, and inorganic p-type semiconductors, have been proposed and applied in solid-state dye-sensitized solar cells (ssDSSCs) (Jang et al., 2019). In general, HTLs that are efficient should possess the following characteristics: (i) high thermal and photostability, (ii) excellent hole mobility, (iii) cost-effectiveness, (iv) high transparency in the visible spectrum, (v) the highest occupied molecular orbital (HOMO) should be greater than the valence band maximum (VBM) of the photosensitizer, and (vi) good solubility for easy film formation (Wang et al., 2020). In addition to facilitating the flow of holes to the cathode, HTLs also prevent the absorber layer from detrimental environmental factors, including moisture and oxygen (Wang et al., 2020).

Charge extraction and transportation from the photosensitive layer to the respective electrodes are enhanced by interfacial layers, including electron transport layers (ETLs) and HTLs (Naqvi & Patra, 2021). Additionally, these layers block the passage of ions that are oppositely charged to the respective electrode. The electron-transfer efficiency and the overall solar cell efficiency have been determined by electron-transmission in n-i-p ssDSSCs. To date, the electronic transmission

materials that have been extensively investigated include tungsten trioxide (WO_3), tin oxide (SnO_2), zirconium dioxide (ZrO_2), zinc (I) oxide (Zn_2O), titania (TiO_2), and zinc (II) oxide (ZnO) (Omar & Abdullah, 2014). While blocking the transport of holes, these materials enhance electron flow. Nevertheless, it is widely recognized that the development of effective ETLs is impeded by a vast scientific challenges, including (i) electron trapping tendencies, (ii) the inherent instability of the air, and (iii) the challenge of aligning the lowest unoccupied molecular orbital (LUMO) of the materials with the work function of the cathode (Lin et al., 2021). Figure 2.1 illustrates the optimization strategies and selection criteria for prospective ETMs.

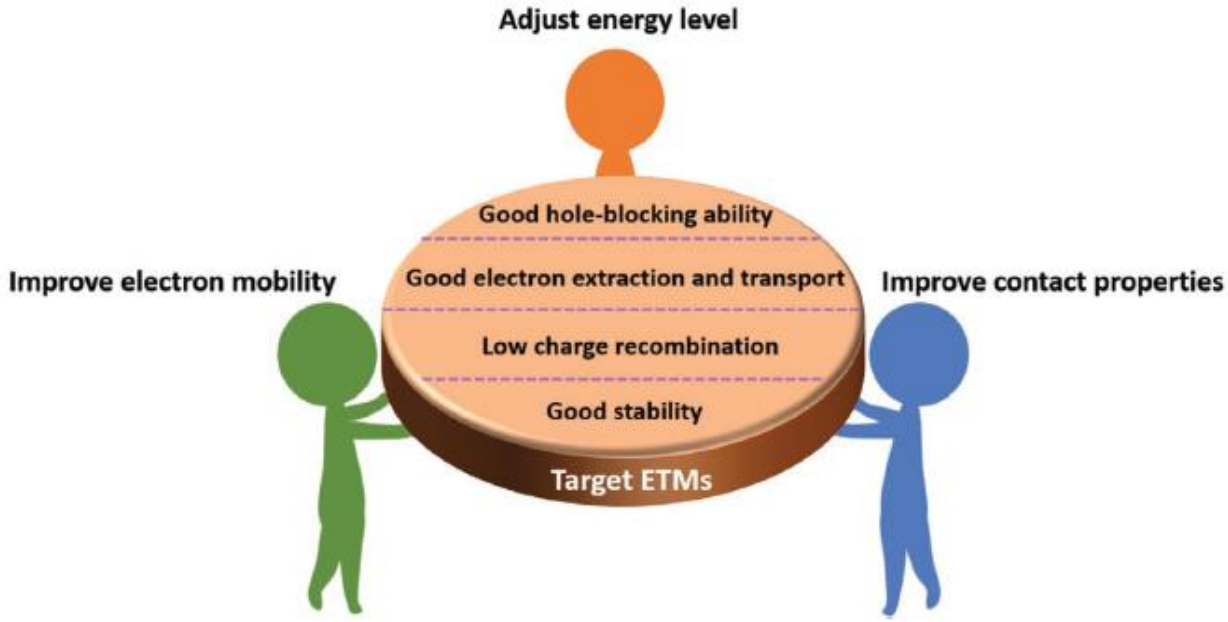

Figure 2.1: Selection criteria and optimization strategies for target electron transport layers (Wang et al., 2020)

Significant research is being conducted to identify better-performing ETLs, HTLs, and dyes for highly efficient DSSCs (Agarwala & Kabra, 2017). To expedite real-world applications, it is essential to investigate the electronic structure and structural properties that influence the optoelectronic properties of target materials. Experimental and theoretical investigations have been employed to calculate optical energy gaps, LUMO and HOMO energy levels, and molecular geometries. Molecular orbital theory (MOT) is closely related to band theory, as the CB and VB represent the LUMO and HOMO energy levels, respectively (Molapo et al., 2012). The energy

gap E_g is the difference between the LUMO and HOMO energy levels (cf. Equation 2.1) (Molapo et al., 2012).

$$E_g = E_{LUMO} - E_{HOMO} \quad (2.1)$$

The gap between VB and CB is the energy gap or the band gap, as depicted in Figure 2.2.

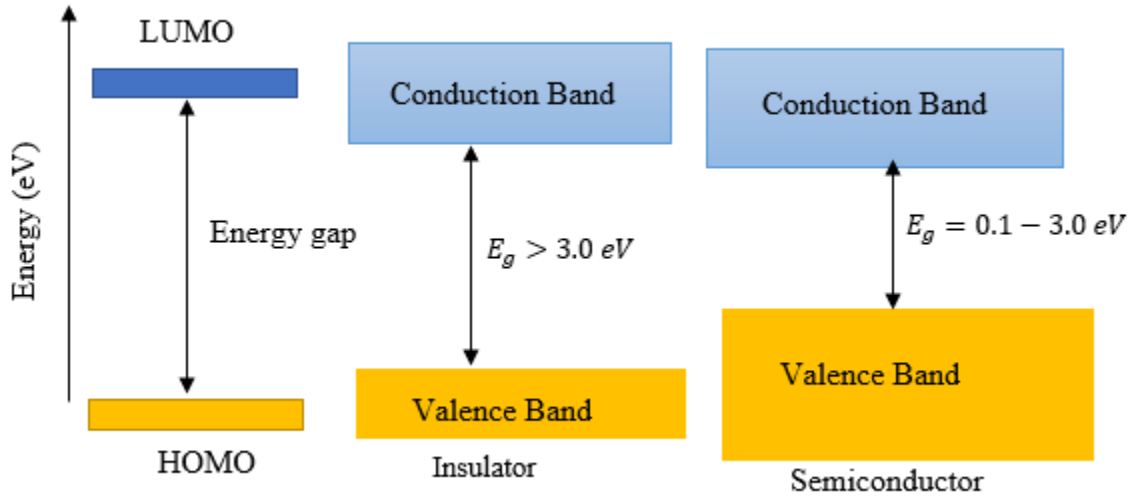

Figure 2.2: Comparison of the HOMO-LUMO and energy band diagram

To scale up photovoltaics, sensitizers with minimum environmental impact are also necessary for solar cells (Yashwantrao & Saha, 2022). The visible photoexcitation of sensitizers in these devices is essential for generating electron-hole pairs, thereby converting solar radiation into usable power. The dyes sensitizers employed in these devices have been the subject of intense investigation by researchers after the groundbreaking work of O'Regan and Grätzel (O'regan & Grätzel, 1991). Currently, numerous publications have examined the theoretical and experimental potential of natural and synthetic dyes for their application in DSSCs. Consequently, significant advancements have been made in the design and synthesis of a variety of metal-free (organic dyes), porphyrin compounds, and ruthenium complexes (Sen et al., 2023). When light is incident on a solar cell, the electrons are excited from the HOMO of the semiconductor to the LUMO of the anchored dye molecule. This is the reason why the theoretical and experimental principles of LUMO and HOMO energy levels of various sensitizers are indispensable for evaluating the performance of DSSCs (Maddah, 2022).

Third-generation solar cells are made up of nanostructured materials that are either entirely organic or a combination of inorganic and organic components. As a result, a diverse array of materials can be optimized to advance solar energy conversion efficiency cost-effectively and sustainably (Doumon et al., 2022). Dye-sensitized solar cells are based on cost-effective materials, relatively compact dimensions, and minimal environmental impact, making them a promising candidate for future advancements (Dhonde et al., 2023). It is worthwhile to note that the industrialization of DSSCs has been slow due to their inability to compete with the extensively deployed silicon-based cells in terms of efficiencies and stabilities (Kunzmann et al., 2018). Studies have shown that the efficiency of a photovoltaic system is dependent on various factors, including irradiance, reflection, spectral response, temperature, light source power intensity, system design, and the nature of the active material (Dhass et al., 2022). To further explore the reputation of DSSCs, data on publication growth year-wise were extracted from the ScienceDirect database (using dye-sensitized solar cell as search keyword). As shown in Figure 2.3b, the numbers of publications on DSSCs have increased from 967 in 2010 to over 1,392 in the first quarter of 2024.

(a) (b)

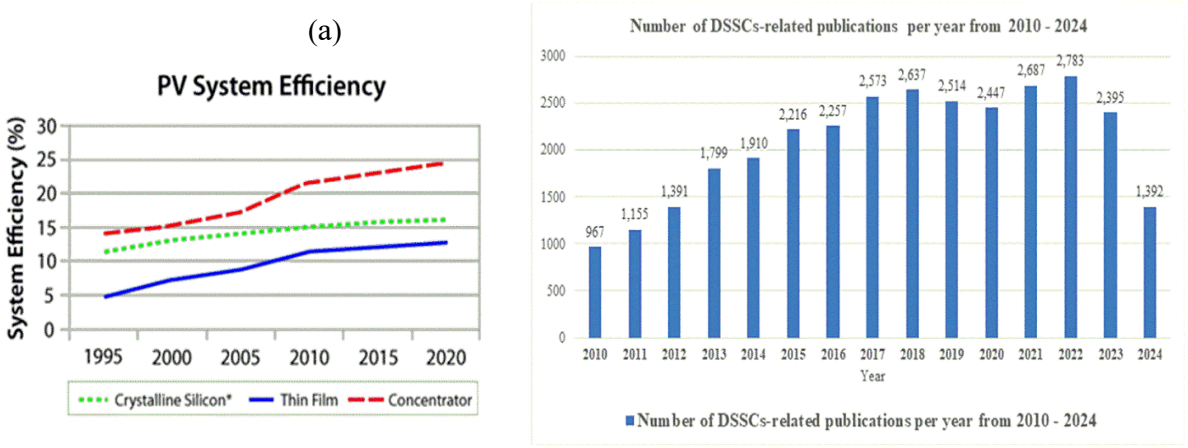

Figure 2.3: PV system efficiency of crystalline silicon, thin film, and concentrator technologies (a) and (b) number of DSSCs-related publications from 2010-2024

Figure 2.3 shows the decades of research activities that have been conducted on photovoltaics to improve their efficiency and cost-effectiveness. Nevertheless, these efforts remain insufficient, necessitating the refinement of their chemical and physical properties to enhance the efficacy and commercialization of DSSCs. The objective of this review is to bind the research findings of numerous researchers and offer a concise summary of the executed work on DSSCs. This review

article is necessary for the purpose of summarizing the research investigations on molecular engineering technologies, the search for superior carrier transport materials (CTMs), efficient sensitizers, and better electrodes. Additionally, this paper includes a concise summary of the research activities in the areas of surface morphologies, doping strategies, modelling and simulation, and characterization. Studies on the roles of the photo-anode, counter electrode, electrolyte, and photosensitizer are scattered. In this context, we have pursued a distinct trend, highlighting a variety of materials that have been investigated, as well as modelling and simulation methodologies, in search of highly efficient DSSCs and emerging applications for this photovoltaic technology.

2.2 The evolution of solar technologies

The first generation of solar technologies is silicon-based solar cells, which continue to dominate the commercial market and play a significant role in shaping the solar energy landscape (Heidarzadeh & Tavousi, 2019). They are divided into three categories based on the type of silicon used in the fabrication process: single-crystalline silicon (c-Si), multicrystalline silicon, and amorphous silicon (a-Si). Single-crystalline silicon with positive-negative junctions (Si p-n) has recorded a maximum efficiency of ~ 25% (Hayat et al., 2019). Conversely, polycrystalline Si, which is sliced into thin wafers after melting, solidifying, and orienting the crystals in fixed directions, has previously achieved efficiencies of 10.1%, 16.8%, and 20.4% (Litvinov et al., 2017). Compared to single-crystalline solar cells, polycrystalline photovoltaic (PV) cells have two main advantages: they are less expensive to make and have a lower number of defects in the crystal (Hayat et al., 2019). Although the development of ribbon silicon technology is anticipated to lower the production costs of first-generation PV devices significantly, the primary disadvantage of c-Si is its high cost and the complex fabrication process involved (Ramanujam & Singh, 2017).

The second generation, based on thin-film technologies, emerged in the market to reduce material dependency and the costs of first-generation silicon technologies (Iqbal et al., 2022). These cells consist of amorphous silicon (a-Si), copper indium gallium diselenide (CIGS), cadmium telluride (CdTe), and copper zinc tin sulphide (CZTS) (Nazeeruddin et al., 2011). Monocrystalline CdTe has a maximal efficiency of ~ 17% (Zhao et al., 2016). The evaporation technique is employed to deposit CdTe on a glass substrate during chemical fabrication. Nevertheless, these cells were not

scaled up in the photovoltaic market due to the toxicity of Cd and the limited availability of tellurium in the Earth's crust (Kumar et al., 2017). Conversely, a: Si has attained a maximum efficiency of 10.1% (Ji et al., 2019). They are cost-effective in terms of the material requirement; however, their performance decreases by 20% over time, and they suffer from instability issues (Hayat et al., 2019). Despite their high efficiency in comparison to CdTe and (a-Si), the energy market dominance of thin-film CIGS is limited by the scarcity and toxicity of the materials used, including Cu, Ga, In, Te, and Cd (Vigil-Galán et al., 2015). On the laboratory scale, their performance reached 20%; however, in commercial applications, it ranges between 12 and 14% (Hayat et al., 2019).

The production of high-efficiency, long-lasting, and thermally and photostable PV cells has been inspired by the "nano-world" in an effort to replace the rapidly depleting fossil fuels. This has resulted in the discovery of novel production techniques and the identification of new materials to address the intrinsic and extrinsic instabilities of solar cells. The advancement of nanotechnology has necessitated researchers to refine and control the nanoscale morphology and interfacial engineering of device architectures to enhance their efficiencies towards the S-Q limit of approximately 33% for single-junction photovoltaic devices (Guillemoles et al., 2019). As a result, these technologies resulted in the development of third-generation solar cells.

2.2.1 Third-generation photovoltaics

The present third-generation solar cells, which have proven to be affordable and capable of overcoming the shortcomings of the first and second generations of solar cells, were developed in response to the fundamental problems of the first two generations of solar cells (Mingsukang et al., 2017). According to Nazeeruddin et al. (2011), DSSCs and organic/polymer solar cells are the two most extensively researched third-generation solar cells. The third generation, which includes dye-sensitized solar cells (DSSCs), perovskites, organic solar cells, and quantum-dot solar cells, possesses outstanding qualities such as ease of manufacturing and affordability compared to conventional silicon technology (Mingsukang et al., 2017). Typically, a ruthenium-polypyridine dye anchored to a wide band semiconductor serves as the photosensitizer in DSSCs. Charge separation occurs at the interface when photo-induced electrons from VB of the dye are injected into the CB of an electron transport material like titanium oxide (TiO_2). The electrons diffuse from

the CB of TiO_2 to the anode where they are collected. Remarkably, after three decades of intensive research, the conversion efficiency of DSSC has increased from 7% to ∼12% (Rudra et al., 2019), and their thermal and photostability last for up to ten years (Raja et al., 2017). Other studies have also reported an efficiency of 13% for this technology, with minimal energy losses at excited states (Rondán-Gómez et al., 2019). Due to their low toxicity, ease of fabrication, affordability, more appealing designs, and high incident power conversion efficiency (IPCE), particularly in low-light conditions, these solar cell devices have piqued the interest of researchers following the seminal work of Grätzel (Amin et al., 2012). Table 2.1 presents a comparison of the durability, cost, and efficiency of the three generations of solar cells.

Table 2.1: Characteristic features of generational solar cells

Solar cell generation	Efficiency	Cost	Stability
First	High	High	High
Second	Medium	Medium	Medium
Third	Medium	Low	Low

The regeneration of dyes is facilitated by the redox couple in DSSCs, which is conventionally iodide/tri-iodide (I^-/I_3^-). Scientific reports have shown that liquid electrolyte-based DSSCs have achieved record efficiencies of 13% (Goh et al., 2022). Despite DSSC being a prospective technology, these liquid electrolytes exhibit low stability and tend to corrode the cell components (Kunzmann et al., 2018). In addition, they volatize (due to solvent leakage) because of the difficulty in achieving perfect sealing in these devices (Singh et al., 2019). Nevertheless, numerous studies have argued that these obstacles can be addressed by substituting liquid electrolytes with organic HTLs, ionic conducting polymers, inorganic p-type semiconductors, and room temperature molten salts (Sharma et al., 2018). Devices fabricated with these materials demonstrated lower efficiencies than DSSCs with liquid electrolytes as a result of (i) inadequate contact between the p-type semiconductor and the dyed TiO_2 porous film and (ii) low hole conductivity in polymer gel electrolytes, organic polymers, and molten salts (Singh et al., 2019). Various HTLs utilized in third-generation solar cells have been the subject of investigation and optimization in recent years. The absorption of a greater fraction of the irradiating photons increases cell efficiency; thus, thicker HTLs with high mobility are essential in device fabrication.

Moreover, these materials reduce charge recombination kinetics by expediting the transportation of charges to the electrodes (Rono et al., 2021a). Figure 2.4 (a) depicts a DSSC with solid-state hole transport material, while (b) is a DSSC with a liquid redox electrolyte.

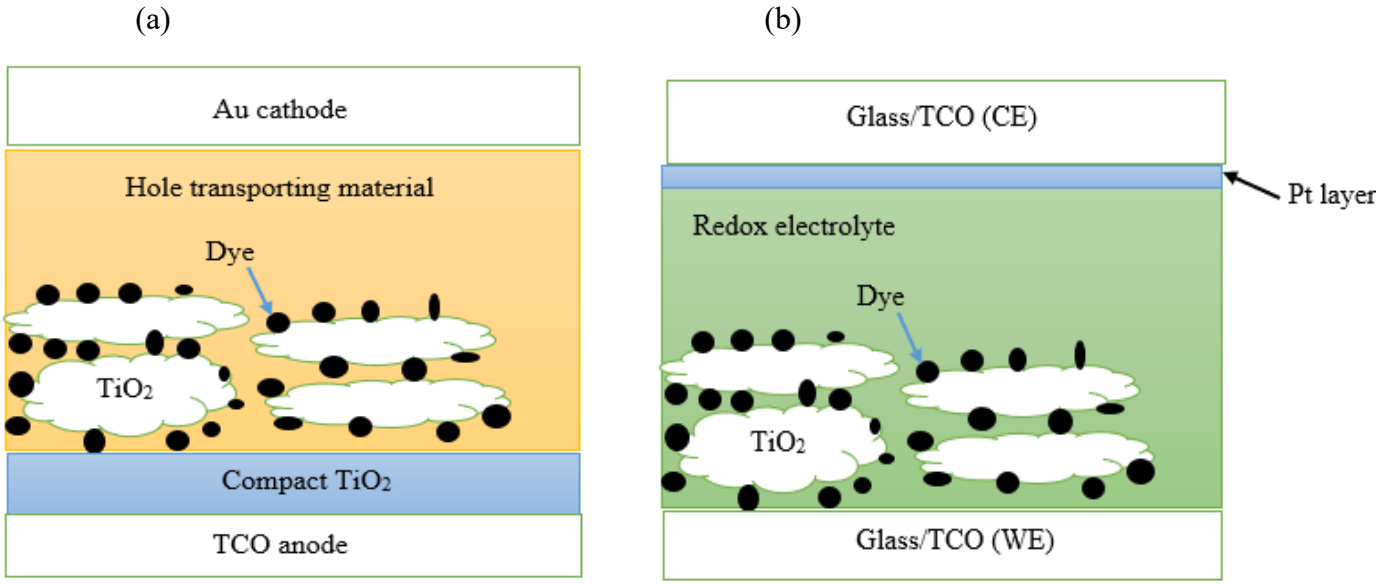

Figure 2.4: Schematic representation of solid-state dye-sensitized solar cell (a) and (b) dye-sensitized solar cell with redox electrolyte

2.3 The principle of operation

Three primary components comprise DSSCs: (1) the electrolytes, which are typically I^-/I_3^- redox couples, (2) the counter electrode (CE) coated with conducting polymer or carbon or platinum-based materials on transparent conducting materials (TCO), and (3) the working electrode (also referred to as the photoanode) composed of TCO-coated substrates with ZnO and TiO_2 films for electron transport, as illustrated in Figure 2.5.

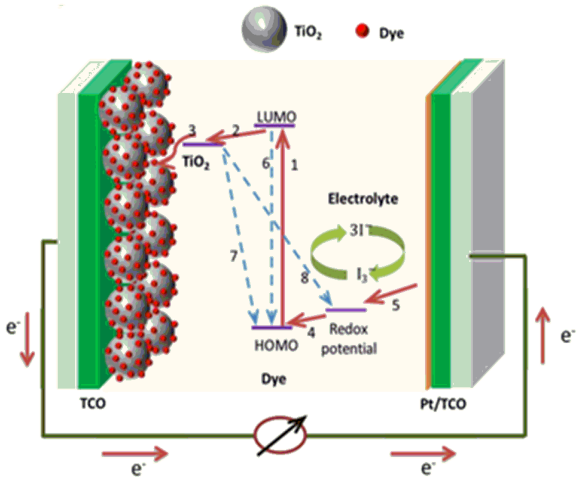

Figure 2.5: The main components of DSSCs (Dawo & Chaturvedi, 2023)

The operating principle of a DSSCs is as follows;

Step 1: Photoexcitation of the electron in the dye

The dye molecules anchored on the metal oxide conductor absorb a broad spectrum of sunlight. When the irradiating photons strike the dye molecules, they change from the HOMO to the LUMO electronic states, called the excited state (D^*), as represented in reaction (Rxn) 2.1;

$D/TiO_2 + hJ \rightarrow D^*/TiO_2$ (photo excitation) (Rxn 2.1)

Step 2: Electron injection

The electrons in the excited state of the dye molecule (D^*) is injected into the conduction band (CB) of the ETM (typically TiO_2), leaving holes (D^+) in the dye (Rxn 2.2). The injected electrons are then transported to the TCO surface. This process initiates the generation of electron-hole pairs within a typical time constant, *k,* of approximately 10^{-12} seconds under one sun illumination (298 K, spectral intensity corresponding to AM 1.5 global standard solar spectrum, and 1000 W/m^2)

$D^*/TiO_2 \rightarrow D^+/TiO_2 + e^-/TiO_2$ ($k \approx 10^{-12}\ s$) (Rxn 2.2)

Step 3: Dye regeneration

When the dye loses electrons, it gets oxidized, ready to accept electrons from I^-/I_3^- redox couple, as shown in Rxn 2.3. The accepted electrons from the redox couple refill the HOMO of the dye,

making it ready to continue absorbing irradiating photons. Then the dye in its ground state continues to generate excited electrons.

$2D^+/TiO_2 + (RE)3I \rightarrow 2D/TiO_2 + I_3^-$ (OX) $(k \approx 10^{-4}\ s)$ (Rxn 2.3)

Step 4: Regeneration of the electrolyte

The tri-iodide ion (I_3^-) in the electrolyte is reduced when the photoexcited electrons travel to the CE through the load (Rxn 2.4). The electrolyte recovers its ground state by accepting electrons from the CE, and the catalyst coated on the CE helps in fast reduction. The time constant for this reaction is $\approx 10^{-6}\ s$.

(OX)$I_3^- + (CE)2e^- \rightarrow (RE)3I^-$ (regeneration of I^-) (Rxn 2.4)

There are recombination reactions with excited electrons at the CB of the TiO_2, which are detrimental to device performance. These are the regeneration of the oxidized dye (Rxn 2.4) and the regeneration of the electrolyte redox couple (Rxn 2.5). The selection of optoelectronic materials that favour regeneration rates and avoid energy losses due to recombinations improves the device performance.

Step 5: Recombination by D^* dark reaction

$e^-/TiO_2 + D^+/TiO_2 \rightarrow D/TiO_2\ (k \approx 10^{-4}\ s)$ (Rxn 2.5)

Step 6: Recombination by OX, dark reaction

$e^-/TiO_2 + OX \rightarrow RE\ \ (k \approx 10^{-2}\ s)$ (Rxn 2.6)

In step 7, the electron transfer from the CB of the TiO_2 to the FTO occurs. The injected electrons convert solar energy into electrical energy. At the same time, recombination reactions may happen in the FTO due to the regeneration of the dye and the redox couple, as expressed in reactions Rxn 2.7 and 2.8, respectively.

Step 7: Electron transportation

$e^-/TiO_2 + FTO \rightarrow e^-/FTO + TiO_2\ \ (k \approx 10^{-3}\ s)$ (Rxn 2.7)

Step 8: Back reaction from FTO to dye

$e^-/FTO + D^*/DFTO \rightarrow D/FTO$ (Rxn 2.8)

Step 9: Back reaction from FTO to electrolyte

$$e^-/FTO + OX \rightarrow RE \quad \text{(Rxn 2.9)}$$

Other energy loss reactions are electrolyte and dye reduction reactions by themselves, as represented in Rxn 2.10 and 2.11, respectively.

Step 10: electrolyte reduction reaction

$$OX + e^- \rightarrow RE \; k \approx 10^{-5}\, s \quad \text{(Rxn 2.10)}$$

Step 11: Dye reduction reaction

$$OX + e^- \rightarrow RE \quad \text{(Rxn 2.11)}$$

To optimize the performance of DSSCs, the electron injection (Rxn 2.1) and the dye regeneration process mediated by the electron donor (step 4) should be faster than the decay of the dye (Rxn 2.5) and the back reaction between the injected electron and the oxidized dye (Rxn 2.6). Efficient" regeneration of the charge mediator at the CE improves the performance of DSSCs.

It is crucial to comprehend the dynamics of charge transportation and loss reactions within junctions to assess the overall performance of DSSCs (Dawo & Chaturvedi, 2023). The electron collection efficiency in DSSCs is directly influenced by the diffusion length, which is the average distance an electron diffuses in TiO_2 before recombining with tri-iodide ions. Consequently, this parameter has a direct impact on short circuit current density. The electron collection efficiency in solar cells is believed to be enhanced by a large electron diffusion length, according to previous reports. It is widely recognized in the literature that the diffusion length must be 2-3 times greater than the TiO_2 film to ensure the efficient collection of electrons in DSSCs. The transportation of photoexcited electrons from the excited dye to the CB of the semiconductor metal oxide should be faster (order of picoseconds and femtoseconds) than the process by which the dye decays from its excited state to the ground state (nanoseconds), as illustrated in Figure 2.6. The loss of photoexcited electrons should be minimized by accelerating the regeneration of I^- at the CE and the dye regeneration by the I^-/I_3^- redox couple. The kinetics view on the operating principle of DSSCs is illustrated by blue arrows (charge transportation) and black arrows (loss reactions).

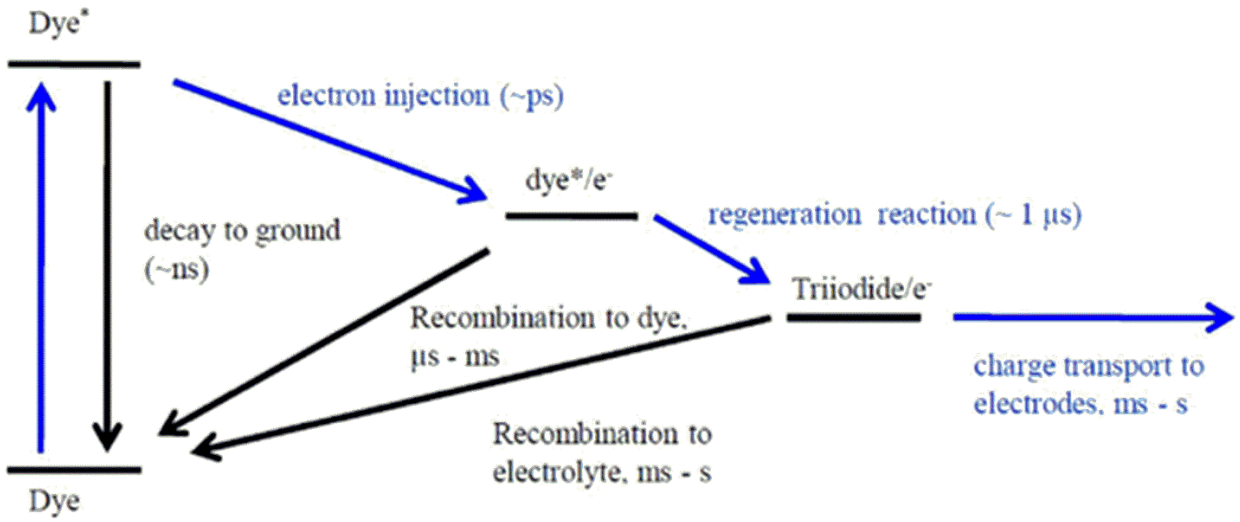

Figure 2.6: The kinetics view of the operating principle of DSSCs (Dawo & Chaturvedi, 2023)

The photovoltaic process is initiated by light absorption, which leads to the quasi-Fermi level splitting of electrons and holes, respectively, denoted as E_{Fn} and E_{Fp} (Xiang et al., 2021). The open-circuit voltage (V_{OC}) in dye-sensitized solar cells (DSSCs) is generated by the separation of the quasi-Fermi level for holes in the HTL (redox potential of the electrolyte) (E_{Fp}) and the quasi-Fermi level for electrons (E_{Fn}) in the metal oxide (Snaith, 2010). As a result, the maximum V_{OC} value is obtained when E_{Fn} is pushed closer to the CB and the LUMO of the absorber material, and when there is minimal potential loss during the transition from the excited state of the absorber material to E_{Fn} of the metal oxide. Charge transport and recombination kinetics are responsible for electronic losses in DSSCs (Snaith et al., 2008). The potential loss in DSSCs is indirectly influenced by charge transport and recombination, whereas the accelerated recombination rates of charge carriers directly influence photocurrent. As charge recombination rates decrease, E_{Fn} is pushed to the CB until the recombination kinetics are in equilibrium with the charge separation rate (Snaith et al., 2008). Fill factor (FF) and short-circuit current (J_{sc}) in specific systems may be improved by the efficient transmission of charge carriers, which in turn enhances charge collection. The operational principle of dye-sensitized solar cells is illustrated in Figure 2.7 (Snaith et al., 2008).

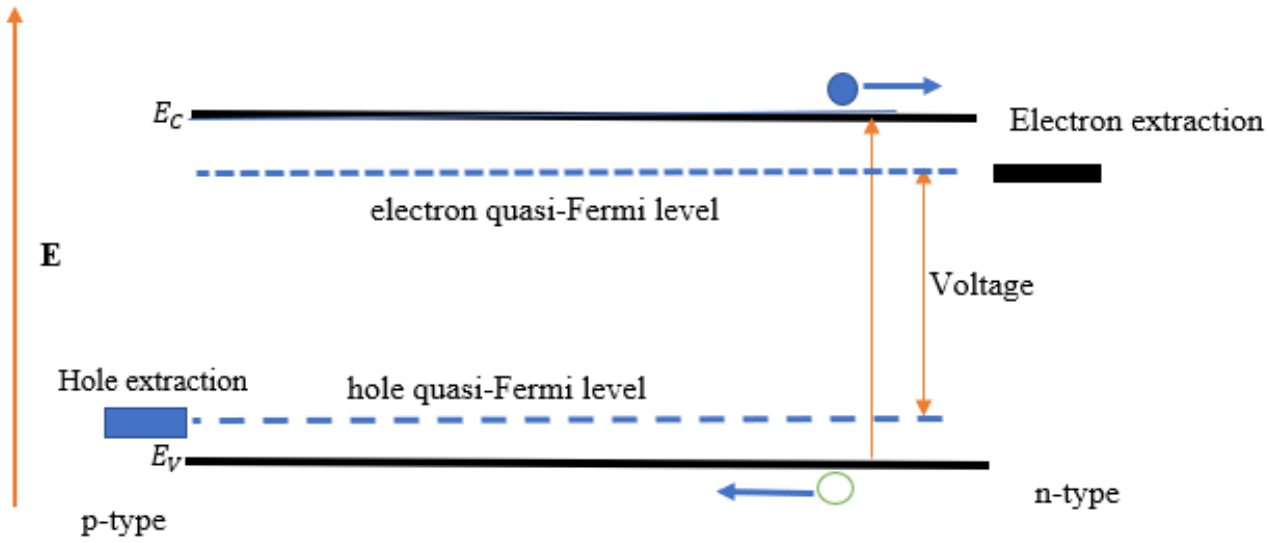

Figure 2.7: Operation principle of a dye-sensitized solar cell under photon illumination

2.4 Hole transport materials

The substitution of platinum (Pt) electrodes with cost-effective materials and the replacement of the liquid electrolyte with a solid conduction system are remarkable advancements in hybrid photovoltaic devices (Singh et al., 2019). The objective is to enhance the safety of cell fabrication and decrease the overall cost. The transition of DSSCs to an industrial production scale is impeded by ineffective encapsulation, volatilization, and solvent leakage. Consequently, the viable alternative is to employ all-solid-state materials in cell fabrication. Despite the prospects of solid-state systems in overcoming volatilization and leakage phenomena, the performance of HTLs remains fundamentally limited. The primary scientific challenge of these materials is the inadequate interfacial contact and permeation within the mesoscopic structure of the photoelectrode. An ideal HTL candidate should possess the following characteristics: good thermal and photochemical stability, long-term stability in the air, suitable energy levels to align with the photosensitive layer, and good hole mobility (Wang et al., 2020). The growing number of studies on HTLs in recent years has attracted significant scholarly attention, as evidenced by the increasing interest in both organic and inorganic HTLs. A summary of the various electrolytes employed in ssDSSCs is illustrated in Figure 2.8.

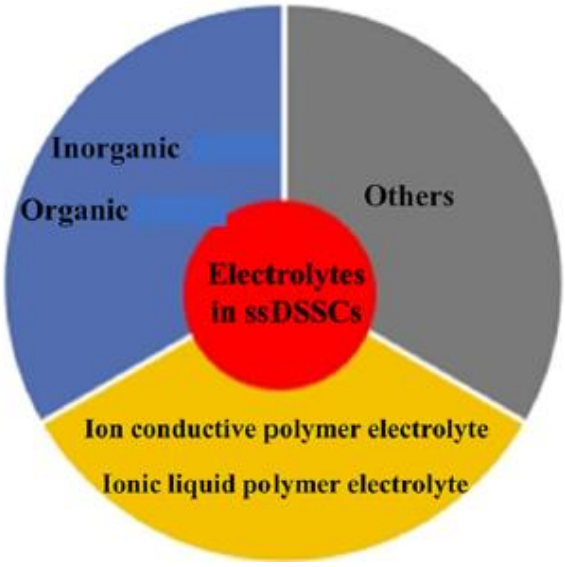

Figure 2.8: A summary of different electrolytes employed in ssDSSCs (Singh et al., 2019)

2.4.1 Organic hole transport layers

After Grätzel and colleagues reported a ssDSSC in 1998 that utilized spiro-OMeTAD as a p-type layer, organic HTLs have been the subject of extensive research (Zhang et al., 2016). In addition, poly(3-hexylthiophene) (P3HT) and poly(3,4-ethylenedioxy-thiophene) (PEDOT) have been examined as potential HTLs in ssDSSCs. Nevertheless, due to the presence of three phenyl rings and a lone pair of electrons at the nitrogen atom, Spiro-OMeTAD has demonstrated superior performance, thereby increasing the stability of the cation and facilitating delocalization (Yang et al., 2018). Abate et al. (2013) noted that Spiro-OMeTAD has relatively reduced hole mobilities and that recombination of charge kinetics is a limiting factor. Nevertheless, research has indicated that the addition of chemical dopants, including $Li[(CF_3SO_2)_2N]$ and $N(PhBr)_3SbCl_6$, can enhance electrolyte conductivity and suppress interfacial recombination (Hsu et al., 2012). In 2011, Grätzel and his colleagues employed a chemical doping strategy by incorporating Co (III) complexes into Spiro-OMeTAD in ssDSSCs. They reported a device performance of 7.2% under a one sun (Air Mass 1.5 Global) (Burschka et al., 2011). Figures 2.9 depict the chemical structures of Spiro-OMeTAD and PEDOT: PSS HTLs utilized in solid-state dye-sensitized solar cells, respectively.

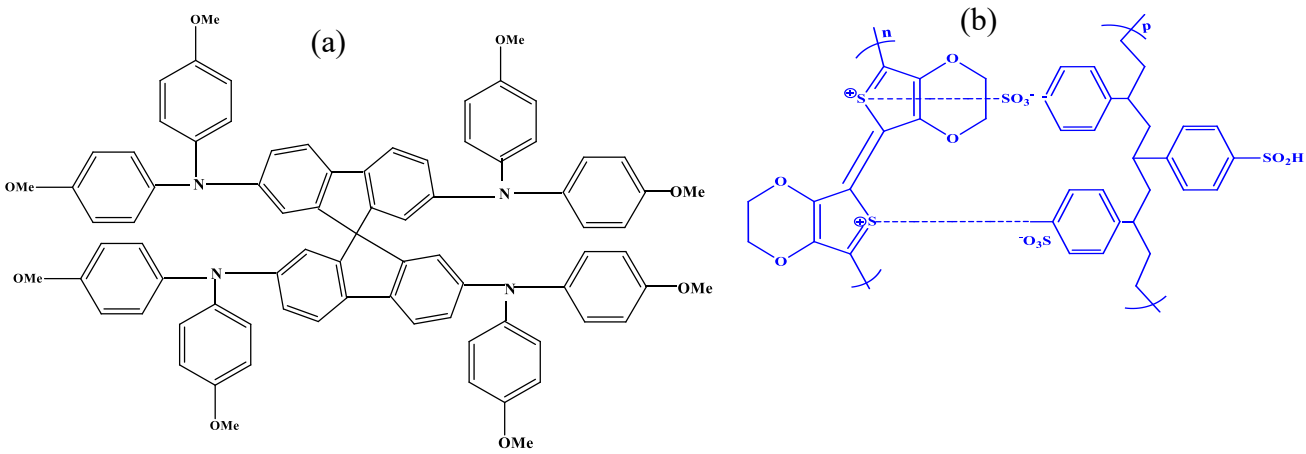

Figure 2.9: Chemical structures of Spiro-OMeTAD (a) and (b) PEDOT: PSS hole transport materials

Poly(3,4-ethylene dioxythiophene) (PEDOT) exhibits remarkable stability at ambient temperatures, high transparency, and superior electrical conductivity across the visible spectrum (300-500 Scm-1), rendering it suitable for applications in ssDSSCs (Wei et al., 2014). Since its development at Bayer AG almost 40 years ago, PEDOT has emerged as the most favoured polymeric organic conductor for electronic, antistatic, and optoelectronic applications. Water-soluble poly(styrene sulfonic acid) (PSS) doping produces PEDOT: PSS. Various doped PEDOT-based materials, including PEDOT: PSS, have been investigated for the fabrication of DSSC cathodes in redox shuttles due to their superior electrocatalytic activity and effective hole transport mechanisms (conducting holes via charge hopping) across cell electrodes (Yang et al., 2018).

Prior researchers, including Wei et al. (2014), examined the performance of DSSCs employing PEDOT as a counter electrode. They polymerized PEDOT on conductive glass, applied N719 dye to nanocrystalline TiO_2, and utilized I_3^{-1}/I^- as the electrolyte in their device. Their work aimed to compare the performance of DSSCs utilizing sputtering platinum electrodes with those employing PSS-doped PEDOT and p-toluenesulfonate (TsO) under air mass (AM) 1.5 Global illumination. Table 2.2 provides a summary of their findings.

Table 2.2: Photovoltaic performance of dye-sensitized solar cells using different counter electrodes

Counter electrode	V_{oc} (V)	J_{sc} (mAcm^{-2})	FF	PCE (%)
Pt	0.68	11.1	0.62	4.27
PEDOT: TsO	0.67	11.2	0.61	4.60
PEDOT: PSS	0.68	11.0	0.28	2.10

The TsO-doped PEDOT counter exhibits comparable current-voltage characteristics to sputtered Pt, as depicted in Table 2.2. Specifically, the PCE, FF, J_{sc}, and V_{oc} are approximately equivalent. This can be attributed to the partial exchange of I_3^- and I^- anions in the electrolyte with TsO- in PEDOT: TsO, which enhances I_3^-/I^- redox reactions. This demonstrates that PEDOT: TsO can serve as an alternative counter electrode in DSSCs. Additionally, it has been observed that the charge-transfer resistance increases as the thickness of the PEDOT: TsO film increases (Saito et al., 2002). Nevertheless, this issue can be resolved by employing thin PEDOT: TsO films as a counter electrode to enhance the efficacy of the device. The low photovoltaic performance of PEDOT: PSS, in contrast, can be attributed to the blockage of I_3^- or I^- from contacting the active sites of PEDOT: PSS by PSS. The blockage of I_3^- or I^- leads to an increase in overpotential and oxidative current, which subsequently diminishes the performance of DSSCs. In addition, the conductivity of PEDOT: PSS is lower than that of Pt and PEDOT: TsO counter electrodes.

The conductivity of the PEDOT: PSS counter electrode can be enhanced by treating it with dimethyl sulfoxide (DMSO), dichloromethane, *N, N*-dimethylformamide, and *N, N*-dimethylacetamide, as demonstrated by other studies (Chen et al., 2007). Additionally, research contends that the conductivity of a PEDOT: PSS counter electrode that has been treated with DMSO can be further improved by doping it with carbon black (Wei et al., 2014). For instance, the efficiency of the DSSC was 5.81% higher than that of the device fabricated using Pt as the counter electrode and 5.66% when the counter electrode was DMSO-treated PEDOT: PSS (with 0.1 wt% carbon black) (Chen et al., 2007). Spiro-OMeTAD and PEDOT: PSS have been extensively employed as HTLs in organic and perovskite solar cells (Jahantigh & Safikhani, 2019). One of the benefits of these materials is that their photovoltaic performance can be enhanced through secondary doping, enabling the production of flexible solar cells. A theoretical

investigation was conducted by Jahantigh and Safikhani (2019) to compare the photovoltaic performance of the HTLs in ssDSSCs. They found that PEDOT: PSS has superior efficiencies compared to Spiro-OMeTAD, as indicated in Table 2.3.

Table 2.3: A comparison of the current-voltage characteristics of DSSCs based on Spiro-OMeTAD and PEDOT: PSS hole transport materials

Counter electrode	$\mathbf{V_{oc}}$ **(V)**	$\mathbf{J_{sc}}$ **(mAcm^{-2})**	**FF**	**PCE (%)**
Pt	0.68	11.1	0.62	4.27
PEDOT: TsO	0.67	11.2	0.61	4.60
PEDOT: PSS	0.68	11.0	0.28	2.10

In a recent study on the photovoltaic performance of solid-state polymerized (SS-PEDOT), Jang et al. (2019) showed promising stabilities based on surface morphology studies. The enhanced penetration depth between conductive PEDOT and TiO_2 nanoparticles, which simultaneously improved the ionic conductivity of the sample and long-term stability of more than 1000 hours, was the reason given by the authors. Furthermore, their results showed that, in contrast to the liquid-based DSSCs, the J-V curve of the proposed ssDSSCs increased over time. Although the stability measurements were not sufficiently improved, the authors suggested a more stable device fabrication by using SSP conductive polymer and a well-known stable amphiphilic ruthenium dye, cis-bis(isothiocyanato)(2,2′-bipyridyl-4,4′-dicarboxylato)(4,4′-di-nonyl-2′-bipyridyl)ruthenium(II) (Z907) (Jang et al., 2019).

In its pure (intrinsic) form, Spiro-OMeTAD exhibits low hole mobility and conductivity due to its twisted spiro-centre, which hinders π–π stacking essential for effective charge transfer, hence limiting device performance (Yang et al., 2018). Doping strategies have been recognized as an effective method that enhances charge transfer in HTLs. P-type dopants, including metallic salts, metal-organic complexes, peroxides, electron acceptors, and protic ionic liquids, have effectively improved the performance of these devices (Abate et al., 2013). However, the currently deployed p-type dopants are limited by their high reactivity in ambient conditions and inadequate solubility in organic solvents. Consequently, research has focused on identifying p-type dopants that exhibit excellent stability in air and possess high solubility in organic solvents. Yang et al. (2018) used a novel p-type dopant, 2,2,6,6-tetramethyl-1-oxopiperidinebromide salt (TEMPO-Br), a stable N-

oxoammonium salt, to improve the photovoltaic performance of Spiro-OMeTAD. This salt has been effectively used in inorganic semiconductors, including Fe_3O_4 (Chen et al., 2013) and TiO_2 (Yang et al., 2018). Yang et al. (2018) examined the electrochemical and photophysical characteristics of TEMPO-Br-doped Spiro-OMeTAD. Their research indicated that TEMPO-Br boosts hole mobility, conductivity, and photovoltaic performance compared to undoped Spiro-OMeTAD. Furthermore, this p-type dopant enhances device stability, proving to be a viable impurity for solution-processed organic semiconductors (Yang et al., 2018).

2.4.2 Inorganic hole transport layers

Although PEDOT: PSS has been regarded as a superior HTL candidate in DSSCs, it is necessary to incorporate an electron-blocking layer due to its inadequate electron-blocking properties. The efficiency loss mechanisms are the consequence of the semi-metallic character of this organic HTL. To address these scientific challenges, researchers have been compelled to develop novel HTLs, particularly those of the organic variety. In ssDSSCs, copper (I) thiocyanate (CuSCN) and copper (I) iodide (CuI) are the most frequently employed inorganic HTMs. These materials exhibit high conductivity, suitable energy conversion, and excellent transparency. Copper(I) thiocyanate (CuSCN) is a semiconductor with a wide bandgap exceeding 3.4 eV (Wijeyasinghe et al., 2018). It has been employed in organic photovoltaics, perovskite solar cells, organic light-emitting diodes (OLEDs), and transparent thin-film transistors (TFTs) due to its lower costs and solution-processability (Wijeyasinghe et al., 2018). Despite its low conductivity (1×10^{-1} $mScm^{-1}$), CuSCN exhibits greater stability (Wang et al., 2018). The introduction of dopants to inorganic semiconductors has enhanced their electrical properties, similar to molecular doping in organic semiconductors. Wijeyasinghe et al. (2018) conducted a thorough experimental and theoretical investigation into the impact of doping CuSCN HTL interlayers with fluorinated fullerene derivatives ($C_{60}F_{48}$). The authors observed that a p-doped CuSCN HTL significantly enhances hole extraction, becomes more conductive, reduces trap density, increases hole concentration, exhibits a decrease in the density of shunting pathways, and increases the density of charge conduction pathways. Arguably, the p-doping strategy of CuSCN HTL has a substantial impact on the hole-transport properties, potentially enabling the development of new device applications and establishing numerous new research avenues. The crystalline phases of copper (I) iodide are alpha

(α), beta (β), and gamma (γ), and its band gap is 3.1 eV. Since the γ crystalline phase exhibits hole-conductivity characteristics and is stable at ambient temperatures, it finds significant use in ssDSSCs (Tennakone et al., 1998). This material has become a focus of numerous scientific investigations after it was reported as a feasible HTL for ssDSSCs in 1995 (Zainun et al., 2013). Its development was slow because scientific reports indicated that CuI could not effectively fill the vacancies of the TiO_2 layer, that it was difficult to control the grain size of CuI, and that it infiltrated the inside of the TiO_2 layer, causing a short circuit (Wang et al., 2020).The photovoltaic performance of several ssDSSCs with CuSCN and CuI as the HTLs is presented in Table 2.4.

Table 2.4: Photovoltaic performance of different DSSCs architectures employing different HTLs and dye sensitizers

HTL	**Dye**	V_{oc} **(V)**	J_{sc} **(mA cm^{-2})**	**FF (%)**	**PCE (%)**	**Ref.**
CuSCN	N3	0.59	7.8	0.44	2	(O'Regan et al., 2002)
	N719	0.58	10.52	0.56	3.39	(Premalal et al., 2012)
CuI	Pigment cyanidin	0.38	2.5	-	2.4	(Tennakone et al., 1995)
	N3	0.59	6.84	0.58	3.8	(Meng et al., 2003)
	N3	0.62	13	0.58	4.7	(Kumara et al., 2004)
	N3	0.73	14.5	0.70	7.4	(Sakamoto et al., 2012)
	D131+D358 +DIPDAB2	0.65	22.0	0.71	10.1	(Kato et al., 2018)

2.5 Electron transport materials

To improve charge-collecting efficiency, DSSCs need electron transport layers (ETLs) (Mahmood et al., 2017). High FF, high V_{oc}, strong light photon absorption, improved directional charge transfer, and thermodynamically better photo-generated carrier population operation all depend on the existence of ETLs (Elseman et al., 2020). Serious research is in progress to find ETL films with the ideal CB, compact morphology, and high carrier mobility. The extensively researched ETLs are classified as organic, inorganic, or a hybrid of organic and inorganic materials. They differ in their costs, transport capabilities, and stabilities. In a DSSC device, the photosensitive

layer is sandwiched between carrier transport materials (CTMs) – HTLs and ETLs. Therefore, it is crucial to identify the most suitable ETLs for DSSCs to enhance the carrier transport in highly efficient devices (Hezam et al., 2018).

Numerous publications have focused on a diverse array of ETLs, such as metal oxide heterostructured nanoparticles, metal oxide composites, and metal oxide materials in thin-film solar devices (Elseman et al., 2020). In addition to the conventional ETL material, TiO_2, transition metal oxides, such as SnO_2, ZnO, WO_3, IGZO, and ZnOS, provide desirable electron extraction characteristics (Elseman et al., 2020). Carbon-60 (C_{60}), phenyl-C_{71}-butyric methyl ester ($PC_{71}BM$), and (6,6)-phenyl-C_{61}-butyric methyl ester ($PC_{61}BM$) are all organic ETLs that have been reported thus far. The J-V curves are enhanced by the efficient charge collection of charge carriers, as the ETL layers are crucial for the extraction and transport of electrons to the electrode (Elseman et al., 2020).

The selection criteria for ETLs include: (1) electrical conductivity, which affects charge transfer and collection at the electrodes; (2) energy level alignment, which influences charge injection and recombination kinetics efficiency; (3) trap states, which affect charge transfer and recombination reactions; (4) carrier management, which affects photo-induced charge and collection; (5) morphology, which affects how it makes contact with the active layer and its deposition; and (6) interfaces, which are essential to comprehending recombination of charge (Elseman et al., 2020). To prevent current leakage from films and pinholes, materials selected for third-generation solar cells should have thick morphologies free of pinholes (Shariatinia, 2020). Additionally, they should not chemically react with cathode electrodes and adjacent light-absorbing layers. For the improved electron-accepting property, it should also have a lower LUMO in comparison to the dye. Figure 2.10 provides a summary of the variables influencing the performance of different ETLs.

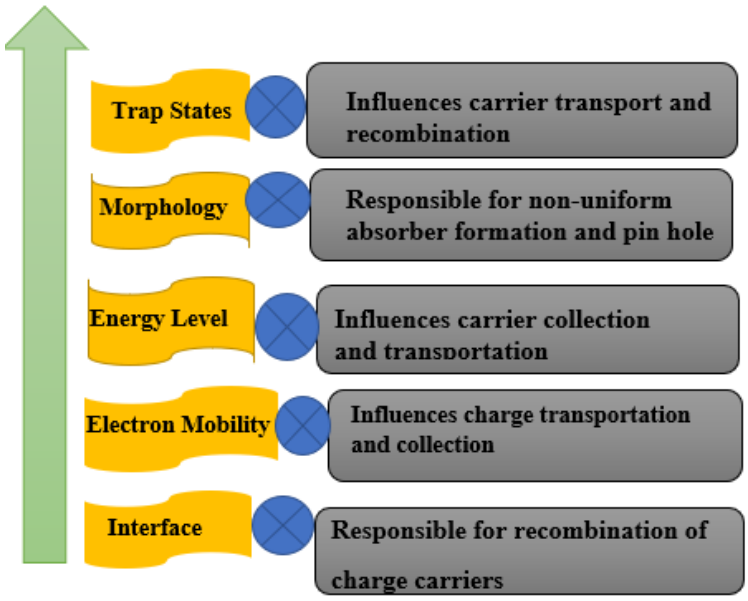

Figure 2.10: Important factors affecting the performance of different electron transport layers employed in DSSCs (Elseman et al., 2020)

2.5.1 Inorganic electron transport layers

The well-known inorganic ETL, titanium (TiO_2), has been used in a variety of thin-film solar systems, including DSSCs and perovskite solar devices (Awsha et al., 2021). According to previous researchers, TiO_2 has been effectively used as a compact mesoscopic double layer in mesoporous perovskite solar cells and as a compact single layer in planar perovskite solar cells (Prajapat et al., 2023). Despite problems with instability and energy loss, studies on TiO_2 suggest that mesoporous perovskite solar cells have greater PCEs than planar perovskite-based solar cells. Furthermore, TiO_2, as the ETL, has shown superior photovoltaic efficiency in DSSCs due to its outstanding stability and desired optoelectronic properties. According to Raj et al. (2021), the valence band minimum (VBM) and conduction band minimum (CBM) of TiO_2 are ~ 7.3 eV and 4.2 eV, respectively, ensuring effective electron collection and hole blocking. Spray pyrolysis, atomic layer deposition, chemical bath deposition, and the spin-coating technique are some of the film formation techniques used in device fabrication employing TiO_2 as ETL (Mayabadi et al., 2014). Different phases, including TiO_{2-} (monoclinic), rutile (tetragonal), anatase (tetragonal), and brookite (orthorhombic), have all been effectively used as ETLs in DSSCs (Akin & Sonmezoglu,

2018). Additionally, perovskite solar cells are frequently fabricated using TiO_2 as the ETL. Non-stoichiometric defects that impair cell performance are the underlying challenges limiting the application of TiO_2, as well as other metal oxides. The formation of oxygen vacancies during thermal annealing processes is linked to these bandgap defects from trap states (Dhonde et al., 2021). The trap states slow photoelectron transport from the active layer to the electrode. Effective electron injection is inhibited when the deep-level states of TiO_2 are located near the interface with the dye (Ho et al., 2017). As a result of increased charge recombination, the performance of the device declines. Several known techniques exist to passivate these traps and reduce the oxygen vacancy density in the TiO_2 coating. These consist of morphological modification, oxygen plasma treatment, and dopants such as Mg[18], Nb[19], Fe[23], Y[20], Sn[21], Fe[22], chromium (Cr), and manganese (Mn) (Dhonde et al., 2017). Additional strategies include use of acetylacetonated additives, graphene quantum dots, self-assembled monolayer Fullerene C_{60} and other ETLs like $PC_{61}BM$ and $PC_{71}BM$, interface engineering, doping, and surface treatment (Dhonde et al., 2019).

Tin dioxide (SnO_2) is a promising ETL contender with superior properties to replace traditional TiO2 in the search for low-temperature processable DSSCs, as it requires low-temperature fabrication procedures. Additionally, it has a deeper CB than TiO_2 to facilitate quicker electron transport and extraction. It also possesses a broader bandgap of 3.6-4.2 eV, which increases optical transmittance, improves conductivity, and lowers UV photocatalytic activity (Sharma, 2020). Tin dioxide (SnO_2) has fewer oxidative holes in the VB under UV light than anatase TiO_2, which improves solar cell stability and inhibits the deterioration of the active layer. Due to undesirable band alignment with the LUMO of the commonly employed N719, black dye, and N3 dyes, SnO_2-based DSSCs have lower PCEs than TiO_2-based DSSCs, despite their good optoelectrical features (Hossain et al., 2017). The decreased V_{OC} is attributed to high overpotentials at dye/SnO_2 contacts, whereas this decreased efficiency may be connected to charge recombination. According to some researchers, doping techniques improve overall photovoltaic performance; hence, creating new designs and coating mesoporous SnO_2 with a different thin metal oxide film could improve DSSC performance (Dong et al., 2014).

In addition, tungsten trioxide (WO_3) has garnered considerable attention in hybrid photovoltaics due to its unique electrical properties. It is a transition metal oxide with a bandgap of 2.6–3.1 eV (Kumar et al., 2019). Although WO_3 has good carrier mobility in the range of TiO_2, it has poor

dye adsorption on its surface, resulting in unfavourable charge recombination and low photocurrent. Recent research indicates that incorporating one-dimensional (1D) nanostructures, such as nanotubes, nanorods, and nanowires, considerably improves DSSCs based on WO_3 ETL (Akin & Sonmezoglu, 2018). According to various published reports, the performance of WO_3 ETL can be enhanced by introducing a blocking layer to reduce charge recombination from FTO to the electrolyte. Thus, manufacturing a photoelectrode with a large surface area for efficient light-harvesting and higher dye loading on the surface is critical (Dhonde et al., 2023).

Strontium titanate ($SrTiO_3$) is another ETL contender for use in DSSCs. This material can be regarded as a doped TiO_2 structure because it has a bandgap of 3.2 eV, which is similar to anatase TiO_2 (Yang et al., 2010). In addition to having a wide bandgap, SrTiO3 has a high dielectric constant ($\varepsilon = 300$), which allows for effective electrostatic shielding of electrons from the oxidized active layer, thereby decreasing charge recombination rates (Chaubey et al., 2014). However, this material has not been extensively researched in the field of hybrid photovoltaics. Cerium (IV) oxide (CeO_2) has also garnered considerable interest due to its appealing photo response, which is attributed to the existence of partially occupied 4f and 5d orbitals (Dias et al., 2018). Furthermore, it has high stability to photo and chemical corrosion, strong light absorption in ~ 380-400 nm, and improved redox nature of Ce^{4+}/Ce^{3+}, and low toxicities (Choudhury et al., 2013). However, weak photocatalytic effectiveness, quicker charge carrier recombination, and low light absorption efficiency pose challenges to its practical application (Yu et al., 2012).

According to Shahpari et al. (2015), iron (III) oxide ($\propto$-Fe_2O_3) has been effectively used as a counter electrode in DSSCs. Consequently, because of its narrow bandgap of 2.2 eV and intriguing optoelectrical characteristics, it has been employed as an ETL. It is noteworthy that around 40% of the photons that are irradiating have photon energies higher than this bandgap energy (Akin & Sonmezoglu, 2018). However, this material has a small optical absorption coefficient, a short lifespan of photo-generated charge carriers, and a reduced charge carrier mobility of 0.2 $cm^2\ V^{-1}s^{-1}$ (Mirzaei et al., 2016). Research has been conducted to address these issues, which include controlling the porosity of hematite structures, adding the appropriate dopants, and regulating the morphology size (Akin & Sonmezoglu, 2018). With a bandgap of 4.0 eV, niobium pentoxide (Nb_2O_5) has also drawn a lot of interest for use in DSSCs as an ETL material, a bilayer on TiO_2, and a blocking layer in the FTO/TiO_2 interface material (Singh et al., 2018). High cell internal

resistances and insufficient surface area for dye molecule anchoring are the causes of the low efficiency of Nb_2O_5-based DSSCs (Akin & Sonmezoglu, 2018).

Due to its significant excitation binding energy at ambient temperature (60 meV), suitable electron band position, high electron mobility, and direct band gap of 3.3 eV, zinc oxide (ZnO) is also attracting considerable interest from the scientific and industrial communities (Akin & Sonmezoglu, 2018). Compared to titania, zinc oxide (ZnO) is more basic and more likely to react chemically with an acidic dye (mostly the carboxylic groups) (Shi et al., 2013). As a result, it inhibits charge injection and decreases dye molecule adsorption. DSSCs based on ZnO currently have low efficiency. Numerous strategies are being attempted, including doping with metallic and non-metallic anions, designing and synthesizing novel dyes, creating new ZnO photoanode topologies, and engineering interfacial modifier layers (Akin & Sonmezoglu, 2018).

2.5.2 Organic electron transport layers

The performance of DSSCs is also significantly influenced by the choice of organic ETLs. Fullerenes and their derivatives, including carbon-60 (C_{60}) and PCBM, have also been used as electron transporters in DSSCs (Janani et al., 2015). Some research groups have reported that C_{60} exhibits superior conductivity and hole mobility in comparison to $PC_{61}BM$ (Liu et al., 2018). Nevertheless, the synthesis of compact and dense C_{60} via solution processing is a challenging process due to the low solubility of C_{60} in common solvents (Cysewski, 2019). For this reason, thermal evaporation is implemented during the deposition of the C_{60} layer (Raiford et al., 2019). Conversely, PCBM is an indispensable ETL due to its low-temperature procedures, straightforward fabrication process, electron extractability, and straightforward fabrication techniques (Zhang et al., 2020).

Unlike inorganic ETLs, organic ETLs are highly flexible and moisture-resistant, and their properties can be modified by adjusting their structures (Zhang et al., 2020). Because organic ETLs have lower conductivity than inorganic ETLs, they should be thin to facilitate charge transmission. In the pursuit for highly efficient ETLs, various aspects must be considered: (i) identification of novel deposition methods for fullerene and its derivatives, (ii) use of efficient interlayers between the dye and the $PC_{61}BM$ layer for efficient charge transport, (iii) mechanical robustness is required, (iv) suppressing molecular aggregation of PCBM by mixing it with poly(methyl methacrylate)

(PMMA), and (v) a combination of inorganic and organic ETLs to improve device performance and enhance long-term stabilities (Zheng et al., 2015).

2.6 Photosensitizers in dye-sensitized solar cells

Currently, the widely deployed solar cell technology, silicon-based, has efficiencies of ~ 27% (Yu et al., 2018). In contrast, DSSCs based on attractive and abundant materials have efficiencies ranging from 13% to 14% (Singh et al., 2019). However, extensive literature reviews have consistently emphasized the importance of optimizing various components of DSSCs, including the dyes used, charge-selective contacts, anodes, and cathodes. The performance of these devices is determined by the dyes used (Ludin et al., 2014). Thus, they must meet characteristics such as outstanding electron lifetime, strong absorption spectrum, efficient transfer to TiO_2, and good adsorption on the TiO_2 surface, among other desirable ETLs. Numerous studies have been conducted on sensitizers that can be utilized in DSSCs, including natural dyes, quantum dot sensitizers, metal-free organic dyes, ruthenium-complex dyes, and mordant dyes.

2.6.1 Natural dyes

All-natural dyes are inexpensive, widely available, and environmentally safe. Plant extracts with a variety of colours and pigments that can be extracted and used in DSSCs include flowers, tree bark, seeds, vegetables, leaves, fruits, and microbes (Maldonado-Valdivia et al., 2013). These dyes are commercially available, have high absorption coefficients, do not require complicated processing, do not require toxicity testing, and are environmentally benign (Shalini et al., 2016). Each pigment is characterized by the colour perceived by humans and the wavelength of maximum absorbance. Tree barks, vegetables, seeds, fruits, and flowers are among the natural dyes that have been investigated for use in DSSCs. Figure 2.11 presents natural dyes, including (a) Anthocyanin pigment obtained from red cabbage plant (*Brassica oleracea L.*), (b) Anthocyanin (Quercetin) pigment extracted from hibiscus flower (*Hibiscus rosasinensis)*, (c) Betalain pigment extracted from parsnip (*Pastinaca sativa*), (d) Anthocyanin (Delphinidin-3-glucoside) pigment obtained from Rengas wood (*Gluta spp.*), (e) Anthocyanin (Delphinidin) pigment obtained from Blackberry (*Rubus fruticosus L.*), (f) Monascin pigment extracted from Monascus plant, (g) Chlorophyll

pigment from spinach leaves (*Spinacia oleracea*), and (h) Flavonoid (Flavonols) pigment extracted from Biota orientalis plants (*Platycladus arientalis*).

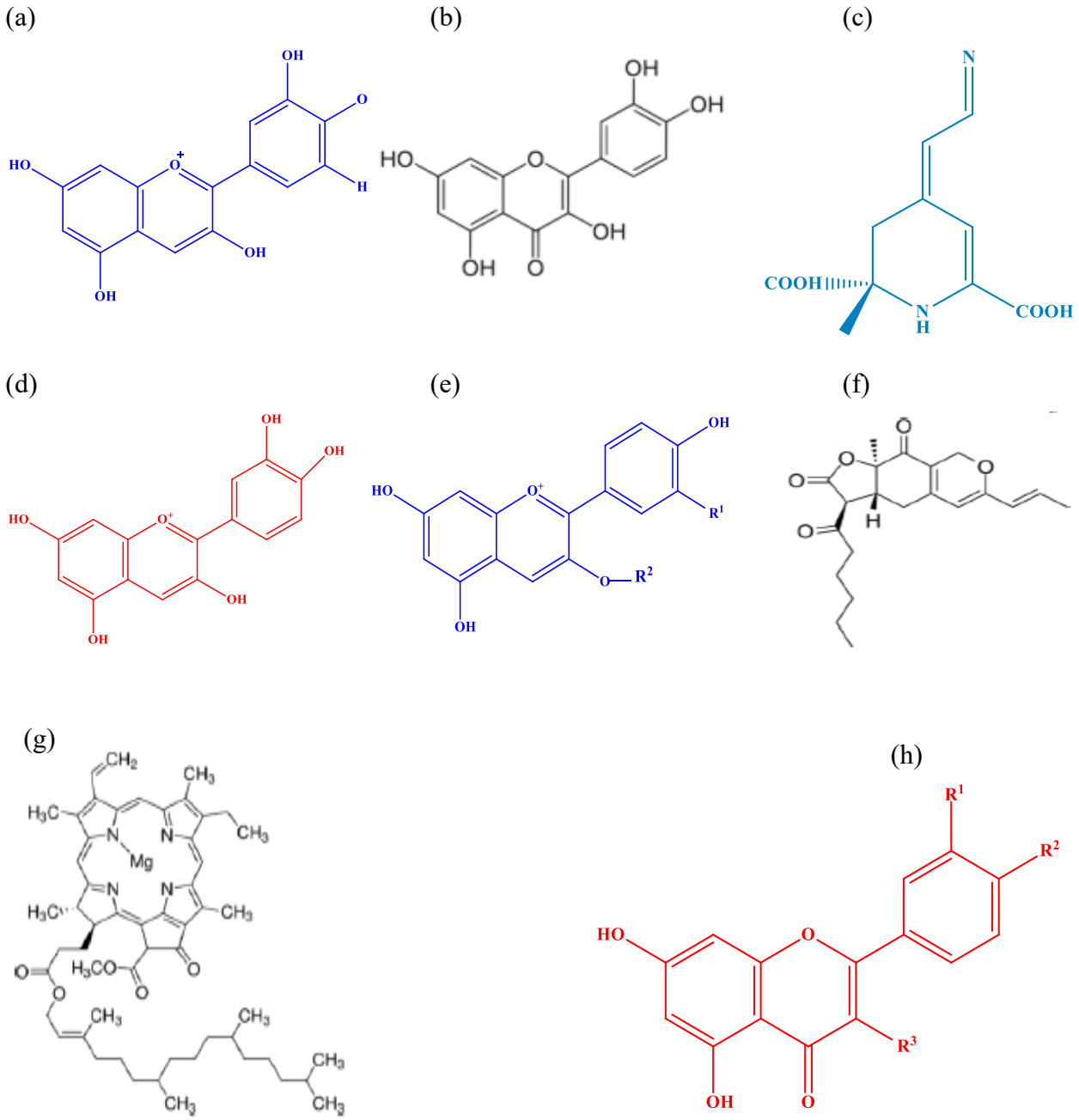

Figure 2.11: Examples of natural dyes that have been explored for application in DSSCs

Typically, dyes should absorb all available light across the electromagnetic spectrum. In this pursuit, research has focused on increasing the efficiency of DSSCs towards S-Q limits by optimizing the performance of photosensitizers. More recently, Das et al. (2020) employed an experimental approach to investigate the light-absorbing properties of natural dyes derived from seeds of pomegranate (*Punica granatum*), red spinach (*Basella rubra L.*), and Malabar spinach. Das et al. (2020) reported various J-V characteristics in solar cells with the three types of dyes, as shown in Table 2.5.

Table 2.5: Photovoltaic performance of DSSCs based on different natural dyes

Dye	$\mathbf{J_{sc}}$ **(μA)**	$\mathbf{V_{oc}}$ **(V)**	$\mathbf{J_{sc} \times V_{oc}}$ $\mathbf{(10^{-6}W)}$	$\mathbf{J_{max}}$ **(μA)**	$\mathbf{V_{max}}$**(V)**	$\mathbf{P_{max}}$ $\mathbf{(10^{-6}W)}$	**FF (%)**	**PCE (%)**
Malabar spinach seeds	510	0.71	362.1	410	0.43	176.3	0.49	9.23
Red spinach	345	0.51	174.23	280	0.32	89.6	0.51	4.69
Pomegranate	300	0.41	123	270	0.218	58.86	0.48	3.08

The solar cell containing Malabar spinach seeds had the highest power conversion efficiency (9.23%), and all the samples exhibited ideal behaviour. Furthermore, the TiO_2 electrode with Malabar spinach seeds is the best solar energy converter, according to research using X-ray diffraction, scanning electron microscopy, and an inductance analyzer (Das et al., 2020). Sanda et al. (2021) conducted a thorough experimental study to investigate the photovoltaic properties of various natural dyes. When comparing the J-V characteristics of the natural dyes with the ruthenium dye (N719 dye), as shown in Table 2.6, the natural dyes have very low J_{sc}, which suggests that their electron injection and exciton separation are poor. According to Sanda et al. (2021), sorghum exhibited high J_{sc}, which suggests high anthocyanin properties. These natural dyes did, however, provide reasonable V_{OC} values. Consequently, when anchoring groups like carbonyl and hydroxyl functional groups are present, the ten natural dyes can be employed as sensitizers in DSSCs.

For the commercial production of ecologically friendly PVs, research on natural dyes is challenging (Omar et al., 2020). They are less efficient than synthetic dyes and have poorer thermal stability, low electron collection efficiency, fast recombination events (requiring graphene and

carbon nanotubes to suppress charge recombination), and the need for additives like phosphinic acid, hexadecyl malonic acid, and chenodeoxycholic acid to reduce dye aggregation at the ETLs, like the TiO_2 layer (Castillo-Robles et al., 2021). To overcome these drawbacks of naturally occurring dyes, research is now focused on developing synthetic sensitizers for DSSCs. Through phytochemical screening, Sanda et al. (2021) determined the photovoltaic characteristics of these molecular sensitizers, as summarized in Table 2.6.

Table 2.6: Phytochemical screening test of different natural dyes employed in DSSCs

Dye extracts (Botanical name)	**Conc. (mg/ mL)**	**λ_{max}**	**J_{sc} (mA/cm^2)**	**V_{oc} (V)**	**P_{max} (mW/cm^2)**	**FF**	**PCE (%)**
Sorghum stalk (*Sorghum bicolor)*	1	538	1.69	0.34	0.18	0.31	0.18
Dawadawa (*Parkia biglobosa)*	10	450	1.22	0.33	0.12	0.29	0.12
Red onion (*Allium cepa)*	5	449	1.68	0.28	0.16	0.34	0.16
Achiote (*Bixa Orellana)*	10	432	1.28	0.35	0.16	0.35	0.16
Flamboyant (*Delonix regia)*	10	458	0.81	0.42	0.1	0.29	0.10
Yellow Frangipani (*Prumeria) rubra)*	10	452	1.12	0.42	0.15	0.32	0.15
Pink Frangipani (*Prumeria rubra)*	20	484	0.55	0.31	0.05	0.3	0.05
Oleander (*Nerium oleander)*	20	544	0.55	0.33	0.07	0.36	0.07
Thevetia (*Thevetia peruviana)*	20	670	0.26	0.30	0.03	0.40	0.03
White trumpet (*Tabebuia rosea)*	20	427	0.88	0.32	0.10	0.36	0.10
Ruthenium dye (N719)		530	8.75	0.53	1.65	0.35	1.65

2.6.2 Ruthenium-complex dyes

The conversion efficiency of the Grätzel cell, which is based on ruthenium, was 7.1% (Nazeeruddin et al., 2001). These dyes have piqued a significant amount of research interest due to the tunable electrochemical, photochemical, and photophysical properties of Ru(II) metal complexes (Kuciauskas et al., 2002). In addition, they are soluble in a variety of solvents (Zhang et al., 2013), possess accessible and stable oxidation states from I to IV, and their geometrical

structures enable the controlled addition of ligands (Shalini et al., 2016). A substantial body of literature demonstrates that solar cells fabricated using Ru(II) complex dyes consistently produce the best photovoltaic performance, primarily due to their relatively longer lifetimes in meta-to-ligand charge transfer (MLCT) properties (Salmahaminati et al., 2020).

Ruthenium dyes are classified into three types: polynuclear bipyridyl Ru, carboxylate polypyridyl Ru, and phosphonate Ru dyes (Shalini et al., 2016). The number of metal centres distinguishes the first type from the second and third, while the absorption groups distinguish the second and third (Shalini et al., 2016). The widely studied Ru dyes include (N3-*cis*-di (thiocyanato) *bis* (2,2-bipyridine-4,4-dicarboxylate) ruthenium (N3 dye), (di-tetrabutyl ammonium *cis*-*bis* (isothiocyanato) *bis* (2,2'-bipyridyl-4,4'-dicarboxylato) ruthenium (II) (N719 dye), and tris *(N, N, N*-tributyl-1-butanaminium) [2,2''6',2''-terpyre -4,4',4''-tricarboxylato (3-)-*N1, N1', N1"*]tris(thiocyanato-N) hydrogen ruthenate (N749 or black dye)) (Mujtahid et al., 2022).

The primary difference between Ru(II) complexes lies in the absorption groups (Shalini et al., 2016). According to Sekar and Gehlot (2010), the N3 dye can absorb electromagnetic radiation up to 800 nm because of its loose attachment to isothiocyanato groups. The HOMO and LUMO molecular orbitals, as well as the MLCT, are responsible for the complex's light absorption. The chromophore (isothiocyanato ligands) of this dye has been used extensively as a sensitizer in DSSCs by shifting the HOMO towards the redshift of its absorption spectra. In the synthesis of N719 dye, the H^+ cations of the carboxyl groups in the N3 dye are substituted with TBA^+, which has been reported as a highly efficient active layer (Grätzel, 2005; Shalini et al., 2016). However, their poorer absorption coefficients have restricted the use of N749 (Shalini et al., 2016). Since thick semiconductor oxide is needed to adsorb enough dye molecules, the N749 dye has been viewed as a less practical material in DSSCs (Sekar & Gehlot, 2010). A drop in V_{OC} and J_{sc} as a result of ineffective electron transport is an inevitable consequence of the thick semiconductor oxide layer. Accordingly, N719 dye is the most widely utilized Ru complex dye due to its stable excitation states, high absorption, and good chemical nature in the visible region of the electromagnetic spectrum (Samuel & Yam, 2020). However, despite widespread interest in Ru complexes in the scientific community, they have been shown to harm the environment due to the presence of heavy metals and complex synthesis methods (Aghazada & Nazeeruddin, 2018). Not only is Ru rare in the earth's crust, but it is also toxic to humans (Das et al., 2020). Metal-free dyes

such as coumarin, thienothiophene-derived, phenothiazine, hemicyanine, and oligothiophene have been identified as viable alternatives (Shalini et al., 2016). Figure 2.12 shows the ruthenium-based dyes that have been tested for DSSCs.

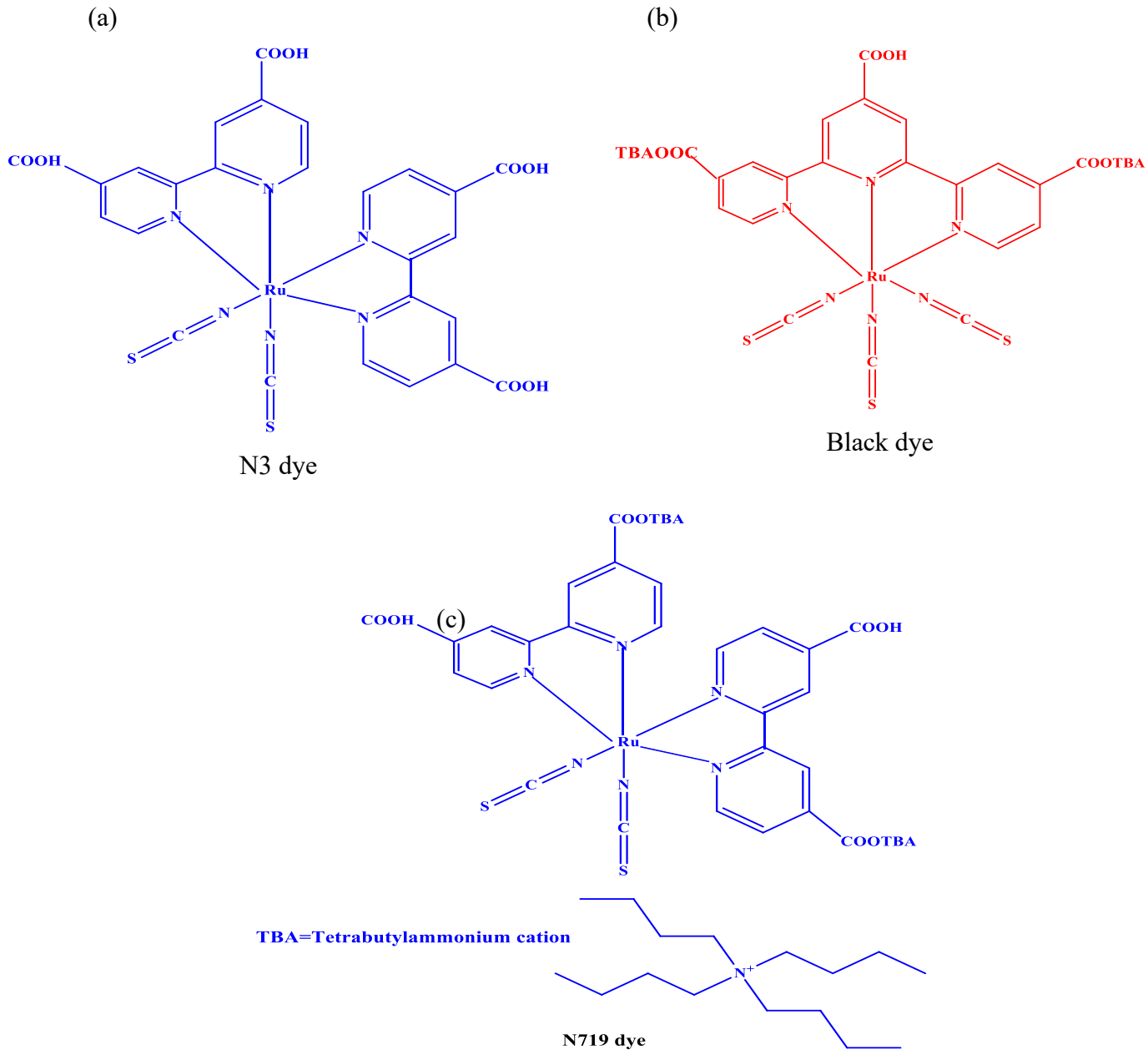

Figure 2.12: Chemical structures of ruthenium-based dyes (a) N3, (b) black dye, and (c) N719 dye

2.7 Application of nanostructured materials as photoelectrodes in dye-sensitized solar cells

The photovoltaic market will evolve to include technologies that provide at least 25 years of continuous PCE for outdoor applications (Tan et al., 2022). Researchers have proposed several strategies to increase the stability and PCEs of DSSC, which include the use of nanostructured materials as photoelectrodes (Duarte et al., 2024). Titania nanoparticles, which are made up of randomly packed nanoparticles, are the most commonly used photoanode material (Wu et al., 2023). However, this structure can impede transport dynamics and increase the recombination of photoelectrons with the redox couple, thereby lowering the collection efficiency in DSSCs. Nanostructured materials have been designed and developed for use in photocatalysis, optoelectronics, sensor devices, electronics, and photovoltaics (Saeed et al., 2024). Modifying DSSC anodes aims to increase PCE by lowering charge recombination, optimizing electron transportation, surface area, trapping power, and light scattering (Cheruku et al., 2023). Various metal oxides, including ZnO, TiO_2, and WO_3, have been used as photoanodes in DSSCs. For example, highly ordered TiO_2 nanotube arrays, translucent TiO_2 nanowires/nanotubes manufactured through a two-step anodization process, and high surface area ZnO nanotubes have all been effectively employed in DSSCs (Boro et al., 2018). The morphology of these materials is crucial in determining DSSC performance, and research initiatives have attempted to utilize one-, two-, and three-dimensional (3D) nanostructures to reduce recombination rates and enhance charge collection efficiencies (Boro et al., 2018).

In addition to TiO_2 (colloids), nanoparticles have been the subject of much research since the inception of DSSCs (Wang et al., 2014). According to Boro et al. (2018), one-dimensional (1D) structures, such as nanowires, nanorods, and nanotubes, have garnered considerable interest. These 1D structures are highly valued because they facilitate charge carrier transit and have fewer charge recombinations at grain boundaries (Boro et al., 2018). In addition, TiO_2/ZnO composites, which can be broadly categorized into 1D, 2D, 3D, and hybrid nanostructures, have been developed and have become attractive options for DSSCs due to their low preparation costs, high efficiency, and environmentally friendly characteristics (Boro et al., 2018). A composite material combines two or more materials (Cai et al., 2017). It possesses great catalytic activity and the capacity to transform pure nanomaterials into nanotips, nanobelts, nanotubes, and nanowires. As a result, composite materials have gained popularity for DSSCs (Boro et al., 2018). Drygała et al. (2023)

reported that 1D nanostructures of the TiO_2/ZnO composite exhibit smooth electron mobility, resulting in lower recombination rates and enhanced charge transport. It is worthwhile to note that TiO_2/ZnO 1D nanostructures have been manufactured using various techniques, including nanowires, nanorods, and nanotubes (Zhu et al., 2010). Titania has also been doped with ZnO nanorods, which improves the PCE of DSSCs (Feng et al., 2016). Other groundbreaking breakthroughs include the usage of coaxial TiO_2/ZnO nanotube arrays prepared electrochemically by depositing ZnO layers inside TiO_2 pores, as shown in Table 2.7. The ZnO layer is composed of small ZnO nanoparticles, which form rough and nanoporous inner layers that improve dye loading and electron transport (Feng et al., 2016). Several findings have also demonstrated that ZnO-decorated TiO_2 nanotubes are more efficient than their TiO_2 equivalent nanoparticles (Boro et al., 2018; Lee et al., 2013; Momeni & Ghayeb, 2015).

Table 2.7: Photovoltaic characteristics of various DSSCs using ZnO and TiO_2 nanoflowers and nanotubes

Nanocomposite	**Materials**	**V_{OC} (v)**	**J_{sc} (mA/cm^2)**	**FF (%)**	**PCE (%)**	**Ref.**
Nanoflower	ZnO nanoflowers/TiO_2	0.82	6.14	0.56	2.82	(Liu et al., 2014)
	Amorphous TiO_2 over ZnO nanoflowers	0.76	6.30	0.60	3.10	(Prabakar et al., 2011)
	ZnO nanoflowers	0.76	7.96	0.45	2.73	(Xin et al., 2013)
Nanotubes	Coaxial TiO_2/ZnO	0.65	7.28	0.60	2.8	(Xie et al., 2011)
	ZnO/TiO_2 nanotube	0.89	5.96	0.70	3.75	(Liu et al., 2012)
	ZnO-decorated TiO_2 nanotubes	0.72	6.77	65.11	3.17	(Lee et al., 2013)
	ZnO coated with TiO_2 nanoparticles	0.94	6.97	0.60	3.94	(Giannouli, 2013)

Due to their improved dye adsorption on the surface and light-scattering effect, 2D TiO_2 nanosheets have demonstrated superior performance over naked TiO_2 (Boro et al., 2018). Furthermore, the distinct morphological properties of 2D ZnO nanosheets have led to their

applications in DSSCs (Hezam et al., 2018). However, ZnO/TiO_2 composite nanostructures are not commonly used in DSSCs due to their low PCE (Boro et al., 2018). Light harvesting and photoelectric performance have been successfully improved by 3D structures like sponge-like TiO_2/ZnO nanodonuts (Li et al., 2015), ZnO nanoflowers/TiO_2 nanocomposite photoanode (Samsuri et al., 2017), ZnO nanorods/nanoflowers on FTO (Ishak et al., 2023), crystalline/amorphous TiO_2 over ZnO electrode (Boro et al., 2018), and 3D heterostructures (Gasso & Mahajan, 2022). According to Boro et al. (2018), hybrid TiO_2/ZnO heterostructured arrays, such as TiO_2 nanowire/ZnO nanosheet or TiO_2 nanowire/ZnO nanorod, have demonstrated exceptional qualities for use in solar cell applications. The photovoltaic properties of DSSCs made with different TiO_2/ZnO nanomaterials are presented in Table 2.8.

Table 2.8: Photovoltaic characteristics of various DSSCs based on various TiO_2/ZnO nanomaterials

Nanomaterial	**Materials**	**V_{OC} (v)**	**J_{sc} (mA/cm^2)**	**FF (%)**	**PCE (%)**	**Ref.**
Nanocomposites	TiO_2/ZnO nanodonuts	0.78	16.70	0.69	9.00	(Li et al., 2015)
	ZnO coated TiO_2	0.75	13.46	0.65	6.62	(Chou et al., 2012)
	ZnO nanoparticles	0.72	0.49	0.69	1.21	(Kim et al., 2005)
	TiO_2 coated ZnO	0.77	8.78	0.72	4.89	(Sakai et al., 2013)
Nanofibres	TiO_2/ZnO core-sheath	0.75	11.3	0.61	5.17	(Du et al., 2012)
Nanowires	ZnO with anatase TiO_2	0.78	4.5	0.58	2.25	(Law et al., 2006)
	TiO_2-coated ZnO	0.79	12.2	0.59	5.65	(Xu et al., 2012)
3D hierarchical heterostructure	1D ZnO nanorod on 2D TiO_2 nanosheet	0.80	3.24	0.17	0.51	(Zheng et al., 2014)
Nanorods	TiO_2 doped with ZnO	0.76	11.4	0.50	5.80	(Pang et al., 2007)

2.8 Theoretical and computational modelling of solar cells

Third-generation solar cells provide an exceptional platform for fundamental investigations into charge and mass diffusion across multi-layer heterogeneous interfaces, solar energy conversion, and electrochemistry (Rahman et al., 2023). Theory and computations are recognized for offering a scientific basis to comprehend isolated elements of DSSCs (e.g., electrodes, dyes) and fundamental processes such as ion/electron transport characteristics at liquid-solid and organic-inorganic interfaces (Muñoz-García et al., 2021). The application of various theoretical methodologies, including sunlight simulation, has proven essential for the scientific community in addressing complex processes and materials that span multiple temporal and spatial scales. Processes, including electron transport, light harvesting, electrode/dye charge transfer, electrolyte diffusion, dye regeneration, and reduction at the counter electrode, occur over varying time scales, ranging from femtoseconds to milliseconds, in different regions (Benazzi et al., 2019). Consequently, the theoretical methodologies must be multi-scale to guarantee the optimization of DSSC components. For any novel photovoltaic technology to be deemed appropriate for commercial application, it must have an outdoor lifespan of approximately 25 years and an indoor deployment of approximately 5 years (Sangpongsanont et al., 2020). Lifetime investigations of these devices require many months of exposure for each iteration, compelling the scientific community to employ both theoretical and computational approaches in the development of innovative materials, hence expediting research advancement (Muñoz-García et al., 2021).

Computer modelling offers valuable atomic-level insights into complex processes and materials, complementing experimental investigations of matter (Corà et al., 2004). It is an essential method, particularly in the industrial sector, where there is a search for new materials with specific electronic properties and structures tailored to specific applications (Gubernatis & Lookman, 2018). An in-depth understanding of the optical, mechanical, and electrical characteristics of various solar cell layers is essential for the development of innovative and highly efficient solar devices. In this context, Density Functional Theory (DFT) is indispensable for describing the ground state properties of a variety of materials (Butt et al., 2020). While the Generalized Gradient Approximation (GGA) and Local Density Approximation (LDA), which are respectively based on non-uniform and uniform electron density distributions, are crucial for estimating ground-state

electronic properties approximation, they yield inaccurate results for excited state DFT calculations. Conversely, the calculation of band gaps and band offsets has been investigated using a variety of DFT hybrid techniques, including HSE06, which are well-established (Labat et al., 2008). The first principles of the Hartree-Fock method are incorporated into a various DFT hybrid methods, and hybrid methods like the B3LYP correlation function are dependent upon the material of interest.

Numerous properties of interfaces and individual components in DSSCs can be predicted and described using the well-established computational tools of DFT and time-dependent Density Functional Theory (TD-DFT) (Labat et al., 2006). According to preliminary research, global parameters like J_{sc} and V_{OC}, as well as microscopic characteristics like the optical characteristics and electronic structure of semiconductor/electrolyte and dye/semiconductor interfaces, have been precisely analyzed using a periodic approach and global hybrid (GH) functional with the aid of DFT and TD-DFT (Labat et al., 2008). The binding energies, equilibrium lattice parameters, band structures, and relative stabilities of rutile and anatase TiO_2 (crucial DSSC semiconductors) have been effectively determined by *ab initio* calculations employing the Hartree-Fock, DFT, and hybrid functionals Perdew-Burke-Ernzerhof (PBE) and Becke 3-Parameter (Exchange), Lee, Yang, and Parr (B3LYP) levels (Labat et al., 2008).

2.8.1 Modelling of DSSCs components

Experimental work has been successfully supplemented by computational and theoretical modelling of isolated DSSC components, such as redox shuttles, semiconductor nanoparticles, and dyes, which have provided insights into the physical and chemical processes that govern their operations (Pastore & Angelis, 2013). The B3LYP level of theory is a reliable method for predicting the electronic structure, geometry, and properties of conjugated materials (Aulakh et al., 2015). The LUMO, HOMO, and band gap energies of small molecules, including triphenylamine (TPA), carbazole, *N, N, N, N*-tetraphenyl-benzidine, triazine, thiophene, and triazatruxene, have been examined by previous authors using B3LYP/6-311g and B3LYP/6-31g(d) levels of theory (Naqvi & Patra, 2021). The B3LYP hybrid functional and 6-311 g and 6-31g(d) as basis sets were employed to optimize the structures of these molecules. All calculations were conducted using the Gaussian 03 program. According to Naqvi and Patra (2021), B3LYP/6-

311g level of theory offers precise predictions for parameters such as atomic orbitals and accurate energy information.

Organic dyes are essential components of DSSCs. Typically, these dyes consist of electron-donating groups (EDG) and electron-withdrawing groups (EWG) (Khanmohammadi et al., 2018). Charge transfer from EDG to EWG of the dye is responsible for the presence of a conduction band in the excited state of these dyes. Xue et al. (2012) used the Gaussian 03 program to perform DFT calculations on the degradation of $Ru(dcbpy)_2(SCN)_2^{2-}$ (N719) dye. Their study employed the B3LYP hybrid technique and LanL2DZ basis set for the Ru atom, along with the 3-21G* basis set for the other elements. They also used the GaussView tool to determine the HOMO and LUMO energies of the optimized structures. The HOMO of the N719 dye is predominantly distributed in SCN-1 and Ru, with a marginal distribution in dcbpy; however, the LUMO is distributed in dcbpy and Ru. The substitution of SCN^{-1} with an iodine (I) ligand alters the orbital makeup of the dye, as demonstrated by Xue et al. (2012); the HOMO and LUMO energies of the dye are altered. The N719 dye has a smaller energy gap (1.76 eV) than $Ru(dcbpy)_2(I)_2^{2-}$ (N719-I), which has a gap of 1.93 eV. As a result, the N719-I dye requires more energy to transfer an electron from the HOMO to the LUMO than the N719 dye. Furthermore, Xue et al. (2012) revealed that the LUMO energy of N719 dye is 0.15 eV lower than that of N719-I.

This finding is attributed to the decreased potential of electron injection from the excited state of N719 dye to the CB of TiO_2 compared to N719-I (Lo et al., 2010). Recently, Aziz et al. (2018) employed GaussView and Gaussian 09w computational programs in *ab initio* molecular orbital theory to determine the excitation energies, electronic configurations, and geometric structures of the squaraine dye – 5-carboxy-2-[[3-[(1,3-dihydro-3,3-dimethyl-1] 2-hydroxy4-oxo-2-cyclobuten-1-ylidene] methyl -3,3-trimethyl-1-methyl-3H-indolium anchoring group on Ti^{+4}, as well as free Ti characteristics. In this work, the partial and total density of states (PDoS and TDoS) were visualized using Multiwfn software. The authors of this work reported that their pure DFT functional (PBEPBE) calculations yielded results consistent with their experimental findings on the UV-Vis spectra of both unbound and bound squaraine dyes (Aziz et al., 2018). Figure 2.13 depicts the HOMO and LUMO energies of N719-I and N719 dyes measured with the GaussView program.

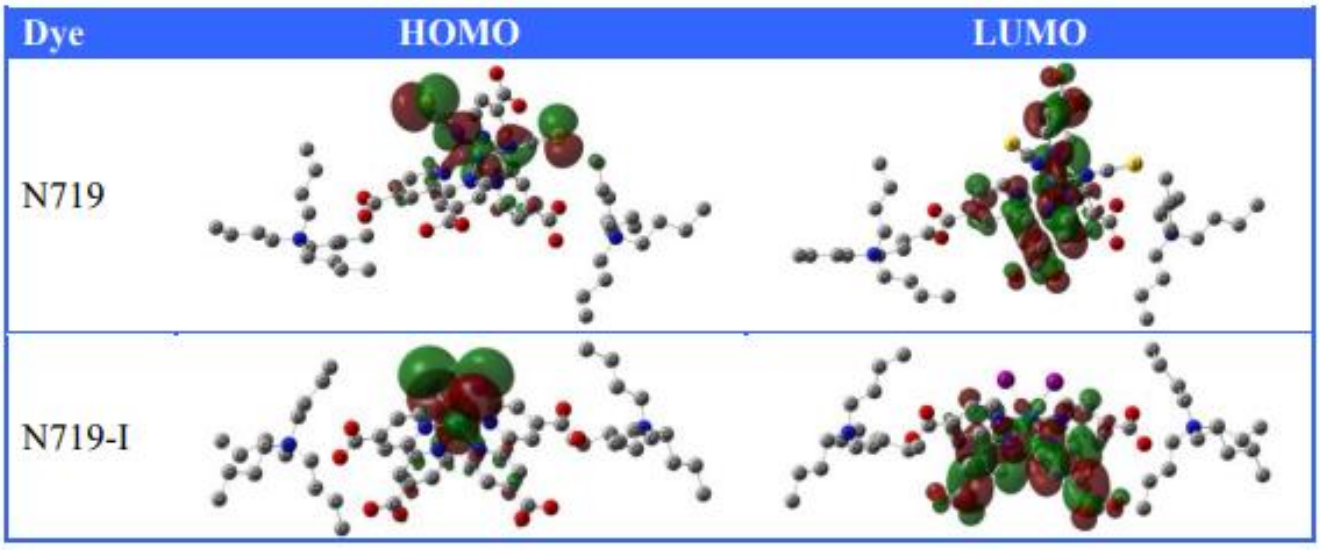

Figure 2.13: The HOMO and LUMO energies of N719-I and N719 dyes pictured using the GaussView program

Metal-free organic dyes with donor-acceptor (D-A) molecular designs have sparked great research interest in the field of DSSCs with outstanding PV performance (Rahman et al., 2023). Carbazole, in particular, is noted for its chemical and thermal stability, as well as the simplicity with which it may be functionalized at various locations. Electron-deficient groups such as cyano and nitro have been examined as potential anchoring/withdrawing units that can be paired with carbazole donors to generate efficient metal-free organic dyes for DSSCs (Naik et al., 2023). For example, Naik et al. (2023) used Biovia Turbomole 22, Chemdraw, and TmoleX 2022 to conduct a theoretical analysis of a new family of carbazole-based chemical chromogens ($R_{1\text{-}6}$). The DFT and TD-DFT were used to study electron delocalization in the HOMO and LUMO energy levels, electronic absorption, vertical excitations, and oscillator strength in chloroform and gas phases. In this theoretical study, the TD-DFT used CAM-B3LYP/def TZVP methods, and the electrostatic potential maps were generated using the B3LYP/def TZVP level.

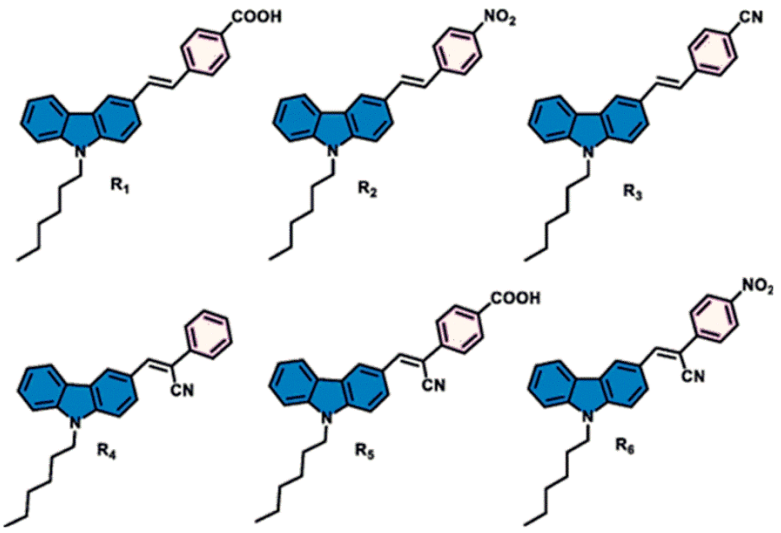

Figure 2.14: Molecular design of R_{1-6} dyes

The research group Naik et al. (2023) investigated Gibbs free energy for dye regeneration (ΔG_{reg}), Gibbs free energy for electron injection(ΔG_{inj}), and Gibbs free energy for charge recombination (ΔG_{rec}) to assess the dye ideal for anchoring on TiO_2. These theoretically calculated parameters are summarized in Table 2.9.

Table 2.9: Electronic and thermodynamic properties of dyes R_{1-6}

Dye	**HOMO (eV)**	**LUMO (eV)**	**Bandgap $E_{0\text{-}0}$, (eV)**	**(ΔG_{reg})**	**(ΔG_{inj})**	**(ΔG_{rec})**
R_1	-5.54	-2.11	3.43	0.34	2.09	1.34
R_2	-5.64	-2.66	2.98	0.44	1.54	1.44
R_3	-5.56	-2.12	3.44	0.36	2.08	1.36
R_4	-5.60	-2.01	3.59	0.4	2.19	1.40
R_5	-5.86	-2.49	3.37	0.66	1.71	1.66
R_6	-5.95	-2.88	3.07	0.75	1.32	1.75

Table 2.9 indicates that dyes provide favourable thermodynamic driving forces for charge injection and regeneration, since they satisfy the thermodynamic criteria for charge transfer across the complete photoelectronic conversion cycle (Naik et al., 2023). Their findings also illustrate the

HOMO-LUMO energy levels and the bandgap requirements (Naik et al., 2023). The energy bandgap of the examined dyes varies from 2.98 to 3.59 eV. The authors simulated the UV-Vis absorption of these dyes in a chloroform solvent phase using the CAM-B3LYP/TZVP method. The greatest absorption values (λ_{abs}) displayed absorption bands between 333 and 385 nm (within the visible spectrum), attributed to intramolecular charge transfer between the accepting units and the carbazole. The findings of their research met the criteria for appropriate sensitizers in DSSC applications. In general, the introduction of DFT and TD-DFT has broadened the scope of computational DSSC modelling (Lu et al., 2018). Density Functional Theory (DFT) methods are reliable for characterizing electrical, mechanical, and optoelectronic properties in systems with hundreds of atoms (Pastore & Angelis, 2013). Because device components can be optimized, these approaches may push DSSC performance parameters closer to the S-Q limits. Future DSSC research is expected to focus on computational and theoretical modelling to optimize cell design.

2.8.2 Numerical simulation of solar cells

It is crucial to evaluate the performance of photovoltaic devices under various conditions, including operating temperatures and solar radiation (Agwa et al., 2020). The performance of these devices is evaluated using the spectrum response of current-voltage plots under standard test conditions (Hayat et al., 2019). Numerical simulations are one of the more cost-effective ways employed in this pursuit. Numerical simulation is a computational technique that involves simulating a computer program on a virtual or real device and analysing its performance. Furthermore, numerical simulations aim to evaluate the performance of a given solar cell design and adjust the modelling output to match reported experimental data, ultimately developing a highly efficient solar cell (Rono et al., 2021a). The simulation technique saves time and money on solar cell fabrication by providing relevant data on how to change parameters during the manufacturing process (Burgelman et al., 2013). It also enables the determination of relevant parameters that would otherwise be difficult to get experimentally. Motivated by prior success with novel computational resources, multiple researchers have sought to optimize various CTMs, sensitizers/photosensitizers, and counter electrodes using numerical simulation programs (Azri et al., 2019). The one-dimensional solar cell capacitance simulator (SCAPS-1D) (Burgelman et al., 2013), COSMOL (Gerlich et al., 2013), analysis of microelectronic and photonic structures

(AMPS), and wxAMPS (Liu et al., 2012) have all been widely used to vary key parameters in solar cells such as bandgap, defect density, doping concentration, and thickness. Table 2.10 summarizes the theoretical results of various solar cell architectures obtained using different numerical simulation programs.

Table 2.10: Photovoltaic characteristics of various solar cell structures from theoretical studies

Solar cell structure	**V_{oc} (V)**	**J_{sc} (mA/cm^2)**	**FF (%)**	**PCE (%)**	**Ref.**
FTO/ZnOS/N719 dye/CFTS/Au	0.56	16.84	59.09	5.53	(Abdullah et al., 2024)
FTO/ZnOS/N719 dye/CZTSe/Au	0.88	20.83	70.86	12.91	(Abdullah et al., 2024)
FTO/ZnOS/N719 dye/CZTS/Au	0.87	19.46	71.77	12.20	(Abdullah et al., 2024)
FTO/ZnOS/N719 dye/CNTS/Au	0.87	19.89	71.76	12.47	(Abdullah et al., 2024)
FTO/TiO_2/LEG4 dye/PEDOT/Ag	0.83	13.40	64.00	7.11	(Zhang et al., 2016)
FTO/TiO_2/N719 dye/CuI/Cr-FTO	0.48	15.3	0.51	3.8	(Ranasinghe et al., 2014)
FTO/TiO_2/BEHP-co-MEH PPV/MoO_2MoO_3/Pt	2.14	4.23	92.93	8.42	(Rondan-Gómez et al., 2020)
FTO/TiO_2/BEHP-co-MEH PPV/PEDOT: PSS/Pt	1.53	6.43	80.58	7.95	(Rondan-Gómez et al., 2020)

Other numerical simulation tools include analysis of silicon amorphous (ASA), photonic computer one-dimensional (PC-1D), and automat for heterojunctions (AFORS-HET), which simulates heterojunction solar cells (Ahmed & Khalid, 2019). The selected published literature reveals that several theoretical alternatives can serve as springboards for scaling DSSCs from the laboratory to commercial production. SCAPS-1D has been primarily used in device simulation due to its capacity to examine up to seven layers and perform deep and batch calculations (Burgelman et al., 2013). It is an analytical tool that solves the continuity and Poisson equations. Furthermore, the SCAPS-1D results are consistent with experimental results reported by other researchers, and it has an easy-to-use interface, making it a dependable software for analyzing DSSC performance (Rono et al., 2021b). SCAPS-1D simulations can be performed on both amorphous and

polycrystalline cells under sunlight and dark conditions, providing manufacturers with critical information during solar cell fabrication. Several simulation software packages have been created to adjust solar cell input parameters and examine changes in quantum efficiency (QE), current-voltage characteristics, and PCEs (Rono et al., 2021b).

SCAPS-1D has been popularly used to study p-i-n or p-n junction multilayer solar cells (Azizi et al., 2019). It determines the solar photon-to-electrical power conversion efficiency (PCE) of a model solar cell. Typically, the efficiency of a solar cell is expressed by Equation 2.2;

$$\mathrm{PCE} = \frac{\mathrm{V_{oc}} \times \mathrm{J_{sc}}}{\mathrm{P_{in}}} \mathrm{FF} \times 100\% \qquad (2.2)$$

where, V_{OC} is the open-circuit voltage, J_{SC} is the short circuit current, FF is the fill factor, and P_{in} is the power input.

The one-dimensional solar cell capacitance simulator (SCAPS 1-D) provides recombination models, including Auger, radiative, and Shockley-Read-Hall (SRH) recombination profiles. Auger recombination is a non-radiative three-particle process whereby an electron (*e*) from the CB transfers its energy either to another electron in the CB (*eeh* process) or a hole (*h*) in the VB (*ehh* process). During these processes, the excess energy is transferred to another particle (*h* or *e*) and released as heat in the lattice (Vossier et al., 2010). The rate of Auger recombination is expressed by Equation 2.3;

$$R_{Auger} = C_n(n^2p - n_0^2p_0) + C_p(n^2p - n_0p_0^2) \qquad (2.3)$$

where C_n and C_p denote Auger recombination for eeh and ehh processes, respectively. Here, *n* and p are electron and hole concentrations under illumination. The subscript *0* represents the concentration values under equilibrium (dark) conditions. Figure 2.15 shows the energy losses through Auger recombination processes.

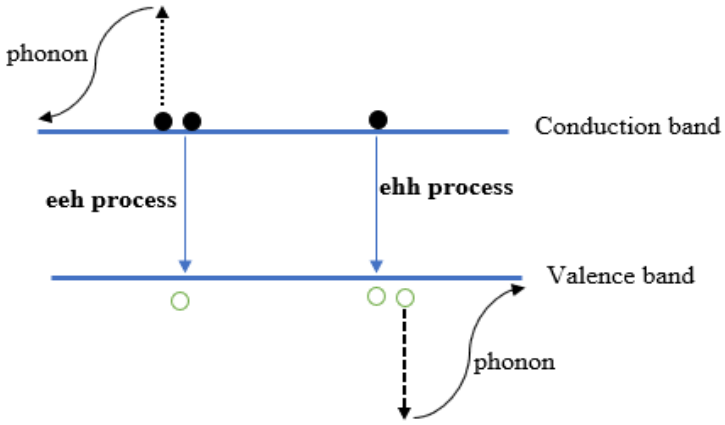

Figure 2.15: Auger recombination processes – ehh and eeh processes

The SRH recombination mechanism, which predominates in DSSCs, typically begins when the energy state traps electrons in the cell's forbidden area. The transport, continuity, and Poisson equations are fundamental equations in semiconductor physics. The Poisson equation is Equation 2.4, while the drift and diffusion equation for electron carriers in the semiconductor device is Equation 2.5. The drift and diffusion equation for hole carriers is Equation 2.6.

$$\frac{d^2\emptyset}{dx^2} = \frac{q}{\epsilon_{o\epsilon_r}} p(x) - n(x) + Nd - Na + \rho p - \rho n \qquad (2.4)$$

Here, $\emptyset(x)$, $\epsilon_{0,}\epsilon_{r,}$ q, $p(x)$, $n(x)$, Nd, Na, ρp, ρn are the electrostatic potential, vacuum permittivity, relative permittivity, electric charge, hole concentration, electron concentration, charge impurities of donor, charge impurities of acceptor, holes distribution and electron distribution, respectively.

$$\frac{dJ\mathrm{n}}{dx} = G - R \qquad (2.5)$$

Jn is the electron current density, R is the recombination rate, and G is the generation rate.

$$\frac{dJ_p}{dx} = G - R \qquad (2.6)$$

J_p, is the hole current density.

Carrier transport in semiconductors occurs by drift and diffusion as expressed by Equations 2.7 and 2.8, respectively.

$$J_{n=}D_{n\frac{dn}{dx}} + \mu_n n \frac{d\emptyset}{dx} \quad (2.7)$$

$$J_{P=D_p} \frac{dp}{dx} + \mu_p \, p \frac{d\emptyset}{dx} \quad (2.8)$$

where Dn, Dp, μ_n and μ_p are the diffusion coefficient of electrons, the diffusion coefficient for holes, the mobility of electrons, and the mobility of holes, respectively.

2.8.2.1 The J-V and fill factor characteristic curves of solar cells

An efficient method for determining the photovoltaic efficiency of the solar cell is the analysis of J-V characteristic curves. These J-V characteristics FF, open-circuit voltage, peak power (P_{max}) and J_{SC} have been the subject of numerous experimental and theoretical explorations. The ideality of the cell is quantified by the fill factor (FF). The quality of the PV cell is determined by the relationship between the maximum power output, P_{max} ($P_{max} = J_{mp} \times V_{mp}$) generated by the solar cell and the product of J_{SC} and V_{OC}, which is defined as the maximum power output divided by the product of J_{SC} and V_{OC} (Equation 2.9). It is generally influenced by shunt and series resistances.

$$FF = \frac{Pmax}{Voc \times Jsc} = \frac{JmpVmp}{Voc \times JSC} \quad (2.9)$$

Here, FF is the Fill factor; $Pmax$ is the maximum power; V_{OC} is the open-circuit voltage; J_{SC} is the short circuit current density; J_{mp} is the current density at the maximum power point and V_{mp} is the voltage at maximum power.

2.8.2.2 Short-circuit current density

The short-circuit current density is the maximum photo-generated current that a solar cell can deliver when its terminals are connected (short-circuited). It is related to the optical properties of the dye and the different dynamic processes in the cell. The net current density is obtained from Equation 2.10;

$$J(v) = J_{SC} - J_{dark} \quad (2.10)$$

where, J_{dark} is the dark current density, which can be obtained from Equation 2.11. This is called the diode equation.

$$J_{dark}(\mathrm{V}) = J_0(e^{qv/mK_BT} - 1) \quad (2.11)$$

Under illumination, the solar behaviour is described using the ideal diode equation and an additional current source J_{sc} during illumination. The illuminated solar equation is expressed by Equation 2.12.

$$J_V = J_{sc} - J_0(e^{qv/mK_BT} - 1) \quad (2.12)$$

where T is the absolute temperature in Kelvins, *Jo* is the dark saturation current density, m is the ideality factor $(1 < m < 2)$, $K_B = 1.38 \times 10^{-23} JK^{-1}$and electronic charge $q = 1.603 \times 10^{-19}$ Coulombs (C).

2.8.2.3 The open-circuit voltage

This is a measure of voltage when no current is flowing through the external circuit and/or when the solar cell terminals are not connected. It is a measure of the difference between the Fermi level of the conductor and the redox potential of the electrolyte. It represents the maximum voltage that a photovoltaic cell can deliver and depends on the photo-generated current density, Jph, as expressed in Equation 2.13.

$$Voc = \frac{mK_BT}{q} \ln\left(\frac{J_{ph}}{J_0} + 1\right) \quad (2.13)$$

2.8.2.4 Incident photon to current conversion efficiency

This corresponds to the photocurrent density produced in the external circuit under monochromatic illumination of the solar cell, divided by the photon flux that strikes the cell. This parameter can be calculated using Equation 2.14.

$$IPCE = 1240 \frac{J_{sc}}{\lambda P_{in}} \quad (2.14)$$

J_{sc} is the short-circuit photocurrent density generated by the monochromatic light, λ is the wavelength, and P_{in} is the intensity of the monochromatic light. The value of Incident power conversion efficiency (IPCE) depends on the dye's light absorption, light intensity, and the regeneration of the oxidized dye. IPCE can also be evaluated by multiplying the light-harvesting efficiency (LHE) by the efficiency of collecting (η_{coll}) the holes at the FTO substrate and the quantum yield of hole injection ($\emptyset_{inj}$) as presented in Equation 2.15.

$$\text{IPCE}\ (\lambda) = LHE(\lambda)\emptyset_{inj}\ \eta_{coll} \quad (2.15)$$

It is also possible to obtain the value of absorbed photon-to-current conversion efficiency (APCE) by finding the ratio of IPCE and LHE as given by Equation 2.16.

$$APCE(\lambda) = \frac{IPCE(\lambda)}{LHE(\lambda)} \quad (2.16)$$

2.9 Electrochemical methods for measurements and characterization of solar cells

The characterization of solar cells is essential for understanding the relevant mechanisms and reactions in dye-sensitized solar cells (DSSCs), including electron-hole recombination and charge transport (Neukom et al., 2018). The comprehension of device limitations and performance is dependent upon the characterization and measurement of solar cells. The analysis of processes in excitonic devices, such as water-splitting cells, hybrid photovoltaics, organic photovoltaics, and DSSCs, is improved by charge extraction and optoelectronic transient measurements (Barnes et al., 2013). The measurement of transient voltages and both large and small perturbation currents is used to acquire data regarding charge transport and recombination within a device (Wang et al., 2009). Conversely, capacitance and charge extraction measurements provide information on the charge retained in the film during operational conditions (Barnes et al., 2013). Cyclic voltammetry (CV), current-voltage (I-V) dynamic polarization, and electrochemical impedance spectroscopy (EIS) are among the standard electrochemical techniques employed to characterize and evaluate solar cells (Çakar et al., 2021). Furthermore, novel electrochemical frequency-domain methods have been developed, such as intensity-modulated photovoltage spectroscopy (IMVS) and intensity-modulated photocurrent spectroscopy (IMPS) (Ravishankar et al., 2019).

Electrochemical impedance spectroscopy (EIS) is an essential tool that provides critical aspects of DSSCs, including the transfer of charges to the counter electrode, electron transport and recombination in ETMs, and electron transport and recombination at the photoelectrode. EIS is typically performed by injecting a small amplitude of alternating current (AC) into DSSCs to generate current and voltage signals at a specific angular frequency, ω. The Bode or Nyquist plots are used to display the impedance values that are obtained (Omar & Abdullah, 2014; Omar et al., 2020). Nyquist plots with three frequency regions are observed in dye-sensitized solar cells (DSSCs). The diffusion properties and Warburg resistance of the redox couple, I_3^-/I^- are responsible for the low-frequency region. The charge transfer resistance at the electrolyte/Pt

interface is designated to the high-frequency region, while the middle-frequency region represents charge transfer recombination resistance at the TiO_2/dye/electrolyte interface (Ammar et al., 2019). Ammar et al. (2019) measured impedance on DSSCs using three natural dyes: chlorophyll pigment from spinach leaves, anthocyanin pigment extracted from red cabbage, and onion peels within the frequency domain of 0.1 - 10^5 Hertz (Hz)and compared them to N719 dye. Figure 2.16 displays the EIS spectra of DSSC based on natural dyes and N719 dye.

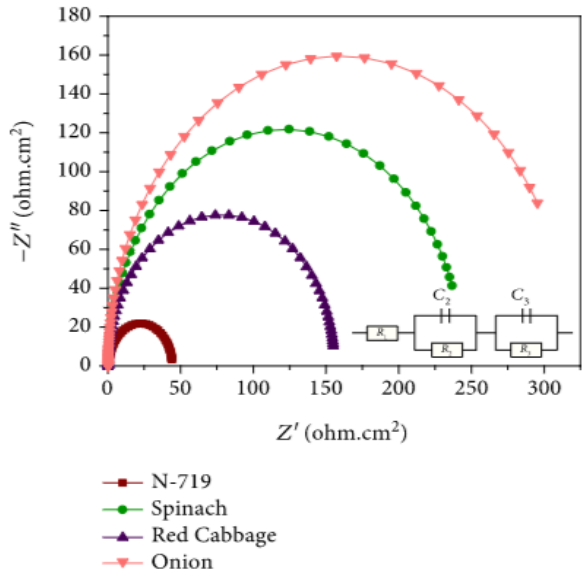

Figure 2.16: The EIS spectra for DSSCs based on different naturally extracted sensitizers and N719 dye (Ammar et al., 2019)

As shown in Figure 2.16, the middle-frequency area has larger semicircles, representing slow charge recombination at the TiO_2/dye/electrolyte interface. A large radius suggests slower recombination kinetics (Wei et al., 2015). Dye sensitized solar cell (DSSC) device based on N719 dye showed lower impedance than natural dyes anchored on TiO_2, resulting in higher performance (Ammar et al., 2019). Intensity-modulated photovoltage spectroscopy (IMVS) and IMPS are generally utilized for nanocrystalline and single-crystal semiconductors, but they have also been applied to DSSCCs to examine charge transfer, electron transport, and recombination processes (Peter, 2007). These strategies rely on a controllable modification of light intensity. While IMVS measures photovoltage responses in an open circuit, IMPS measures frequency-dependent photocurrent responses to a sinusoidally modulated incident light stimulus with the cell held in position (Pockett et al., 2021). Previous studies have suggested that IMVS and IMPS are effective

methodologies for analyzing charge transfer and electron transport dynamics in DSSCs (Wang et al., 2022; Xiang et al., 2018). These investigations will provide insights into the limiting parameters for electron-collecting efficiency, allowing researchers to maximize charge transfer and electron transport efficiency for the best performance of dye-sensitized solar cells (DSSC).

2.10 Practical applications of dye-sensitized solar cells

DSSCs have garnered considerable research interest due to their emerging applications, which include wearable and highly integrated microelectronic devices, the Internet of Things (IoT), and portable power supply (Dhonde et al., 2022). The rising demand for these emerging applications is driven by several DSSC characteristics, including adaptability, roll-to-roll compatibility, and ultra lightness (Aslam et al., 2020). Autonomous IoT devices can be powered by indoor photovoltaics, especially DSSCs. This new generation of technology offers sensing, data processing, artificial intelligence, and ad networking capabilities through an intelligent fusion of automation and computing power. The goal of the Internet of Things (IoT) is to balance productivity and efficiency in order to make human life more automated, comfortable, and easy. DSSCs have drawn remarkable attention for their capacity to power actuators, sensors, and other IoT communication devices. Internet of Things (IoT) devices require a reliable and uninterrupted power source (Rahmatian et al., 2024). The successful development of “independent,” “smart,” and “portable” devices relies on the infrastructure and technological advancements of DSSCs, which are known to perform effectively in both indoor and ambient light conditions (Barichello et al., 2024). Remarkably, DSSCs can function well in a range of interior lighting or intensity conditions, such as dimly lit living rooms (200 lux), highly illuminated supermarkets (1000 lux), and low-light intensity conditions (50 lux), suggesting a huge potential impact on IoT ecology (Aslam et al., 2020). However, to support the entire IoT system, a huge IoT network will require an enormous off-grid power source (Aslam et al., 2020).

As a rising star in the solar cell market, DSSCs are attractive for use in portable devices powered by indoor lighting such as incandescent, light-emitting diodes (LEDs), and fluorescent light (Yadagiri et al., 2023). It is commonly understood that DSSCs can power sensors in healthcare systems, industrial automation, and environmental monitoring (Nath et al., 2023). In indoor situations with limited natural light, DSSCs have been integrated with building automation systems

and electrical appliances to reduce reliance on finite fossil energy sources (Aslam et al., 2020). Furthermore, in the field of biomedical therapies and devices, DSSCs have found application in photodynamic therapy (PDT), which uses light-sensitive medicines to limit cancer cell proliferation (de Aberasturi et al., 2015). These photovoltaic devices emit light, which activates a photosensitizing chemical, generating oxygen, which is known to kill cancer cells. Dye-sensitized solar cells are also used to power biomedical implants such as drug delivery devices and pacemakers (Biswas et al., 2024).

Dye-sensitized solar cells are more capable than traditional silicon solar cells of producing power from indoor light. Therefore, in locations where diffused light is more prevalent than direct solar light, DSSCs have been utilized as power supply sources for light (Aslam et al., 2020; Biswas & Kim, 2020). To ensure that buildings are self-sufficient in their energy generation, photovoltaic cells have been incorporated into building windows (Aslam et al., 2020). Thin, translucent sheets of DSSCs have also been used to generate electricity by installing them in skylights, common windows, and glass facades (Salas Castillo et al., 2022). According to other studies, in addition to their energy-saving benefits, DSSCs can be integrated with windows and other building materials due to their aesthetically appealing appearance (Prajapat et al., 2023). Additionally, companies like G24 Power have developed a range of electronic gadgets, including wireless keyboards using Bluetooth (Sekaran & Marimuthu, 2024).

3. Conclusions and outlook

This review has shown that dye-sensitized solar cells (DSSCs) have garnered international research attention due to their potential for high power conversion efficiency, extended lifespans, and low manufacturing costs. This study presents cutting-edge advancements and serves as a foundation for the design and development of dye-sensitized solar cells (DSSCs) utilizing durable ruthenium and natural dyes, paving the way for future large-scale manufacture. Integrating ruthenium metal complex dyes with highly absorptive organic dyes is a crucial strategy for enhancing light harvesting to improve energy extraction. This study primarily addresses the necessity for enhanced carrier transport materials, improved dye sensitizers, and cost-effective counter electrodes. A significant advancement in dye-sensitized solar cells (DSSCs) involves substituting the liquid electrolyte with a solid-state p-type material and replacing the non-cost-

effective platinum-based counter electrode. This study examines the current research undertakings in interfacial engineering, doping methodologies, and surface morphology control to enhance the photovoltaic performance of hole-transporting layers and electron-transporting layers in dye-sensitized solar cells (DSSCs).

Numerous researchers have investigated materials used in alternative excitonic solar cells, including perovskites and organic solar cells, for potential applications in dye-sensitized solar cells. The pursuit of novel and robust materials seeks to address the issues associated with current materials, which are considered costly, hazardous, and exhibit poor charge transport, resulting in low efficiency and reduced lifespans. With the advancement of nanoscience, nanostructured materials, including nanobelts, nanorods, nanotubes, nanowires, and nanoparticles, have been created for applications in photocatalysis, optoelectronics, sensor devices, electronics, and photovoltaics. The emergence of diverse computational methods, including density functional theory and the solar cell capacitance simulator (SCAPS-1D), has proven crucial in broadening the applicability of dye-sensitized solar cells (DSSCs). The Becke 3-Parameter (Exchange), Lee, Yang, and Parr (B3LYP) quantum level of theory and Gaussian 09w and GaussView computational algorithms have been employed primarily to study the electrical, mechanical, and optoelectronic characteristics of potential DSSC materials. Understanding the optoelectronic characteristics of electronic materials in DSSCs has also been facilitated by various numerical simulation methods. Manufacturers have found these numerical codes to be crucial in determining the ideal parameters needed for cell fabrication. Among these numerical simulations, SCAPS-1D is superior and is consistent with experimental results. Characterization and measurement techniques of DSSCs are essential. They facilitate an understanding of pertinent DSSC mechanisms and reactions, such as charge transport and electron-hole recombination. The increasing demand for these new applications is attributed to several attractive features of DSSCs, including their ultra-light weight, roll-to-roll compatibility, and adaptability. Applications for this technology can be found in various fields, including biomedical implants, portable electronics, and the Internet of Things.

One important electrochemical tool for DSSCs is electrochemical impedance spectroscopy (EIS), which provides information on important processes like ionic diffusion in the electrolyte, electron transport and recombination in ETLs, electron transport and recombination at the photoelectrode,

and charge transfer to the counter electrode. In addition, other complementary electrochemical techniques like intensity-modulated photovoltaic spectroscopy (IMVS), cyclic voltammetry (CV), current-voltage (J-V) dynamic polarization, and intensity-modulated photocurrent spectroscopy (IMPS) have been employed to learn more about the factors that limit electron-collecting efficiency to maximize charge transfer and electron transport efficiency to enhance the performance of DSSCs. Current materials that have been tested in various dye-sensitized solar cell configurations are also within the scope of this article. As a result, the technology and infrastructure for DSSCs are still in their early stages for large-scale manufacturing. To the best of our knowledge, research is presently focused on designing and developing DSSCs using stable carrier transport materials. Lower efficiencies are the primary issue with employing solid-state p-type materials in DSSCs, and this appears to be a significant disadvantage when fabricating high-quality dye-sensitized solar cells. Stable HTLs like Spiro-OMeTAD, CuSCN, and PEDOT, both in their natural states and when doped with metallic salts, metal-organic complexes, peroxides, electron acceptors, and protic ionic liquids, hold promise for enhancing the photovoltaic performance of DSSCs for safe and sustainable energy in the future.

CHAPTER THREE
SIMULATED PERFORMANCE OF A NOVEL SOLID-STATE DYE-SENSITIZED SOLAR CELL BASED ON PHENYL-C_{61}-BUTYRIC ACID METHYL ESTER ($PC_{61}BM$) ELECTRON TRANSPORT LAYER

Abstract

The unabated use of conventional transport fuels has led to increased exhaust emissions, resulting in unprecedented consequences on climate change. Renewable energy sources have become a crucial component for the sustainability and development of human society, with solar energy being the primary contender. In this study, the one-dimensional solar cell capacitance (SCAPS-1D) software has been used to numerically model a novel solid-state dye-sensitized solar cell composed of solid layers with the configuration FTO/$PC_{61}BM$/N719/CuSCN/Au. The primary objective of the numerical simulation employed in this study is to optimize the performance of the electron transport layer, specifically phenyl-C_{61}-butyric acid methyl ester ($PC_{61}BM$). Accordingly, the performance of the model cell has been evaluated by modulating working temperature, absorber thickness, defect density, and metallic back contact. The model solar cell showed the best photovoltaic performance with a power conversion efficiency of 5.38%, open circuit voltage (V_{oc}) of 0.885 V, a short-circuit current density (J_{sc}) of 8.563 $mAcm^{-2}$ and a fill factor (FF) of 70.94%. From the Mott-Schottky curve and band diagrams, an estimated built-in voltage of $\sim$1.0 V was determined. Notably, the power conversion efficiency of the model solar cell is robust and is toxic-free compared to lead-based perovskite solar cells. The findings of this study are valuable for the development and manufacturing of high-performance dye-based solar cells suitable for large-scale production.

3.1 Introduction

Traditional transport fuels, including coal, petroleum, and fossil fuels, have caused significant environmental degradation and continue to be depleted in the contemporary energy landscape (Wang et al., 2017). Consequently, researchers have recently focused on renewable energy sources, including biodiesel and solar power, which are recognized for their ability to mitigate environmental impacts (Gustavsson et al., 2017). One of the promising research areas to fulfil the

ever-growing energy demands without negatively affecting the planet is the transformation of sunlight into electricity. Achieving the United Nations (UN) Sustainable Development Goals requires a focus on photovoltaic technology as a pathway to a more sustainable and positive future (Santika et al., 2019). Theoretical simulations have been used to complement experimental research undertakings, reduce costs, and save time in solar cell design and fabrication. Through innovative technologies, the inexhaustible solar energy can be sustainably exploited to power our heating, electricity, and transportation needs, thereby contributing to a more sustainable and greener future. In 1.5 days, the energy capacity from the sun is $\sim 1.7 \times 10^{22}$ Joules, which is equivalent to the energy that can be extracted from three trillion barrels of all finite oil reserves on the Earth's crust (Crabtree & Lewis, 2007). The global annual energy consumption exceeds 4.6×10^{20} Joules, which is equal to the sun's energy output in one hour (Crabtree & Lewis, 2007). Solar energy is not only environmentally benign but also inexhaustible and accessible to most regions of the globe. In one day, the Earth receives 1.2×10^{7} watts, which is sufficient to satisfy energy demand for two decades (Chu & Meisen, 2011). The demand for sustainable energy resources is driven by the exponential growth of the human population, the advancement of industrial systems, environmental and human health concerns, climate change, and the demand for quality living standards (Caruso et al., 2020). Consequently, the world's energy demand is anticipated to be met in the future through the development of solar infrastructure, contributing to a transition towards a more sustainable and resilient energy future (Santika et al., 2019).

The research community has given dye-sensitized solar cells (DSSCs) a lot of attention because of their desirable qualities, which include low toxicity and simplicity in fabrication. Moreover, these devices have attractive features, including affordability, high incident photon conversion efficiency (IPCE), adaptability, and efficient light-harvesting efficiency (LHE) in diffuse light. (Gong et al., 2017). Typically, DSSCs are fabricated using an n-type layer, known as the electron transport layer (ETL), with a photoactive layer deposited on its surface and a liquid electrolyte as the acceptor-type layer (Lee et al., 2017). A DSSC is an embodiment of five major components, including a transparent conductive oxide (TCO) layer, a photosensitizer, a semiconductor, a counter electrode, and an electrolyte, as depicted in Figure 3.1. Previous studies have reported the success of using solid-state redox electrolytes due to limitations of liquid-state redox electrolytes, such as electrolyte sublimation, corrosive nature, instability, and evaporation of iodine/tri-iodide

electrolytes (Dissanayake et al., 2017). Consequently, all-solid-state layers in the cell device have been utilized to address the issues posed by iodine/tri-iodide liquid electrolytes, which are not only corrosive but also sublimes.

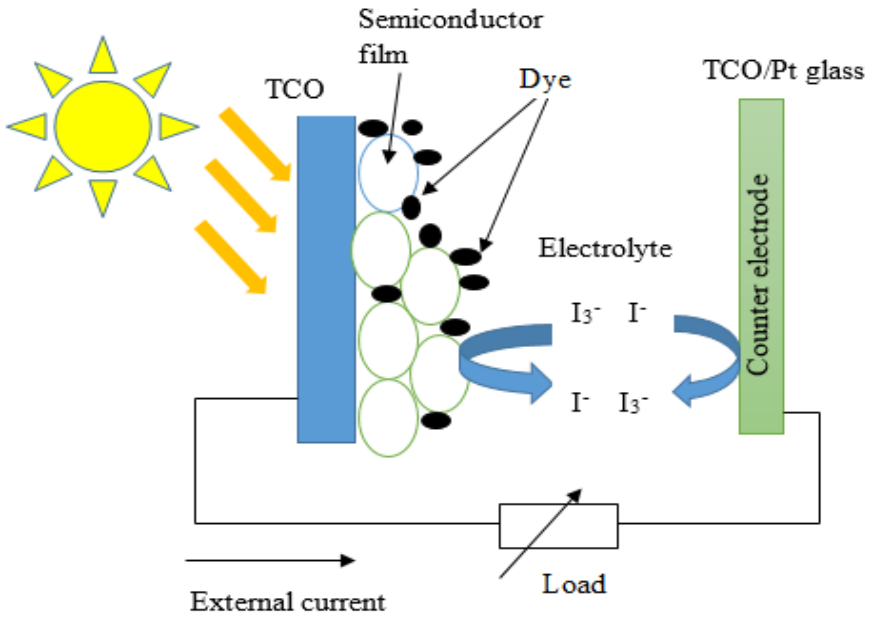

Figure 3.1: The main components of DSSCs (Gong et al., 2017)

Due to their remarkable benefits compared to the iodide/triiodide system – specifically the elimination of charge leakage and solvent volatility, which enhances device long-term stability, solid hole transport layers (HTLs) have been utilized in DSSCs (Manfredi et al., 2014). Organic and inorganic polymers, and p-conducting molecules are used as HTLs due to enhanced temperature stability and lower corrosiveness. Both inorganic and organic HTLs have been reported to mitigate the challenges associated with liquid electrolytes (Calio et al., 2016). In addition to sealing complications, their efficiencies continue to be very poor (Syafiq et al., 2020).

Titanium dioxide (TiO_2) has been the most economical ETL for decades, finding several applications in photovoltaic systems with dye-sensitized and perovskite photoactive layers that enhance solar cell performance (Jahantigh & Safikhani, 2019). Nonetheless, it has been observed that the material degrades over time due to prolonged ultraviolet (UV) exposure and the presence of oxygen vacancies, which activate surface traps (Madan et al., 2020). Consequently, it is essential to explore innovative materials that could serve as suitable ETLs in thin-film technology. Tin

dioxide (SnO_2), tungsten trioxide (WO_3), $PC_{61}BM$, and zinc oxide (ZnO) have been examined as alternative ETLs (Almeida, 2020).

Prior research has documented solid-state dye-sensitized solar cells utilizing N719 photoactive material, a TiO_2 mesoporous photoanode, and caesium tin iodide ($CsSnI_3$) as HTL, characterized by a direct bandgap of 1.3 eV and a hole mobility of 585 $cm^2V^{-1}s^{-1}$ (Shum et al., 2010). The cell with all solid-state layers attained an optimized power conversion efficiency (PCE) of 8.5% and a peak photocurrent (J_{sc}) in ssDSSCs of 19.2 $mAcm^{-2}$ (Shum et al., 2010). However, the oxidation-induced deterioration of $CsSnI_3$ under ambient conditions was attributed to the cell instability over time (Shum et al., 2010). Organic hole-conducting materials such as poly(3-octylthiophene) (POT) and poly(3-hexylthiophene) (P3HT) were first employed in the production of ssDSSCs, showing PCE less than 1% due to pores of the polymer HTLs that were not sufficiently filled in the mesoporous TiO_2 film (Lancelle-Beltran et al., 2008). This led to both low charge extraction efficiencies and ineffective charge separations. A ssDSSCs with TiO_2/N719 dye/P3OT/Au configuration achieved an efficiency of 1.3% and exhibited remarkable stability following the optimization of TiO_2 parameters such as architecture, layer thickness, and porosity (Lancelle-Beltran et al., 2006). Research shows that stoichiometrically increased quantities of SCN^{-1} do not create surface traps in CuSCN, and that the inorganic layer CUSCN does not easily decompose to SCN^{-1}. The CuSCN-based simulated ssDSSCs exhibit the highest stable V_{oc} and longevity (Perera & Tennakone, 2003). Due to their minimal hole conductance characteristics, the DSSCs employing TiO_2 as ETL and CuSCN as HTL exhibited a PCE of 2%.

Sun et al. (2014) reported $PC_{61}BM$ as a comparatively effective electron acceptor layer. The typical current-voltage (I-V) characteristics of the cell were demonstrated using the cell configuration ITO/PEDOT: PSS/$CH_3NH_3PbI_3$/Au and $PC_{61}BM$ as the electron transport layer. The device yields a fill factor (FF) of 0.671%, PCE of 3.33%, and 5.961 $mAcm^{-2}$ as the J_{sc}, and 0.832 V as the V_{oc} (Sun et al., 2014). Conversely, the solar cell that did not contain $PC_{61}BM$ showed no meaningful photovoltaic performance. These findings underscore the feasibility of $PC_{61}BM$ as a feasible electron acceptor with high electron affinity. A ssDSSC with configuration TiO_2/N719 dye/ $PC_{61}BM$/P3HT exhibited a poor PCE of 1.4% under standard test conditions (STCs) of 1000 W/m^2 and AM 1.5 solar spectrum (Yue et al., 2011). Yue et al. (2011) reported that the photoelectric response of DSSCs is enhanced by a P3HT/$PC_{61}BM$ heterojunction layer, which

promotes carrier transfer and photon extraction from sunlight (Yue et al., 2011). The present simulation study employs the $PC_{61}BM$ as the electron transport compact layer to optimize the output PV characteristics and stability.

This article presents the effect of modulating the defect density of the photoactive materials on the PCE of the model ssDSSC cell. Furthermore, the impact of changing the working temperature and the metal back contact is considered. Also, this study presents the Mott-Schottky curve, the Nyquist plot, energy band diagrams and the optical absorption graphs of the simulated solar cell configuration. This study reports the solar cell parameters: PCE, FF, V_{oc}, and J_{sc}. The findings of this study are intended to enhance the future development and fabrication of durable, less toxic dye-based solar cells with extended lifetimes. The solar cell under investigation can essentially function at practical temperatures between 260 and 300 K, suggesting that it can be deployed practically anywhere in the world despite its relatively low power conversion efficiency. The simulated performance of the potentially high-performance dye-based solar cells can be injected into the production workflow.

3.2 Numerical simulation methodology

Computational modelling techniques have been utilized in photovoltaic (PV) technology to comprehend its operational principles thoroughly (Rouway et al., 2020). Nevertheless, it is crucial to elucidate the electrical, optical, and mechanical properties, as well as the effect of these microscopic properties on complex solar systems (Messmer et al., 2018). This study utilizes SCAPS-1D 3.3.08 software for computational electronics analysis. The SCAPS-1D program is a numerical software developed by Professor Marc Burgelman and his colleagues at the Electronics and Information Systems (ELIS) department of the University of Gent, Belgium (Burgelman et al., 2013). When the program is launched, a new window – "action panel" is displayed. This panel contains the "working platform" and also the "action menu" (Jhuma et al., 2019). To perform simulations, one needs to click "set problem", which opens up in a new window. In this window, the user constructs a stack of layers by inputting specific parameters. After constructing the solar cell model, measurements to be taken are specified; quantum efficiency (QE), current-voltage (I-V), capacitance-frequency (C-f), and capacitance-voltage (C-V). Upon selecting the "single-shot", the code computes the specified measurements. The input parameters used in this study have been

judiciously sourced from experimental data. The performance of the model is optimized by making reasonable adjustments to the layer defect densities, layer thickness, and working temperature.

The SCAPS-1D version 3.3.08 has been used to study the current-voltage (I-V) photovoltaic characteristics of model ssDSSCs under air mass (AM 1.5G) illumination at 1000 W/m^2. This numerical simulation tool provides recombination models, including Shockley-Read-Hall (SRH), radiative and Auger recombinations. SHR recombination models are predominant in DSSCs, typically occurring when an electron is trapped in the forbidden zone. SCAPS-1D has been shown to be an effective tool for simulating the electronic properties of thin films with heterojunction technologies (HJT), in which the basic semiconductor equations for Poisson and continuity are solved (Burgelman et al., 2004; Movla, 2014).

3.3 Results and discussions

The model ssDSSCs used in this simulation investigation is a one-dimensional planar heterojunction n-i-p cell structure. The architecture comprises FTO/$PC_{61}BM$/N719/CuSCN/Au, where FTO represents fluorine-doped tin oxide, $PC_{61}BM$ serves as the electron acceptor layer, N719 is the photoactive layer- di-tetrabutylammonium cis-bis(isothiocyanato)bis(2,2'bipyridyl-4,4'dicarboxylato) ruthenium (II), CuSCN represents copper (I) thiocyanate, and Au is gold, which serves as the back contact. Figure 3.2a illustrates the structural assembly of the cell layers, whereby the n-region constitutes the ETL, the i-layer serves as the intrinsic layer (N719 dye), which acts as the active area, and the p-region denotes the HTL (CuSCN). When the photoactive layer is illuminated, the electron-hole carriers are created. Consequently, at the i-p interface, the excitons are dissociated, with holes moving to the p-type region while the remaining electrons diffuse to the n-type region. At the n-i interface, the excitons are dissociated, causing the electrons to migrate to the n-junction while the remaining holes transition to the p-type region. Figure 3.2b depicts the movement of excitons upon illumination. The numerical simulator can be used to model ssDSSCs by constructing a stack of various semiconductor layers, which are described by electron affinities, donor densities, bandgap energies, or by changing the physical parameters of the materials, as well as the thickness of the materials (Decock et al., 2012).

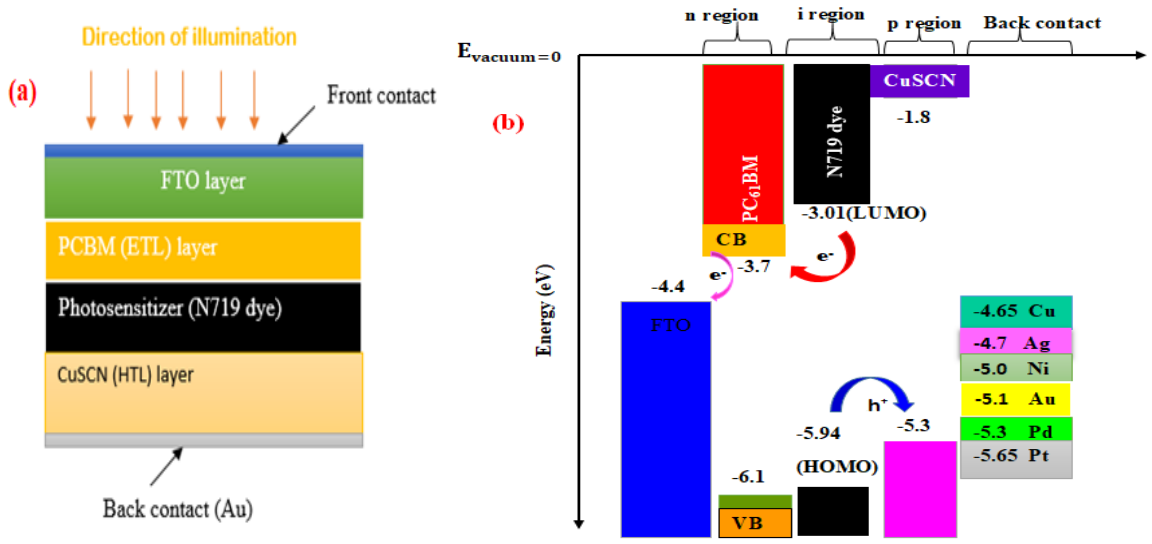

Figure 3.2: Device structure of the n-i-p primary dye-based solar cell (a) and (b) band alignment – electron transport layer, and the proposed hole transport layers

Upon illumination, the SCAPS-1D software gives the illuminated J-V characteristics of the solar cell configuration. This simulator offers a reliable method for evaluating the photovoltaic performance of solar cells. Figure 3.2a, *vide supra*, depicts the simulated solar cell model with illumination incident on the front contact, entering the FTO, then ETL ($PC_{61}BM$), N719 photoactive layer, and finally through the HTL (CuSCN). The interface defect properties of the CuSCN/N719 dye are summarized in Table 3.1.

Table 3.1: The interface defects properties of the CuSCN/N719 dye interface

Defect type	**Neutral**
Capture cross-section electrons (cm^2)	1.00×10^{-19}
Capture cross-section of holes (cm^2)	1.00×10^{-19}
Energetic distribution	single
Reference for defect energy level Et	Above the highest eV
The energy with respect to Reference (eV)	0.600
Total density (integrated over all energies) ($1/cm^2$)	1.00×10^{12}

The simulated device includes all solid-state layers with specific parameters, such as thickness, input parameters of thickness, bandgap energy (E_g), the electron affinity (χ), acceptor density (N_A), relative dielectric permittivity (ϵ/ϵ_r), the donor density (N_D), defect densities N_t, mobility of electrons (μ_e), hole electron mobility (μ_p), conduction band densities (N_C) and the valence band densities (N_V. The selected input parameters used in this study were judiciously extracted from the literature (Azri et al., 2019; Gan et al., 2020; Jahantigh & Safikhani, 2019; Rai et al., 2020; Rondan-Gómez et al., 2020; Zhang et al., 2014), based on theoretical and experimental studies presented in Table 3.2. The optimum defect density (N_t) of $PC_{61}BM$ and HTL – CuSCN considered in this study was 2.0×10^{17} cm^{-3} and 1.0×10^{22} cm^{-3}, respectively.

Table 3.2: Material properties applied in the simulation of the solar cell device reported in this research

Parameter	**FTO**	**$PC_{61}BM$**	**CuSCN**	**N719 dye**
Thickness (nm)	400	30	6000.00	200
Band-gap energy (eV)	3.50	2.0	2.33	3.60
Electron affinity (eV)	4.00	3.90	3.90	1.70
Relative permittivity(e_r)	9.00	3.90	30.00	10.00
Effective density of conduction band N_C (cm^{-3})	9.20×10^{18}	2.2×10^{21}	2.40×10^{20}	1.00×10^{21}
Effective density of valence band N_V (cm^{-3})	1.80×10^{19}	2.2×10^{21}	2.50×10^{20}	1.00×10^{21}
The thermal velocity of electrons (cm/Vs)	1.00×10^{7}	1.00×10^{7}	1.00×10^{7}	1.00×10^{7}
The thermal velocity of holes (cm/Vs)	1.00×10^{7}	1.00×10^{7}	1.00×10^{7}	1.00×10^{7}
Electron mobility (cm^2/s)	20	0.2	5.00	100.00
Hole mobility (cm^2/s)	10	0.2	5.00	25.00
Density of acceptors (cm^{-3})	0.00	0.00	1.00×10^{17}	1.00×10^{17}
The density of donors (cm^{-3})	1.00×10^{19}	2.93×10^{17}	0.00	0.00
Total density N_t ($1/cm^3$)	-	2.0×10^{17}	-	1.00×10^{22}

3.3.1 Quantum efficiency of the model solar cell

Accordingly, internal quantum efficiency (IQE) and external quantum efficiency (EQE) are the two parameters to characterize the quantum efficiency of a solar cell. The EQE is the ratio of collected charge carriers to the number of incident photons in a photovoltaic system, whereas the IQE is the ratio of created electron-hole pairs to the total number of absorbed photons, also referred to as quantum yield (Karmalawi et al., 2020). The EQE (%) of the simulated ssDSSCs analyzed in this study is presented in Figure 3.3. The external quantum efficiency (EQE) of the cell increases from 48.5% at 300 nm to a peak of 97.6% at 370 nm, then drops to 3.80% at approximately 610 nm. Ruthenium (II) dyes such as N719 are highly desirable for dye-sensitized solar cells (DSSCs) due to their robust absorption spectra, ranging from ultraviolet to near-infrared wavelengths. Between 300 and 900 nm, the N719 pigment absorbs solar light because of transitions in metal-to-ligand charge transfer (Aghazada & Nazeeruddin, 2018; Barrera et al., 2016). Low molecular coefficients have an impact on this dye and frequently cause intramolecular charge transfer within the same wavelength range. Co-sensitizing the N719 dye with organic dyes, such as triphenylamines, can enhance the light-harvesting efficiency of N719 dye-based solid-state dye-sensitized solar cells (Sharma et al., 2013; Wu et al., 2014).

This spectrum is consistent with the optimal absorption spectra of N719 dye (Han et al., 2010) and illustrates the conversion of solar radiation into electricity as a function of measured wavelengths (Markvart & Castañer, 2013). In most instances, the IPCE (QE) of a typical PV cell exhibits "square-like" graphs, as the IPCE value remains reasonably stable over the measured wavelengths (300–900 nm) (Ranjusha et al., 2011). The photoactive substance (N719 dye) chosen for this study exhibits a significant electron affinity, turning nearly all absorbed photons into usable energy within the 360 nm to 520 nm spectrum. Furthermore, it seems to exhibit relative compatibility with various semiconductor materials, comprising both n-type and p-type layers. It is clear from this analysis that energy losses due to charge carriers are recombined before being collected by the external circuit. Nonetheless, the external quantum efficiency diminishes progressively at longer wavelengths, despite its capacity to absorb a larger quantity of photons that are effectively transformed into energy. The efficiency of the cell diminishes around 610 nm due to the absorber's inability to capture photons of longer wavelengths, attributed to a high rate of charge

recombination within the absorber. The quantum efficiency (QE) can be expressed as a function of wavelength. Equation 3.1 gives the relation between QE and J_{sc}.

$$J_{sc} = q \int \emptyset(\lambda) QE(\lambda) d(\lambda) \quad (3.1)$$

From Equation 3.1, $\emptyset(\lambda)$ is the photon flux per wavelength.

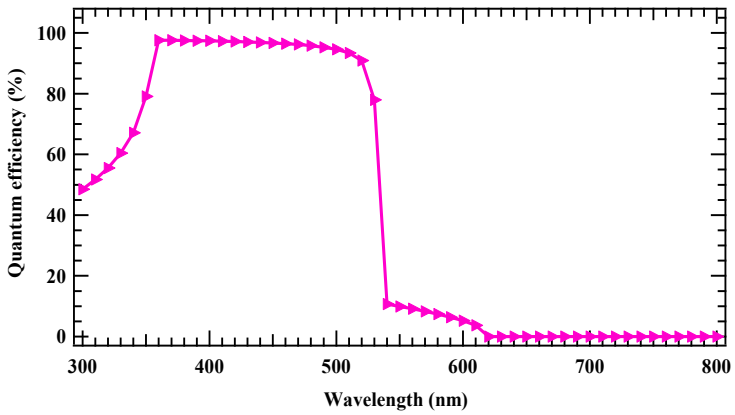

Figure 3.3: External quantum efficiency (EQE) of the cell as a function of the photon wavelength

3.3.2 Effect of CuSCN/N719 interface defects

The modelled solar cell structure, employing various semiconductor layers, is presented in Figure 3.4. Prior research has demonstrated that the overall efficiency of a solar cell configuration is significantly influenced by the quality of interface junction (Gan et al., 2020). According to Devi et al. (2018), high defect densities not only lower the quality of the PV layers but also increase the rate of charge recombination. The defects at the CuSCN and N719 contact were evaluated in this study. Figure 3.4 illustrates the measurements that can be specified for numerical simulation, located at the very top right. As shown, these measurements comprise the current reference settings, the direction of illumination, and the direction of voltage applications.

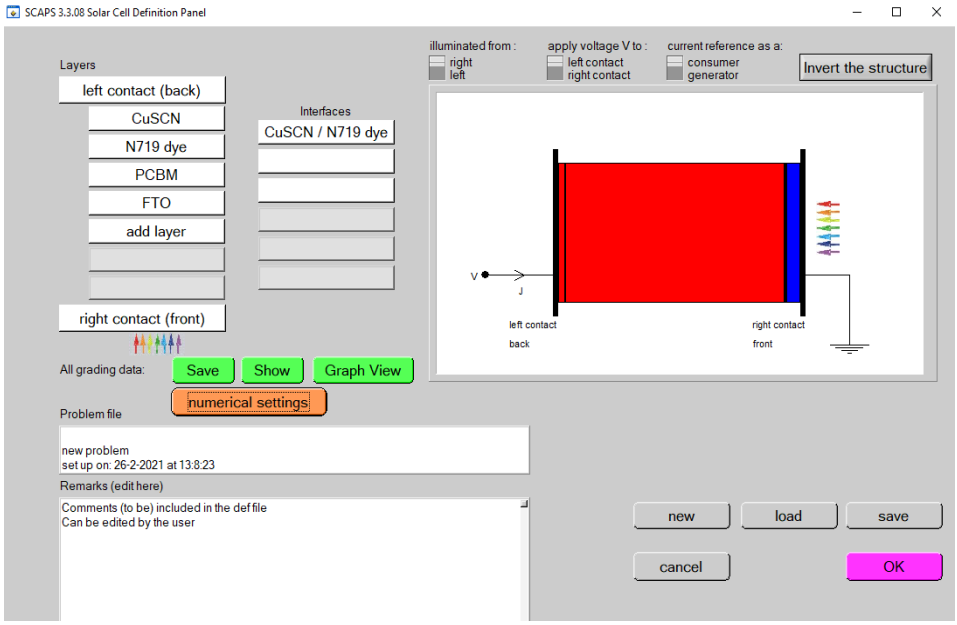

Figure 3.4: The constructed stack of layers for the simulated ssDSSCs in the SCAPS-1D

The performance of the ssDSSCs decreased as the density of defects at the interface increased, as indicated in Table 3.3. This is attributed to the increased availability of surface traps and an increase in recombination centres. This aligns with earlier research findings documented in the literature (Gan et al., 2020).

Table 3.3: The J-V characteristics of the simulated solar cell when the CuSCN/719 dye interface defect densities are varied

Defect densities ($1/cm^2$)	**V_{oc} (V)**	**J_{sc} ($mAcm^{-2}$)**	**FF (%)**	**PCE (%)**
1.00×10^{1}	0.9704	8.924	67.18	5.82
1.0×10^{3}	0.9704	8.924	67.18	5.82
1.0×10^{5}	0.9704	8.924	67.18	5.82
1.0×10^{7}	0.963	8.909	67.57	50.80
1.0×10^{9}	0.900	8.656	70.54	5.50
1.0×10^{10}	0.8875	8.578	70.90	5.40
1.0×10^{12}	0.885	8.563	70.94	5.38

3.3.3 Current-voltage (J-V) characteristics

The simulation findings under AM 1.5 at 1000 W/m^2 were as follows: V_{oc} = 0.885 V, J_{SC} = 8.563 $mAcm^{-2}$, FF = 70.94%, and PCE = 5.38%. The external peak open circuit voltage of the circuit, V_{oc} (0.885 V), represents the voltage at which current flows when the terminals of the ssDSSCs are disconnected. This is the peak voltage that this solar device can produce. The value of V_{oc} is determined by the photogenerated current density. The current generated by the solar cell when its terminals are short-circuited under light, J_{SC} = 8.563 $mAcm^{-2}$. The fill factor (FF) of 70.94% is defined as the ratio of the maximum achievable power to the product of the V_{oc} and the J_{SC}. This parameter helps assess the quality of the solar device (Bartesaghi et al., 2015). The fill factor (FF) quantifies the "squareness" of the current-voltage (J-V) curve features, as depicted in Figure 3.5(a). The PCE value is calculated by the ratio of the maximum power P_{max} to the incidence power P_{in}. The rate at which electron carriers (e^-) and hole carriers (h^+) recombine when incident photons are photo-converted by the solar cell is depicted by the current recombination curves.

Figure 3.5(b) depicts the absorption coefficients of the layers in the simulated ssDSSCs as a function of wavelength. The absorption coefficients of the layers $PC_{61}BM$, CuSCN, FTO, and N719 are unique, as illustrated in Figure 3.5(b), indicating variability in their photon absorption capabilities. The conduction band of the semiconductor is stimulated by photons that are preferentially absorbed by the layer with the highest absorption coefficient ($PC_{61}BM$). The absorption coefficients indicate the degree to which light of a specific wavelength is absorbed by the solar device (Kabir et al., 2019). Wavelength energies below the band gap are insufficient to excite an electron from the valence band to the conduction band. The HTL-CuSCN exhibits a markedly low absorption constant, leading to poor photon absorption relative to the layer with a high absorption coefficient, $PC_{61}BM$. Equation 3.2 depicts the absorption coefficient s and the extinction coefficient of the proposed material layers of the solar cell.

$$\alpha = 4\pi k \frac{1}{\lambda} \tag{3.2}$$

where α, k, and λ is the absorption coefficient, extinction coefficient and wavelength of photons in (nm), respectively (Kabir et al., 2019). The value of α is multiplied by 10^7 and the absorption coefficient is given in cm^{-1}.

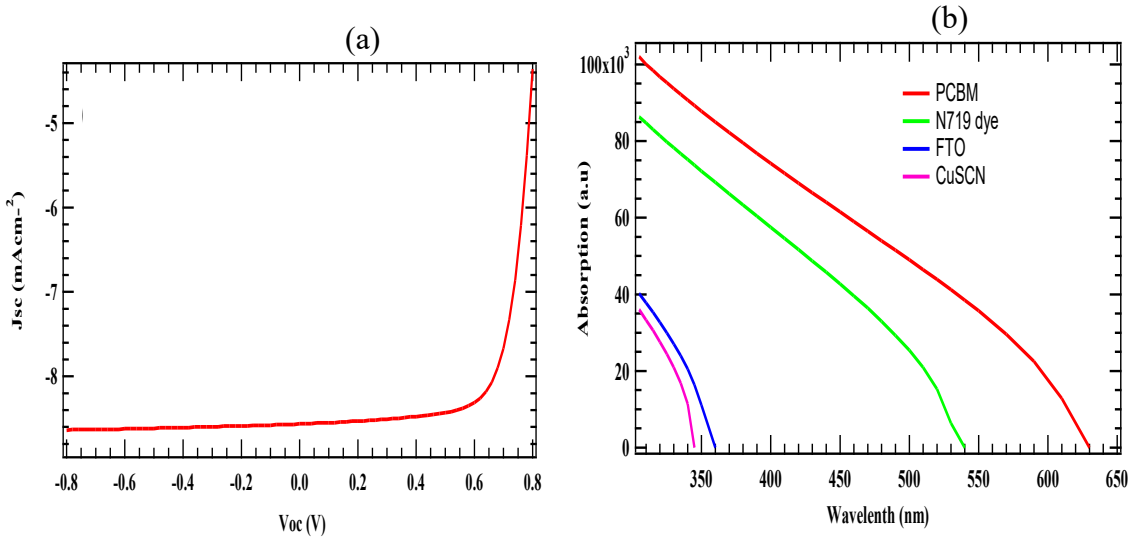

Figure 3.5: The J-V characteristics (a) and (b) the optical absorption of the simulated PV device

3.3.4 Effect of working temperature

The performance of ssDSSCs is significantly affected by the prevailing temperature conditions in a particular environment (Kim et al., 2015). Solar cell devices are generally utilized outdoors; their thermal stability degrades due to the effects of peak temperatures, especially in summer (Kersten et al., 2015). Typically, solar cells operate at temperatures above 300 K. Nonetheless, contemporary third-generation solar cells exhibit efficiency under diffuse conditions and can be easily mounted on windows (Reynaud et al., 2019). Therefore, it is essential to investigate the effects of temperature variations on solar cell functionality. This study evaluated temperatures ranging from 260 to 310 K. Figure 3.6 (a) depicts that the open-circuit voltage (V_{OC}) diminished while the short-circuit current (J_{sc}) rose when the operating temperature increased from 260 to 300 K. The PCE diminished as the FF increased, as depicted in Figure 3.6(b). The temperature was varied within the range of 260 to 300 K. The operational lifespans of semiconductors are reduced with increasing temperature. PV devices exhibit instability at high temperatures, resulting in degradation and reduced efficiency (Lim et al., 2021).

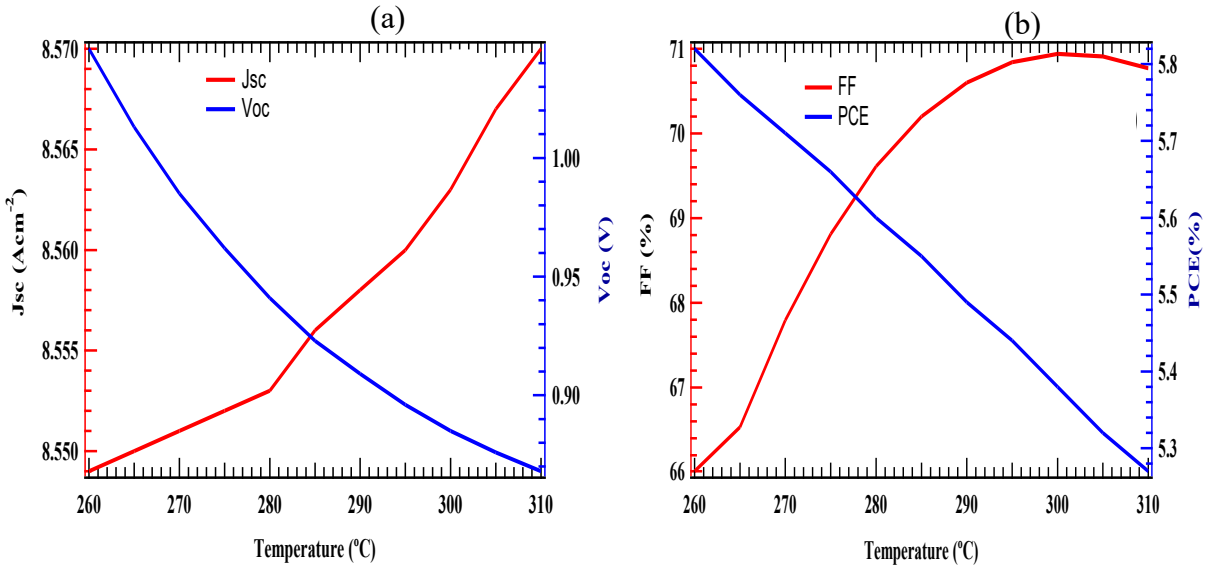

Figure 3.6: Temperature effects on J_{sc} and V_{oc} (a) and (b) FF and PCE

As the temperature rises from 260 to 310 K, the short circuit current, J_{sc}, progressively rises from 8.549 to 8.57 mAcm^{-2}, as seen in Figure 3.6(b). As the thermal activation energy rises as a result of higher temperatures, there is a decrease in charge recombination at the heterojunction barrier, which is associated with this increase. Additionally, it is noted that when the temperature rises from 260 to 300 K, the V_{oc} drops from 1.046 to 0.868 V. This decline is ascribed to high rates of carrier charge recombination caused by an increase in the value of the dark saturation current, J_0. Equation 3.3 predicts that the V_{oc} is dependent on J_{sc}

$$V_{oc} = \frac{nk_BT}{q} \ln\left[\frac{J_{sc}}{J_o} + 1\right] \qquad (3.3)$$

where J_{sc} is the photogenerated current in the presence of light illumination, J_0 is the dark saturation current, T is the absolute temperature in Kelvins (K), k_B is the Boltzmann constant ($k_B = 1.38 \times 10^{-23} JK^{-1}$), q is the electronic charge ($q = 1.603 \times 10^{-19}\ C$) and n, ($1 < n > 2$) as the ideality factor. The term $\frac{nk_BT}{q}$ gives the thermal voltage or flow of elementary current.

The efficiency of the solar cell device is significantly influenced by the diffusion length of the charge carriers, particularly in the presence of the photosensitizer (Kaiser et al., 2001). The rate at which charge carriers recombine increases with an increase in defect densities. The problem can be addressed by employing a thicker absorber layer comparable to the thickness of the depletion layer (Kaiser et al., 2001). As the dye thickness increases from 1000 nm to 6000 nm, the overall

cell efficiency begins to increase, as shown in Figure 3.7(a). The efficiency rises from 4.29% at 1000 nm to 5.38% at 6000 nm. The PCE rises with increasing layer thickness as more photons are absorbed; consequently, the performance of the cell approaches an optimal value. Conversely, the FF experiences a gradual increase from 71.14% to 71.16% as the absorber layer thickness increases from 1000 nm to 1500 nm, and a subsequent decrease to 70.94% as the absorber layer thickness increases from 1500 nm to 6000 nm.

3.3.5 Absorber thickness

The efficiency of ssDSSCs depends on the thickness of the photosensitizer, which in this study is the N719 dye. The dye is responsible for absorbing photons, which are subsequently converted into electricity at the p-i-n junction of the cell (Xiang et al., 2019). The dyes employed in PV technology should be capable of absorbing solar radiation in the visible and near-infrared (NIR) regions of the spectrum (300–900 nm) (Cai et al., 2019). The thickness of the absorber layer has a significant impact on the values of V_{oc} , PCE, FF, and J_{sc}. The SCAPS-1D computational code was used to adjust the absorber thickness from 1000 to 6000 nm in this study. The output in Figure 3.7 (a) suggests that the J_{sc} increases progressively as the thickness of the absorber layer increases. The power conversion efficiency increases gradually and reaches a maximum of 5.38% at 6000 nm, while the J_{sc} reaches a maximum value of 8.885 $mAcm^{-2}$. The generation of electron-hole pairs (e^- h^+ pairs) is a consequence of the absorbers' thicker layers, which absorb a greater number of photons. Due to the incomplete absorption of incident photons, V_{oc} and J_{sc} are relatively lower (0.869 V and 7.557 $mAcm^{-2}$, respectively) when the absorber layer thickness is 1500 nm (Mohamed, 2014). The efficiency of power conversion at this thickness (1500nm) is notably low, at 4.29%. This is due to the limited diffusion length of the photosensitizer and the recombination of charge carriers (photogenerated charge) at the back contact, which is typically located near the depletion region in the cell. These observations are in agreement with other investigations in the literature (Yang et al., 2018).

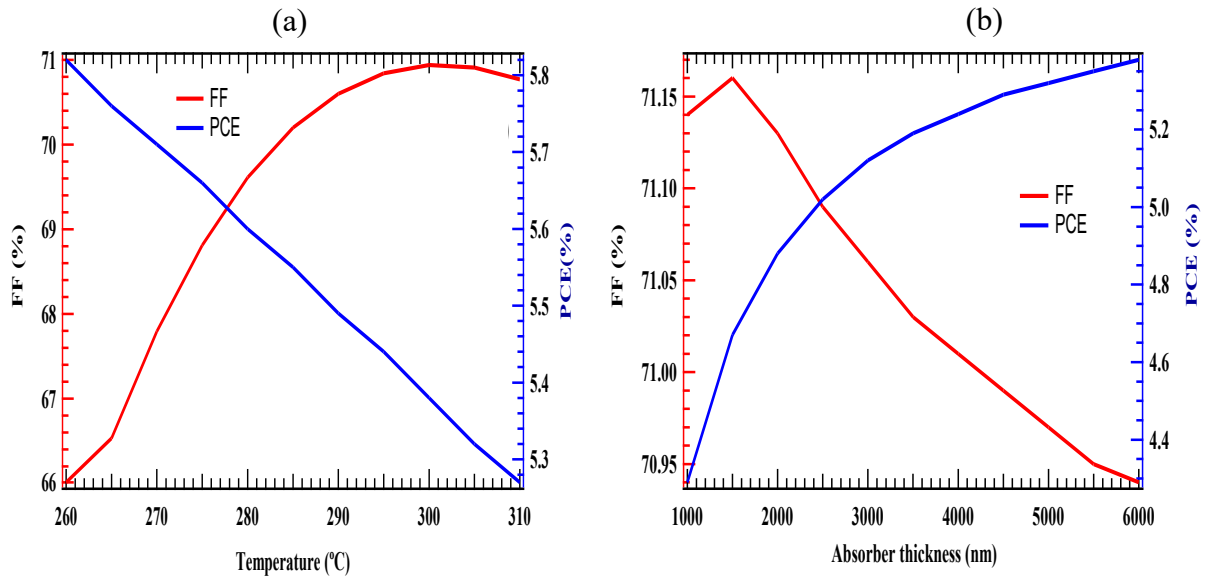

Figure 3.7: Variation in absorber thickness with (a) J_{sc} and V_{oc} and (b) FF and PCE

3.3.6 Effect of CuSCN and FTO thickness

The FTO and HTL are crucial components in assessing the overall efficacy of a solar cell, as they enhance the optimization of power conversion efficiency and photo-thermal stability. As the thickness of CuSCN was augmented from 100 to 1000 nm, the cell parameters FF, PCE, V_{oc} and J_{sc} remained constant at 70.94%, 5.38%, 0.885 V, and 8.563 $mAcm^{-2}$, respectively. This indicates that the HTL maintains consistent efficiency across all simulated thicknesses and can interact with the N719 dye more efficiently. The PCE decreased progressively from 5.44% to 5.31% as the FTO thickness rose from 100 to 1000 nm. As shown in Table 3.4, V_{oc} values decrease from 0.886 to 0.855 V as the thickness of FTO increases from 100 to 1000 nm, as demonstrated in Table 3.4. The photo-generated current (J_{sc}) decreases from 8.655 to 8.463 $mAcm^{-2}$. An increase in the recombination rate of charge carriers and an increase in dark saturation current, J_0, resulting in a reduction in V_{oc}. Nonetheless, the fill factor (FF) is enhanced by a decrease in photogenerated current J_{sc} and V_{oc} (cf. Table 3.4). The ideal thickness of FTO is 100 nm. The thickness range in which the cell demonstrates a high V_{oc} of 0.886 V, a J_{sc} of 8.655 mA/cm², and a power conversion efficiency (PCE) of 5.44%. Within the range of 100 to 700 nm, the fill factor (FF) remained stable; however, it increased to 70.95% when the layer thickness increased from 800 to 1000 nm. Consequently, thicker FTO layers exhibit superior thermal and chemical stabilities, along with

good optical transparency and electrical conductivity, making them suitable for application in ssDSSCs (Huang et al., 2009).

Table 3.4: The output parameters of V_{oc}, J_{sc} and PCE when the thickness of CuSCN and FTO is varied

Thickness in (nm)	Material	V_{oc} (V)	J_{sc} (mAcm^{-2})	FF (%)	PCE (%)
100	FTO	0.886	8.655	70.94	5.44
	CuSCN	0.885	8.563	70.94	5.38
200	FTO	0.886	8.619	70.94	5.42
	CuSCN	0.885	8.563	70.94	5.38
300	FTO	0.886	8.589	70.94	5.4
	CuSCN	0.885	8.563	70.94	5.38
400	FTO	0.885	8.563	70.94	5.38
	CuSCN	0.885	8.563	70.94	5.38
500	FTO	0.885	8.541	70.94	5.36
	CuSCN	0.885	8.563	70.94	5.38
600	FTO	0.885	8.521	70.94	5.32
	CuSCN	0.885	8.563	70.94	5.38
700	FTO	0.885	8.504	70.94	5.34
	CuSCN	0.885	8.563	70.94	5.38
800	FTO	0.885	8.489	70.95	5.33
	CuSCN	0.885	8.563	70.94	5.38
900	FTO	0.885	8.475	70.95	5.32
	CuSCN	0.885	8.563	70.94	5.38
1000	FTO	0.885	8.463	70.95	5.31
	CuSCN	0.885	8.563	70.94	5.38

3.3.7 Effect of the back contact work function

The performance of photovoltaic devices is greatly affected by the electrical characteristics of the back contact. Molybdenum (Mo) has proven to be an efficient rear contact material in thin-film

photovoltaic systems. Nonetheless, its insufficient power conversion efficiency makes it unsuitable as a substitute (Altamura et al., 2014). Gold (Au) is recognized as the most efficient back contact material; however, its utilization is hindered by its high cost and the diffusion of Au atoms into other solar cell layers, which compromises performance (Teixeira et al., 2019). We evaluated the performance of ssDSSCs by changing the metal back contact, which possesses differing metal work functions, to demonstrate the potential of the most dependable, economical, and high-performing back contact. Table 3.5 lists the simulated materials and corresponding photovoltaic performance: copper (Cu), gold (Au), nickel (Ni), platinum (Pt), silver (Ag), and palladium (Pd). The metal front contact is selected to be flat bands and the SCAPS-1D software is able to automatically give the work function of the metal.

The performance of the solar cell is improved when the back contacts have higher metal work functions, as demonstrated in Table 3.5. Correspondingly, the FF values increase with a high metal work function of the rear contact, leading to an enhancement in power conversion efficiency, as ascribed in Table 3.5. The results of this study demonstrate that the feasible back contact metals are Au, Ni, and Pt. These metallic back contacts are ideal for application in solar cells. Gold (Au) and platinum (Pt) are costly back contact materials (Hall et al., 2021). In the simulated ssDSSCs, nickel is the optimal material for the metal back contact owing to its superior performance, as ascribed in Table 5. Unlike palladium, nickel is abundantly available in nature, cost-effective, possesses a higher work function, is reliable, and exhibits good power conversion efficiency (cf. Table 3.5).

Table 3.5: The ssDSSCs cell performance characteristics for different metal back contacts

Back contact metal work function	**V_{oc} (V)**	**J_{sc} ($mAcm^{-2}$)**	**FF (%)**	**PCE (%)**
Copper (4.65)	0.881	8.562	70.39	5.31
Silver (4.7)	0.885	8.563	70.85	5.37
Nickel (5.0)	0.885	8.563	70.94	5.38
Gold (5.1)	0.885	8.563	70.94	5.38
Palladium (5.3)	0.885	8.563	70.94	5.38
Platinum (5.65)	0.885	8.563	70.94	5.38

3.3.8 Effect of absorber defect densities and $PC_{61}BM$ donor densities

In addition, this study investigated the impact of N719 dye defect densities (N_t) on the performance of the proposed photovoltaic device. It was evident that the device's overall performance decreased as the concentration of defect densities increased. Additionally, when the defect density was increased to 1.33×10^{17}cm^{-3}, the defect concentration in the absorber layer – N719 dye was increased from 1.00×10^{14}cm^{-3}, resulting in a decrease in J_{sc} from 8.386 mAcm^{-2} to 5.174 mAcm^{-2}. In contrast, the V_{oc} remained relatively consistent at 0.886 V, although Nt increased from 1.0×10^{14} to 2.0×10^{15} cm^{-3}, Subsequently, the V_{OC} decreased to 0.87 V when the Nt concentration increased to 1.33×10^{17}cm^{-3}. The graph of J_{sc} and V_{oc} as a function of Log N_t is depicted in Figure 3.8(a). In addition, the PCE decreased from 5.26% to 2.99%, and the FF decreased from 70.75% to 66.47% as the concentration of Nt increased from 1.00×10^{14}cm^{-3} to 1.33×10^{17}cm^{-3}, as demonstrated in Figure 3.8(b). The device's power conversion efficiency (PCE) was 5.26% at a concentration of 1.00×10^{14}cm^{-3}. However, it experienced a significant decline to 2.99% at a concentration of 1.33×10^{17}cm^{-3}. The fill factor of the device decreased from 70.75% at a concentration of 1.00×10^{14}cm^{-3} as the number of absorber defects increased. The fill factor was 66.47% at a defect concentration of 1.33×10^{17}cm^{-3}. The relationship between FF (%) and PCE (%) as a function of Log N_t is illustrated in Figure 3.8 (b).

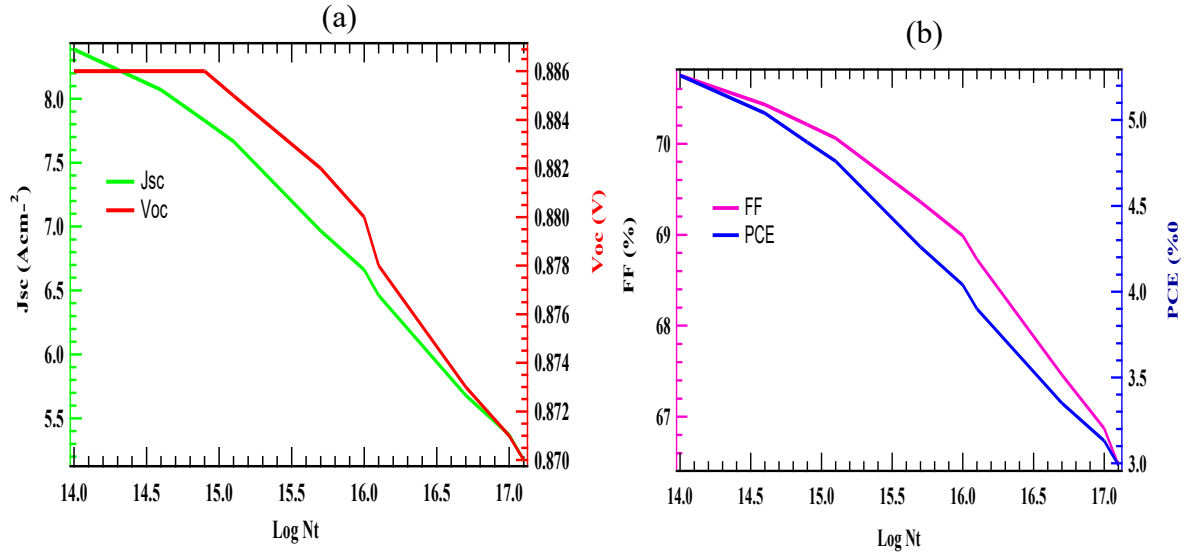

Figure 3.8: The effect of absorber defect density on J_{sc} and V_{OC} (a) and (b) PCE and FF as a function of absorber defect density

The photovoltaic performance of the ssDSSCs was further assessed by modulating the concentration of the acceptor donors. The cell exhibits an overall effectiveness of 5.17% at a donor density concentration (N_D) of $PC_{61}BM$ is 2.00 $\times 10^{15}$ cm^{-3}. The cell performance rises to 5.44% at a concentration of $1.00 \times 10^{17} cm^{-3}$ as the N_D concentration of $PC_{61}BM$ is gradually raised. When the concentration of N_D is 7.00 x 10^{17} cm^{-3}, the efficiency of the cell drops to 5.26%. Conversely, the concentration of N_D rises from 2.00 $\times 10^{15}$ cm^{-3} and 1.00 x 10^{17} cm^{-3}, yielding a 70.57% increase in FF and a 70.96% enhancement in FF. The FF subsequently drops to 58.22% as the concentration of N_D rises to 7.00 x 10^{17} cm^{-3}. As the concentration of N_D in the ETL – $PC_{61}BM$ drops from 2.00 $\times 10^{15}$ cm^{-3} - 7.00 x 10^{17} cm^{-3}, the open-circuit voltage (V_{oc}) climbs progressively from 0.862 V to 1.057 V. The graphs of J_{sc} and V_{oc} as a function of Log N_D, illustrate that both J_{sc} and V_{oc} consistently rise with increasing concentrations of N_D. Nonetheless, the J_{sc}, experiences a sudden decline when the N_D concentration reaches $7.00 \times 10^{17} cm^{-3}$, as illustrated in Figure 3.9 (a). The FF values remained rather stable when the donor density concentration N_D, was set between $2.00 \times 10^{15} cm^{-3}$ and $3.00 \times 10^{17} cm^{-3}$, but they exhibited a significant decline when N_D climbed to $7.00 \times 10^{17} cm^{-3}$. The PCE values (Figure 3.9b) rose with the increase of secondary dopant concentrations. The $PC_{61}BM$ layer demonstrates an optimal donor density N_D of 5.0 x 10^{17} cm^{-3}, a peak J_{sc}, of 8.565 $mAcm^{-2}$, a power conversion efficiency (PCE) of 5.44%, a fill factor (FF) of 68.87%, and an open-circuit voltage V_{oc} of 0.922 V.

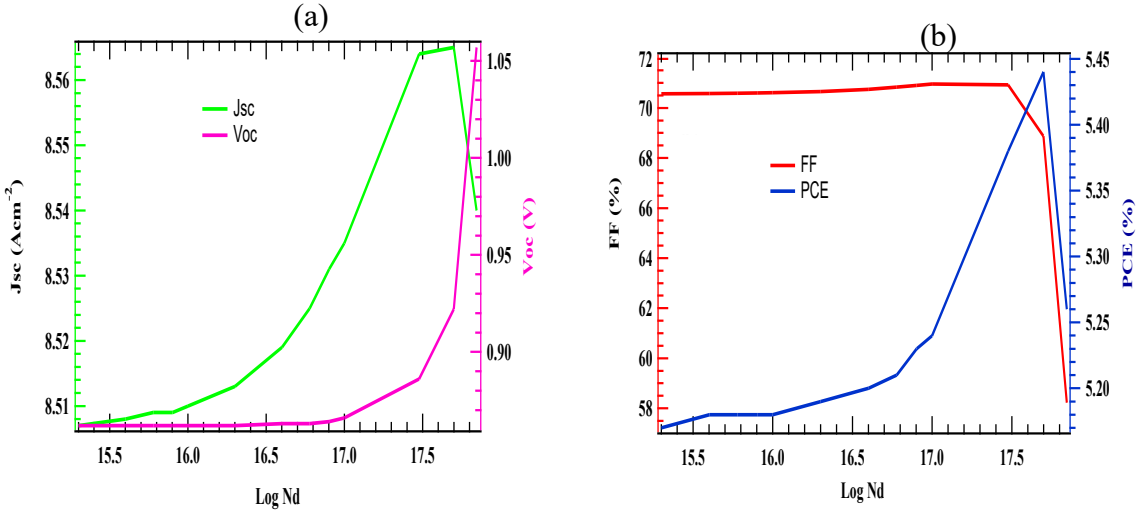

Figure 3.9: Variation of Log N_D with J_{sc} and V_{oc} (a) and (b) FF and PCE

3.3.9 Heterojunction and conductance-voltage (G-V) characteristics

At the p-n junction of a heterojunction cell, charge carriers diffuse into either layer, resulting in a depletion region with a corresponding potential V_{ib} defined by the general relation. This is referred to as the built-in voltage, as given by Equation 3.4.

$$V_{ib} = E_{g2} - (E_f - E_{C2}) + X_2 - X_1 - (E_{C1} - E_f) \quad (3.4)$$

where E_g, X, $E_C$and E_f are bandgap energy, electronic affinities of semiconductor material, conduction band level and Fermi level, respectively. Figure 3.10 depicts the band energy diagram of the simulated ssDSSCs, where; $\Delta E_v = \Delta E_C + \Delta E_g$ whereby the component ΔE_g designate bandgap energies of the materials, as depicted at the heterojunction, ΔE_C jump from the conduction bands of the n-type and p-type semiconductors due to the difference in their electron affinities. The value of ΔE_C The value of +1.52 eV demonstrates that there is no energy barrier for collecting electrons by the n-type layer generated by the p-type layer under illumination. The eV_{bi} (0.88 V) is the built-in voltage and is obtained by considering Equation 3.5.

$$eV_{bi} = EF_n - EF_p \quad (3.5)$$

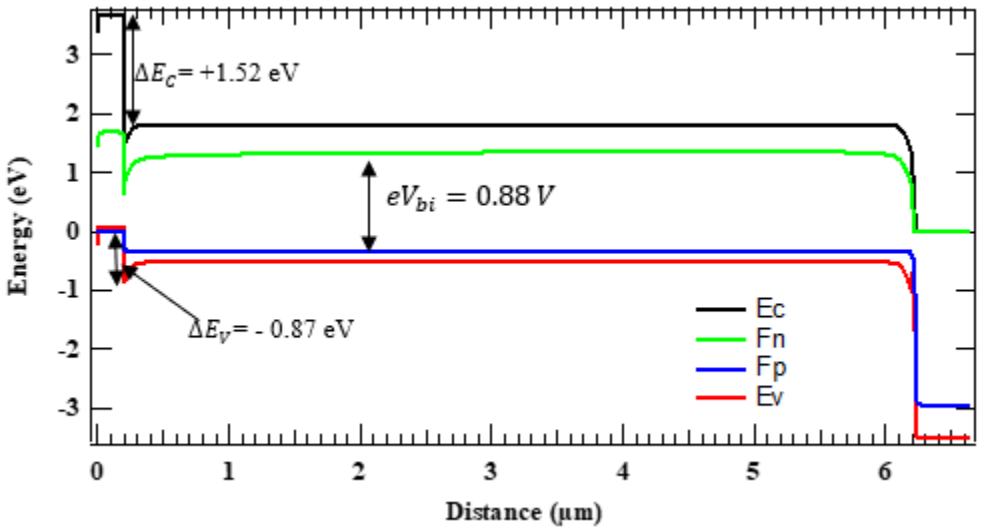

Figure 3.10: Band energy diagram of ssDSSCs at equilibrium

The impedance of a solar device can be measured using the SCAPS-1D code at various frequencies, typically ranging from 1 MHz to 0.1 Hz. Figure 3.11(a) shows the Nyquist plot, arguably the most effective method for characterizing impedance in solar cells. Both the

imaginary (y-axis) and real (x-axis) components of impedance (Z) are described by it. The relationship between solar cell performance and operating frequency and voltage is demonstrated in the Nyquist plot. The capacity of the PV cell to absorb the most photons determines the operating voltage. The inverses of capacitance and conductance are represented by the imaginary and real parts of the Nyquist plot, respectively. This finding aligns with theoretical and experimental research that has already been published in the literature (Bouzidi et al., 2020).

The conductance-voltage (G-V) characteristics are displayed in Figure 3.11(b). When describing the densities of interface states, the G-V graphs are essential. The frequency at which the current simulation investigation was carried out was 10^5 Hz. Energy losses resulting from the capture and emission of charge carriers by interface traps are represented by the conductance. The curve displays interface states and traps in these interface states by taking into account a constant time of carrier capture with its corresponding energy position.

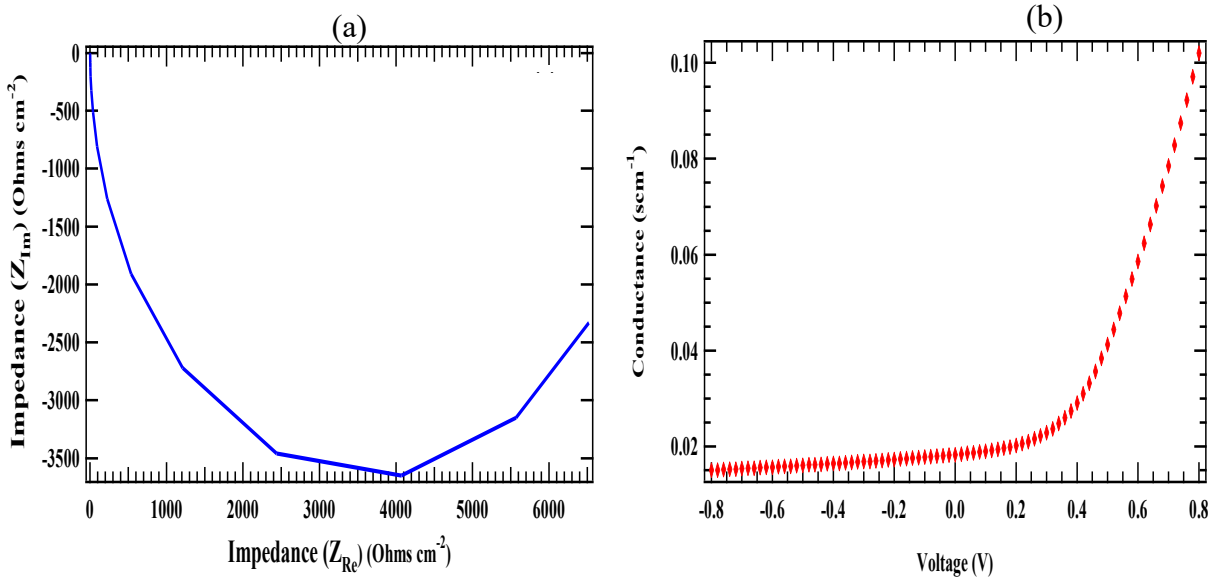

Figure 3.11: Imaginary impedance as a function of real impedance (a) and (b) conductance as a function of voltage

The density of charge carriers, anomalies in interface states, deep levels, and non-uniformities in polycrystalline and amorphous materials have all been explained through the characterization of capacitance-voltage measurements (Hailegnaw et al., 2020). The Mott-Schottky plot of the simulated ssDSSCs is shown in Figure 3.12. The charge density distribution can be derived from these plots using Equation 3.6.

$$N_C(W) = \frac{2}{qK_S\epsilon_0 A^2\left[\frac{d(1/C^2)}{dv}\right]} \quad (3.6)$$

where, $N_C(W)$, ϵ_0 , A, q, K_S and $\frac{d(1/C^2)}{dv}$ is charge density, permittivity of free space, surface area, electron charge, relative permittivity, and the Mott-Schottky slope, respectively. The built-in voltage and acceptor defect densities of the photoactive layer are determined by Mott-Schottky analysis of C-V measurements and voltage modulation in the depletion region (Almora et al., 2016). Additionally, the drive-level capacitance profile (DLCP) can be derived with the aid of alternating current (AC) variation (Eisenbarth et al., 2010). In accordance with observations from the literature, the value of V_{bi} derived from the Mott Schottky curve (0.9 V) is approximately the same as the value derived from the energy band diagram (0.88 V) (Olusola et al., 2018).

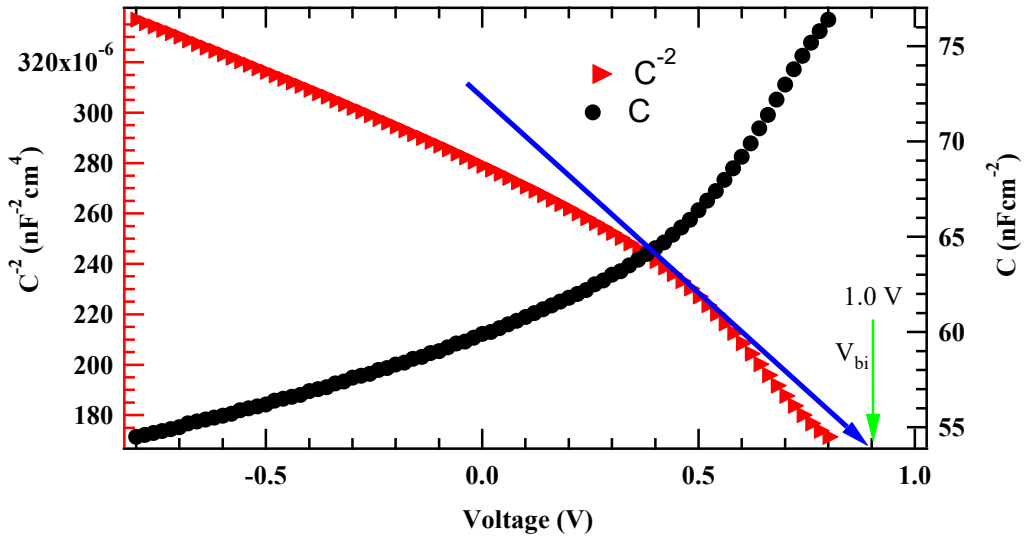

Figure 3.12: Mott-Schottky curves of the simulated ssDSSCs derived from C-V characterization

The results of the current simulation are crucial for understanding how parameters can be adjusted to achieve remarkable performance in the actual fabrication of ssDSSCs. The proposed $PC_{61}BM$ as ETL possesses desirable semiconductor properties, including a high electron affinity and an excellent electron acceptor, making it an ideal material for the design and fabrication of solar cells. The cell device is stable, toxic-free, and has longer cell lifetimes because the HTL layer (CuSCN) does not decompose to SCN^{-1}. Table 3.6 compares various PV parameters of the model cell that result from the use of different materials as electron transport compact layers. In contrast to prior

research on dye-based sensitized solar cells, which employed inorganic TiO_2 as the ETL, this study uses an organic material, $PC_{61}BM$, and still obtains a robust power conversion efficiency (PCE).

Table 3.6: The photovoltaic (J-V) characteristics of various ssDSSCs cell configurations

Device architecture	**Experimental /Simulation**	**V_{OC} (V)**	**J_{sc} ($mA\ cm^{-2}$)**	**FF (%)**	**PCE (%)**	**Ref.**
ITO/PEN/TiO_2/N719 dye/PCBM/P3HT	Experimental	0.87	3.0	0.54	1.43	(Yue et al., 2011)
FTO/TiO_2/BEHP-co-MEH PPV/PEDOT : PSS/Pt	Simulation (SCAPS-1D)	1.53	6.43	80.58	7.95	(Rondan-Gómez et al., 2020)
ITO/CuSCN/P3HT/P3HT : PCBM/Al	Experimental	0.56	7.70	0.57	2.6	(Takahashi et al., 2007)
FTO/TiO_2/BEHP-co-MEH PPV/MoO_2MoO_3/Pt	Simulation (SCAPS-1D)	2.14	4.23	92.93	8.42	(Rondan-Gómez et al., 2020)
FTO/$PC_{61}BM$/N719/ CuSCN/Au	Simulation (SCAPS-1D)	0.89	8.56	70.94	5.38	This work

4. Conclusions

The overall efficiency of the cell was optimized by making appropriate adjustments to the layer thickness, operating temperature, N719 dye thickness, carrier densities, and defect densities of the different materials. When compared to other solar cell architecture designs documented in earlier experimental and theoretical investigations, the optimal PCE of the solar cell proposed in this work was 5.38%, which is comparatively robust. The lowest operating temperature of the device is 260 K, with a PCE of 5.82%, a V_{OC} of 1.046 V, FF is 66.01%, and J_{sc} is 8.549 $mAcm^{-2}$. This illustrates that the model solar cell is capable of maintaining various energy requirements in low-temperature environments, such as winter. At 300 K, the power conversion efficiency was optimized to 5.38%, making it appropriate for humid subtropical climates in Africa and Latin America. This investigation has also demonstrated that the Ni back contact can be substituted with Au, Pt, Ag, or

Pd as back metals. This is because these metals are readily available and offer comparable power conversion efficiency to gold, silver, platinum, and palladium. Additionally, numerical simulations indicate that the optimal thickness of the N719 layer is between 5000 and 6000 nm at a working temperature of 300 K. Conversely, the $PC_{61}BM$ material should have a thickness of 30 nm. FTO and HTL (CuSCN) have optimum layer thickness ranges of 100–300 nm and 200–1000 nm, respectively. Therefore, if the fabrication conditions are effectively controlled, solar power can improve energy security. Providing critical information to solar cell manufacturers through numerical simulation of solar cell designs results in a reduction in both time and cost. Nevertheless, it is recommended to employ an experimental approach to validate the simulated performance of the ssDSSCs photovoltaic cell model.

CHAPTER FOUR

COMPUTATIONAL SIMULATION OF A HIGHLY EFFICIENT HOLE TRANSPORT-FREE DYE-SENSITIZED SOLAR CELL BASED ON TITANIUM OXIDE (TiO_2) AND ZINC OXYSULPHIDE (ZnOS) ELECTRON TRANSPORT LAYERS

Abstract

This study investigated a dye-sensitized solar cell configuration with remarkable photovoltaic efficiency that is inexpensive and does not require a hole-transport layer (HTL). The proposed solar cell technology utilizes a metallic layer for dye generation, thereby eliminating the need for costly hole-transport layers, such as Spiro-OMeTAD, CuSCN, CuI, and PEDOT: PSS. This investigation examines how the performance of the solar cell model is influenced by series and shunt resistances, conduction band offsets, Schottky barriers, operating temperature, the metal work function of the back contact, and the electron affinities of the electron transport layers (ETLs). Two ETLs, TiO_2 and ZnOS, are assessed in the FTO/ETL/N719 dye/Au simulated solar cell configuration. A maximum power conversion efficiency (PCE) of 11.54%, a short circuit current (J_{sc}) of 18.50 $mAcm^{-2}$, a fill factor (FF) of 62.71%, and an open-circuit voltage (V_{oc}) of 0.99 V were obtained by the optimized solar cell configuration FTO/ZnOS/N719 dye/Au. The FTO/TiO_2/N719 dye/Au solar cell design, on the other hand, had a fill factor of 63.58%, a short-circuit current density of 16.50 $mAcm^{-2}$, and a peak power conversion efficiency (PCE) of 10.22%. The results of this investigation show that ZnOS is a suitable electron transport layer for the solar cell model under investigation. ZnOS has a tunable bandgap, is abundant in nature, and is less toxic than conventional TiO_2. Additionally, its remarkable PCE makes it a competitive alternative to silicon-based solar cells and a viable replacement for TiO_2 in the design and manufacturing of HTL-free DSSCs.

4.1 Introduction

The persistent climate challenge and serious global warming trends resulting from the utilization of traditional fossil fuels have prompted the research community to investigate sustainable energy options (York & Bell, 2019). Various renewable energy options have been studied and advanced, including biofuels, nuclear energy, solar energy, wind energy, geothermal energy, and hydropower

(Yikun et al., 2021). Among all potential alternatives, solar energy has emerged as a viable, cost-efficient, and secure source of energy regarded as environmentally sustainable (Meyer et al., 2025). Various materials, including perovskites, dye-sensitized solar cells (DSSCs), amorphous silicon (a-Si), and cadmium telluride (CdTe), have been investigated for their impressive photovoltaic (PV) performance in the advancement of solar cell technology (Lunardi et al., 2021). Nonetheless, the advancement of these technologies is constrained by significant scientific challenges, including the scarcity and toxicity of tellurium (Te), gallium (Ga), and indium (In) (AlZoubi et al., 2021). Recently, numerous studies have demonstrated that perovskite solar cells exhibit thermal and photostability properties (Roghabadi et al., 2019; Sutherland, 2017). Silicon solar cells require higher temperatures for manufacturing thin silicon wafers (Chen et al., 2017). Conversely, the performance of dye-sensitized solar cells (DSSCs) is limited by the volatile nature and corrosiveness of previously used redox electrolytes (Rono et al., 2021a). Dye-sensitized solar cells (DSSCs) currently predominate the photovoltaic research undertakings and are emerging as cost-effective alternatives to conventional silicon-based solar cells.

The new generation of solar cells uses cost-effective, readily available materials and cost-effective fabrication techniques (Periyasamy et al., 2023). Furthermore, these materials are ecologically friendly and suitable as sustainable energy sources. Perovskite solar cells have achieved photovoltaic efficiencies of 25%, surpassing those of dye-sensitized solar cells since their introduction to the market (Al-Ashouri et al., 2020). Consequently, there is an urgent need for improved adaptive nanotechnology techniques that can make dye-sensitized solar cells competitive in the solar energy market. Solar device manufacturing has extensively utilized metal oxide semiconductors due to their excellent mechanical and chemical stability, as well as their tunable band gap energies. Metal oxide semiconductors can be produced as thin films, nanorods, nanowires, and nanoparticles, and find applications in sensors, optoelectronics, storage devices, and catalysis. Doping them with foreign elements enhances light harvesting capabilities (Patel et al., 2017). Transparent conductive oxide (TCO) thin films, such as fluorine-doped tin oxide (FTO) with a metal work function of 4.4 eV and indium-tin-oxide (ITO) with a metal work function of 4.9 eV, are critical components of photovoltaic devices utilized in dye-sensitized solar cells (DSSCs) and perovskite solar cells (Genesio et al., 2018). FTO is preferred over ITO due to its cost-effectiveness, enhanced high-temperature resistance, improved transmission of visible light,

and higher tolerance to physical abrasion (Abrol et al., 2020; Patni et al., 2018). The application of indium is limited by its rarity in the Earth's crust and its high toxicity. Indium has also been reported as a teratogen, which contributes to embryotoxicity and carcinogenicity in both animals and humans (Chaitra et al., 2021; Li et al., 2020).

Titanium dioxide (TiO_2) has been extensively utilized in DSSCs due to its favourable optoelectronic properties, such as a high refractive index, good optical transmittance in the visible portion of the electromagnetic spectrum, high electrical resistivity, and non-toxicity (Yi et al., 2019). Moreover, it has a high dielectric constant, making it suitable for solar cell applications. Perovskite solar cells based on TiO_2 ETL with a PCE of 24.66% have been reported in the literature (Cheng et al., 2020). However, the application of this material in solar cells has been limited by deep traps resulting from prolonged UV illumination, the intrinsic low electron mobility, and high thermal input. These factors hinder effective charge transport, resulting in hysteresis energy losses and reduced material lifetimes.(Cheng et al., 2020). For these reasons, various ETL materials such as tin dioxide (SnO_2), zinc oxide (ZnO), tungsten disulphide (WS_2), and zinc oxysulphide (ZnOS) have been explored as suitable replacements for the conventional TiO_2 material (Singh et al., 2021). Zinc oxysulphide (ZnOS) has a tunable band gap energy, low toxicity, and is cost-effective, making it a suitable replacement for TiO_2 (Shin et al., 2021). This material can be fabricated using chemical bath deposition (CBD) and features a tunable band gap (2.6–3.8 eV), which enhances the photocurrent (Rahman et al., 2017).

Recently, liquid electrolytes in dye-sensitized solar cells (DSSCs) have been replaced with solid-state hole transport layers (HTLs) to enhance their valuable lifetimes (Lenzmann et al., 2005). The proposed solid-state p-type materials include copper thiocyanate (CuSCN), copper (I) iodide (CuI), 2,2′, 7,7′-Tetrakis(N,N-di-p-methoxyphenyl-amine)-9,9′-spirobifluorene (Spiro-OMeTAD), and poly(3,4-ethylene dioxythiophene) polystyrene sulfonate (PEDOT: PSS) (Li et al., 2016). Nonetheless, their power conversion efficiencies (PCE) remain lower when compared to devices fabricated with liquid electrolytes (Lenzmann et al., 2005). Prior studies have reported factors such as rapid interfacial recombination, prolonged instabilities, and decreased hole mobility as causes for the low efficiencies observed in dye-sensitized solar cells with solid-state p-type materials (Rono et al., 2021a). Research has identified solid-state dye-sensitized solar cells (ssDSSCs) that utilize inexpensive materials and production methods, thereby eliminating the need for costly p-

type materials such as Spiro-OMeTAD and PEDOT: PSS (Lenzmann et al., 2005). In these systems, the metallic layers enhance the regeneration of the dye. Gold (Au) and silver (Ag) have been reported as metallic layers that regenerate dye with remarkable performance (Cahen et al., 2000).

Solar cells have been modelled using computer programs designed to solve fundamental semiconductor equations. Consequently, the numerical modelling and analysis of solar cells have recently garnered significant scholarly interest from researchers. Prior researchers have documented numerical simulation findings obtained from various modelling tools, including SCAPS-1D, SILVACO ATLAS, Finite-Difference Time-Domain (FDTD), Automat for Simulation of Hetero-junctions (AFORS-HET), and wxAMPS, for the investigation of microelectronic and photonic systems (Ouslimane et al., 2021). Computational studies are crucial for augmenting experimental studies to enhance and optimize the performance of dye-sensitized solar cells (DSSCs). Simulations have proven critical for analyzing the effect of modulating material properties on the commercialization of next-generation high-efficiency solar cells. The simulation results demonstrate consistency with the experimental findings (Ahmed et al., 2021). Accordingly, SCAPS-1D allows the simulation and analysis of multijunction and heterojunction photovoltaic devices, making it preferable to numerical simulation programmes (Karthick et al., 2020). It is a one-dimensional program developed by the Department of Electronics and Information Systems at Ghent University, Belgium (Burgelman et al., 2013). Recently, Rondan-Gómez et al. (2020) and Ojotu and Babaji (2020) reported theoretical results on the modelling and simulation of ssDSSCs using SCAPS-1D, achieving optimized PCEs of 5.38%, 8.42%, 4.90%, and 17.72%, respectively. Despite the extensive use of TiO_2 as an electron transport material in highly efficient solar cells, it has been observed that it degrades over time due to prolonged UV irradiation. Therefore, this study examined the feasibility of ZnOS ETL in the proposed cell architecture using the SCAPS-1D (Burgelman et al., 2013). Zinc oxysulphide (ZnOS) exhibits promising performance in thin-film solar cells. Nonetheless, this material has garnered minimal attention as a potential electron transport layer (ETL) in both experimental and theoretical investigations of solid-state dye-sensitized solar cells (SSDSSCs). The band gap and electron affinity of ZnOS are tuned by the ratios of oxygen (O) and sulphur (S). By changing these ratios. Additionally, the conductivity and conduction band offset (CBO) of the ETL can be carefully

optimized to improve performance (Slami et al., 2019). Consequently, ZnOS has taken a new place in thin-film solar cells due to its capacity to absorb a large percentage of photons, resulting in remarkable photocurrent generation. The challenges associated with traditional ETLs have prompted the investigation of novel materials that pose no risk to human or environmental health. Previous experimental and simulation work using various ETLs is presented in Table 4.1.

Table 4.1: A summary of PV characteristics of different cell configurations reported in the literature

Cell configuration	**V_{OC} (V)**	**J_{sc} ($mAcm^{-2}$)**	**FF (%)**	**PCE (%)**	**Type of study**	**Ref.**
FTO/TiO_2/N719/Spiro-OmeTAD/Au	0.9	22.87	53.7	12.20	Simulation (SCAPS-1D)	(Jahantigh & Safikhani, 2019)
Glass/Mo/SnS/Zn(O,S)/ZnO/ITO	0.2	19.40	42.9	2.90	Experimental	(Sinsermsuksakul et al., 2013)
FTO/dye & TiO_2 (TNA)/Pt	0.7	17.97	66.3	8.34	Experimental	(Ge et al., 2021)
FTO/TiO_2&Dye/P3HT/Au	0.7	11.83	0.56	4.90	Simulation (SCAPS-1D)	(Ojotu & Babaji, 2020)
CZTS/Zn($O_{0.7}$,$S_{0.3}$)Al:ZnO	0.9	18.03	30.2	14.90	Simulation (SCAPS-1D)	(Slami et al., 2019)

This study presents a highly efficient HTL-free solid-state dye-sensitized solar cell that uses metallic layers as the dye regeneration material. SCAPS-1D is employed to analyze the current-voltage (J-V) characteristics of the FTO/ETL/N719 dye/Au solar cell configuration. The effect of varying various working conditions on photovoltaic characteristics, including power conversion efficiency, fill factor, and quantum efficiency, has been investigated. Moreover, the presence of oxygen vacancies that activate surface traps in TiO_2 material reduces its longevity. Consequently, it is essential to investigate better electrical transport layers. This study reports zinc oxysulphide (ZnOS) as a superior electron transport layer for enhancing the performance of photovoltaic solar cell systems.

4.2 Computational methodology

The Solar Cell Capacitance Simulator (SCAPS-1D) version 3.3.08 is used for all numerical computations presented in this work. Numerical simulation is crucial for designing, analysing, and predicting the performance of actual photovoltaic devices (Burgelman et al., 2013; Slami et al., 2019; Verschraegen & Burgelman, 2007). It also offers valuable insights on how to vary parameters to improve the geometric and technical features for enhanced solar cell performance. The program can simulate up to seven layers, with the ability to adjust nearly all input parameters (Burgelman et al., 2013; Verschraegen & Burgelman, 2007). Additionally, SCAPS-1D offers various direct current (DC) and alternating current (AC) measurements that can be computed under both illuminated and dark conditions at different working temperatures (Slami et al., 2019). Upon launching the software, an "Action panel" window appears. In this window, selecting "set problem" enables the user to construct a stack of layers in the "Solar cell definition panel" window. The input parameters for each layer are then defined. Specific measures, including current-voltage (I-V), quantum efficiency (QE), capacitance-frequency (C-f), and capacitance-voltage (C-V), are defined. Upon selecting "calculate single shot," the software executes the selected simulated measurements. The simulation findings are presented in graphs in the "Energy Bands Panel," "Generation-Recombination Profiles Panel," "I-V Panel," and "AC Energy Bands Panel." The numerical data in this investigation were collected at 300 K under air mass 1.5 global (AM 1.5 G). The model device is illuminated via the FTO material. The SCAPS-1D code reproduces cell characteristics using continuity and Poisson equations. This tool allowed the study of input parameters, including absorber layer thickness, doping concentrations, energy levels of the electron transport layer, and the operational temperature of the model device. The light source is directed through FTO/ETL/N719 dye/Au at a temperature of 300 K under air mass 1.5 global (AM 1.5 G) at 1000 W/m².

FTO is fluorine-doped tin oxide, ETL denotes either ZnOS or TiO_2, and N719 dye is di-tetrabutylammonium cis-bis(isothiocyanato) bis (2,2′-bipyridyl-4,4′ dicarboxylato). Ruthenium (II) acts as the photoactive material layer. Gold (back contact) serves as the metallic dye regeneration material. In the proposed cell architecture, the charge carrier transfer occurs through the following mechanism: (i) an electron is injected from the N719 dye into the conduction band of the electron transport layer (ETL), and (ii) the dye is regenerated to its ground state by the

metallic layer (Lenzmann et al., 2005). This simulation study reported the effect of series and shunt resistance on device performance. The influence of electron affinities of the electron transport layer, working temperatures, and defect densities of the absorber layer on cell performance has been investigated. The proposed solar cell configuration is shown in Figure 4.1. The material specifications of the proposed cell architecture were judiciously extracted from the previous experimental and theoretical studies (Rahman et al., 2017; Rono et al., 2021b), as presented in Table 4.2. The parameters of the back and front contacts are detailed in Table 4.3.

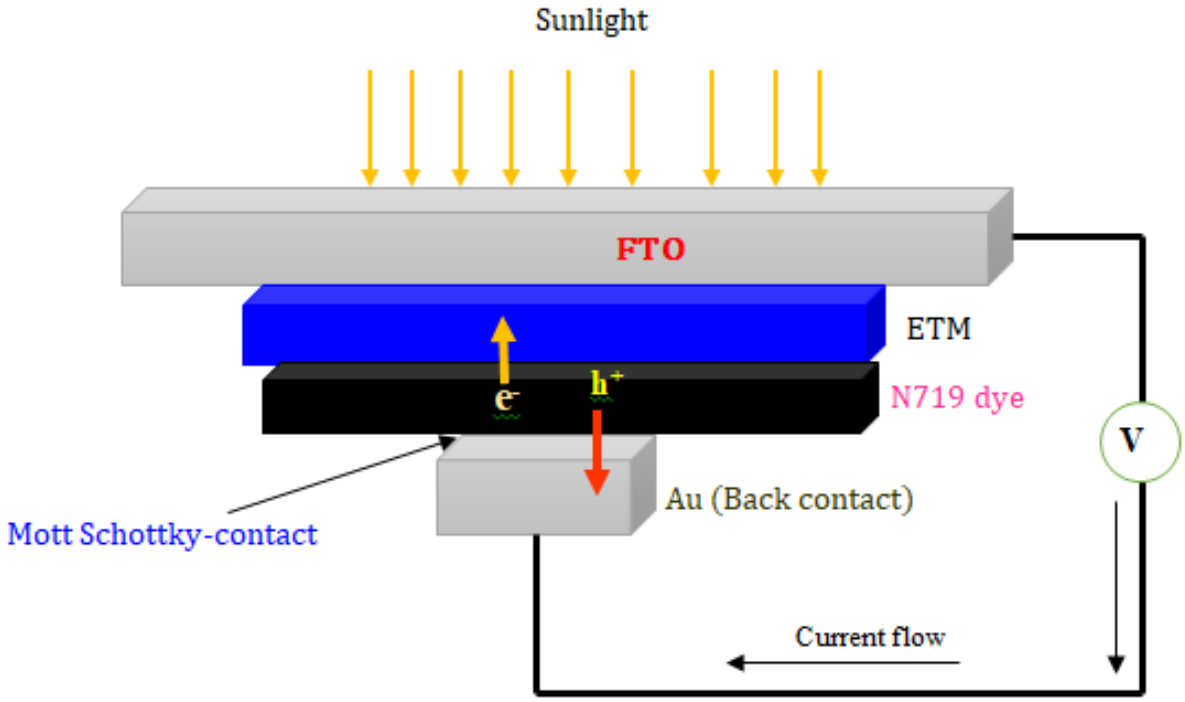

Figure 4.1: The proposed solar cell configuration explored in this study

Table 4.2: Input parameters used in the numerical simulations of the model solar cell, extracted from literature

Parameter	**FTO**	**TiO_2**	**ZnOS**	N719 dye
Thickness (nm)	400.0	2000.0	50.0	500.0
Band gap energy (eV)	3.5	3.2	2.83	1.6
Electron affinity (eV)	4.0	3.9	3.6	3.9
Relative permittivity (e_r)	9.0	32	9.0	30.0
Effective density of conduction band N_C(cm^{-3})	9.2×10^{18}	1.0×10^{19}	2.2×10^{18}	2.4×10^{20}
Effective density of valence band N_v(cm^{-3})	1.8×10^{19}	1.0×10^{19}	1.8×10^{18}	2.5×10^{20}
Thermal velocity of electrons (cm/Vs)	1.0×10^{7}	1.0×10^{7}	1.0×10^{7}	1.0×10^{7}
Thermal velocity of holes (cm/Vs)	1.0×10^{7}	1.0×10^{7}	1.0×10^{7}	1.0×10^{7}
Electron mobility (cm^2/s)	20	20.0	100.0	5.0
Hole mobility (cm^2/s)	10	10.0	25.0	5.0
Density of acceptors ($1/cm^3$)	0.0	0.0	0.0	1.0×10^{17}
Density of donors ($1/cm^3$)	1.0×10^{19}	1.0×10^{17}	2.0×10^{18}	0
Total density N_t($1/cm^3$)	-	1.0×10^{16}	1.0×10^{15}	5.0×10^{16}
Ref.	(Rono et al., 2021b)	(Rono et al., 2021b)	(Bhavsar & Lapsiwala, 2021)	(Bhavsar & Lapsiwala, 2021)

Table 4.3: Input parameters of the back and front contacts

Parameters	Back contact		Front contact
Metal work function (eV)	5.1 (varied)		Flat bands selected
Thermionic emission/surface recombinationvelocity (cm/s)	Electrons	1.0×10^5	1.0×10^7
	Holes	1.0×10^7	1.0×10^5
Majority carrier barrier height (eV)	Relative to EF	0.4	Flat bands
	Relative to EV or EC	0.1974	

where E_F, E_v, and E_c are the Fermi, valence band, and conduction band energy levels, respectively. The simulation environment was set as standard test conditions (STCs): 1000 W/m², AM 1.5 G solar spectrum, and 300 K (Rono et al., 2021a). Figure 4.2 presents the optical absorption graphs of the solar cell models simulated in this research.

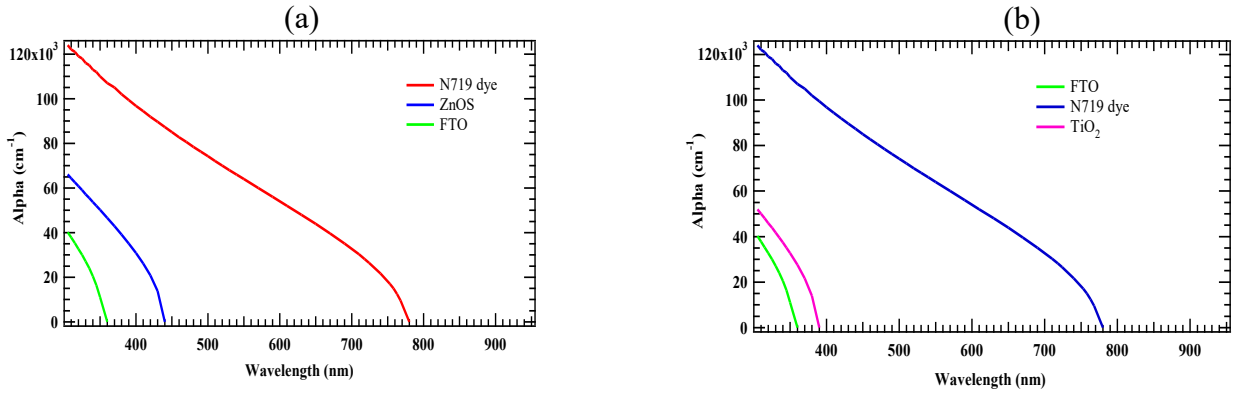

Figure 4.2: The absorption coefficients of the model solar cells based on ZnOS (a) and (b) based on TiO_2 ETLs

N719 dye, FTO, ZnOS, and TiO_2 exhibit distinct absorption coefficients and varying capacities to absorb incident photons. The N719 dye exhibits the highest absorption coefficient, thereby facilitating greater photon absorption. Nonetheless, the absorption coefficients of each layer decrease as the photon wavelength increases. This might be ascribed to the fact that photons with longer wavelengths possess lower energy and are insufficiently energetic to excite an electron from its valence shell into the conduction band. The FTO layer exhibits a low absorption coefficient in both device configurations.

4.3 Results and discussions

Numerical simulations with SCAPS-1D demonstrate consistency between simulation findings and experimental data, confirming its superiority as a solar cell simulator (Minbashi et al., 2017). The AC and DC photovoltaic parameters, including fill factor (FF), open-circuit voltage (V_{OC}), power conversion efficiency (PCE), and short-circuit current density (J_{sc}) were simulated under illuminated conditions and varying temperatures. The characteristic parameters of the simulated device are derived from the J-V curves, as seen in Figure 4.3(b). The photovoltaic device configuration FTO/TiO_2/N719 dye/Au achieved a maximized PCE of 10.22%, an FF of 63.58%, a V_{OC} of 0.97 V, and a J_{sc} of 16.51 $mAcm^{-2}$, whereas the FTO/ZnOS/N719 dye/Au architecture gave an optimized PCE of 11.55%, an FF of 62.71%, a J_{sc} of 18.50 $mAcm^{-2}$, and a V_{OC} of 0.99 V.

4.3.1 Quantum efficiency and current-voltage characteristics

The solar cell model with ZnOS ETL exhibits a superior quantum efficiency compared to TiO_2, as illustrated in Figure 4.3. The observation can be attributed to the lower band gap energy of ZnOS (2.83 eV) compared to TiO_2 (3.2 eV), indicating that more incident photons possess energies exceeding their band gap energy. Consequently, more photons are converted into current within the visible spectrum. At 300 nm, the quantum efficiency (QE) of the TiO_2 solar cell design depicted in Figure 4.1 is 2.86%, rising gradually to 88.1% at a photon wavelength of 390 nm. The quantum efficiency subsequently decreases gradually as the wavelength extends from 390 nm to 770 nm. Beyond 770 nm, excitons are not generated, resulting in a decrease in solar cell efficiency. The ZnOS-based solar cell exhibits a quantum efficiency of 23.6% at 300 nm, which rises to 92.5% at 360 nm. The quantum efficiency decreases to 24.0% at a wavelength of 770 nm. No electron-hole carriers are created beyond this wavelength range. The results indicate that ZnOS absorbs a greater proportion of high-energy irradiating photons and turns them into current more effectively than TiO_2 ETL. Consequently, ZnOS is an excellent alternative to conventional TiO_2 due to its superior transparency to irradiating photons, resulting in an excellent light-harvesting efficiency (LHE). Zinc oxysulphide (ZnOS) exhibits superior electrical performance compared to TiO_2, primarily due to its tunable band gap and enhanced electron affinity.

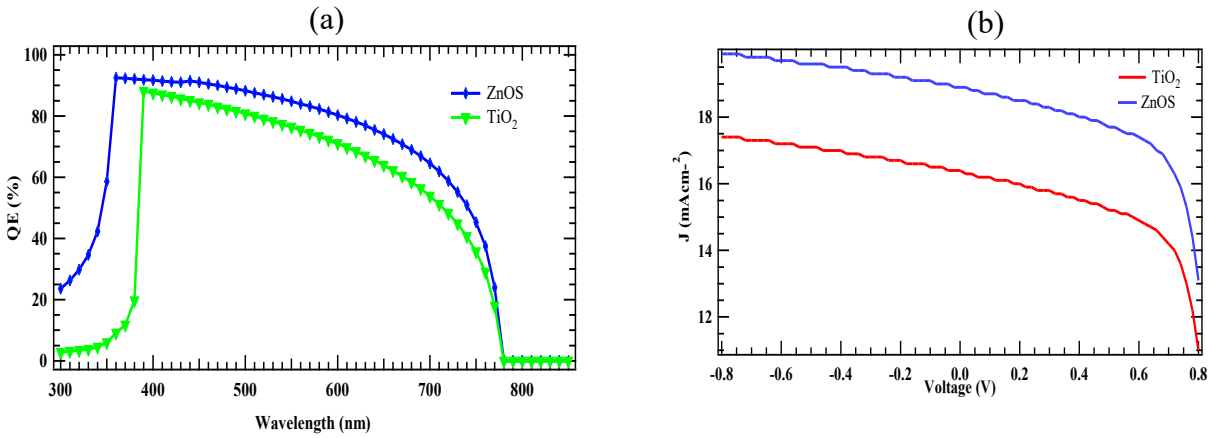

Figure 4.3: Quantum efficiency curves (a) and (b) current-voltage curves of the simulated devices

The current-voltage (I-V) characteristics, depicted in Figure 4.3(b), evaluate the performance of photovoltaic devices and the efficiency of a solar cell (Li et al., 2013). A photovoltaic device generates direct current (DC) electricity, and the power generated by the solar cell is calculated by multiplying the current by the voltage. Consequently, a J-V curve shows the correlation between voltage (V) and current (J) under varying conditions of photon irradiance at a specified operating temperature. After describing the relationship between J and V, the output power of the model solar cell can be predicted utilizing Equation 4.1. Figure 4.3(b) illustrates the J-V curve of the simulated device utilizing various ETL materials.

$$\text{Power (P)} = J \times V \qquad (4.1)$$

The J-V curve is crucial for understanding the internal physical mechanics of complex solar cells. The solar device models employing either ZnOS or TiO_2 electron transport layers have similar J-V curves. Short-circuit current density (J_{sc}), fill factor (FF), open-circuit voltage (V_{OC}) and power conversion efficiency (PCE) can be used to predict the performance of an actual device. Zinc oxysulphide (ZnOS) exhibits superior, short-circuit current density (J_{sc}) relative to titanium dioxide (TiO_2) within the identical voltage scan range (0.8–0.8 V) due to its enhanced photon transparency and a lower band gap energy of 2.83 eV.

4.3.2 Heterojunction characteristics

Band alignment is a critical physical characteristic that affects charge carrier recombination at the interface, Fermi level splitting, the transport of photogenerated carriers, and performance. The

values of CBO may be either positive or negative and are determined by adjusting the electron affinity of the ETL. Figure 4.4 illustrates the energy band diagram and Nyquist plots of the model photovoltaic cells at equilibrium, obtained from SCAPS-1D software. The various optoelectrical properties, including the Fermi levels of holes (F_P), Fermi levels of electrons (E_n), and the energies of the conduction and valence bands ($E_c$and E_v), are depicted as a function of the distance travelled by charge carriers from the back contact to mitigate rapid recombination.

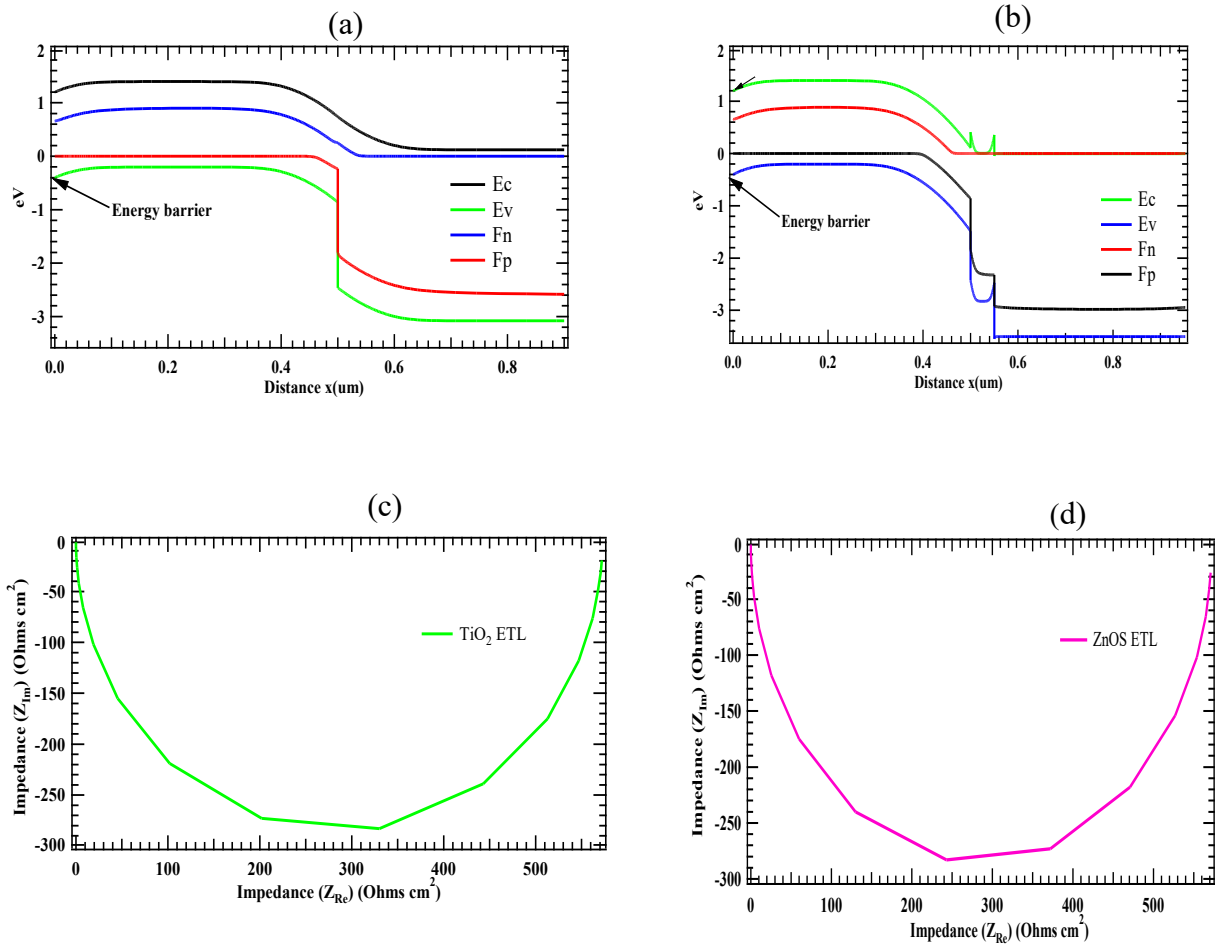

Figure 4.4: Energy band diagram for TiO_2-based solar cell device at equilibrium (a), (b) the energy band diagram of the model cell with ZnOS as ETL at equilibrium, (c) imaginary versus real impedance of TiO_2-based device, and (d) imaginary versus real impedance of ZnOS-based device

4.3.3 Effect of metal work function

Prior research has shown that dye-sensitized solar cells rely on metallic contacts for dye regeneration, resulting in promising device performance (Lenzmann et al., 2005). To address the scientific challenges associated with liquid electrolytes without resorting to costly hole transport layers (HTLs), silver (Ag) and gold (Au), with their respective work functions of 4.7 eV and 5.1 eV, have been suggested as viable materials for dye regeneration. Nonetheless, their high cost impedes their application in producing affordable solar cell devices. In this study, the suitability of metallic materials for low-cost solar cell devices was investigated. Copper (Cu), silver (Ag), nickel (Ni), palladium (Pd), and platinum (Pt) have been tested as potential dye-regenerating metallic contacts. Figure 4.5 presents the photovoltaic performance of the simulated solar cell device comprising TiO_2 and ZnOS electron transport layers. Figure 4.5(a) illustrates that the power conversion efficiency (PCE) of the model cell rises with an increase in the metal work function of the back contact. In the case of the ZnOS-based device, a metal work function of 5.6 eV yields a power conversion efficiency (PCE) of 12.14%, whereas the TiO_2-based device exhibits a PCE of 10.57%.

Conversely, the devices exhibit decreased photovoltaic performance when the metal work function is low. In the TiO_2-based model, the power conversion efficiency (PCE) is 5.63% at a metal work function of 4.65 eV, whereas the ZnOS-based architecture exhibits a PCE of 6.44%. Figure 4.5 (a) suggests that increasing the metal work function of the back contact leads to an increase in efficiency. Figure 4.5(b) shows that varying the metal work function of the back contact influences the fill factor (FF). In the ZnOS-based device, increasing the metal work function from 4.65 eV to 5.0 eV enhances the fill factor from 62.08% to 64.2%. In contrast, for the TiO_2 cell, the fill factor rises from 62.24% to 63.86%. Furthermore, increasing the metal. The work function range of 5.1 eV to 5.6 eV results in a reduction of the fill factor (FF) in both model solar cells, decreasing from 62.57% to 61.85% for the TiO_2-based device and from 62.78% to 61.95% for the ZnOS electron transport layer (ETL) material. It occurs because hole carriers are not energetically viable to move toward the electrode, as the electric field near the metallic layer becomes negative (Lenzmann et al., 2005). Figure 4.5 (c) presents the outcomes for J_{sc}, whereas Figure 4.5 (d) displays the results for V_{oc}, based upon various metal back contacts. The J_{sc} of both model cells (utilizing TiO_2 and ZnOS as ETLs) gradually rises with an increase in the metal work function of the metallic back

contact. The optimum J_{sc} of the ZnOS-based solar cell is 19.49 $mAcm^{-2}$, and the V_{OC} is 1.0 V when the metal work function of the back contact is 5.6 eV. Conversely, the J_{sc} of the TiO_2-based device is 17.18 $mAcm^{-2}$, with a V_{OC} of 1.0 V, as depicted in Figure 4.5(c) and (d), respectively. The Schottky contact at the N719 dye/Au interface gives the built-in potential, which is derived using Mott-Schottky capacitance curves.

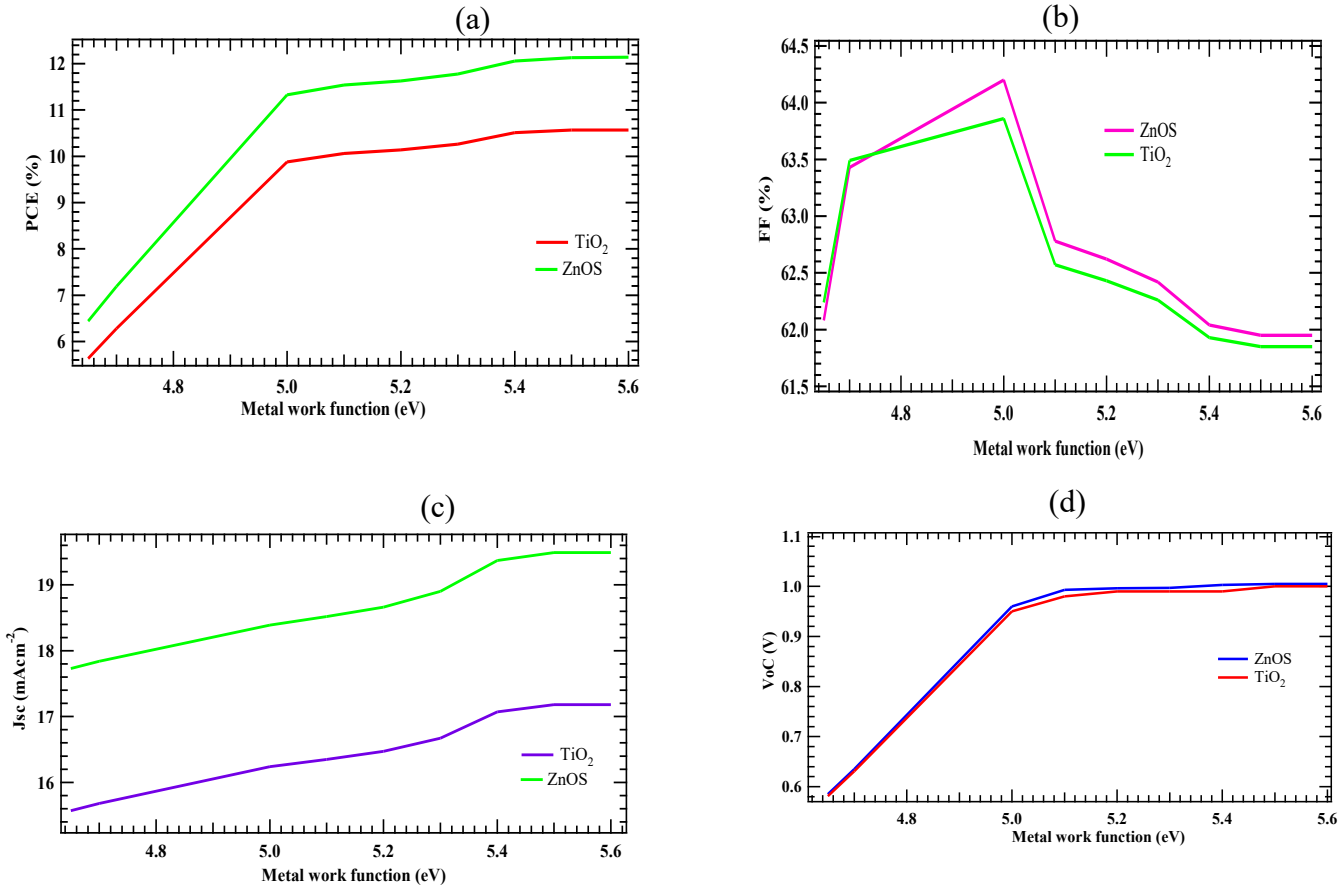

Figure 4.5: (a) Effect of metal work function of the back contact on PCE, (b) FF, (c) J_{sc}, and (d) V_{OC} of the model solar cell based on TiO_2 and ZnOS materials

Metallic back contacts form Schottky contacts with the n-type layer, resulting in high Schottky barriers when paired with metals of low work functions. Consequently, back contacts with high metal work functions represent feasible materials for solar cell designs (Hall et al., 2021). Consequently, lower efficiencies are observed when the metal work functions of the back contact are low due to the presence of high-energy Schottky barriers. Contacts with metal work functions

over 5.1 eV are considered robust for enhanced cell performance. Nonetheless, Pt (5.65 eV) and Au (5.1 eV) are costly materials for photovoltaic devices, suitable solely for laboratory research. Carbon/nickel (5.0 eV) and palladium (5.3 eV) are viable choices for back contacts due to their high metal work functions, which effectively reduce Schottky barriers and enhance photovoltaic performance. This study advocates for the utilization of carbon/nickel (5.0 eV) and palladium (5.3 eV) as candidates for dye regeneration in ssDSSCs, owing to their favourable work functions and economic feasibility.

4.3.4 Generation-recombination profiles

Shockley-Read-Hall (SR-H) recombination is predominant in DSCCs and arises from defect states within the bandgap between the valence and conduction bands. Interface states also contribute to recombination losses in dye-sensitized solar cells (DSSCs) (Filipič et al., 2012). The charge generation rate is related to recombination rates; thus, greater generation rates indicate increased recombination rates in the photoactive material, specifically the N719 dye, in this investigation (Bhattarai et al., 2020). Previous research has expressed scientific challenges in understanding the kinetics of charge transfer and recombination due to the complexities in interface systems (Meng & Kaxiras, 2010). Frequently cited factors that induce the kinetics of charge separation and recombination include molecular geometry, binding groups, dissociations, additive ionic potential, and surface orientation (Meng & Kaxiras, 2010). Charge separation is crucial for converting sunlight into electricity in solar cells. The mechanisms of charge generation and recombination in DSSCs remain poorly understood, which complicates targeted improvements in solar cell designs (Bartesaghi et al., 2015).

The Shockley-Read-Hall recombination was analysed by plotting charge recombination as a function of distance (μm). Figure 4.6(a) illustrates that the electron charge carrier generation rate in ZnOS rises when TiO_2 is employed as the electron transport layer (ETL). Consequently, ZnOS serves as an appropriate electron transport layer (ETL). The net generation-recombination rate for charge carriers is approximately the same, as illustrated in Figure 3.6(b). The total recombination rates for several ETLs are illustrated in Figure 4.6(c). As depicted, the TiO_2-based model cell recombines more rapidly than the ZnOS-based solar cell device. Figure 4.6(d) illustrates the recombination rates of charge carriers in a ZnOS-based solar cell device. The accelerated kinetics

of charge carrier recombination reactions, relative to the rate of charge carriers in the external circuit, result in decreased overall performance of the simulated devices.

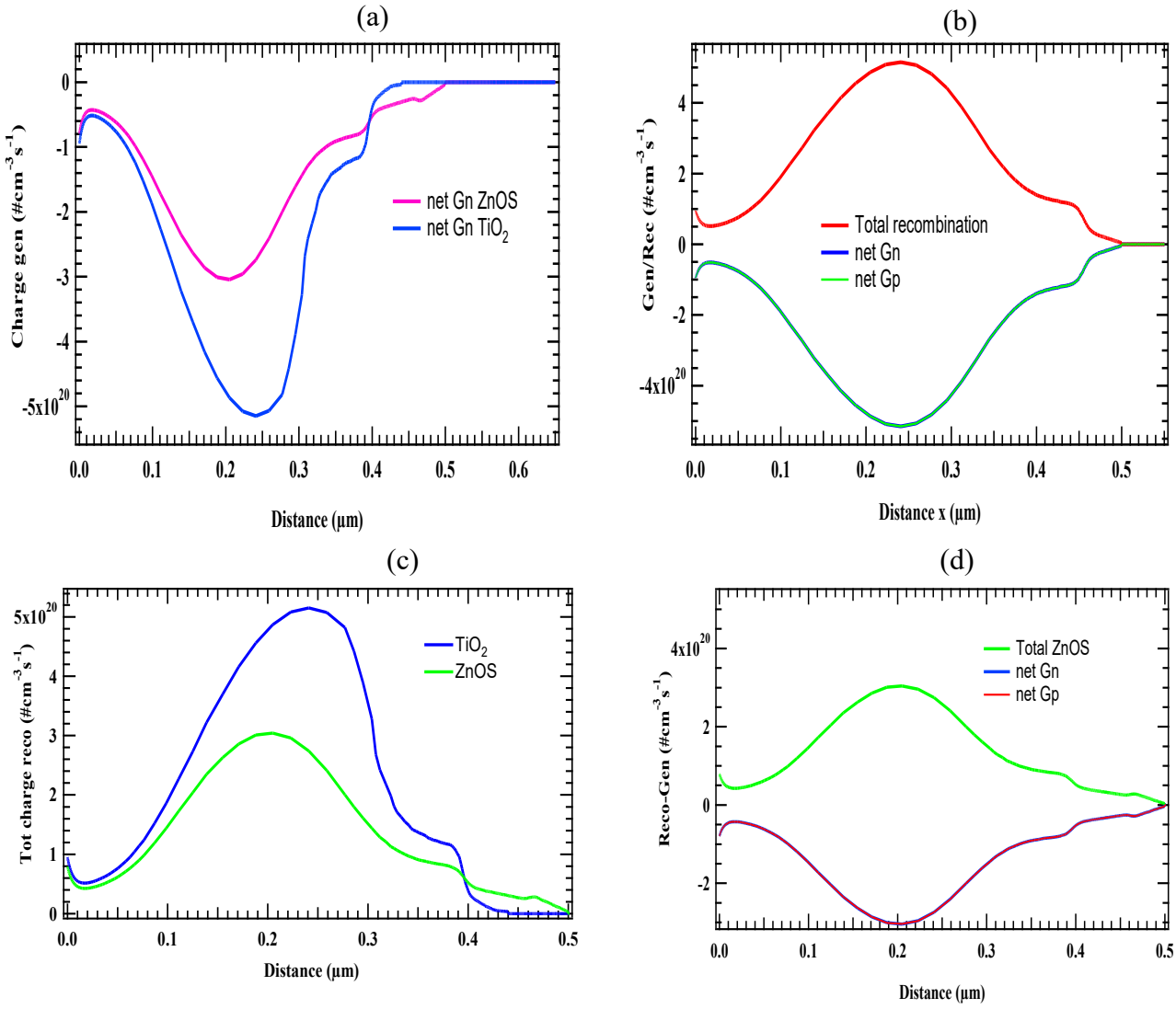

Figure 4.6: Net electron generation in TiO_2 and ZnOS ETLs (a), (b) Net generation and total recombination of charge carriers, (c) Total charge recombination in TiO_2 and ZnOS ETLs, and (d) shows the generation-recombination rates of the charge carriers of ZnOS as a function of distance

4.3.5 Effect of temperature

Studying the behaviour of solar cells in relation to temperature is important for determining their optimal operating conditions and maximizing efficiency. The current solar cell design specifies a

working temperature range of 13 °C (260 K) to 52 °C (325 K), with higher temperatures applicable for concentrator systems and space heating (Moses et al., 2020). Solar cell performance decreases with higher temperatures due to significant charge recombination and a shortened device lifespan (Rono et al., 2021a). The photovoltaic performance of the proposed solar cell models is assessed by analyzing the parameters such as fill factor (FF), open-circuit voltage (V_{OC}), short-circuit current density (J_{sc}), and power conversion efficiency (PCE). Altering the operational temperature influences these factors and the overall performance of the cell. Figure 4.7 illustrates the impact of photovoltaic properties at different operational temperatures. The influence of temperature on fill factor (FF), power conversion efficiency (PCE), and open-circuit voltage (V_{OC}) is influenced by the diode properties of photovoltaic cells, including the ideality factor (n), shunt resistance (Rsh), series resistance (Rs), and reverse saturation current density (j_0) (Singh & Ravindra, 2012). Previous research indicates that J_{sc} increases while V_{OC} diminishes with rising operating temperature (Rono et al., 2021a). This study simulated the performance of the solar cell by varying the operating temperature from 260 K to 400 K.

Increasing the operational temperature of the device from 260 K to 400 K leads to a reduction in power conversion efficiency, as illustrated in Figure 4.7(a). The operating temperature significantly influences PCE; thus, a noted reduction in PCE can be ascribed to the degradation of the photosensitive material (Mehdizadeh-Rad & Singh, 2019). Furthermore, higher working temperatures (330–400 K) can impair the power conversion efficiency by inducing localized defects that may substantially alter the chemical and physical properties of the semiconductor (Mehdizadeh-Rad & Singh, 2019). Even at increased temperatures, the solar cell model with ZnOS exhibits superior power conversion efficiency compared to its TiO_2 counterpart, owing to its higher electron affinity and enhanced transparency to incident photons. As illustrated in Figure 4.7(b), the fill factor of the simulated solar cell models exhibits an exponential increase with rising temperature. As the temperature rises, V_{OC}, diminishes due to a reduction in band gap energy.

Figure 4.7(c) shows the impact of increasing temperature of the device on J_{sc}. An increase in temperature increases the thermal energy of excitons, thus enhancing the J_{sc}. The rise in J_{sc} is small compared to the increase in V_{OC}, as shown in Figure 4.7(d), resulting in decreased overall cell efficiency.

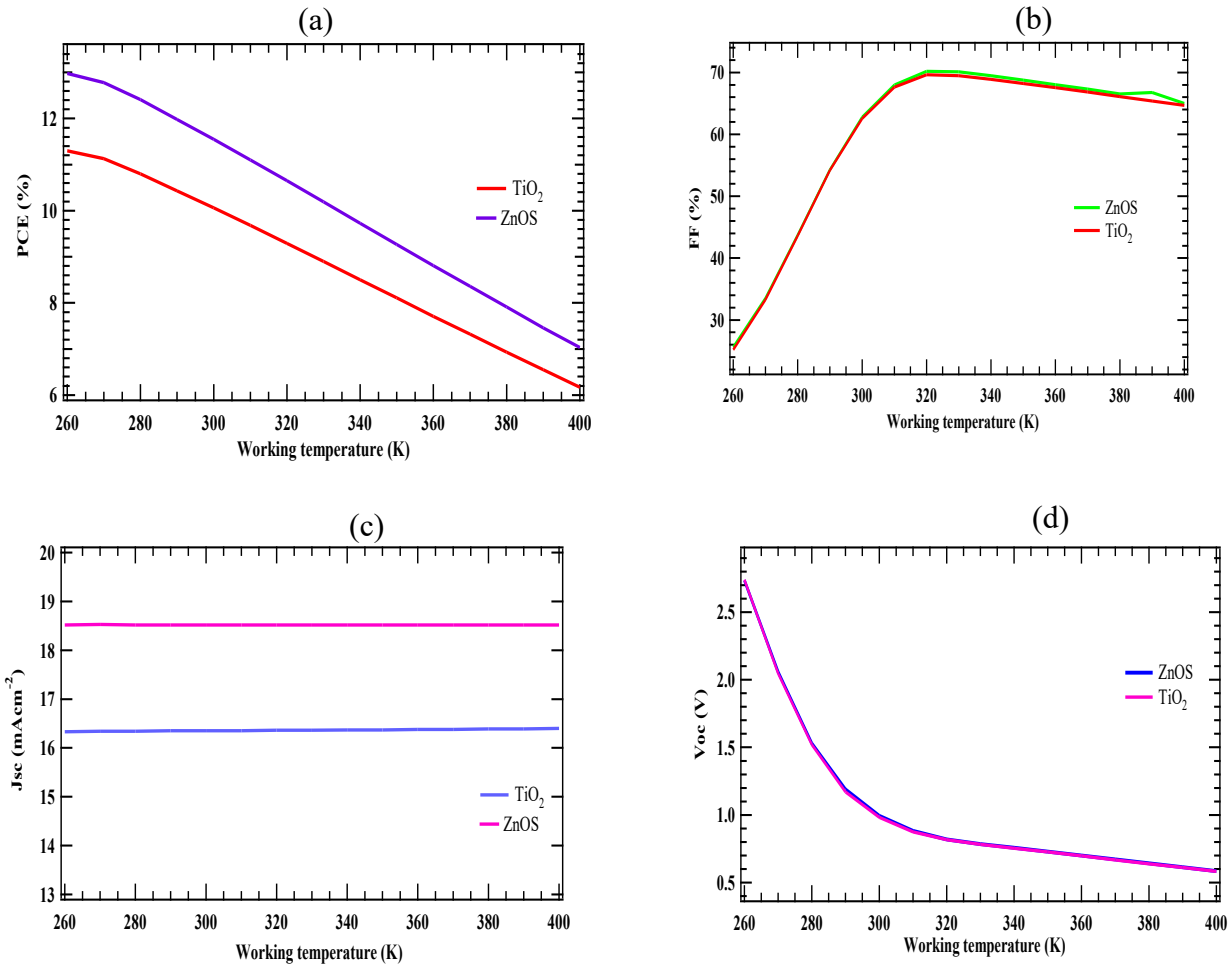

Figure 4.7: The effect of working temperature on PCE (a), (b) FF, (c) J_{sc}, and (d) V_{OC} of the simulated solar cell configuration

Figure 4.7(d) shows that increasing the operating temperature enhances the dark or recombination current, reducing the V_{OC} of solar cell models (Sinha et al., 2021). Moreover, increasing the temperature increases the thermal energy of excitons, hence increasing the energy gap of the material. Additionally, an increase in thermal energy leads to a significant reduction in V_{OC}. Increased temperatures degrade the quality of the interfaces, resulting in a voltage drop. Consequently, increasing the operating temperature reduces the band gap, enhancing the transfer of charge carriers from the valence band to the conduction band. This results in increased photocurrent generation. Moreover, as the band gap narrows, the rate of charge carrier recombination increases, resulting in a reduced V_{OC} value (Qu & Li, 2019). The poor charge

separation at the ETL/N719 dye interface results in a decrease in V_{OC} and is attributed to increased series resistance.

4.3.6 Effect of series resistance

Resistive losses, including charge carrier recombination and current leakage, limit the efficiency of DSSCs. The losses result from shunt and series resistances. Accordingly, series and shunt resistances (Rs and Rsh, respectively) influence the performance of heterojunction solar cells (Rangel-Kuoppa et al., 2018). These characteristic losses influence the behaviour of the J-V curve. Notably, series resistance (R_S) lowers J_{sc} and significantly affects FF and PCE. However, it does not influence V_{OC}. Consequently, it is essential to examine the influence of series and shunt resistances on cell performance to inform structural optimization during the actual manufacture of the cell. Prior research indicates that higher Rs values reduce J_{sc} but have little influence on the V_{OC} of the solar cell device (Singh et al., 2019). In this study, we fixed the shunt resistance (Rsh) at 1.0×10^3 Ω cm^2 a typical value in the production of commercial solar cells while varying the series resistance (RS) from 0 to 6.5 Ω cm². Figure 4.8 illustrates that the efficiency of the simulated device is influenced by variations in Rs.

Interface barriers, the resistance of the photoactive layer, metal-based electrodes, and charge-collecting layers are the leading causes of series resistance (Singh et al., 2019). The PCE of model cells based on TiO_2 and ZnOS decreases as RS rises. As shown in Figure 4.8(a), raising the RS in the TiO_2-based model cell from 0.0 Ω cm^2 to 6.5 Ω cm^2 gradually causes the PCE to drop from 9.53 to 0.27%. According to Figure 4.8(b), the FF also drastically decreased for the ZnOS-based solar cell device, from 60.8 to 2.28% when the R_S is raised from 0.0 Ω cm^2 to 6.5 Ω cm^2. Similarly, the FF for the TiO_2-based solar cell device dropped from 60.28% to 54.26%, resulting in a reduction in overall cell performance.

Consequently, FF drops if Rs rises and vice versa. Increasing the thickness of the ETL increases absorption losses in the solar cells while simultaneously decreasing RS (Jeyakumar et al., 2020). The model solar cell with thicker TiO_2 has a lower R_S and a higher FF, as shown in Figure 4.8(b), since ZnOS and TiO_2 with thicknesses of 50 nm and 2000 nm, respectively (cf. Table 4.2), were simulated in this study. Figure 4.8(c) illustrates how J_{sc} changes as Rs rises. When the series resistance in the TiO_2-based device is varied from 0.0 to 6.5 Ω cm^2, the J_{sc} gradually drops from

16.35 to 16.05 $mAcm^{-2}$. However, for the solar cell device with ZnOS as the ETL, the J_{sc} dropped from 18.52 to 12.25 $mAcm^{-2}$. As ascribed in Figure 4.8(d), variation in Rs does not affect V_{OC}. Since all current flows through the device and the total series resistance (R_S) is zero, the V_{OC} is unaffected by RS, as shown in Figure 4.8(d). Generally, a decrease in R_S results in an increase in FF and the overall photovoltaic performance of the solar cell models.

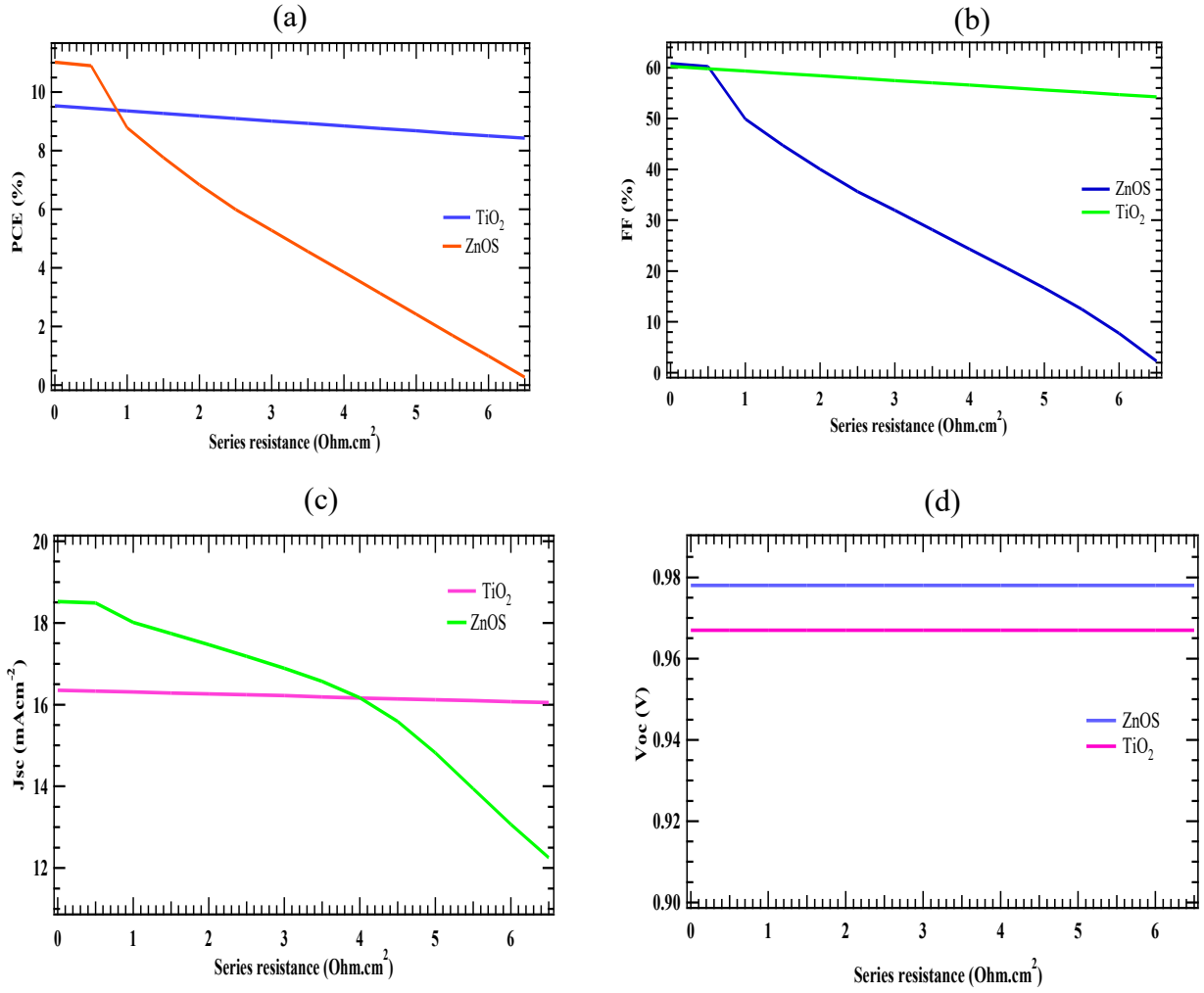

Figure 4.8: The effect of series resistance on PCE (a), (b) FF, (c) J_{sc}, and (d) V_{OC} of the simulated models

4.3.7 Effect of shunt resistance

Another parasitic factor influencing the J-V properties of solar cells is shunt resistance (Rsh). The practical fill factor (FF) of solar devices is significantly decreased by Rsh (Wu et al., 2017).

Notably, the effects on V_{OC} are due to Rsh. Although these resistive losses exist in real devices, Rsh is absent from ideal solar cell devices. Two types of losses are caused by shunt resistance: ohmic and nonohmic (complex processes). Increasing the Rsh causes PCE to increase, as shown in Figure 4.9(a)—low PCE results from increased charge carrier losses with low Rsh. Increasing the Rsh causes charge carrier losses to decrease, which raises the overall efficiency of model cells (cf. Figure 4.9(a) and (b). Thus, by creating an alternating current (AC) channel for the photogenerated current, low shunt resistance impairs solar cell performance (Malik et al., 2021). Shunt resistance (Rsh) usually denotes shunts or parallel conductivity pathways across the p-n junctions on the margins of solar cells (Dhass et al., 2012). Consequently, the shunt component restricts the current flow in the intended load by directing the current through unintended pathways. The formation of the shunt path, which results in the shunt current, is caused by impurities and crystal scratches.

As Figure 4.9(c) illustrates, Rsh has little effect on J_{sc} since J_{sc} mostly relies on band gap energy (Dhass et al., 2012). J_{sc} varies significantly in both devices as Rsh rises, but stays almost constant when Rsh rises from 250 Ω cm^2 to 950 Ω cm^2. Rsh and open-circuit voltage (V_{OC}) are related, as shown in Figure 4.9(d). An increase in Rsh results in fewer exciton losses, which raises V_{OC}. Consequently, it is found that for the suggested devices to have the best photoelectric conversion, the Rsh should be raised while the Rs should be carefully reduced during solar cell design and workflow large-scale production for commercial applications. When the Rsh is raised from 10 Ω cm^2 to 950 Ω cm^2, the PCE for the ZnOS-based device is seen to increase from 0.76% to 10.76%, while the V_{OC} increases from 0.18 to 0.98 V. However, for the Rsh is raised from 10 Ω cm^2 to 950 Ω cm^2, the PCE of the TiO_2-based PV device rises from 0.6% to 9.33%, and the V_{OC} increase from 0.16 V to 0.97 V. As shown in Figure 4.9, as Rsh rises, so does overall cell performance. Consequently, a highly efficient HTL-free solar cell device would have a high Rsh.

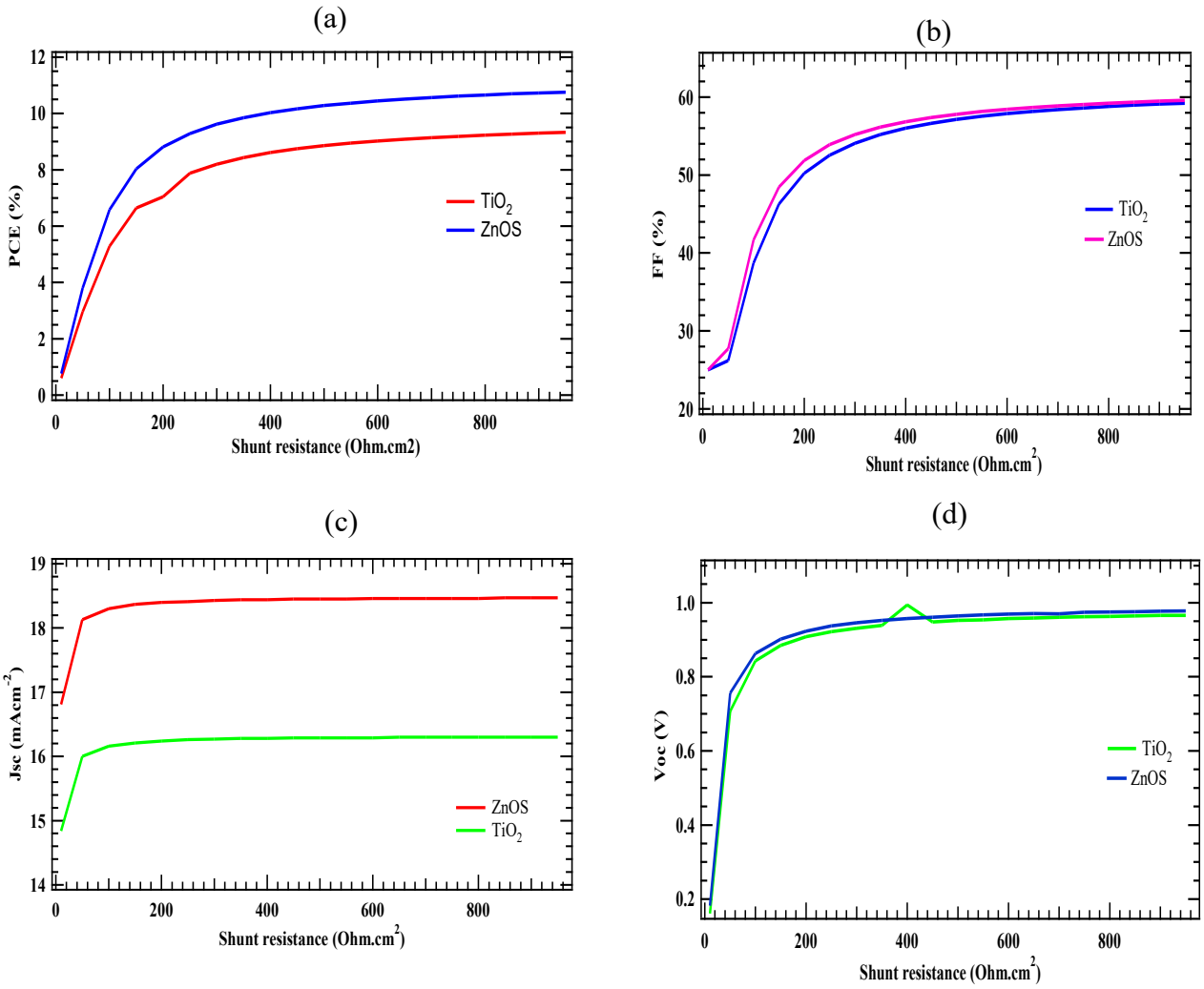

Figure 4.9: The effect of shunt resistance on (a) PCE, (b) FF, (c) J_{sc}, and (d) V_{OC} of the model solar cells

4.3.8 Effect of electron affinity

A thorough theoretical examination of ETLs with low electron affinity (EA) and high bandgap energies for their use in light-emitting diodes has already been carried out and well-documented in the literature (Smith et al., 2020). Moreover, the analysis in this study has been crucial in helping to design and fabricate the best ETLs and HTLs for achieving high overall efficiency and device stability in thin-film solar cells (Bansal & Aryal, 2016). Conduction band offset (CBO), which measures the V_{OC} and charge carrier recombination at the interfaces, is known to significantly impact PV devices (Bansal & Aryal, 2016). In solar cell devices, EA determines how charge

carriers are distributed at the interface between two layers. According to earlier research, adjusting the EA (conduction band offset) of the ETLs is a practical way to maximize PV performance (Raoui et al., 2021). To get the required CBO, the electron affinity of the ETLs under consideration was adjusted between 3.6 and 4.2 eV; this is the difference between the absorber layer's and ETL's electron affinities ETL ($\chi_{\mathrm{N719\,dye}} - \chi_{\mathrm{ETL}}$). While keeping constant E_g, the CBO of ETL/N719 dye was adjusted between 0.3 eV and 0.3 eV. The cell device with ZnOS ETL produced the highest PCE (11.54%), as shown in Table 4.4. PCE drops to 10.63% when the CBO is 0.3 eV and decreases gradually when the CBO drops to 0.3 eV. Conversely, the PCE is 10.06% when the CBO of TiO_2/N719 dye is 0 eV and rises to 10.22% when the CBO is 0.1 eV. When the CBO is raised to 0.3 eV, the device's performance drops to 9.16%.

Due to a more selective charge collection and low exciton recombination rates, the simulated device designs notably show high PCE when the CBO is positive (0–0.3 eV). These findings align with earlier research documented in the literature (Bansal & Aryal, 2016). When the CBO is negative in both device configurations, the forward current increases, and the FF drops dramatically. J_{sc} for ZnOS ETL is higher than TiO_2, as indicated in Table 4.4, because a larger proportion of short-wavelength photons are absorbed, as shown by the quantum efficiency curve (cf. Figure 4.3). The creation of a "spike," which prevents the photogenerated current when CBO is positive, causes the constant changes in J_{sc}. The photogenerated current has no barrier when the CBO is negative. Usually, band gap energies—rather than CBO, which primarily controls how J_{sc} varies with electron affinity—determine J_{sc}. When the CBO is positive (between 0 and 0.3 eV), J_{sc} is at its best in both devices. Because of the quick recombination of charge, the PCE decreases from 10.06 to 9.16% when the CBO of the TiO_2/N719 dye interface is increased from 0 to 0.3 eV. Conversely, a negative CBO (-0.1 to -0.2 eV) raises the PCE from 10.06 to 10.32%, which is attributed to a decrease in surface recombination (Chen et al., 2018) but degrades to 9.98% when the CBO is lowered to -0.3 eV because of an increase in charge carrier surface recombination (Chen et al., 2018).

Electron affinity significantly affects the PV properties of the model cells, as indicated in Table 4.4. When both electron affinities of both ETLs are adjusted to 3.6 eV, the ZnOS-based cell configuration yields a PCE of 11.54% compared to TiO_2 (9.16%), or a 20.6% percentage difference. Similarly, the ZnOS-based cell design shows a higher FF of 62.78%, almost 5.4%

higher than the FF noted for the TiO_2-based model. Furthermore, the ZnOS-based solar cell architecture reported J_{sc} is 18.52 $mAcm^{-2}$, while that of TiO_2 ETL is 16.72 $mAcm^{-2}$. Between the two ETL materials, ZnOS and TiO_2, there is a variation of about 9.7% in J_{sc}. The reported PCE for TiO_2-based solar cell design is optimal (10.22%) if the electron affinity is raised to 3.8 eV for both ETLs, whereas the ETL reaches 11.54% for ZnOS. These efficiencies indicate that ZnOS performs better. The model cell using TiO_2 as ETL has a comparatively lower PCE of 9.98% and 10.63% for ZnOS-based devices when the EA of both ETLs is fixed at 4.2 eV. The TiO_2-based solar cell configuration exhibits poor cell quality at an electron affinity of 4.2 eV, as the fill factor (FF) for TiO_2-based devices is extremely low (32.32%) compared to ZnOS (59.43%).

Table 4.4: Effect of changing electron affinity of ETL on PV characteristics of the simulated model cell

EA (eV)	**ETL**	**PCE (%)**	**FF (%)**	**J_{sc} ($mAcm^{-2}$)**	**V_{oc} (V)**
3.6	TiO_2	9.16	59.38	16.72	0.92
	ZnOS	11.54	62.78	18.52	0.99
3.7	TiO_2	10.2	63.1	16.64	0.97
	ZnOS	11.54	62.71	18.50	0.99
3.8	TiO_2	10.22	63.58	16.51	0.97
	ZnOS	11.52	62.76	18.t46	0.99
3.9	TiO_2	10.06	62.57	16.35	0.98
	ZnOS	11.46	62.89	18.35	0.99
4.0	TiO_2	10.07	54.86	16.17	1.13
	ZnOS	11.29	62.72	18.19	1.00
4.1	TiO_2	10.32	36.31	15.97	1.78
	ZnOS	10.99	62.16	18.00	0.98
4.2	TiO_2	9.98	32.32	15.76	2.02
	ZnOS	10.63	59.43	17.81	1.00

The significant reduction in surface recombination at the ZnOS/N719 dye interface results in improved cell quality, as indicated by a high FF value. It is clear from the results shown in Table 4.4 that the EA of ZnOS should be between 3.6 eV and 3.8 eV (positive CBO). Generally speaking,

ZnOS outperforms TiO_2 in the simulated EA range (3.6–4.2 eV). Because ZnOS material has greater overall cell efficiencies due to reduced surface recombination of charge carriers, an optimal electron affinity of 3.7 eV is proposed. As a result, in real-world solar cell applications, ZnOS devices attain high PV performance.

5. Conclusions

The characteristics of HTL-free DSSCs can be changed during the solar cell fabrication process for commercial manufacturing, according to the findings of this study. Model solar cell efficiency was optimized by varying the temperature, absorber layer thickness, and electron affinity of the ZnOS and TiO_2 transport layers. SCAPS-1D has been utilized to investigate the impact of various ETLs, including TiO_2 and ZnOS. Compared to the TiO_2-based device, which produced an optimum photocurrent of 16.51 $mAcm^{-2}$, the ZnOS-based model solar cell exhibited a higher photocurrent of 18.50 mA cm^{-2}. Furthermore, using ZnOS as the ETL material instead of the TiO_2-based material, which had a V_{oc} of 0.97 V, resulted in a higher V_{oc} of 0.99 V. It is evident that a p-type or particular hole conductive layer can be successfully created as the dye-regeneration material. Because of its lower band gap energy (2.83 eV), zinc oxysulphide (ZnOS) demonstrated greater external quantum efficiencies than TiO_2. Given the same voltage scan range (0.8 V–0.8 V), it was clear from J-V curves that ZnOS had a higher current density than TiO_2 due to its superior optoelectrical characteristics and good photon transparency. Therefore, compared to using TiO_2 as the electron transport layer, a greater number of photons are converted into usable current. Additionally, due to its earth-abundant nature, low toxicity, and tunable band gap energy, ZnOS is a superior ETL layer compared to the widely studied TiO_2.

Back contact material should have a metal function greater than 5.0 eV to lower the Schottky energy barrier. Therefore, Ni, Pd, and C are appropriate, affordable, and easily accessible materials. Research on the impact of parasitic resistances (Rsh and Rs) revealed that for strong PV performance, Rs should be at least 2.0 Ωcm^2, and Rsh should be around 1.0 ×103 Ωcm^2. A highly effective ZnOS-based solar device requires a positive CBO while tuning the ETLs, which revealed that the CBO of TiO_2 should be negative for best performance. The ZnOS-based cell architecture had the best power conversion efficiency of 11.54%, whereas the TiO_2-based solar cell design achieved 10.06%. Due to its superior optical performance, ZnOS is undoubtedly a

better electron-conducting material than TiO_2. It is also easily accessible and inexpensive. The findings of this work promote the production of inexpensive DSSCs for practical applications without the need for expensive HTL materials or liquid electrolytes. However, from an experimental standpoint, this solar cell architecture must be manufactured and its commercial feasibility tested.

CHAPTER FIVE
THEORETICAL ANALYSIS IN DFT AND SCAPS-1D ON THE INFLUENCE OF DIFFERENT PHOTOELECTRODES OF N719 DYE-BASED SOLAR CELL

Abstract

Through the combination of density functional theory (DFT) formalism and numerical simulation approaches, the photovoltaic and optoelectronic properties of isolated layers of dye-sensitized solar cells (DSSCs) have been meticulously explored. Considering the inherent limitations of titanium dioxide in harnessing visible light, the potential of other metal-conducting oxides to act as photoelectrodes is assessed. This study aimed to optimize the combination of copper thiocyanate (CuSCN) hole transport layer (HTL), titania (TiO_2), tin oxide (SnO_2), and zinc oxysulphide (ZnOS) photoelectrodes with N719 absorber using the one-dimensional solar cell capacitance simulator (SCAPS-1D) software. Additionally, structural properties of isolated layers have been evaluated using first principles computations in the DFT framework to investigate the suitability of SnO_2, TiO_2, and ZnOS as potential photoelectrodes. SCAPS-1D program was used to study the solar cell configuration FTO (Fluorine doped tin oxide)/ ETL (electron transport layer)/N719 (Di-tetrabutylammonium cis-bis(isothiocyanato)bis(2,2'-bipyridyl-4,4'dicarboxylato) ruthenium (II) dye)/HTL (hole transport layer)/Au. Advanced device characterization methods, such as Mott-Schottky (M-S) and capacitance-frequency, were also performed to elucidate the effects of interfaces on device performance. Accordingly, the solar device with configuration FTO/ZnOS/N719/CuSCN/Au achieves an outstanding performance of power conversion efficiency (PCE) of 10.87%, short circuit current (J_{sc}) of 20.32897mA/cm^2, fill factor (FF) of 68.56% and open circuit voltage (V_{OC}) of 0.7800 V. Also, the *ab initio* calculations of the device layers show that the highest occupied molecular orbital-lowest unoccupied molecular orbital (HOMO-LUMO) gap is very similar to the findings of previous studies. The computational studies of reduced density gradient (RDG) and molecular electrostatic potential (MEP) agree with earlier studies on statistical physics that N719 dye chemically bonds with photoelectrodes via two carboxylic groups of a bidentate bridging configuration. Accordingly, this synergic approach in DFT and SCAPS-1D allows a deeper understanding of how microscopic insights (atomic-scale) phenomena influence electronic structure and translate into device-scale performance in DSSCs.

5.1 Introduction

One of the challenges of future living is associated with the environmental impacts and scarcity of energy resources occasioned by the unabated combustion of conventional fossil fuels (Singh, 2021; Ukoba et al., 2024). It has triggered considerable development of clean and secure energy resources (Izam et al., 2022). In particular, solar energy is the most promising alternative, maintaining a clear lead over other energy resources due to its vast capacity, inexhaustible source, and high efficiency with minimum environmental impacts (Izam et al., 2022; Veeramachaneni, 2025). Regarding this technology, silicon-based photovoltaics are probably the most deployed technology for commercial and industrial applications. However, it is associated with downsides, including high thermal input, and has reached its practical efficiency limits (Zhou et al., 2022). Nevertheless, the motivation surrounding the advancements and prospects of dye-sensitized solar cells (DSSCs) to compete with the dominant silicon-based solar cells is remarkable. The output power of the emerging DSSCs to compete with the dominant silicon-based solar cells has not been achieved, and thus, has piqued intense scholarly attention.

The embodiment of DSSCs includes a monolayer of photosensitive material, wide-gap semiconductors, and the redox shuttle. Various factors influence the photovoltaic performance of dye-sensitized solar cells, but the structure and shape of the photoanode material are crucial in enhancing photoelectric conversion (Kumar et al., 2023). Considerable research efforts have focused on the optoelectrical properties of working electrode materials and their influence on photovoltaic performance (Han et al., 2022; Ravidas et al., 2023). The working electrode plays a pivotal role in injecting the light-generated electrons into the conduction band of the semiconductor and transporting them to the conductive glass. When a photon hits the photosensitizer, an electron is excited to the lowest unoccupied molecular orbital (LUMO) and is readily injected into the conduction band (CB) of titanium dioxide (TiO_2) (Mustafa et al., 2023). The subsequent process is the electron transport to the external circuit as the redox couple regenerates the photosensitizer (mainly iodide/triiodide, I^{-1}/I_3^{-1} electrolyte). The critical step in DSSCs is the electron injection from the dye to the CB of TiO_2, an ultrafast interfacial electron transfer process (Mustafa et al., 2023).

Titanium oxide (TiO_2), also known as titania, is a transition metal oxide that has demonstrated its applications in renewable energy, environmental protection, and medical fields (Javed et al., 2022).

It has been widely employed as a semiconductor in dye-sensitized solar cells (DSSCs) and electron transport layer (ETL) in perovskite solar cells based on nanostructured TiO_2 (Ghosh et al., 2022). The interest in TiO_2 is due to its attractive optical, electrical, and chemical properties. It is one of the most studied semiconductor metal oxides because it depicts good stability upon illumination, is nontoxic, and has lower costs (Bencherif et al., 2022). Similarly, tin oxide (SnO_2) has promising optoelectronic properties, becoming an ideal alternative to TiO_2, which is limited by high-temperature processing and high UV photocatalytic activity under prolonged UV irradiation (Hoang Huy & Bark, 2023). The tetragonal rutile structure of SnO_2 has emerged as a promising ETL due to increased bulk electron mobility (200 – 300 $cm^2V^{-1}s^{-1}$), relatively low-temperature processing requirements, favourable CB energy level, and lower UV photocatalytic activity due to solar irradiance.

Zinc sulphide (ZnS) and zinc oxide (ZnO) are important II-VI semiconductors due to their abundance on the earth, low cost, efficient photovoltaic performance, and low toxicity (Ayodhya, 2023). However, they have a poor response to irradiating photons due to their wide band gaps (3.7 eV and 3.4 eV for ZnS and ZnO, respectively), which only absorb ultraviolet (UV) light. This photo-response behaviour limits the applications of their materials in photovoltaic devices (Badola et al., 2023). Consequently, engineering has been conducted to couple ZnO and ZnS nanoarchitectures to enhance their responsiveness to visible light. This advancement has led to the band gap narrowing to 2.8 eV in the resulting ternary zinc nanostructure, zinc oxysulphide (ZnOS) (Wu et al., 2016). The difference in electron-negativities and atomic radii between sulphur (S) and oxygen (O) atoms brings about a dramatic change in their optical and electrical properties, consequently depicting the desired response in visible light for the photovoltaic response (Uppal et al., 2019). Prior authors have synthesized various ZnOS with varying O/S mole ratios and reported that $ZnO_{0.6}S_{0.4}$ has a band gap of 2.7 eV, the narrowest of all the synthesized ZnOS series (Wu et al., 2016). Studies on energy-dispersive X-ray (EDX) suggest that both O and S compounds should have chemical bonding to Zn in the compositional architecture of the ZnOS lattice. Conveniently, Zn preferably exists in a positive state, whereas S and O prefer to exist in an anionic form, as observed in the ZnO_xS_{1-x} mass spectra (Uppal et al., 2019). A plethora of experimental and theoretical investigations have probed the optoelectronic properties and tested the feasibility of ZnOS in solar cell applications (Abdullah et al., 2024; Hossen et al., 2025; Shin et al., 2021).

Zinc oxysulphide (ZnOS) has attracted considerable interest as a top ETL contender in DSSCs due to its electronic and structural richness (Abdullah et al., 2024; Rahman et al., 2017). It is a non-hazardous material that can be fabricated through chemical bath deposition (CBD) methods, is readily available, and has a tunable band gap (Gour et al., 2020). Further, optimizing the "tunability" of the band gap energy increases the photocurrent.

Typical DSSCs contain inorganic or organic dyes, mainly composed of ruthenium (Ru) (II)-coordination complexes and nanocrystalline TiO_2 anatases (101) anchored on the dye molecule (Yahya et al., 2021). Ru (II) based complex dyes, particularly [*cis*-(dithiocyanato)-Ru-bis(2,2'-bipyredine-4,4'-dicarboxylate)] complex (N3 dye), alongside its doubly protonated tetrabutylammonium salt (N719 dye), have been popular solar absorbers due to the low metal-to-ligand charge transfer (MLCT) energy gap (Nam et al., 2019). In these complex dyes, the bipyridine ligands serve as stable anchoring groups on the semiconductor surface through their carboxylic groups. Conversely, thiocyanate ligands in these dyes facilitate the rapid regeneration of the oxidized dye. Other experimental and theoretical studies have also reported DSSCs based on trithiocyanato (4,4'4"-tricarboxy-2,2':6', 2'-terpyridiene) Ru (II) complex (black or the N749 dye) (Tahir et al., 2022). They have proven to compete with N3 and N719-based DSSCs in photovoltaic performance. Black dye, commonly known as N749 dye, shows spectral response in the red to infrared (IR) electromagnetic regions of the electromagnetic spectrum, a property lacking in most organic and inorganic dyes (Grifoni et al., 2021). Moreover, its superior spectral response is attributed to effective incident-photon-to-conversion efficiency (IPCE) within the visible region up to 920 nm (Tayeb et al., 2022).

Whereas considerable research efforts have been conducted to systematically develop molecular guidelines to elucidate the structure of the new dyes and their behaviour when anchored to various photoanodes (De Angelis et al., 2007; Yildiz et al., 2021), other reports have described the use of a hole transport layer (HTL) instead of the conventional redox potential, I^{-1}/I_3^{-1}, as a significant breakthrough in extending valuable lifetimes, overcoming volatilities and corrosion due to I^{-1}/I_3^{-1} electrolyte, and guaranteeing the photo-thermal stabilities of solid-state dye-sensitized solar cells (ssDSSCs) (Mehrabian & Dalir, 2018). Various HTLs in the inorganic-organic electronic field have been explored to promote hole transport and prevent direct contact between the lower electrode and the photosensitive material. Until recently, the HTLs that have been predominantly

used in n-i-p solar cell structures include copper thiocyanate (CuSCN) and 2,2'7,7'-tetrakis-[*N,N'*-di(4-methoxyphenyl)amine]-9,9'-spirobifluorene (Spiro-MeOTAD) as inorganic and organic semiconductors, respectively (Baumeler et al., 2023). Additionally, the optoelectronic properties of the photoanodes to which these dyes "anchor" dictate the corresponding device photovoltaic response. One of the conditions is that the LUMO of the active layer should lie well above the CB of the photoanode for ultrafast electron injection. Moreover, to avoid recombination of charge and achieve fast dye regeneration, the HOMO energy of the active layer should be lower than the redox potential of the electrolyte (Nalçakan et al., 2023).

Computation and theoretical calculations based on density functional theory (DFT) have been effectively utilized to elucidate the electronic structures of various isolated molecules in DSSCs (Periyasamy et al., 2023). In addition to the Gaussian 09w, other well-defined computation methods in computational chemistry, such as Chemissian, Gauss Sum, and one-dimensional solar cell capacitance simulator (SCAPS-1D), have been used to predict the optical response and photovoltaic performance of various materials that have been tested in solar cells (Elroby & Jedidi, 2020; Wazzan et al., 2023). Prior studies have used the Chemissian program to simulate multiple optoelectronic properties, including emission and absorption profiles (Chartrand & Hanan, 2014), while computational chemists have successfully used DFT to perform geometry optimization (Seeger & Izgorodina, 2020). Furthermore, time-dependent density functional theory (TD-DFT) has been employed to investigate the optical properties and characterize the excited states of the optimized molecules (El Mouhi et al., 2022).

In this context, isolated molecules used in dye-sensitive solar cells, such as the N719 dye, TiO_2, SnO_2, CuSCN, and ZnOS, have been simulated using various computational programs, including Gaussian 09w, GaussSum, Chemissian, and SCAPS-1D, to probe their optoelectronic and structural properties. Chemissian and Gaussian 09w can be conveniently used to analyze the optoelectronic behavior, optimized geometries, ground-state properties, band gaps, LUMO, and HOMO energies of various materials used in DSSCs. These approaches are cost-effective, have relatively low material and labor costs, and allow for rapid screening of a vast range of potential materials, thereby accelerating the selection process of candidates that warrant further experimental investigation.

5.2 Theory and computational details

The objectives of the study were achieved via computational calculations using the Gaussian 09w, solar cell capacitance simulator in one dimension (SCAPS-1D), and the Chemissian program. Theoretical studies rooted in DFT using Gaussian 09w have been used to obtain the optimized geometries of materials under investigation. The geometries of the molecular structures were optimized using the B3LYP/LanL2DZ functional and basis sets for transition metals- Ru, Cu, Sn, and Zn. Molecular electrostatic potentials (MEP) and reduced density gradient (RDG) computational tools were used to visualize electrostatic potentials and non-covalent interactions (steric effects, hydrogen bonding, and van der Waals), respectively (Jumabaev et al., 2025; Rezaei-Sameti et al., 2025). Prior research groups have underscored that RDG plots reveal regions of low electron density gradient (Morales-Pumarino & Barquera-Lozada, 2023), while MEP maps analysis helps predict how various DSSCs layers interact with other components (Abusaif et al., 2021). For the case of N719 dye, simplifications were made, which were considered in this study because the counterions (tetrabutylammonium, TBA) were predicted to have a marginal effect on the ground- and excited-state energy levels of the structure. Figure 5.1(a) presents the N719 dye chemical structure and (b) the DFT-optimized structure of N719 dye taken from GaussView.

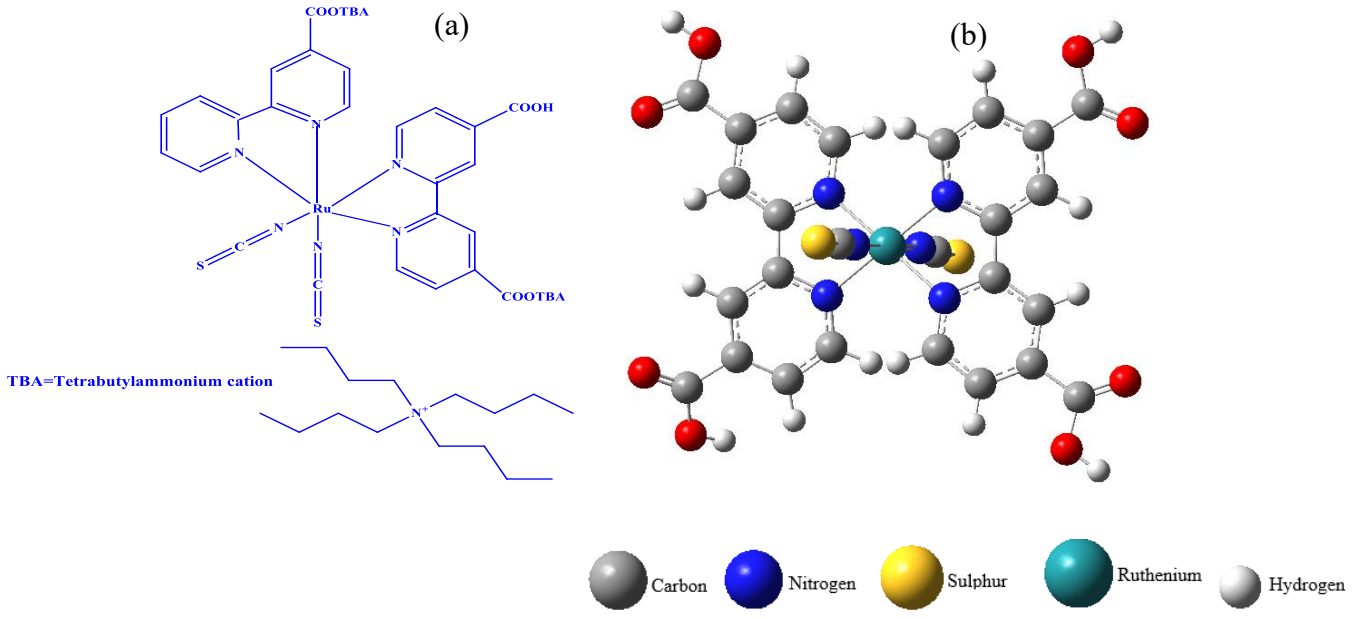

Figure 5.1: N719 dye chemical structure (a) and (b) simplified structure of N719 in DFT optimization

Numerous studies have been conducted on the electronic structures of TiO_2 anatase structures for various applications in both DSSCs and gas sensors, due to their chemical inertness, long-term photo-corrosion resistance, and chemical stability (Berger, 2022; Luo et al., 2021; Merlinsky et al., 2024; Prayogi & Marzuki, 2022). Typically, in the TiO_2 nanocluster (anatase 101), each oxygen (O) atom nearly binds with two Ti atoms (Yang et al., 2020). Accordingly, $(TiO_2)n$ clusters (for n = 1 to 16) have been used as a representative of 10^1 anatase surfaces (Eithiraj & Geethalakshmi, 2013). Various anatase surfaces $(TiO_2)_{16}$, $(TiO_2)_{28}$, $(TiO_2)_{38}$, and $(TiO_2)_{46}$ have been studied due to their ability to reproduce the physical parameters of TiO_2 semiconductors (Lamiel-Garcia et al., 2017). However, bulk titania has a large band gap that has been considered to limit electron transport.

Theoretical and experimental investigations have endeavoured to design new TiO_2 clusters via a defect engineering approach (Nowotny et al., 2015; Stashans et al., 1996). Oxygen-deficient clusters have been documented to have an increasing density of states (DoS) and a narrow band gap that enables them to be sensitive to more of the sun's visible spectrum (Nisar et al., 2013). Conveniently, suboxides of TiO_2 with the general formula Ti_nO_{2n-x} ($x > 0$), which can easily be sensitized from bulk TiO_2 materials, have enhanced catalytic activity compared to their stoichiometric counterpart, unique optical properties, and are non-toxic (Garcia et al., 2021). Oxygen (O) deficient TiO_2 – also called the Magneli phase- contains large fractions of O deficient, which act as active sites for catalytic activity, thereby increasing its electrical conductivity, as reported by Garcia et al. (2021). Accordingly, the effect of O vacancies on the optoelectrical properties such as the HOMO, LUMO, and band gap energies is examined in this theoretical investigation. Therefore, the magneli phase with the formula Ti_nO_{2n-2} (n=5) will be investigated – Ti_5O_8 using Gaussian 09w, GaussView, and Chemissian software. As Figure 5.2 shows, the terminal O is absent, and the remaining O atoms are bridged between two Ti atoms. Previous authors have reported that the presence of O vacancies in the sub-nanometer of TiO_2 improves visible-light absorption (Hou et al., 2018).

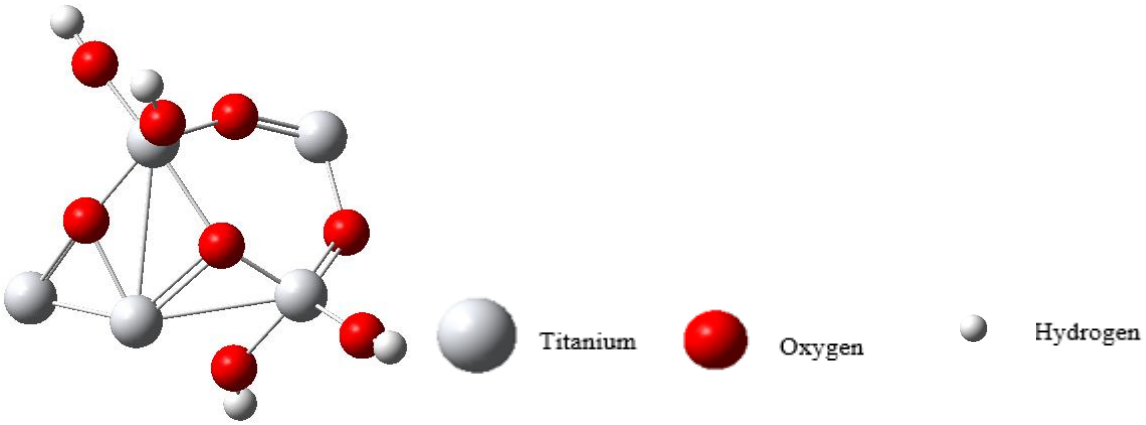

Figure 5.2: The optimized geometry of Ti_5O_8 in B3LYP/LanL2DZ method

Conventionally, the tetragonal rutile structure of SnO_2 is a top ETL contender owing to its attractive optoelectronic properties (Mali et al., 2018). Tin oxide (SnO_2) forms oxides with different valences, allowing it to participate in photocatalysis (Pinto et al., 2022). Furthermore, it has better chemical stability and exhibits high UV resistance, making it an ideal ETL candidate in DSSCs (Dalapati et al., 2021; Gebreslassie & Gebretnsae, 2021). Considerable research also suggests that SnO_2 exhibits tunable electronic properties, which can enhance the optoelectronic performance of DSSCs. Its performance can also be improved by doping it with foreign materials such as gallium (Ga), phosphorous (P), tantalum (Ta), fluorine (F), molybdenum (Mo), tungsten (W), and antimony (Sb) (Dalapati et al., 2021). Although SnO_2 has gained considerable scientific acceptance as a potential standard ETL, the analysis of its structural and optoelectronic properties is less explored in the literature. Due to its enormous potential for clean and sustainable energy applications, this study aims to explore the different optoelectrical properties of SnO_2 from a novel perspective, diverging from the existing literature.

In this context, Gaussian 09w, GaussView 5.0, GaussSum, SCAPS-1D, and Chemissian will be used to explore various optoelectronic properties of SnO_2, including HOMO, LUMO, energy gap, the molecular electrostatic potential, and photovoltaic performance in DSSCs. The SCAPS-1D program was developed at the Department of Electronic and Information Systems (ELIS) of the University of Gent, Belgium. This program can numerically solve the continuity and carrier transport equations for holes and electrons and the Poisson equation. Conveniently, this simulation tool is capable of calculating various PV parameters such as the energy conversion efficiency,

open circuit voltage (V_{OC}), fill factor (FF), short-circuit current density (J_{sc}), the recombination profile, energy conversion efficiency, current-voltage (J-V) characteristics, and the energy band diagram. In this present investigation, theoretical optimization of optoelectronic properties of various ETLs for DSSCs is performed. Accordingly, the current optimization sought to probe the optimized optoelectronic properties of planar heterojunction solar devices with the architecture glass/FTO/ETL/N719/CuSCN/Au, as illustrated in Figure 5.3.

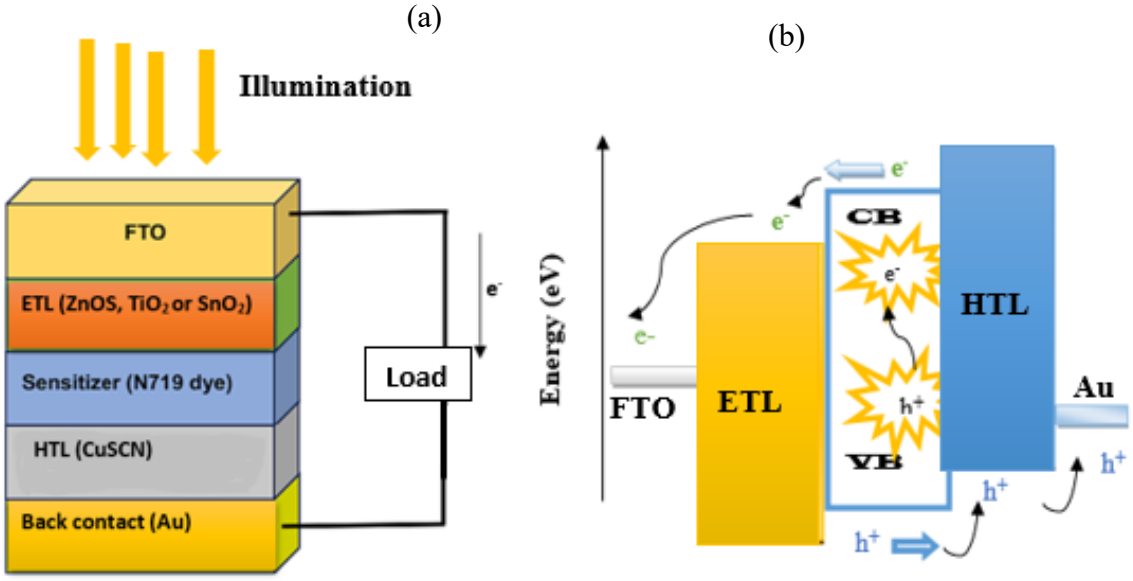

Figure 5.3: Schematic representation of the simulated n-i-p architecture (a), and (b) the energy band diagram of the device

In this study, back contact material, series and shunt resistance, absorber thickness, defect densities, and working temperature. Furthermore, the study sought to identify device structures with optimal J-V characteristics and characteristic quantum efficiency curves. The SCAPS-1D input parameters used in this theoretical investigation have been judiciously selected from previous experimental works and published literature. Moreover, the absorption coefficient (α) of the material layers is dependent on the photon energy (hv) and band gap energy (E_g) is given by the expression; $\alpha = A_a(hv - E_g)^{\frac{1}{2}}$ where A_a is the pre-factor, will be set as 1×10^5 in numerical simulation. The input parameters of various layers of the proposed device structure are listed in Tables 5.1 and 5.2. Table 5.1 presents input parameters for the FTO, absorber (N719 dye), and HTLs. In the SCAPS-1D program, the "Single Shot" calculation is based on solving the Gummel

iteration scheme with Newton-Raphson sub-steps. Most of the simulation environment is set at 300 K under AM 1.5 G solar illumination, equivalent to one sun (1000 W/m²).

Table 5.1: Parameters extracted from literature

Parameters	**FTO**	**N719 dye**	**CuSCN**
Thickness (nm)	varied	varied	varied
Bang gap,(E_g), (eV)	3.50	1.6	3.40
E. affinity (χ) (eV)	4.00	3.90	1.90
D.perm. (ϵ/ϵ_r), (eV)	9.00	30.00	10.00
c (1/cm^3)	2.20×10^{18}	2.40×10^{20}	1.70×10^{19}
N_V (1/cm^3)	1.80×10^{19}	2.50×10^{20}	2.50×10^{21}
μ_e (cm^2/Vs)	20.00	5.00	1.0×10^{-3}
μ_p (cm^2/Vs)	10.00	5.00	1.0×10^{-1}
V_e (cm/s)	1.00×10^{7}	1.00×10^{7}	1.00×10^{7}
V_h (cm/s)	1.00×10^{7}	1.00×10^{7}	1.00×10^{7}
N_D (1/cm^3)	2.00×10^{19}	0.00	0.00
N_A (1/cm^3)	0.0	1.00×10^{16}	1.00×10^{18}
Nt (1/cm^3)	-	1.0×10^{17}	1.00×10^{14}
Ref.	(Bhavsar & Lapsiwala, 2021)	(Bhavsar & Lapsiwala, 2021)	(Bhavsar & Lapsiwala, 2021)

In this investigation, various input parameters of the material layers were optimized using SCAPS-1D. Furthermore, Gaussian 09w and Chemissian computational codes were used to gain meaningful insights into various solar cell parameters, PCE, optoelectronic, and structural properties to investigate specific applications of the device. The findings of this study were then validated by comparing them with earlier studies of theoretical and experimental investigations. Table 5.2 provides the input materials for various ETLs modulated in the study.

Table 5.2: Input parameters of various ETL materials

Parameters	**SnO_2**	**ZnOS**	**TiO_2**
Band gap	3.6	2.83	3.20
Electron affinity (eV)	3.90	3.60	3.90
Dielectric perm.	8.00	9.00	32.00
N_C (1/cm^3)	3.16×10^{18}	2.20×10^{18}	1.00×10^{19}
N_V (1/cm^3)	2.50×10^{19}	1.8×10^{18}	1.00×10^{19}
μ_e (cm^2/Vs)	15	100.00	20.00
μ_h(cm^2/Vs)	0.1	25.00	10.00
V_e (cm/s)	1.00×10^{7}	1.00×10^{7}	1.00×10^{7}
V_h (cm/s)	1.00×10^{7}	1.00×10^{7}	1.00×10^{7}
N_D (1/cm^3)	1.00×10^{18}	2.00×10^{19}	1.00×10^{17}
N_A(1/cm^3)	0.00	0.00	0.00
N_t (1/cm^3)	1.00×10^{18}	1.00×10^{17}	1.00×10^{15}
Ref.	(Bhavsar & Lapsiwala, 2021)	(Mohammadian-Sarcheshmeh & Mazloum-Ardakani, 2018)	(Bhavsar & Lapsiwala, 2021)

5.3 Results and discussions

5.3.1 Density functional theory calculations

5.3.1.1 Frontier molecular orbitals

Understanding frontier molecular orbitals (FMOs), particularly HOMO and LUMO, helps in optimizing the light-harvesting efficiency of DSSCs. The HOMO-LUMO gap directly influences the electronic and optical properties of solar cell layers (Krishnan & Senthilkumar, 2021). As reported in previous scholarly findings, sub-nanoclusters of TiO_2 with a large number of defect sites have structural distortions, particularly in the local symmetry of metal centres, that significantly impact recombination and charge transport during photocatalytic activity. In this study, the magneli phase of Ti_5O_8 was studied, and HOMO and LUMO energies were calculated using Gaussian 09w and visualized in GaussView. The molecular electrostatic potential (MEP) exhibits the unique catalytic and electrical conductivity of the reduced Ti ions and oxygen

vacancies. The blue plates in the MEP show the high concentration of Ti^{3+}. In contrast, the red plate corresponds to surfaces of low electron density (electron-deficient sites), and the green plates show that the oxygen defects are ordered (the intermediate state between the red and blue regions). As observed in this investigation, the HOMO-LUMO gap has decreased by multiple eV due to the absence of an O atom compared to the conventional TiO_2 structure. These findings strongly correlate with other publications that reported that HOMO and LUMO primarily localize on the Ti atoms in Ti_nO_{2n-2} (Garcia et al., 2021). The HOMO shifts from an O 2p-orbital to a Ti 3d-orbital; when there are increased O vacancies, the unoccupied and occupied orbitals shift towards the Fermi level such that all these orbitals become closer in energy in the CB (Garcia et al., 2021).

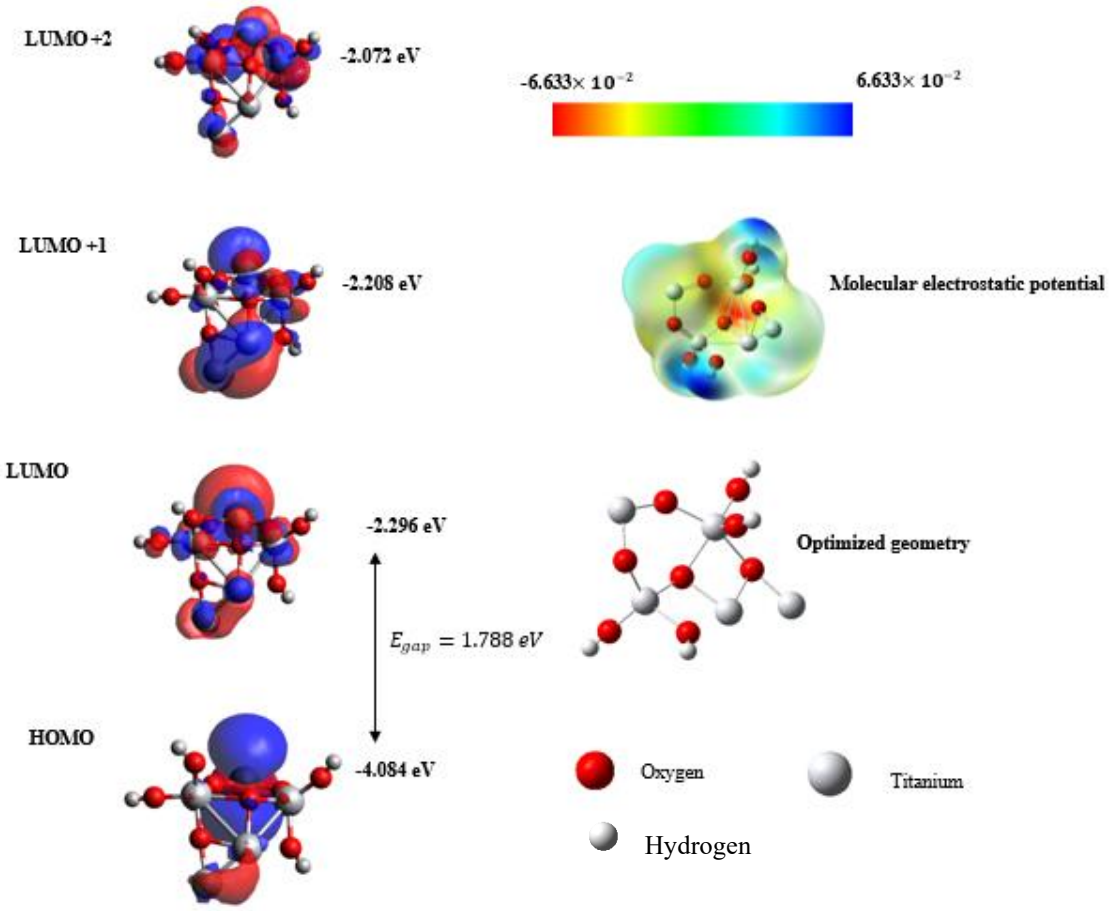

Figure 5.4: The optimized structure, highest occupied molecular orbital, the molecular electrostatic potential, and lowest unoccupied molecular orbitals of the Magneli phase of Ti_5O_8 at the B3LYP/LanL2DZ level of theory

The observations in this study indicate that defect engineering, where the HOMO-LUMO gap can be tuned by changing structures and size, provides a better way of tuning optical and electronic characteristics for photovoltaic applications. Besides HOMO and LUMO levels analysis, the molecular electrostatic potential (MEP) surface was visualized. MEP depicts the electrostatic potential distribution (nuclei and electrons), shape, size, and dipole moments of the isolated DSSCs molecules, where relative polarity can be visualized (Barman et al., 2025). It is a key way to determine how acceptors and donors work and hydrogen-bonding interactions. As shown in Figure 5.4, the three colours— blue, red, and green — indicate the electrostatic potential. The blue colour indicates a strong attraction, the green colour reveals zero potential, and the red colour shows strong repulsion. The existence of nucleophilic and electrophylic sites (the adsorbent and adsorbate) predicts the stability of the proposed systems.

Alongside copper-based materials such as copper iodide (CuI) and copper bromide (CuBr), CuSCN is a highly transparent, robust, and solution-processable HTL for DSSCs reported in many studies (Liang et al., 2022; Nizamuddin et al., 2021). Studies on the energy-level alignment of these new series of materials have proved pivotal in exciton dissociation, J_{sc}, V_{OC}, photovoltaic performance, charge collection, and transport (Nizamuddin et al., 2021). In particular, the work function of CuSCN impacts charge transport and collection. In this study, the B3LYP level was employed, which is a commonly accepted ab initio method for predicting energy levels of CuSCN (cf. Figure 5.5).

In the MEP, the negative potential (blue region) around the nitrogen atom indicates an electron-rich site that blocks electrons and allows for the selective transport of holes. The green region (between the thiocyanate groups and copper) is an area of neutral potential, reducing undesirable recombination events, while the red region (around the copper atom) is an area of positive potential that attracts electron-rich species, enhancing charge separation and transport. As depicted in Figure 5.5, the calculated band gap of CuSCN at B3LYP/LanL2DZ is 2.03 eV. It was observed that the HOMO and LUMO energies are -5.85 eV and -3.82 eV, respectively. However, the experimental work function of CuSCN is 5.35 eV (Bhargav et al., 2019). Therefore, the computational calculation overestimates the HOMO of CuSCN by $\sim$ 0.5 eV because the B3LYP method does not adequately consider electron correlation in predicting FMO energies (Bhargav et al., 2019).

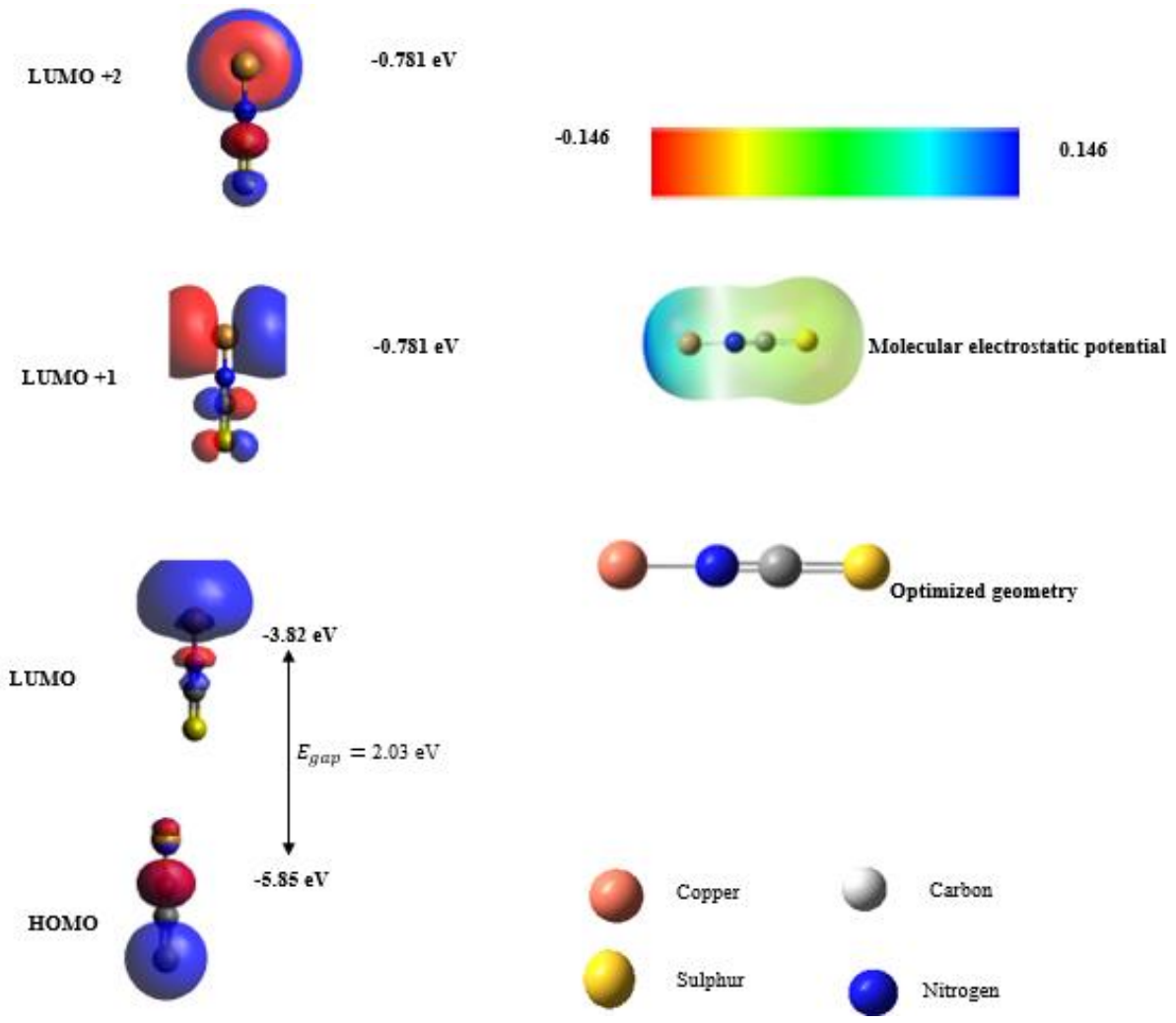

Figure 5.5: The optimized structure, highest occupied molecular orbital, the molecular electrostatic potential, and lowest unoccupied molecular orbitals of CuSCN at the B3LYP/LanL2DZ level of theory

Zinc oxysulphide (ZnOS) belongs to the abundant group II-IV compound semiconductors that have attracted numerous applications in solid-state laser devices, transparent conductors, solar cells, and photodetectors (Ameri et al., 2013; Es-Smairi et al., 2024). Few theoretical and experimental studies have been conducted on the alloy due to difficulties associated with synthesizing the material. (Ameri et al., 2013). In this study, we adopted the $ZnO_{0.6}S_{0.4}$ structure proposed by Wu et al. (2016). The HOMO-LUMO energy gap is 0.43 eV (cf. Figure 5.6), which significantly deviates from the experimental value of 2.7–3.2 eV. This observation can be

attributed to the exchange-correlation function, which underestimated the band gap values. Also, Ameri et al. (2013) observed that the band gap of ZnOS alloys varies non-linearly with sulphur and oxygen composition, which was not accounted for in our current DFT calculations.

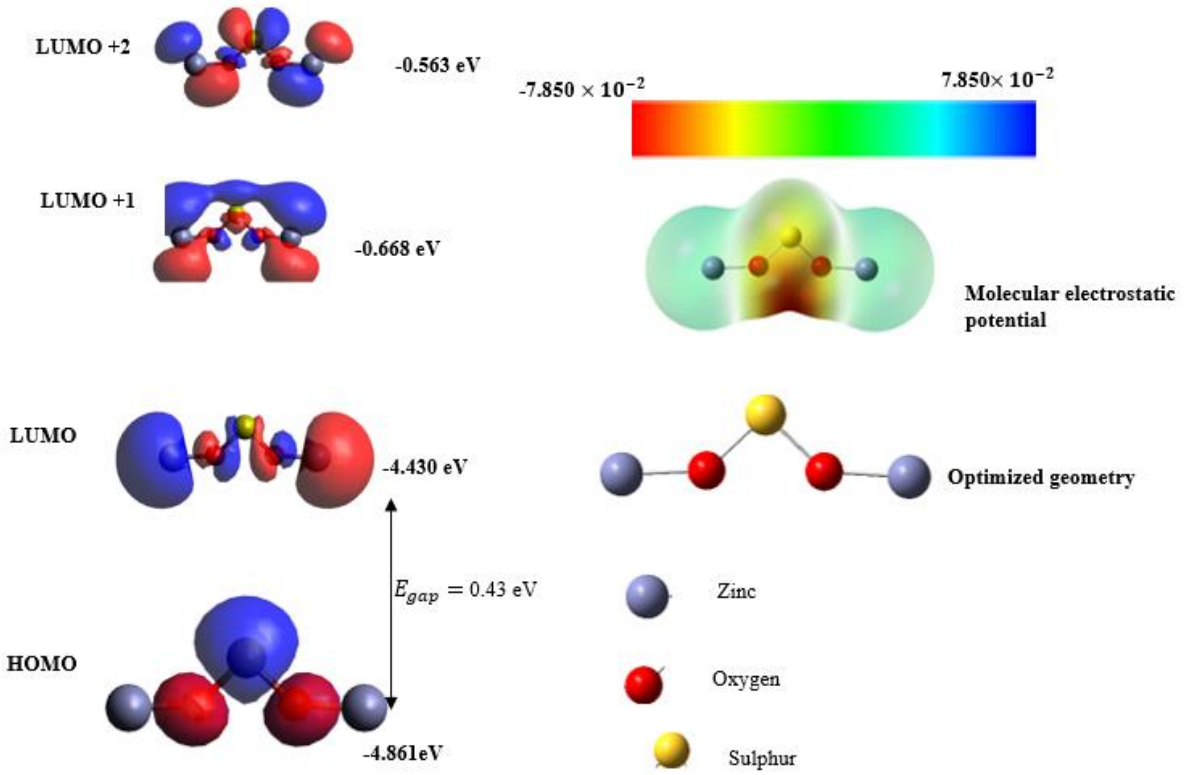

Figure 5.6: The optimized structure, highest occupied molecular orbital, the molecular electrostatic potential, and lowest unoccupied molecular orbitals of ZnOS at the B3LYP/LanL2DZ level of theory

The theoretical analyses of HOMO, LUMO, and the energy gap of SnO_2 were then performed and compared with the literature. The HOMO energy (E_{HOMO}) is -8.31 eV, while the LUMO energy is E_{LUMO}) is -3.89 eV, giving a HOMO-LUMO gap of 4.42 eV, as shown in Figure 5.7. This value is consistent with what is reported in the literature, ranging from 3.6 to 4.0 eV, allowing it to exhibit high transmittance in the visible region (Dalapati et al., 2021). Moreover, its tunable band gap is crucial in engineering energy levels for multi-junction solar cells (Pandit & Ahmad, 2022). Earlier studies have also discussed the optoelectronic properties of SnO_2 in detail, particularly its impacts on device performance (dos Santos et al., 2022). In view of this, the computational screening of SnO_2 indicates that it has a reliable and efficient band for application in DSSCs.

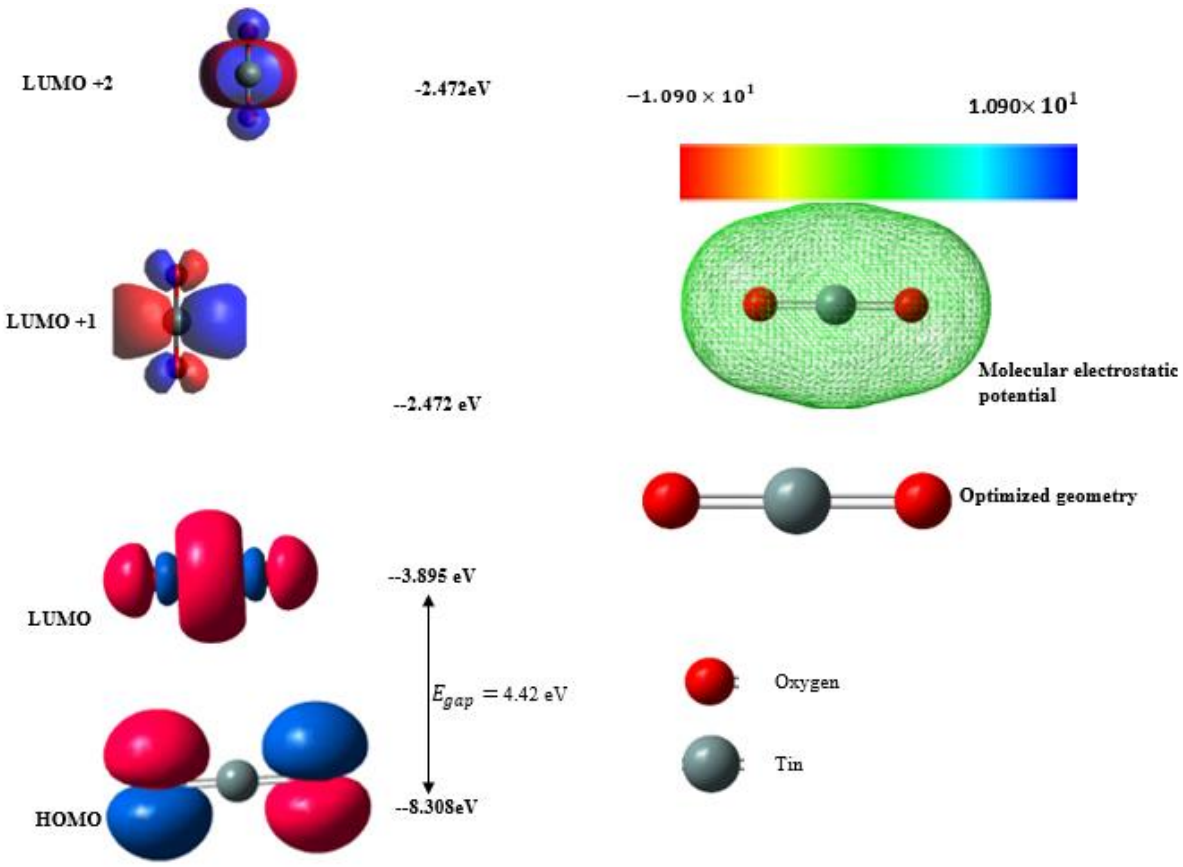

Figure 5.7: The optimized structure, highest occupied molecular orbital, the molecular electrostatic potential, and lowest unoccupied molecular orbitals of SnO_2 at the B3LYP/LanL2DZ level of theory

Furthermore, DFT calculations provided insight into the electronic structure of the N719 dye. The molecular geometry of the N719 dye was calculated using the B3LYP method and the LanL2DZ basis set with Gaussian 09w, and then visualized using GaussView 5.0. The B3LYP method has been widely used to probe organic compounds, while the LanL2DZ basis set is an appropriate choice for transition metals (Ru), which justifies its use in this investigation. Figure 5.8 shows the optimized geometry and molecular orbital diagram of the dye. As depicted in Figure 5.8, the HOMO and LUMO are localized over the central Ru atom because it is coordinated to phenyl pyridine and bipyridine ligands (Portillo-Cortez et al., 2019). The electron density is concentrated around the Ru atom, playing a key role in the N719 structure. The dye is fully protonated (neutral system) – bond lengths and angles near the Ru atom are similar in all molecules, independent of molecular charges and the substituents. The calculated energy value is 1.13 eV, which reflects a

recent study that for highly efficient DSSCs, the HOMO-LUMO gap should be between 1.1 -1.7 eV (Portillo-Cortez et al., 2019). As shown in Figure 5.8, the red colour in the molecular electrostatic potential (MEP) depicts the strongest repulsion (Bradha et al., 2021), which is associated with the four carboxylic groups of the N719 absorber, which interacts with the positively charged species such as SnO_2, TiO_2, and ZnO, ZnOS surfaces in DSSCs. The blue region in the MEP reveals the electron-deficient region associated with the positively charged regions in the dye, while the green region represents a region of nucleophilic and electrophilic balance, contributing to the structural stability (Manaa et al., 2020).

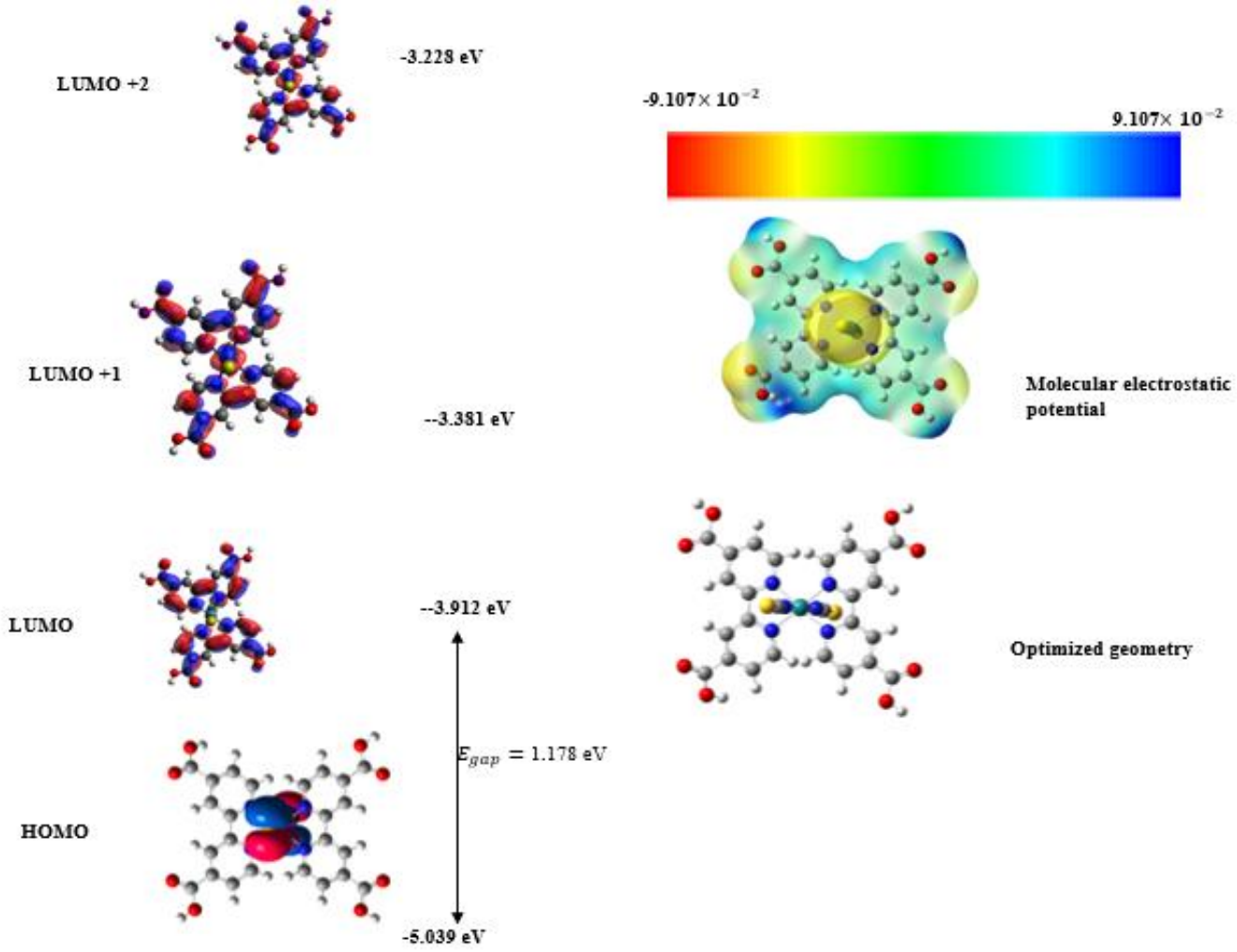

Figure 5.8: The optimized structure, highest occupied molecular orbital, the molecular electrostatic potential, and lowest unoccupied molecular orbitals of N719 dye at the B3LYP/LanL2DZ level of theory

5.3.1.2 Reduced density gradient analysis

To validate the anchorage of photoanodes on the N719 dye, reduced density gradient (RDG) plot analysis and isosurface interactions were studied using Multiwfn program. As shown in Figure 5.9, the red plate is attributed to a strong steric effect (repulsive interactions), the green plates are related to the Van der Waals interactions, while the blue plates depict strong interactions (Manaa et al., 2020). The isosurface shows that electrons are more concentrated near the carboxylate groups and around the Ru centre. The electron-dense region is a chemically reactive site that anchors on the photoanode surface. The blue spots, in particular, show the bidentate chelate linkages of the carboxylate ion group in the ruthenium complex (Alnakeeb et al., 2022). This shows the strong intermolecular interactions between the dye and photoanodes via the carboxylic group (Alnakeeb et al., 2022). These results coincide with previous studies determined by infrared absorption and Raman scattering spectroscopy that suggested that the carboxylate ion group of N719 dye binds to ZnO or TiO_2 either through bidentate bridging and bidentate bridging linkages at all stages of adsorptions (Manaa et al., 2020).

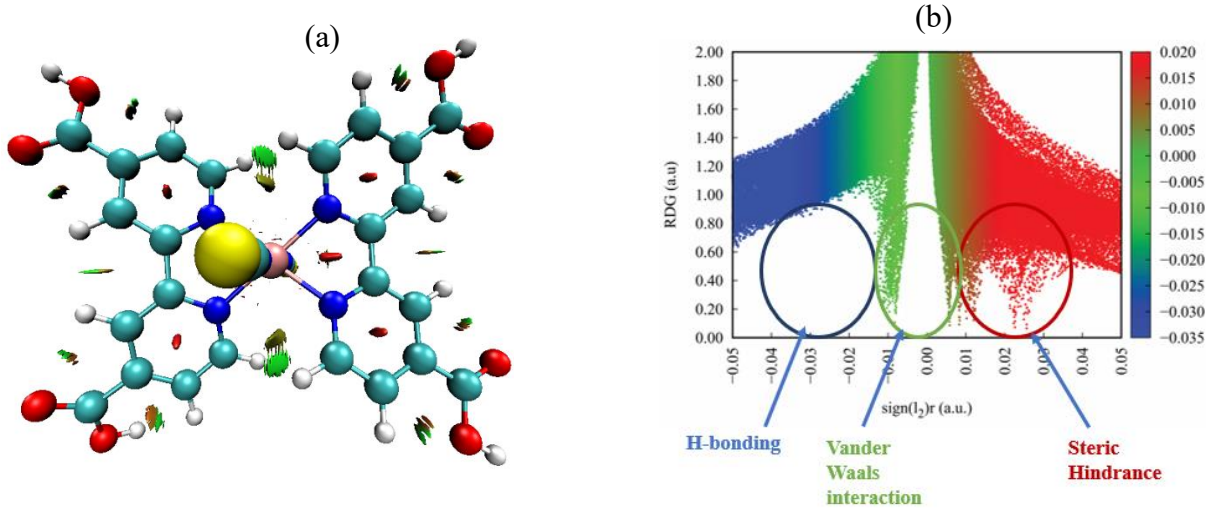

Figure 5.9: The iso surfaces (a) and (b), the reduced density gradient (RDG) maps showing the interaction modes of N719 dye

5.3.1.3 Density of states and ultraviolet spectra

The DoS plots have been studied to understand the density distribution around HOMO and LUMO with the aid of the GaussSum 3.0 program. Accordingly, DoS provides information about the

magnetic, optical, and electronic properties of device layers by showing their electron energy levels and distribution. The DoS around HOMO and LUMO for the proposed cell layers are calculated using DFT/B3LYP/Lanl2DZ method. In Figure 5.10 (a-e), the DoS reveals the energy levels of both unoccupied and occupied molecular orbitals, as well as the trajectories of charge transfers (Hossain et al., 2023; Hossain et al., 2022).

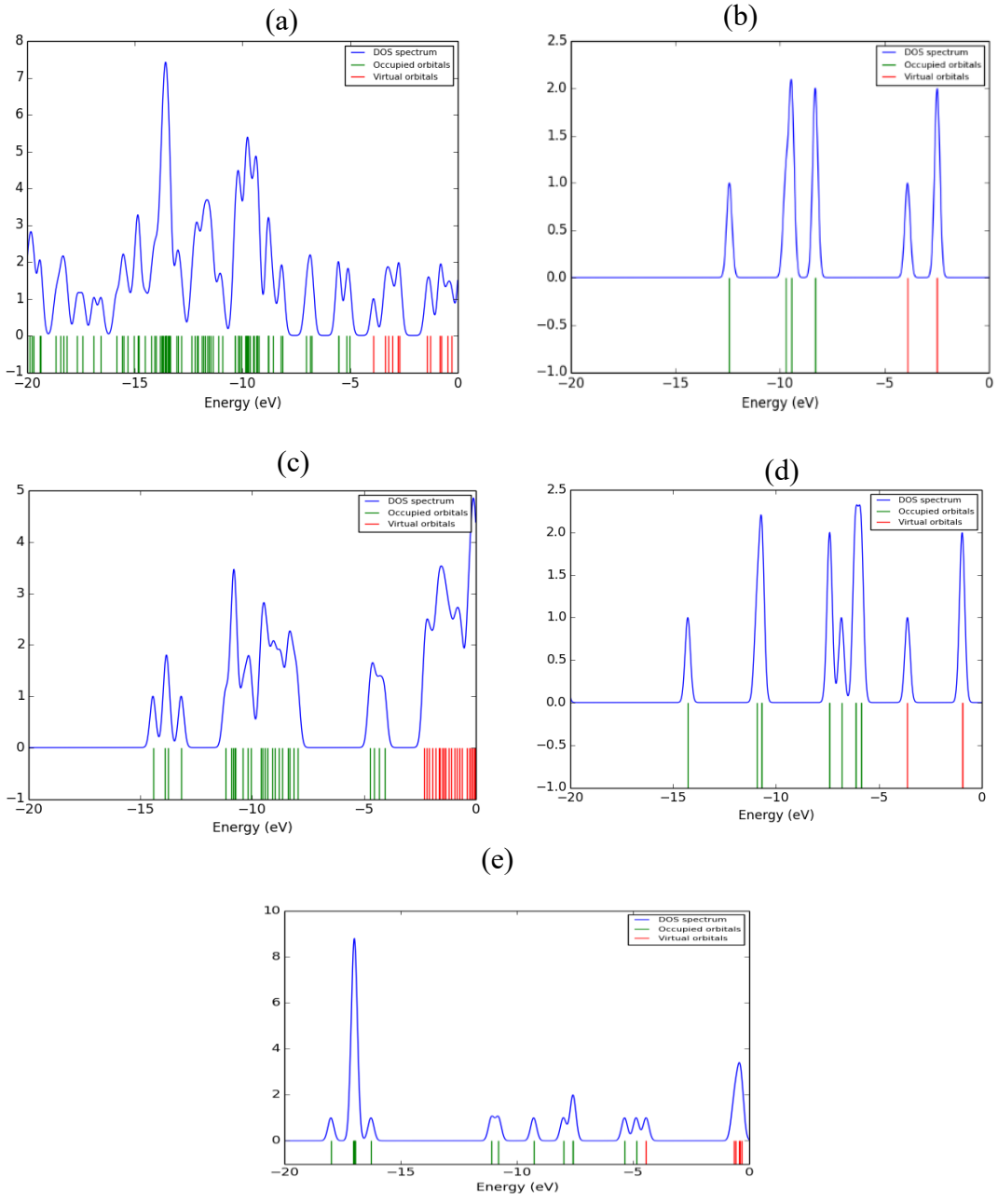

Figure 5.10: N719 dye (a), (b) SnO_2, (c) TiO_2, (d) CuSCN, and (e) ZnOS density of states

As depicted in Figure 5.10 (a), the DoS plot exhibits a narrow HOMO-LUMO, having its HOMO localized at the Ru centre while the LUMO is localized around the bipyridyl ligands. SnO_2 has a wide band gap, with its MOs localized primarily in the 5s orbitals. In Ti_5O_8, the oxygen vacancies exhibit localized states within the band gap, which narrows the band gap. In contrast, the CuSCN DoS is dominated by the S 3p and Cu 3d orbitals, thereby enhancing hole transport. The DoS of ZnOS reveals a mix of Zn 4s orbitals and S 3p orbitals. The absorption spectra in the UV-Vis region were simulated using the TD-DFT method with the B3LYP exchange-correlation potential and the LanL2DZ basis set. The UV-Vis spectroscopy of SnO_2 exhibits a strong absorption peak at approximately 300 nm, consistent with the findings of other studies (cf. Figure 5.11). This confirms the potential application of this material as a photoanode in DSSC. We did not report the UV-Vis spectra for N719 dye, ZnOS, CuSCN, and TiO_2 because they did not reach an acceptable level of accuracy (absorption peaks in the range of 300-500 nm for all molecules) due to the computational limitations of the B3LYP/LanL2DZ method for larger molecules.

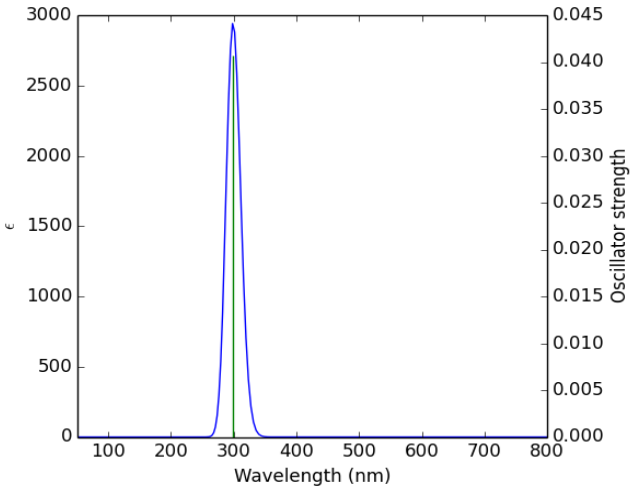

Figure 5.11: The UV-Vis spectrum of ZnOS visualized in GaussSum software

5.3.2 Analysis of SCAPS-1D results

5.3.2.1 Effect of series and shunt resistance

Shunt (Rsh) and series (Rs) resistances are considered crucial factors that strongly influence the performance of DSSCs (Mazumder et al., 2022). The presence of contact resistance at interfaces, resistances at circuit terminals, and the metallic contact between the back and front electrodes, as

well as the bulk, creates Rs in most solar cells. Accordingly, Rs is a detrimental factor significantly reducing the fill factor; thus, manufacturing solar cells with a 100% fill factor is difficult. A decrease in fill factor occasioned by Rs impacts the power conversion efficiency of the device. Conversely, Rsh is mainly due to the reverse saturation current of the active junction (Bansal et al., 2023). For a high conversion efficiency and high FF, make Rsh large and Rs small. In this research, Rs is varied from 0.5 – 10 Ω cm^2 after setting Rsh at 1.0 × 10^3 Ω cm^2 to describe its effect on cell performance. The PCE values for all the simulated models drop significantly with an increase in Rs (Figure 5.12a). Series resistance (Rs) limits the flow of electric current in the circuit, reducing the overall cell performance. At higher Rs, the incident photons cannot be efficiently converted into usable energy, affecting the overall cell performance. Figure 5.12 shows that as Rs is increased, the values of FF and PCE drop significantly due to reduced current flow.

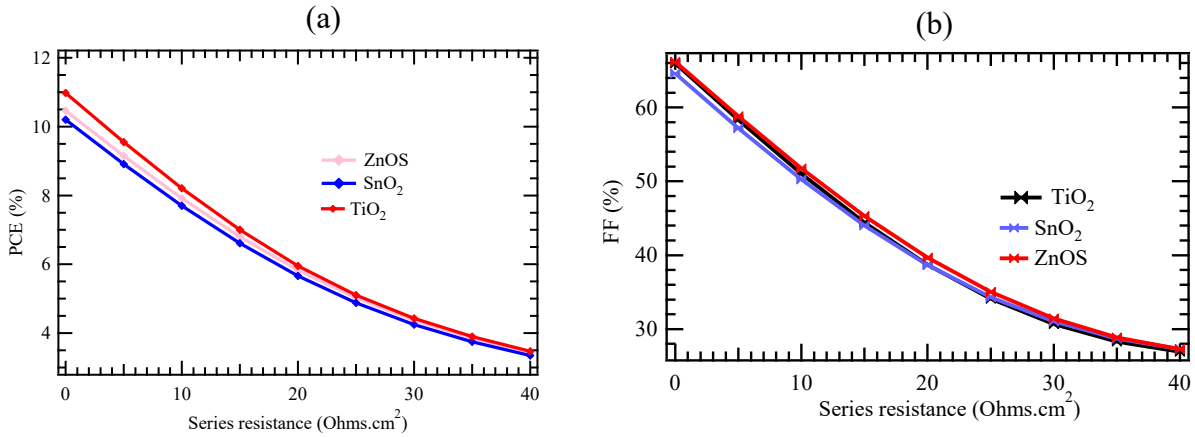

Figure 5.12: The effect of series resistance on PCE(a) and (b) on FF

For all the model cells with ZnOS, TiO_2, and SnO_2 ETLs, the FF dramatically dropped from 66.17% to 27.3%, 65.96% to 26.93%, and 64.58% to 27.28%, respectively, when the Rs increased from 0 to 40 Ω-cm^2. Similarly, the efficiency of ZnOS, TiO_2, and SnO_2-based cells dropped from 10.46% to 3.43%, 10.98% to 3.47%, and 10.2% to 3.35%, respectively, when the resistance (Rs) is increased from 0 to 40 Ω.cm². The negative impact of Rs on PCE and FF is attributed to poor current flow in the circuit and contact losses (soldering breakdown), respectively (cf. Figure 5.12b) (Bansal et al., 2023). This simulation study also revealed that Rs does not affect the voltage at the open circuit but causes a deviation in Jsc when Rs is increased from 0 to 10 Ω cm² (Figure 5.13). The V_{oc} for cell devices with ZnOS, TiO_2, and SnO_2 ETLs gave a constant efficiency of 0.778 V,

0.780 V, and 0.769 V when Rs s increased from 0 to 40 Ω cm^2. In addition, the J_{sc} for ZnOS, TiO_2, and SnO_2 cell structures dropped to 16.16449, 16.51137, and 15.95204 mAcm^{-2} from 20.32897, 21.34735, and 20.53950 mAcm^{-2}, respectively, as shown in Figure 5.13 (a-b). The drop in J_{sc} is due to optical transmission losses, which further exacerbate a drop in FF, which is proportional to the maximum power output to the V_{OC} multiplied by the J_{sc}. The mathematical relationship (Equation 5.1) shows that it will result in a decrease in the J_{sc} (Bansal et al., 2023).

$$I = I_{ph}\left[exp\frac{q(V+IR_s)}{nkT} - 1\right] - \frac{V+IR_s}{R_{sh}} \qquad (5.1)$$

where *I, q,* I_{ph}*, n, k, T,* R_{sh}*, and* R_s is load current, the electron charge, light-generated current, ideality factor, Boltzmann's constant, shunt resistance, and series resistance, respectively.

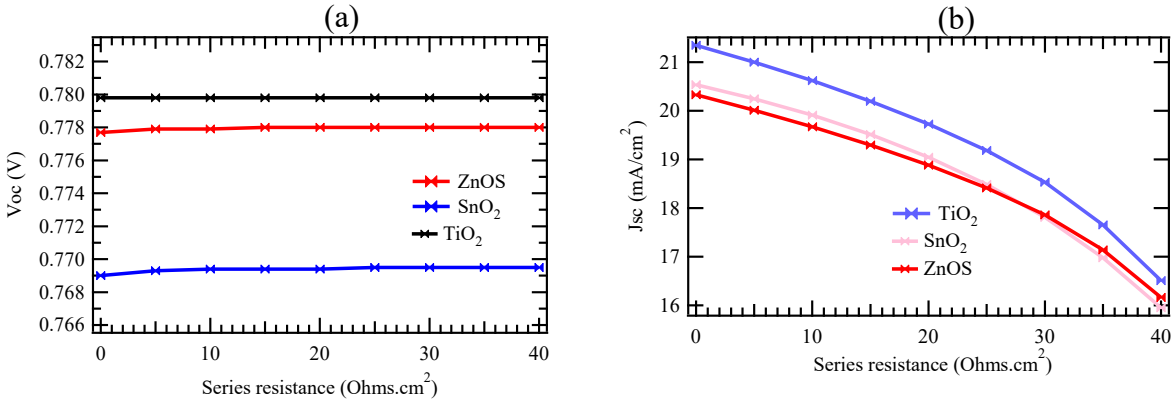

Figure 5.13: The effect of series resistance on V_{OC} (a) and (b) on J_{sc}

Next, the electronic and optical behaviour of the cell structures was also studied by varying the Rsh from 10 Ω cm² to 500 Ω cm², while the Rs was fixed at 0.5 Ω cm². Figure 5.14 (a-d) shows that all the performance parameters are low when Rsh is low. Higher Rsh implies that the charge recombination inside the cells has been suppressed and thus increased V_{OC} (Bansal et al., 2023). The V_{OC} and J_{sc} increase with an increase in Rsh up to 100 Ω cm^2. But with a further increase in Rsh, the cell parameters become saturated. On the other hand, FF and PCE increased from 0 Ω cm² to 500 Ω cm^2, a reduction in leakage current which relates to higher Rsh. With a further decrease in Rsh to 500 Ω cm^2, the FF reaches the saturation point with no significant changes with further increase in Rsh.

As shown in Figure 5.14 (d), a lower Rsh creates alternative pathways that allow the passage of current, thereby reducing the overall J_{sc} of the device (Mendes et al., 2022). The J_{sc} of the cell increases at high Rsh due to a reduced shunting effect before it reaches saturation, Figure 5.14(d). The performance of the solar cell models increases with increased Rsh due to fewer unwanted current leakages. However, it reaches a point where an increase in Rsh does not show any discernible gain due to optimized current collection; thus, overall performance remains constant. Thus, superior solar cell designs exhibit lower Rs and higher Rsh. In this analytical investigation, optimal Rsh was found to be 1.0×10^3 Ω cm², while the optimal Rs was determined to be 0.5 Ω cm². Therefore, achieving the right Rsh balance, typically in the modelling and design of solar cells, is essential to optimize PV performance.

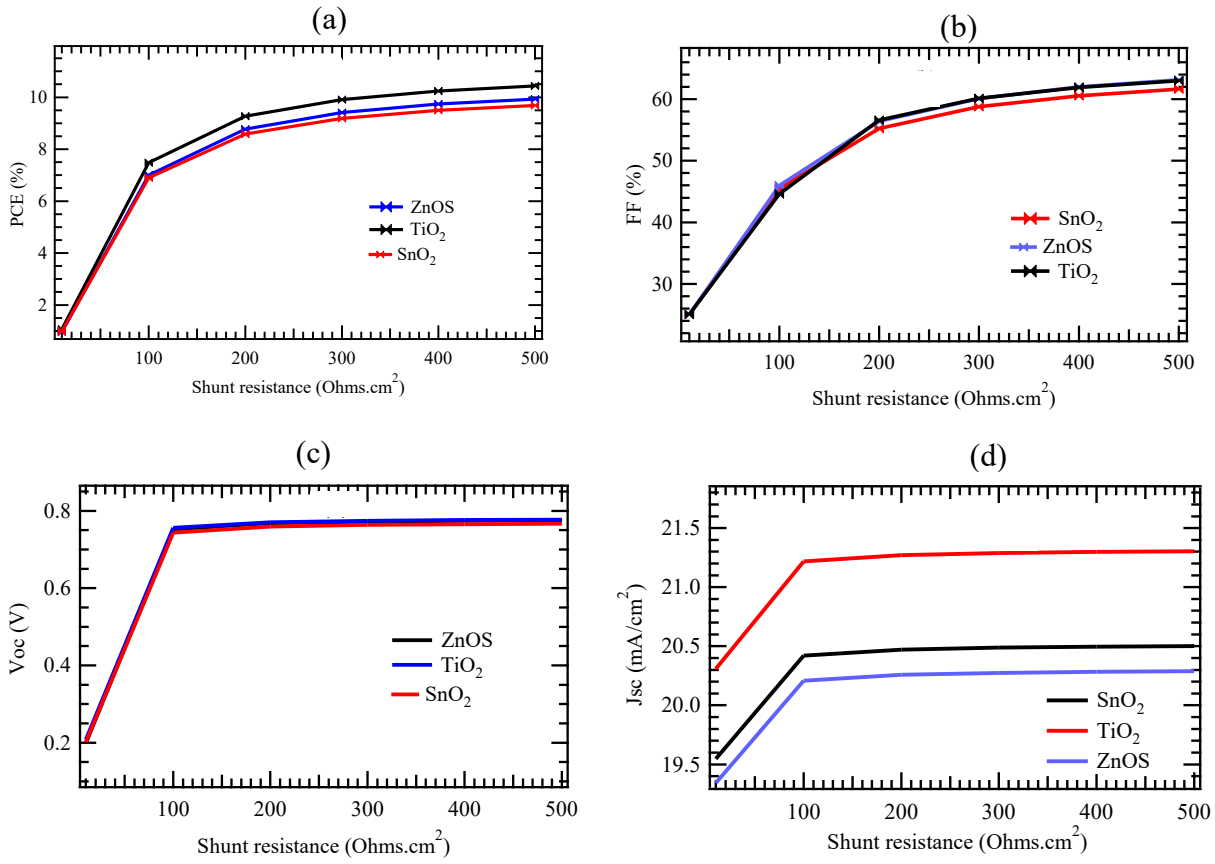

Figure 5.14: The effect of shunt resistance on (a) PCE, (b) FF, (c) V_{OC} and (d) J_{sc}

5.3.2.2 Effects of operating temperature

Prior studies have shown that temperature has many effects on conversion efficiency, fill factor, and open-circuit voltage of a solar cell. Photovoltaic devices are sensitive to temperature since an increase in temperature decreases the bandgap of the semiconductor (Sahoo & Manik, 2023). This decrease in bandgap affects semiconductor parameters and is attributed to the decrease in bonding energy and an increase in the energy of the electrons. Typically, solar cells operate at room temperature; however, it is known that their efficiency deteriorates when the temperature rises during the summer season. It is also well-established in the literature that defects and trap states arise with the increment in temperature, and thus, Shockley-Read Hall (S-RH) recombination becomes dominant, which has a detrimental effect on V_{OC} (Bansal et al., 2023). In this research, the effect of operating temperature on cell performance was examined by varying it from 260 to 360 K. The simulated results showed that temperature significantly affects the V_{OC}, which also reduces the cell efficiency, as illustrated in Figure 5.15 (a-b).

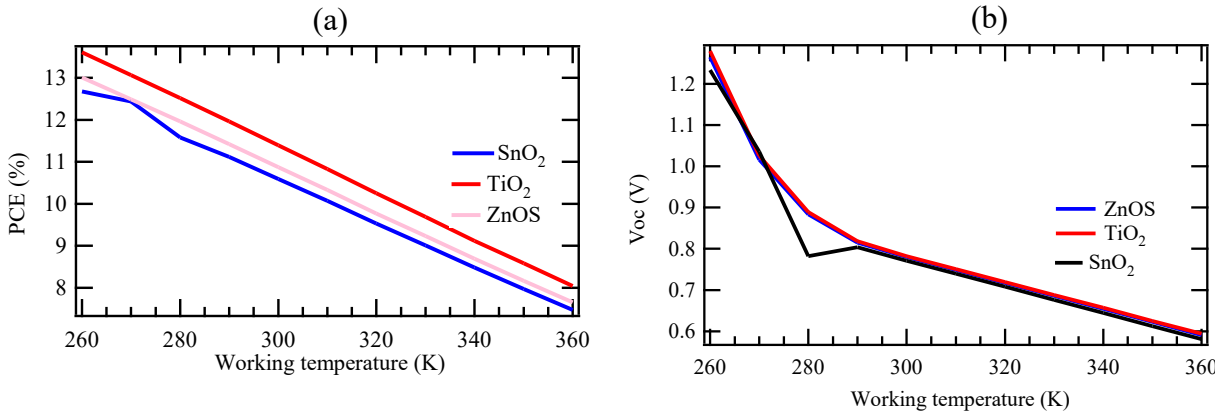

Figure 5.15: The effect of operating temperature on PCE (a) and (b) on V_{OC}

As shown in Figure 5.15(a), the PCE decreases with an increase in the working temperature of the solar cell, since higher temperatures result in increased thermal energy, which promotes the recombination of photogenerated holes and electrons. This performance also demonstrates that temperature-dependent characteristics, such as charge carrier mobility and energy levels, can significantly impact solar cell performance. Therefore, as temperature increases, the materials deteriorate, affecting the overall performance and stability. The optimal temperature for the N719 layer was selected as 260 K, yielding PCEs of 12.68%, 13.01%, and 13.61% for SnO_2, ZnOS, and

TiO_2 solar models, respectively. The decrease in open-circuit voltage with an increase in operating temperature is attributed to a rise in the reverse saturation current (J_0). Furthermore, the increase in thermal energy leads to high-energy electrons, which are more likely to recombine with holes at a higher rate. The optimum V_{oc} values of the models were 1.2334 V, 0.7777V, and 1.2796 V 12.68%, 13.01%, and 13.61% for SnO_2, ZnOS, and TiO_2 solar models, respectively.

As illustrated in Figure 5.16(a), Jsc did not change significantly with the increase in operating temperature (260 to 300 K) because the electrons had sufficient thermal energy, which overcame the barriers. Additionally, high temperature generates more electron-hole carriers, which increases the J_{sc}. Furthermore, FF improved as the operating temperature increased from 260 to 300 K, due to reduced charge recombination and enhanced mobility of electron-hole carriers (Abd Wahab et al., 2023), as shown in Figure 5.16(b). However, a further increase in temperature beyond 300 K will reduce the Rsh, enhance Rs, and put the cell device under strain while resulting in a drop in the FF (Bansal et al., 2023). Additionally, high temperature may also increase recombination rates, lowering the FF.

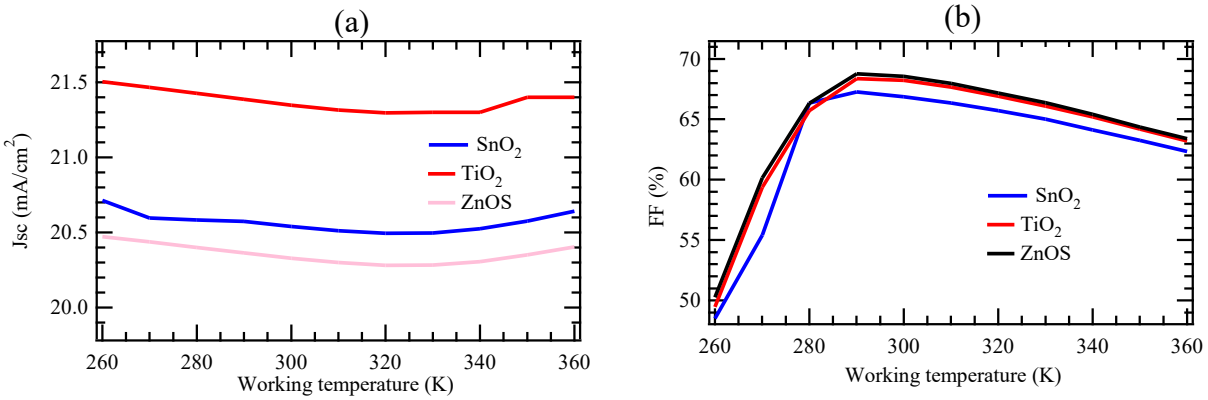

Figure 5.16: The effect of operating temperature on J_{sc} (a) and (b) on FF

5.3.2.3 Quantum efficiency and current-voltage characteristics

Quantum efficiency is another figure of merit that defines the ratio of the collected charge carriers to the number of incident photons (Bordovalos et al., 2023). The J-V and QE curves (cf. Figure 5.17) provide insights into the spectral response comparison of different ETLs in FTO/ETL/N719/CuSCN/Au solar cell configuration. Regions of high external quantum efficiency (EQE) values describe efficient photon-to-voltage conversion and usually correlate with higher

V_{OC} . Moreover, higher EQE values also correspond to higher J_{sc}, due to improved photocurrent generation. The higher EQE values also correspond to decreased recombination losses, thus enhancing the FF. Among the ETLs tested, SnO_2 and TiO_2 recorded quantum efficiencies exceeding 95% in the visible range, indicating minimum recombination and superior charge extraction. Accordingly, SnO_2, and TiO_2 ETLs recorded a high J_{sc} of 20.53 mA/cm^2.and 20.34 mA/cm^2, respectively. TiO_2-based solar cell configuration demonstrates a higher PCE of 11.39%, driven by a higher V_{OC} 0.781878 V, indicating good charge separation. However, its FF is slightly lower (68.24%) than that of ZnOS (68.56%), suggesting that charge collection and recombination are areas of concern in TiO_2-based ssDSSCs. The SnO_2-based solar cell configuration has the lowest FF of 66.73%, indicating that the device also faces charge extraction and recombination inefficiencies. Also, ZnOS has better performance with a quantum efficiency reaching 94% with J_{sc} approximately 20.33 mA/cm^2, making it a viable ETL alternative in DSSCs.

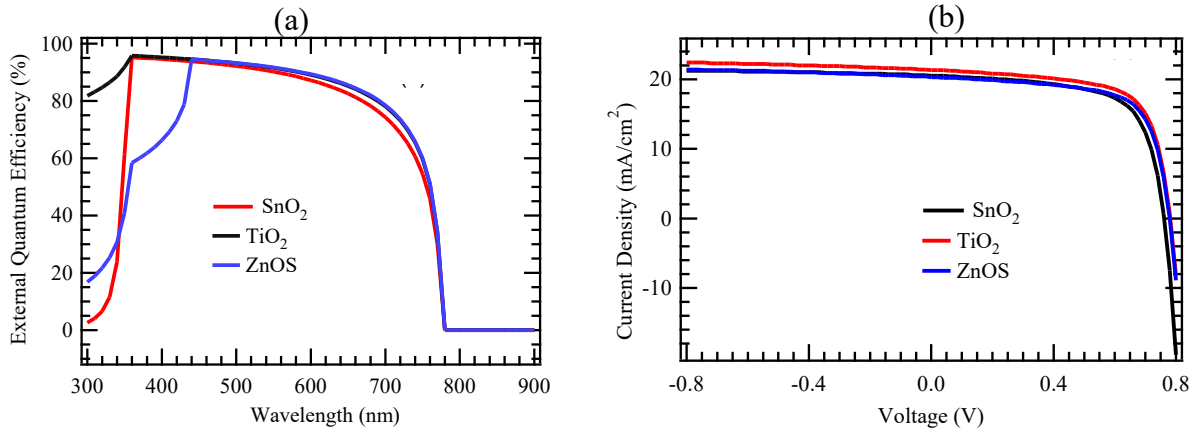

Figure 5.17: External quantum efficiency (a) and (b) current-voltage characteristics of the simulated solar cell configurations

5.3.2.4 Effect of absorber layer thickness

Research shows that absorber layer thickness impacts the FF by influencing charge transport and recombination processes (Noman et al., 2023). When the N719 layer is too thin, there will be insufficient light absorption, and the electron injection process will be negatively affected. Conversely, the thick N719 layer implies that the electrons will have to cover a longer distance before reaching the electrode, potentially increasing the recombination of charge carriers. Scientific reports have also shown that thicker photoactive layers increase charge recombination

due to longer carrier diffusion paths, thus having a detrimental effect on V_{OC} The thickness of the layer may also impact light absorption and electron injection because of possible internal reflections and light scattering, which decreases the J_{sc}.

On the other hand, the PCE depends on J_{sc}, FF, and V_{OC} and their specific effect may widely vary due to the materials used and the device architectures. The N719 layer thickness varied from 500 to 6000 nm to optimize the overall efficiency of the proposed devices. As shown in Figure 4.18, increasing the thickness to N719 leads to a sharp increase in J_{sc}, FF, PCE, and V_{OC} since a thicker N719 layer absorbs more incident photons, enhances charge generation, and improves carrier density. Accordingly, all the solar cell models attained their optimized performance when the N719 layer thickness was 1000 nm, and it did not show any significant effects on J_{sc}, FF, PCE, and V_{OC} when the N719 layer thickness was increased to 6000 nm, as illustrated in Figure 5.18 (a-d).

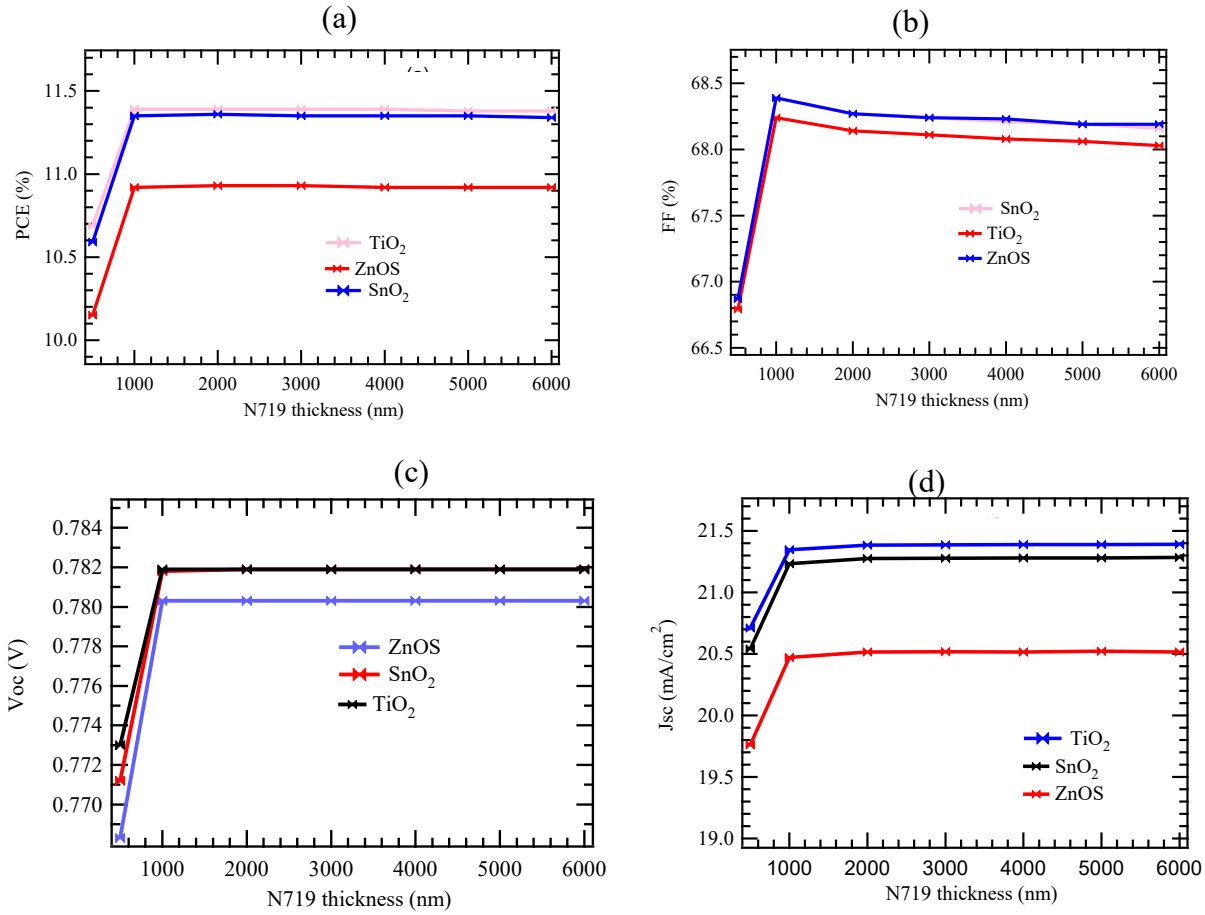

Figure 5.18: The effect of N719 layer thickness on (a) PCE, (b) FF, (c) V_{OC}, and (d) J_{sc}

5.3.2.5 Effect of defect density of the absorber layer

In a semiconductor, two parameters are directly linked to defect density. The first parameter is mobility, which is limited by the scattering of the mobile carriers at the defects. Secondly, non-radiative recombination is very sensitive to defects in the semiconductor. Defects (or impurities) in N719 dyes affect V_{OC}, J_{sc}, FF, and PCE by influencing charge transfer capabilities of the device. For instance, impurities can introduce charge recombination sites or energy levels that trap and recombine holes and electrons (charge carriers). This study theoretically investigated the effect of changing the defect density (N_t) of N719 dye from 1.0×10^{17} cm^{-3} to 9.0×10^{17} cm^{-3} on efficiency. The device performance would be enhanced due to lower defect densities and better charge extraction. Conversely, higher defect densities decrease solar cell performance due to more recombination losses. Similarly, in this study, the increase in defect densities increases the recombination rates, thus leading to a decrease in V_{OC} of the simulated solar cell models. For instance, as ascribed in Table 5.3, the V_{OC} of SnO_2-based solar cells dropped from 0.7712 V to 0.6473 V when defect densities were increased from 1.0×10^{17} cm^{-3} to 9.0×10^{17} cm^{-3}. Further to this, the increase in defect densities also resulted in a drop in J_{sc} (20.539496 to 13.566080 mA/cm^2, FF (66.87 to 48.11%), and PCE (10.59 to 4.22%).

These findings indicate that the sharp decline in PV characteristics of the devices is primarily attributed to enhanced non-radiative recombination within the N719 layer. Generally, the performance of solar models decreased when there were more recombination routes, traps, and defect sites as the defect density increased. Similarly, when the defect densities were varied in the same range, the PCE declined (11.39 to 5.09%), J_{sc} dropped (21.347345 to 14.311718 mA/cm^2), FF decreased from 68.24 to 53.58% and V_{OC} reduced from 0.7819 to 0.6606 V for the TiO_2 solar device. This photovoltaic behaviour was also similar to that of the ZnOS-based solar cell model. Accordingly, impurities or defects also alter the photo response and electron injection process. As such, the increase in defects hinders light absorption and affects electron injection into the semiconductor material (such as TiO_2, SnO_2, ZnOS), decreasing the J_{sc}. The presence of impurities also leads to a decrease in FF and efficiency. Thus, the defect concentration must be controlled to fabricate a highly efficient material.

Table 5.3: The effects of N719 material defect densities on ssDSSCs performance

N719 defect density (cm^{-3})	V_{OC} (V)			J_{sc} (mA/cm^2)			FF (%)			PCE (%)		
	SnO_2	TiO_2	ZnOS	SnO_2	TiO_2	ZnOS	SnO_2	TiO_2	ZnOS	SnO_2	TiO_2	ZnOS
1.0×10^{17}	0.7712	0.7819	0.7800	20.539496	21.347345	20.331279	66.87	68.24	66.56	10.59	11.39	10.87
2.0×10^{17}	0.7365	0.7465	0.7444	19.264801	19.884687	18.921872	62.33	64.89	65.07	8.84	9.63	9.17
3.0×10^{17}	0.7145	0.7248	0.7225	18.157702	18.727326	17.765744	59.03	62.49	62.50	7.66	8.48	8.02
4.0×10^{17}	0.6981	0.7088	0.7061	17.181791	17.753878	16.773881	54.42	60.54	60.39	6.77	7.62	7.15
5.0×10^{17}	0.6848	0.6961	0.6929	16.311205	16.908289	15.902037	54.27	58.89	58.60	6.06	6.93	6.46
6.0×10^{17}	0.6736	0.6854	0.6819	15.527015	16.158705	15.123310	52.42	57.41	57.05	5.48	6.36	5.88
7.0×10^{17}	0.6638	0.6761	0.6722	14.814996	15.484783	14.419722	50.78	56.09	55.66	4.99	5.87	5.40
8.0×10^{17}	0.6551	0.6678	0.6637	14.164211	14.872510	13.778497	49.38	54.93	54.44	4.58	5.46	4.98
9.0×10^{17}	0.6473	0.6606	0.6560	13.566080	14.311718	13.190143	48.11	53.85	53.31	4.22	5.09	4.61

5.3.2.6 Effect of metal contacts

Metal contact layers (MCLs) are essential in collecting electrons from the photosensitive layer. Materials such as copper (Cu), nickel (Ni), silver (Ag), iron (Fe), gold (Au), and platinum (Pt) with work functions of 4.53, 4.61, 4.74, 4.81, 5.1, and 5.65 were varied to explore the effect of MCLs on cell structure. The comparative data for these materials are illustrated in Table 5.4.

Table 5.4: The effect of back contact material on photovoltaic performance

Metal work function (Ev)	ETL material	V_{OC}	J_{sc} (mA/cm^2)	FF (%)	PCE (%)
Pt (5.65)	TiO_2	0.78	21.34737	68.24	11.39
	ZnOS	0.78	20.32897	68.56	10.87
	SnO_2	0.77	20.5395	66.88	10.59
Au (5.1)	TiO_2	0.78	21.34735	68.24	11.39
	ZnOS	0.78	20.32897	68.56	10.87
	SnO_2	0.77	20.5395	66.87	10.59
Fe (4.81)	TiO_2	0.78	21.33257	67.68	11.29
	ZnOS	0.78	20.31554	68.01	10.78
	SnO_2	0.77	20.52826	66.31	10.51
Ag (4.74)	TiO_2	0.78	21.25334	64.4	10.70
	ZnOS	0.78	20.24227	64.78	10.23
	SnO_2	0.77	20.46587	63.09	9.96
Ni (4.61)	TiO_2	0.78	20.94092	52.35	8.57
	ZnOS	0.78	19.95248	52.68	8.19
	SnO_2	0.77	20.19913	50.96	7.94
Cu (4.53)	TiO_2	0.78	20.69883	44.55	7.21
	ZnOS	0.77	19.72935	45.31	6.89
	SnO_2	0.78	19.97237	42.61	6.65

As observed in Table 5.4, MCLs can affect the overall cell performance in various ways. The PCE of the solar cell models with different ETLs showed reasonably good simulated performance when the work function is 5.1 eV (Au) and 5.65 eV. However, Pt is not viable for commercial use due

to its rarity and high costs. Simulated solar models with Ni (4.61 eV) exhibit moderate performance; however, the application of this material as a back contact material is hindered by surface oxidation. As ascribed in Table 5.4, FF is influenced by contact resistance and the function of the back contact. The metal work function impacts the energy-level alignment at the interface between the N719 layer and the ETL. The MCL with a well-matched function enhances the FF by increasing charge transport and reducing charge recombination. Secondly, the voltage decreases when there is higher contact resistance, increasing the FF. The simulated findings of the solar cell models utilizing various back contact materials show that the overall performance steadily increases with high work function metals ($\geq$ 5.0 eV) due to a superior energy level at the back contact. Furthermore, higher metal work functions also enhance charge extraction and reduce the kinetics of charge recombination. The choice of back contact material also affects the variation of the optical and reflectivity properties. It affects the light absorption in the N719 layer, whereby high reflectivity increases the amount of incident light and thus increases J_{sc}. Additionally, V_{OC} is primarily affected by the energy-level alignment between the electrolyte and the photosensitive layer. In some cases, MCLs with high metal work function create a barrier for electron injection, decreasing the V_{OC}. Contrastingly, an appropriate MCL may reduce charge recombination, thereby improving the V_{OC} For practical feasibility, high stability, and enhanced efficiency, Au was selected as the most appropriate MCL for the N719-based solar cell configuration.

5.3.2.7 Capacitance frequency measurement

The capacitance frequency (C-f) analysis provides a qualitative understanding of the behaviour of DSSCs with different layers. Nyquist plot analysis is a basic representation of electrochemical impedance spectroscopy (EIS) that helps understand the capacitive and resistive behaviour of solar cells. The impedance plot better explains recombination rates, capacitance, and resistive losses (Bhattarai et al., 2023). Here, the Y-axis (imaginary part) represents the geometric capacitance of the solar device, showing that carriers accumulate at the interface layers, while the X-axis (real part) represents the resistance due to recombination (Bhattarai et al., 2023). In Figure 5.19(b), it is evident that the highest value of the impedance (real part) is 497 ohm.cm^2 for the solar cell with ZnOS ETL, 472 ohm.cm^2 for the TiO_2-based cell, and 590 ohm.cm^2 for the SnO_2-based model. Specifically, TiO_2 has the smallest semi-circle, signifying lower impedance, improved charge mobility, smoother charge transfer, and improved interface properties than SnO_2 and ZnOS.

Notably, ZnOS and SnO_2 ETL-based structures exhibit larger semi-circles than TiO_2, indicating high resistance or impedance within the system due to increased charge transfer resistance and hindered charge transport kinetics (Ishraq et al., 2024). Each figure shows one semi-circle, and a reduction in radii exhibits a change in charge transport properties (Mortadi et al., 2024). The Nyquist plot (impedance versus real part) for the simulated solar models is quadratic, confirming the symmetric nature of current densities. Additionally, the radii of the Nyquist plots decrease with an increase in junction resistance or enhanced carrier mobility, as observed with thicker N719 dye.

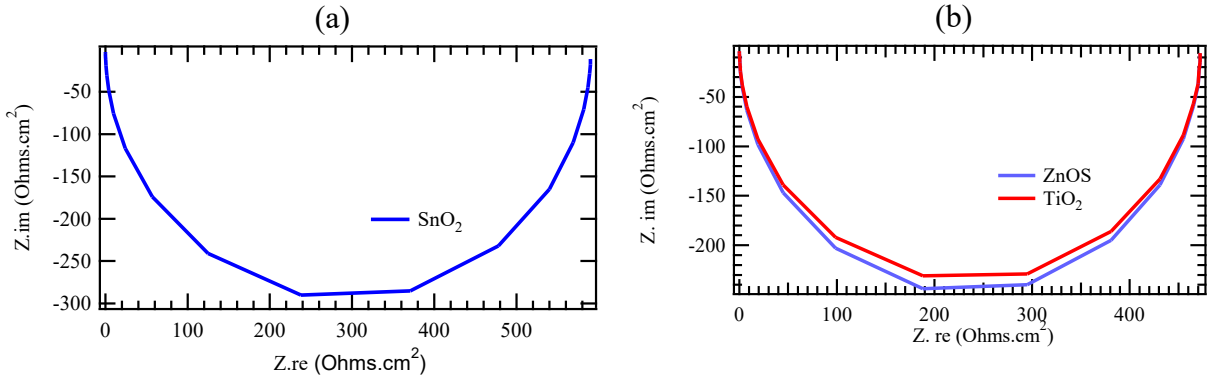

Figure 5.19: Nyquist plot for SnO_2 (a), (b) ZnOS and TiO_2 ETL-based structures

Mott-Schottky (M-S) theory has been used to assess the doping level and the difference between the functions of the electrode operation, specifically the built-in potential (V_{bi}) (Samiul Islam et al., 2021). While M-S theory was conventionally used in studying p-n junction properties, it has also been used in DSSCs. Equation 5.2 presents the M-S expression.

$$\frac{1}{C_s^2} = \frac{2}{q\varepsilon\varepsilon_0 N}\left(V - V_{bi} - \frac{kT}{e}\right) \qquad (5.2)$$

where q is the elementary charge, C_s is the space charge capacitance per unit area, ε is the electric constant, ε_0 is the permittivity of free space, V is the applied potential, V_{bi} is the built-in potential, T is the operating temperature, N is carrier density, and k is the Boltzmann constant.

Figure 5.20 (a) and (b) depict the variation in capacitance and M-S curve, respectively, when the voltage was varied from -0.8 to 0.8 V for the three devices, and the frequency was fixed at 1.0×10^6 Hertz (HZ). As demonstrated in Figure 5.20 (a), the capacitance increases with the applied voltage before reaching its maximum. In all simulated models, increasing the forward bias voltage improves capacitance in accordance with the M-S relationship. These findings also reflect

prior studies that have demonstrated that at low voltages, the current is lower than the saturation current, but it reaches the contact's saturation current when there is a spike in voltage. Figure 5.20 (b) shows M-S analysis that has been prominently used to determine the V_{bi}. It is evident that the M-S values are progressively lower when there is an increase in applied voltage (Figure 5.20b), which is reflected in prior studies. Typically, the x −axis in the M-S theory represents the $V_{bi,}$ while the slope of $1/c^2$ (V) gives the concentration of trapping centres. From this study, the V_{bi} = 0.98 V for TiO_2, 0.97 V for SnO_2, and 0.98 V for ZnOS and $1/c^2$ = 0. This shows that a small voltage is required to transfer electron-hole carriers across the interface in the simulated devices. That means the largest V_{oc} is produced when the device has a higher $V_{bi,}$ which is why TiO_2 gave the highest V_{oc} of 0.7818 V, while SnO_2 produced the lowest V_{oc} of 0.7712 V because of a comparatively lower V_{bi} of 0.97 V.

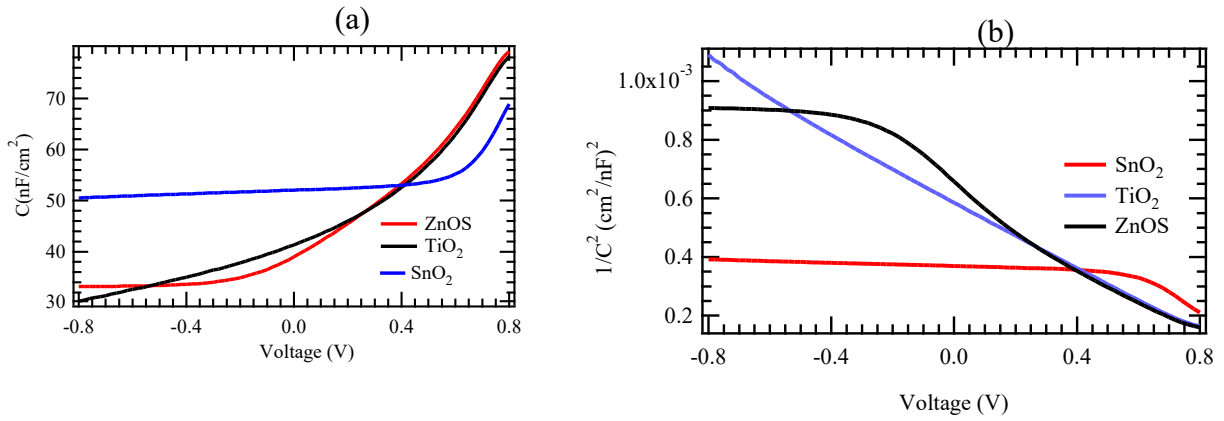

Figure 5.20: Capacitance-voltage relationship (a) and (b) Mott-Schottky curves of the simulated cell configurations

5.3.2.8 Band diagrams

An energy band diagram is crucial for understanding the overall performance of a solar cell. It describes the energy levels that electrons can occupy within the device, emphasizing the distinction between the CB and VB. The photosensitive layer absorbs the irradiating photons, stimulating the electrons from the VB to CB and generating an electric current. There are two types of band alignment: Type I (Cliff) and Type II (staggered), and each impacts charge flow across the interface. For instance, in Type I band alignment, the VB maximum of one layer is lower or aligned with the CB minimum of the other layer, thereby enhancing electron flow from higher to lower

energy levels. Figure 5.21 displays the DSSC energy band diagram of different device models at room temperature. As depicted in the Figure 5.21, the "cliffs" may be due to the non-uniformity of the band diagram or the suppression of charge recombination, thus enhancing photovoltaic performance (Meyer et al., 2025). The band gap value of more than or equal to 1.03 eV is sufficient for converting photons of irradiating light into energy. Therefore, the CB of the ETL needs to be positioned lower than or aligned with the CB of the active layer for efficient electron extraction. Figure 5.21 presents the energy level alignment of the studied N719 dye, FTO, CuSCN, and ETLs.

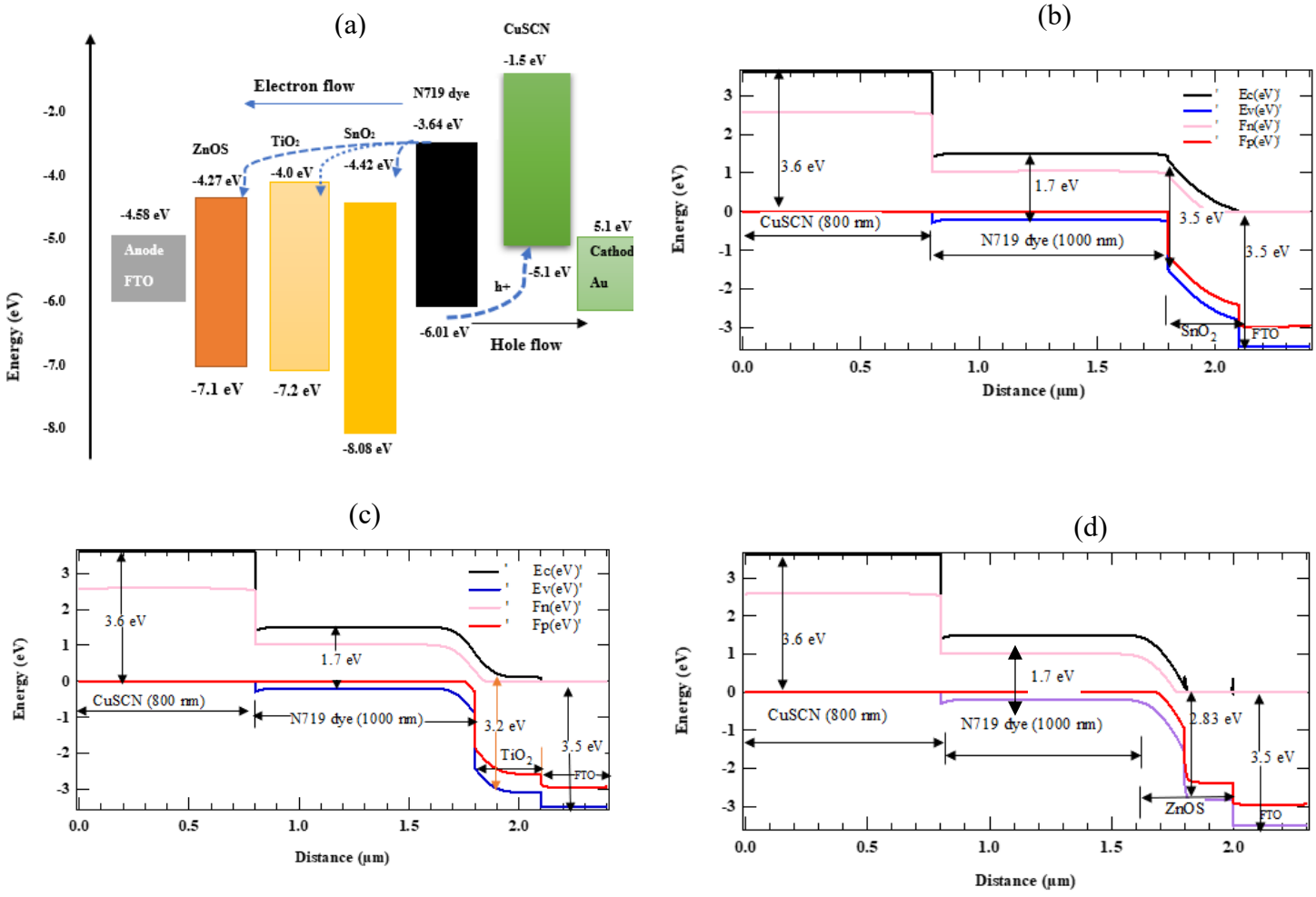

Figure 5.21: Energy diagram of N719 dye-based DSSCs with CuSCN as the HTL (a) representation of the simulated architecture, and (b) SnO_2, (c) TiO_2, and (d) ZnOS as ETLs

As illustrated in Figure 5.21 (b-d), the quasi-Fermi levels F_n and F_p of each device cohabit with the Ev and Ec, respectively. In all the optimized ETLs, the Ec and Fn exhibited harmonically

comparable behaviour, while Fp overlapped with Ev, an anticipated behaviour for typical n-type and p-type materials, respectively. The electron-hole carriers are being generated and separated effectively in the model solar cells. Electron extraction efficiency from the photoactive layer into the ETL is enhanced when the conduction band offset is negative, suggesting that the CB of the photoactive layer should have a higher energy than CB of the ETLs. Due to the similar nature of energy band diagrams, the performance of ZnOS, SnO_2, and TiO_2 photoanodes was similar. To achieve the optimal PV performance for the proposed structure, various ETL materials were employed, and their performance was compared. Table 5.5 compares the FF, efficiency, J_{sc}, and V_{OC}.

Table 5.5: The photovoltaic characteristics of solar cell models based on different ETLs

ETL material	**V_{OC} (V)**	**J_{sc} (mA/cm^2)**	**FF (%)**	**PCE (%)**
TiO_2	0.7819	21.34735	68.24	11.39
SnO_2	0.7712	20.5395	66.87	10.59
ZnOS	0.7800	20.32897	68.56	10.87

As depicted in Table 5.5, TiO_2 has the highest V_{OC} (0.7819 V), followed by ZnOS (0.7800 V), and SnO_2 achieves the lowest V_{OC} of 5.0.7712 V. ZnOS exhibits competitive light-harvesting capabilities with a J_{sc} of 20.32897 mA/cm^2, slightly lower than that of TiO_2 with 21.34735 mA/cm^2 and SnO_2 with 20.5395 mA/cm^2. However, ZnOS records the highest FF of 68.5% and a PCE of 10.87%. Notably, SnO_2 has the lowest FF and PCE of 66.87% and 10.89%, respectively, while TiO_2 has the highest PCE of 11.39%. This study highlights how the PV performance of a solar cell can be enhanced through the strategic combination of semiconducting layers. A deeper understanding of interfacial behaviour and charge transport mechanisms, ssDSSCs are poised to be competitive in terms of efficiencies and stabilities, capable of meeting energy demands more sustainably in the near future. Nonetheless, ZnOS stands out as a top ETL contender owing to its high V_{OC} and higher FF better electron mobility that enhances its light-harvesting capabilities. Additionally, ZnOS has material advantages – it is a zinc-based oxysulphide with a tunable

bandgap and inherits the properties of ZnO nanostructures, in addition to being attractive in terms of synthesis and scalability.

6. Conclusions

In this investigation, two computational techniques that combine DFT theory and numerical simulation were employed to optimize the solar cell parameters and study the optoelectronic and electronic properties of isolated layers. This article unveiled the optical, structural, and electronic properties of N719 dye-based solar cells using the SCAPS-1D and first principles DFT simulations. From the optimization, ZnOS ETL exhibited superior performance with TiO_2 compared to SnO_2 ETL. In this study, three models were selected to explore the effects of Rs, Rsh, absorber thickness, temperature, defect densities, and back contacts on their performance, as well as their corresponding QE, J-V, M-S, and capacitance characteristics. This theoretical investigation demonstrates that SnO_2 and ZnOS are alternative photoelectrodes to conventional TiO_2 in harnessing visible light. The configuration FTO/ZnOS/N719/CuSCN/Au achieves an outstanding PCE of 10.87%, complemented by remarkable values of FF and J_{sc}. The RDG and MEP computational tools validated the suitability of the proposed materials, particularly the bidentate bridging through the carboxylate groups. Furthermore, the MEP mapping of green (neutral), nucleophilic (blue), and electrophilic (red) regions reflected prior theoretical and experimental investigations, providing valuable insights into recombination and charge transfer behaviours. The device robustness is augmented by CuSCN, which is chemically stable, solution-processable, and highly transparent. The energy-level alignment highlights the crucial role of CuSCN in enhancing charge collection and transport efficiency. Accordingly, this study bridges the experimental and computational domains by providing a pathway for commercializing DSSC technologies. The ongoing research undertakings in the organic-inorganic photovoltaics field will transition to the seamless integration of optoelectronic simulations, DFT calculations, and advanced device characterization techniques, which will significantly impact the design of high-performance optoelectronics and device structures.

CHAPTER SIX
GENERAL DISCUSSION, CONCLUSIONS AND RECOMMENDATIONS

6.1 General discussion

6.1.1 Rationale of the study

In the near future, the commercialization of DSSCs still calls for thorough investigations of structure-property interplay and novel techniques for device configuration. Despite DSSCs becoming a popular research topic in the new generation solar cell technology, their transition from laboratory to commercial scale has been slowed by scientific challenges associated with intrinsic and extrinsic stabilities, interfacial recombination loss kinetics, and energy losses in dye regeneration kinetics. It has inspired the scientific community to leverage emerging theoretical approaches, such as theoretical and computational modelling, to complement experimental studies. The motivation behind this research was to utilize DFT and TD-DFT to investigate the HOMO-LUMO energy levels and electronic absorption properties. Accordingly, the DFT formalism methods were used to describe the electronic and optoelectronic properties of systems containing a few tens of atoms. The photovoltaic characteristics of solar cell models based on three ETLs-ZnOS, TiO_2, and SnO_2 were simulated using SCAPS-1D under STCs to obtain valuable data on how their parameters can be varied during the production workflow. The present study provided a springboard for state-of-the-art advances in developing robust N719 dye-based photoelectrodes. This study expanded the scope of DSSC research to achieve sustainable and secure energy for the future.

6.1.2 Findings of the study

Using the metallic layer for dye regeneration instead of the hole transport material is poised to simplify the fabrication process and reduce manufacturing costs. In this simulation study, SCAPS-1D was employed to investigate the impact of various parameters, including shunt and series resistance, electron affinity, working temperature, Schottky barriers, and conduction band offset, on the photovoltaic characteristics of the model solar cells. This study compared two ETLs, TiO_2 and ZnOS, and the solar cell model with ZnOS achieved a higher efficiency of 11.54%, while TiO_2

achieved an optimal efficiency of 10.22%. The ZnOS-based solar cell also achieved a fill factor (FF) of 62.71%, while that of the TiO_2-based solar cell was 63.58%. It was also noted that the ZnOS-based model has a higher V_{OC} and J_{sc} than the TiO_2-based model, which can deliver consistent photovoltaic performance across varying conditions. This study demonstrated that ZnOS is a suitable alternative to TiO_2, which is abundant in nature, cheap, and non-toxic. The study also reported that the electronic properties of ZnOS can be optimized by tuning its bandgap. Furthermore, the findings of this study serve as a pathfinder in the development and advancement of solar cell technologies, aiming to reduce dependence on non-renewable energy sources and address global energy challenges.

The solar cell configuration FTO/ZnOS/N719 dye/CuSCN/Au achieves an optimal PCE of 10.87% short circuit current (J_{sc}) of 20.32897 mA/cm^2, fill factor (FF) of 68.56% and open circuit voltage. (V_{OC}) of 0.7800 V. The computational studies of reduced density gradient (RDG) and molecular electrostatic potential (MEP) agree with earlier studies on statistical physics that N719 dye chemically bonds with photoelectrodes via two carboxylic groups of a bidentate bridging configuration. The HOMO-LUMO gap of the magneli phase of Ti_5O_8 was reported to decrease by multiple eV due to the absence of an O atom compared to the conventional TiO_2 structure. These findings strongly correlate with other publications that report HOMO and LUMO primarily localize on the Ti atoms in TiO_{2n-2}. The HOMO shifts from an O 2p-orbital to a Ti 3d-orbital; when there are increased O vacancies, the unoccupied and occupied orbitals shift towards the Fermi level such that all these orbitals become closer in energy in the CB. The study reported the calculated HOMO and LUMO energies as -5.85 eV and -3.82 eV, respectively. The computational calculation overestimates the HOMO of CuSCN by ~ 0.5 eV because the B3LYP method does not consider sufficient electron correlation in predicting FMOs energies. The HOMO-LUMO energy gap of ZnOS showed a greater discrepancy from the experimental values due to the underestimation of the exchange-correlation function. The energy gap computed using the B3LYP/LanL2DZ of SnO_2 was 4.42 eV, consistent with prior studies that have reported up to 4.5 eV, allowing it to have high transmittance in the visible region. The DFT analysis of N719 dye shows that the HOMO and LUMO are localized over the central Ru atom because it is coordinated to phenyl pyridine and bipyridine ligands. The RDG and MEP analysis of N719 dye suggests that the carboxylate ion group of N719 dye bind to ZnOS or TiO_2 through bidentate bridging and bidentate bridging

linkages at all stages of adsorption. The DoS analysis of the optimized structures confirmed the density distribution around the HOMO-LUMO and trajectories of charge transfer. The UV-Vis spectroscopy of SnO_2 exhibits a strong absorption peak at approximately 300 nm. However, the UV-Vis spectra of N719 dye, ZnOS, CuSCN, and TiO_2 were not reported because they did not reach acceptable limits due to the computational limitations of B3LYP/LanL2DZ methods.

The study also found that Rsh in solar cells is due to reverse saturation and the active junction, which are detrimental to solar cell performance. Similarly, solar cell performance increases when the right Rsh balance and working temperature are achieved. In the three optimized solar cell models, TiO_2 achieves an efficiency of 11.39%, while the SnO_2-based solar cell models achieve efficiencies of 10.59% and 10.87%, respectively. From this theoretical optimization study, ZnOS stands out as a top ETL contender due to its relatively higher FF, Jsc, and PCE, which enhance its light-harvesting capabilities. Also, ZnOS has a competitive V_{OC} enhancing its optoelectronic properties for solar energy applications.

6.2 Conclusions

This study optimized the optoelectronic properties of ETLs for DSSCs using the SCAPS-1D program. Besides the conventional TiO_2 ETL, other photoanodes – ZnOS and SnO_2 were assessed as potential materials to replace TiO_2 in solar cell fabrication. The results of this study showed that:

i. The optimized optoelectronic properties of various ETL shows that ZnOS is a strong candidate for advancing DSSC technology owing to its tunable bandgap properties, cost advantages, and environmental sustainability.
ii. N719 dye pairs with ZnOS with remarkable photovoltaic characteristics, including a PCE of 14.83%, high V_{OC} and J_{sc}, supporting its suitability for high-efficiency DSSCs configuration.
iii. Theoretical studies using SCAPS-1D and DFT offer helpful insights into studying the charge-transfer dynamics and the interactions between the photoanodes and the N719 dye.
iv. The design rationale of the proposed solar cell configuration is supported by the molecular-level bonding analysis that shows how N719 dye bonds strongly with the photoanodes through the carboxylic groups.

6.3 Recommendations

This study thoroughly investigates the potential of DSSCs in advancing the sustainability agenda, paving the way for a net-zero carbon emissions roadmap. It is well-established that solar energy can be the cheapest energy source in the sunniest locations on earth. This work reaffirms the role of solar energy technologies in solving challenges associated with using finite energy sources and the worrying trends of climate change. However, this research has the following recommendations;

i. Experimental investigations are needed to validate the theoretical predictions from SCAPS-1D and DFT calculations, focusing on optimizing the bandgap of ZnOS material.
ii. Further research needs to be conducted on alternative ETLs and dyes to enhance the cost-effectiveness and efficiency of DSSCs.
iii. Optimizing the device parameters and quantum efficiency of DSSCs can potentially deliver PCE beyond those of state-of-the-art single junctions and perovskite solar cells. Today, their performance is limited by large deficits in PCE, FF, V_{OC}, and J_{sc}. As DSSCs stride towards commercialization, there is a need to assess the degradation mechanisms, long-term stability, and practical scalability of ZnOS-based devices under varied environmental conditions.
iv. Integration of advanced characterization techniques such as electrochemical impedance spectroscopy and time-resolved photoluminescence are necessary to deepen understanding on optoelectronic behaviour of potential ETLs, thus, guiding the design of high-efficiency solar cell configurations.

6.4 Suggestions for further research

This study has provided valuable insights into the optimization of various ETLs for DSSCs using computational tools. Zinc oxysulphide (ZnOS) has been identified as a promising ETL, but several gaps remain that warrant further theoretical and experimental studies:

i. In the present study, the UV-Vis spectra for N719 dye, ZnOS, CuSCN, and TiO_2 were not reported due to computational limitations. Thus, there is a need for experimental spectroscopy to refine theoretical models and validate absorption profiles of these molecules.

ii. Future theoretical research requires experimental corroboration, particularly in synthesizing ZnOS-based DSSCs and characterizing their real-world performance in outdoor conditions.

iii. Future studies should expand beyond the conventional ETLs and N719 dye to explore novel materials with superior charge-transfer efficiencies and high light absorption capabilities, to improve device stability and performance.

iv. Studies on the environmental resilience of the champion ETL presented in this study will be critical in transitioning ZnOS-based DSSCs from laboratory scale to industrial scale.

REFERENCES

Abate, A., Leijtens, T., Pathak, S., Teuscher, J., Avolio, R., Errico, M. E., Kirkpatrik, J., Ball, J. M., Docampo, P., & McPherson, I. (2013). Lithium salts as "redox active" p-type dopants for organic semiconductors and their impact in solid-state dye-sensitized solar cells. *Physical Chemistry Chemical Physics*, *15*(7), 2572-2579. https://doi.org/10.1039/c2cp44397j

Abd Wahab, N. Z., Abdulhameed, A., Ismail, A. G., Ramli, M. M., Sidek, R. M., Shafie, S., & Mohtar, M. N. (2023). Charge Carrier Mobility of Organic Thin Film Transistor: Intrinsic and Extrinsic Influencing Factors Based on Organic Semiconducting Materials. *ECS Journal of Solid State Science and Technology*, *12*(4), 044002. https://doi.org/10.1149/2162-8777/acc75c

Abdullah, A. S., Ahmad, F., Ibrahim, M. H. I., & Ibrahim, M. H. (2024). A numerical simulation of novel solid-state dye-sensitized solar cell based on kesterite as the electrolyte. *Results in Optics*, *1*(1), 100625. https://doi.org/10.1016/j.rio.2024.100625

Abrol, S. A., Bhargava, C., & Sharma, R. (2020). Selection of Glass Substrates to be used as Electrodes in Dye-Sensitized Solar Cells. In *Smart Nanotechnology with Applications* (pp. 145-151). CRC Press. https://doi.org/10.1201/9781003097532-10

Abusaif, M. S., Fathy, M., Abu-Saied, M., Elhenawy, A. A., Kashyout, A., Selim, M. R., & Ammar, Y. A. (2021). New carbazole-based organic dyes with different acceptors for dye-sensitized solar cells: Synthesis, characterization, dssc fabrications and density functional theory studies. *Journal of Molecular Structure*, *1225*(1), 129297. https://doi.org/10.1016/j.molstruc.2020.129297

Agarwala, P., & Kabra, D. (2017). A review on triphenylamine (TPA) based organic hole transport materials (HTMs) for dye sensitized solar cells (DSSCs) and perovskite solar cells (PSCs): evolution and molecular engineering. *Journal of Materials Chemistry A*, *5*(4), 1348-1373. https://doi.org/10.1039/c6ta08449d

Aghazada, S., & Nazeeruddin, M. K. (2018). Ruthenium complexes as sensitizers in dye-sensitized solar cells. *Inorganics*, *6*(2), 52. https://doi.org/10.3390/inorganics6020052

Agwa, A. M., El-Fergany, A. A., & Maksoud, H. A. (2020). Electrical characterization of photovoltaic modules using farmland fertility optimizer. *Energy Conversion and Management*, *217*(1), 112990. https://doi.org/10.1016/j.enconman.2020.112990

Ahmed, S., Jannat, F., Khan, M. A. K., & Alim, M. A. (2021). Numerical development of eco-friendly Cs_2TiBr_6 based perovskite solar cell with all-inorganic charge transport materials via SCAPS-1D. *Optik*, *225*(1), 165765. https://doi.org/10.1016/j.ijleo.2020.165765

Ahmed, S. F., & Khalid, M. (2019). Simulation of CIGS based solar cells with SnO_2 window layer using SCAPS-1D. 2019 International Conference on Power Electronics, Control and Automation (ICPECA), *1*(1), 1-4. https://doi.org/10.1109/icpeca47973.2019.8975461

Akin, S., & Sonmezoglu, S. (2018). Metal oxide nanoparticles as electron transport layer for highly efficient dye-sensitized solar cells. In *Emerging materials for energy conversion and storage* (pp. 39-79). Elsevier. https://doi.org/10.1016/b978-0-12-813794-9.00002-8

Al-Ashouri, A., Köhnen, E., Li, B., Magomedov, A., Hempel, H., Caprioglio, P., Márquez, J. A., Vilches, A. B. M., Kasparavicius, E., & Smith, J. A. (2020). Monolithic perovskite/silicon tandem solar cell with> 29% efficiency by enhanced hole extraction. *Science*, *370*(6522), 1300-1309. https://doi.org/10.1126/science.abd4016

Almeida, M. A. (2020). Recent Advances in Solar Cells. In *Solar Cells* (pp. 79-122). Springer. https://doi.org/10.1007/978-3-030-36354-3_4

Almora, O., Aranda, C., Mas-Marzá, E., & Garcia-Belmonte, G. (2016). On Mott-Schottky analysis interpretation of capacitance measurements in organometal perovskite solar cells. *Applied Physics Letters*, *109*(17), 173903. https://doi.org/10.1063/1.4966127

Alnakeeb, A., Fadda, A. A., Ismail, M. A., & Elmorsy, M. R. (2022). Efficient co-sensitization of novel trimethoxybenzene-based dyes with N-719 for highly efficient dye-sensitized solar cells. *Optical Materials*, *128*(1), 112344. https://doi.org/10.1016/j.optmat.2022.112344

Altamura, G., Grenet, L., Roger, C., Roux, F., Reita, V., Fillon, R., Fournier, H., Perraud, S., & Mariette, H. (2014). Alternative back contacts in kesterite $Cu_2ZnSn(S_{1-x}Se_x)_4$ thin film solar cells. *Journal of Renewable and Sustainable Energy*, *6*(1), 011401. https://doi.org/10.1063/1.4831781

AlZoubi, T., Moghrabi, A., Moustafa, M., & Yasin, S. (2021). Efficiency boost of CZTS solar cells based on double-absorber architecture: Device modeling and analysis. *Solar Energy*, *225*(1), 44-52. https://doi.org/10.1016/j.solener.2021.07.012

Ameri, M., Eddine, D. S., Sebane, M., Boudia, K., Al-Douri, Y., Bentouaf, A., Hachemane, D., Bouhafs, B., & Touia, A. (2013). First Principles Study of Structural and Electronic Properties of O_xS_{1-x} Zn Ternary Alloy. *Materials Sciences and Applications, 4*(1), 63-69. https://doi.org/10.4236/msa.2013.41008

Amin, N., Chelvanathan, P., Hossain, M. I., & Sopian, K. (2012). Numerical modelling of ultra thin Cu (In, Ga) Se_2 solar cells. *Energy Procedia*, *15*(1), 291-298. https://doi.org/10.1016/j.egypro.2012.02.034

Ammar, A. M., Mohamed, H. S., Yousef, M. M., Abdel-Hafez, G. M., Hassanien, A. S., & Khalil, A. S. (2019). Dye-sensitized solar cells (DSSCs) based on extracted natural dyes. *Journal of Nanomaterials*, *2019*(1), 1-10. https://doi.org/10.1155/2019/1867271

Aslam, A., Mehmood, U., Arshad, M. H., Ishfaq, A., Zaheer, J., Khan, A. U. H., & Sufyan, M. (2020). Dye-sensitized solar cells (DSSCs) as a potential photovoltaic technology for the self-powered internet of things (IoTs) applications. *Solar Energy*, *207*(1), 874-892. https://doi.org/10.1016/j.solener.2020.07.029

Aulakh, R. K., Sandhu, S., Kumar, S., Mahajan, A., Bedi, R., & Kumar, S. (2015). Designing and synthesis of imidazole based hole transporting material for solid state dye sensitized solar cells. *Synthetic Metals*, *205*(1), 92-97. https://doi.org/10.1016/j.synthmet.2015.03.030

Awsha, A. A., Alazoumi, S., & Elhub, B. (2021). A Review on the development of TiO_2 photoanode for Solar Applications. *Albahit journal of applied sciences*, *2*(2), 9-16. https://albahitjas.com.ly/index.php/albahit/article/view/27

Ayodhya, D. (2023). Semiconductors-based Z-scheme materials for photoelectrochemical water splitting: A review. *Electrochimica Acta*, *448*(1), 142118. https://doi.org/10.1016/j.electacta.2023.142118

Aziz, S. G., Osman, O. I., Elroby, S. A., Hassan, W. M., Jedidi, A., & Hilal, R. H. (2018). Proton-coupled electron transfer in dye-sensitized solar cells: a theoretical perspective. *Structural Chemistry*, *29*(4), 983-997. https://doi.org/10.1007/s11224-018-1080-x

Azizi, T., Toujeni, H., Karoui, M. B., & Gharbi, R. (2019). A comprehensive device modeling of solid state dye sensitized solar cell with SCAPS-1D. 2019 19th International Conference on Sciences and Techniques of Automatic Control and Computer Engineering (STA), *1*(1), 336-340. https://doi.org/10.1109/sta.2019.8717282

Azri, F., Meftah, A., Sengouga, N., & Meftah, A. (2019). Electron and hole transport layers optimization by numerical simulation of a perovskite solar cell. *Solar Energy*, *181*(1), 372-378. https://doi.org/10.1016/j.solener.2019.02.017

Badola, S., Shah, J., Gaur, A., Khasa, S., Rawal, D., Mandal, T., Srivastava, A., & Kotnala, R. (2023). Strategic enhancement of oxygen defects in ZnO from ZnS for water splitting to generate green electricity by hydroelectric cell. *Applied Materials Today*, *34*(1), 101904. https://doi.org/10.1016/j.apmt.2023.101904

Bansal, N. K., Porwal, S., Dixit, H., Kumar, D., & Singh, T. (2023). A theoretical study to investigate the impact of bilayer interfacial modification in perovskite solar cell. *Energy Technology*, *11*(4), 2201395. https://doi.org/10.1002/ente.202201395

Bansal, S., & Aryal, P. (2016). Evaluation of new materials for electron and hole transport layers in perovskite-based solar cells through SCAPS-1D simulations. 2016 IEEE 43rd Photovoltaic Specialists Conference (PVSC), *1*(1), 0747-0750. https://doi.org/10.1109/pvsc.2016.7749702

Barichello, J., Mariani, P., Vesce, L., Spadaro, D., Citro, I., Matteocci, F., Bartolotta, A., Di Carlo, A., & Calogero, G. (2024). Bifacial dye-sensitized solar cells for indoor and outdoor renewable energy-based application. *Journal of Materials Chemistry C*, *12*(7), 2317-2349. https://doi.org/10.1039/d3tc03220e

Barman, B., Deka, R., Bora, S. R., & Kalita, D. J. (2025). Tuning Optical and Charge Transfer Properties of Tetrathiafulvalene-Based DA′-π-A Dyes for DSSCs: A DFT and TDDFT Investigation. *Nanoscale*. https://doi.org/10.1039/d5nr00537j

Barnes, P. R., Miettunen, K., Li, X., Anderson, A. Y., Bessho, T., Gratzel, M., & O'Regan, B. C. (2013). Interpretation of optoelectronic transient and charge extraction measurements in dye-sensitized solar cells. *Advanced Materials*, *25*(13), 1881-1922. https://doi.org/10.1002/adma.201201372

Barrera, M., Crivelli, I., & Loeb, B. (2016). On the performance of ruthenium dyes in dye sensitized solar cells: a free cluster approach based on theoretical indexes. *Journal of molecular modeling*, *22*(5), 118. https://doi.org/10.1007/s00894-016-2984-2

Bartesaghi, D., del Carmen Pérez, I., Kniepert, J., Roland, S., Turbiez, M., Neher, D., & Koster, L. J. A. (2015). Competition between recombination and extraction of free charges determines the fill factor of organic solar cells. *Nature communications*, *6*(1), 1-10. https://doi.org/10.1038/ncomms8083

Basak, A., & Singh, U. P. (2021). Numerical modelling and analysis of earth abundant Sb2S3 and Sb2Se3 based solar cells using SCAPS-1D. *Solar Energy Materials and Solar Cells*, *230*(1), 111184. https://doi.org/10.1016/j.solmat.2021.111184

Baumeler, T., Saleh, A. A., Wani, T. A., Huang, S., Jia, X., Bai, X., Abdi-Jalebi, M., Arora, N., Grätzel, M., & Dar, M. I. (2023). Champion Device Architectures for Low-Cost and Stable Single-Junction Perovskite Solar Cells. *ACS Materials Letters*, *5*(9), 2408-2421. https://doi.org/10.1021/acsmaterialslett.3c00337

Bella, F., Gerbaldi, C., Barolo, C., & Grätzel, M. (2015). Aqueous dye-sensitized solar cells. *Chemical Society Reviews*, *44*(11), 3431-3473. https://doi.org/10.1039/c4cs00456f

Benazzi, E., Mallows, J., Summers, G. H., Black, F. A., & Gibson, E. A. (2019). Developing photocathode materials for p-type dye-sensitized solar cells. *Journal of Materials Chemistry C*, *7*(34), 10409-10445. https://doi.org/10.1039/c9tc01822k

Bencherif, H., Dehimi, L., Mahsar, N., Kouriche, E., & Pezzimenti, F. (2022). Modeling and optimization of CZTS kesterite solar cells using TiO_2 as efficient electron transport layer. *Materials Science and Engineering: B*, *276*, 115574. https://doi.org/10.1016/j.mseb.2021.115574

Berger, O. (2022). Understanding the fundamentals of TiO_2 surfaces. Part I. The influence of defect states on the correlation between crystallographic structure, electronic structure and physical properties of single-crystal surfaces. *Surface Engineering*, *38*(2), 91-149. https://doi.org/10.1080/02670844.2022.2063482

Bhargav, R., Chaudhary, N., Rathi, S., Shahjad, Bhardwaj, D., Gupta, S., & Patra, A. (2019). Copper bromide as an efficient solution-processable hole transport layer for organic solar cells: effect of solvents. *ACS omega*, *4*(3), 6028-6034. https://doi.org/10.1021/acsomega.8b03038

Bhattarai, S., Pandey, R., Madan, J., Tayeng, S., Kalita, P., Ansari, M. Z., Farhat, L. B., Amami, M., & Hossain, M. K. (2023). Comparative study of distinct halide composites for highly efficient perovskite solar cells using a SCAPS-1D simulator. *RSC advances*, *13*(38), 26851-26860. https://doi.org/10.1039/d3ra04134d

Bhattarai, S., Sharma, A., & Das, T. (2020). Efficiency enhancement of perovskite solar cell by using doubly carrier transport layers with a distinct bandgap of $MAPbI_3$ active layer. *Optik*, *224*(1), 165430. https://doi.org/10.1016/j.ijleo.2020.165430

Bhavsar, K., & Lapsiwala, P. (2021). Numerical simulation of perovskite solar cell with different material as electron transport layer using SCAPS-1D software. *Semiconductor Physics, Quantum Electronics & Optoelectronics*, *24*(3), 341-347. https://doi.org/10.15407/spqeo24.03.341

Biswas, S., & Kim, H. (2020). Solar cells for indoor applications: Progress and development. *Polymers*, *12*(6), 1338. https://doi.org/10.3390/polym12061338

Biswas, S., Lee, S. W., Lee, Y., Choi, H.-J., Chen, J., Yang, X., Du, Y., Falcone, N., Barros, N. R. d., & Lee, S.-M. (2024). Emerging energy harvesters in flexible bioelectronics: From wearable devices to biomedical innovations. *Small Science*, *4*(3), 2300148. https://doi.org/10.1002/smsc.202300148

Bordovalos, A., Subedi, B., Chen, L., Song, Z., Yan, Y., & Podraza, N. J. (2023). Implications of Electron Transport Layer and Back Metal Contact Variations in Tin–Lead Perovskite Solar Cells Assessed by Spectroscopic Ellipsometry and External Quantum Efficiency. *ACS*

Applied Materials & Interfaces, *15*(15), 19730-19740. https://doi.org/10.1021/acsami.3c01849

Boro, B., Gogoi, B., Rajbongshi, B., & Ramchiary, A. (2018). Nano-structured TiO_2/ZnO nanocomposite for dye-sensitized solar cells application: A review. *Renewable and Sustainable Energy Reviews*, *81*(1), 2264-2270. https://doi.org/10.1016/j.rser.2017.06.035

Bouzidi, A., Jilani, W., Yahia, I., & Zahran, H. (2020). Impedance spectroscopy of monocrystalline silicon solar cells for photosensor applications: Highly sensitive device. *Physica B: Condensed Matter*, *596*(1), 412375. https://doi.org/10.1016/j.physb.2020.412375

Bradha, M., Balakrishnan, N., Suvitha, A., Arumanayagam, T., Rekha, M., Vivek, P., Ajay, P., Sangeetha, V., & Steephen, A. (2021). Experimental, computational analysis of Butein and Lanceoletin for natural dye-sensitized solar cells and stabilizing efficiency by IoT. *Environment, Development and Sustainability*, *24*(6), 8807-8822. https://doi.org/10.1007/s10668-021-01810-5

Burgelman, M., Decock, K., Khelifi, S., & Abass, A. (2013). Advanced electrical simulation of thin film solar cells. *Thin Solid Films*, *535*(1), 296-301. https://doi.org/10.1016/j.tsf.2012.10.032

Burgelman, M., Verschraegen, J., Degrave, S., & Nollet, P. (2004). Modeling thin-film PV devices. *Progress in Photovoltaics: Research and Applications*, *12*(2-3), 143-153. https://doi.org/10.1002/pip.524

Burschka, J., Dualeh, A., Kessler, F., Baranoff, E., Cevey-Ha, N.-L., Yi, C., Nazeeruddin, M. K., & Grätzel, M. (2011). Tris (2-(1 H-pyrazol-1-yl) pyridine) cobalt (III) as p-type dopant for organic semiconductors and its application in highly efficient solid-state dye-sensitized solar cells. *Journal of the American Chemical Society*, *133*(45), 18042-18045. https://doi.org/10.1021/ja207367t

Butt, M. K., Yaseen, M., Bhatti, I. A., Iqbal, J., Murtaza, A., Iqbal, M., mana AL-Anazy, M., Alhossainy, M., & Laref, A. (2020). A DFT study of structural, magnetic, elastic and optoelectronic properties of lanthanide based $XAlO_3$ (X= Nd, Gd) compounds. *Journal of*

Materials Research and Technology, *9*(6), 16488-16496. https://doi.org/10.1016/j.jmrt.2020.11.055

Cahen, D., Hodes, G., Graetzel, M., Guillemoles, J. F., & Riess, I. (2000). Nature of photovoltaic action in dye-sensitized solar cells. *The Journal of Physical Chemistry B*, *104*(9), 2053-2059. https://doi.org/10.1021/jp993187t

Cai, H., Li, J., Xu, X., Tang, H., Luo, J., Binnemans, K., Fransaer, J., & De Vos, D. E. (2017). Nanostructured composites of one-dimensional TiO_2 and reduced graphene oxide for efficient dye-sensitized solar cells. *Journal of Alloys and Compounds*, *697*(1), 132-137. https://doi.org/10.1016/j.jallcom.2016.10.189

Cai, W., Zhang, Z., Jin, Y., Lv, Y., Wang, L., Chen, K., & Zhou, X. (2019). Application of TiO_2 hollow microspheres incorporated with up-conversion $NaYF_4$: Yb^{3+}, Er^{3+} nanoparticles and commercial available carbon counter electrodes in dye-sensitized solar cells. *Solar Energy*, *188*(1), 441-449. https://doi.org/10.1016/j.solener.2019.05.081

Çakar, S., Soykan, C., & Özacar, M. (2021). Polyacrylonitrile/polyindole and poly (glycidyl methacrylate)/polyindole composites based quasi solid electrolyte materials for dye sensitized solar cells. *Solar Energy*, *215*(1), 157-168. https://doi.org/10.1016/j.solener.2020.12.039

Calio, L., Kazim, S., Graetzel, M., & Ahmad, S. (2016). Hole-transport materials for perovskite solar cells. *Angewandte Chemie International Edition*, *55*(47), 14522-14545. https://doi.org/10.1002/anie.201601757

Caruso, G., Colantonio, E., & Gattone, S. A. (2020). Relationships between Renewable Energy Consumption, Social Factors, and Health: A Panel Vector Auto Regression Analysis of a Cluster of 12 EU Countries. *Sustainability*, *12*(7), 2915. https://doi.org/10.3390/su12072915

Castillo-Robles, J. A., Rocha-Rangel, E., Ramírez-de-León, J. A., Caballero-Rico, F. C., & Armendáriz-Mireles, E. N. (2021). Advances on Dye-Sensitized Solar Cells (DSSCs) Nanostructures and Natural Colorants: A Review. *Journal of Composites Science*, *5*(11), 288. https://doi.org/10.3390/jcs5110288

Chaitra, U., Ali, A. M., Mahesha, M., Kompa, A., Kekuda, D., & Rao, K. M. (2021). Property evaluation of spin coated Al-doped ZnO thin films and Au/AZO/FTO Schottky diodes. *Superlattices and Microstructures*, *155*(1), 106903. https://doi.org/10.1016/j.spmi.2021.106903

Chartrand, D., & Hanan, G. S. (2014). Optoelectronic Properties and Structural Effects of the Incremental Addition of Pyridyl Moieties on a Rhodium Dimer. *The Journal of Physical Chemistry A*, *118*(45), 10340-10352. https://doi.org/10.1021/jp502243c

Chaubey, A., Scudino, S., Khoshkhoo, M. S., Prashanth, K., Mukhopadhyay, N., Mishra, B., & Eckert, J. (2014). High-strength ultrafine grain Mg–7.4% Al alloy synthesized by consolidation of mechanically alloyed powders. *Journal of Alloys and Compounds*, *610*(1), 456-461. https://doi.org/10.1016/j.jallcom.2014.05.029

Chen, D., Kim, M., Stefani, B. V., Hallam, B. J., Abbott, M. D., Chan, C. E., Chen, R., Payne, D. N., Nampalli, N., & Ciesla, A. (2017). Evidence of an identical firing-activated carrier-induced defect in monocrystalline and multicrystalline silicon. *Solar Energy Materials and Solar Cells*, *172*(1), 293-300. https://doi.org/10.1016/j.solmat.2017.08.003

Chen, F., Cai, Z., Huang, Y., Luo, W., & Chen, J. (2013). Synthesis and characterization of copolymer grafted magnetic nanoparticles via surface-initiated nitroxide-mediated radical polymerization. *Polymer Engineering & Science*, *53*(5), 956-962. https://doi.org/10.1002/pen.23343

Chen, J.-G., Wei, H.-Y., & Ho, K.-C. (2007). Using modified poly (3, 4-ethylene dioxythiophene): Poly (styrene sulfonate) film as a counter electrode in dye-sensitized solar cells. *Solar Energy Materials and Solar Cells*, *91*(15-16), 1472-1477. https://doi.org/10.1016/j.solmat.2007.03.024

Chen, L., Chen, W.-L., Wang, X.-L., Li, Y.-G., Su, Z.-M., & Wang, E.-B. (2019). Polyoxometalates in dye-sensitized solar cells. *Chemical Society Reviews*, *48*(1), 260-284. https://doi.org/10.1039/c8cs00559a

Chen, Y., Tan, X., Peng, S., Xin, C., Delahoy, A. E., Chin, K. K., & Zhang, C. (2018). The influence of conduction band offset on CdTe solar cells. *Journal of Electronic Materials*, *47*(2), 1201-1207. https://doi.org/10.1007/s11664-017-5850-9

Cheng, M., Zuo, C., Wu, Y., Li, Z., Xu, B., Hua, Y., & Ding, L. (2020). Charge-transport layer engineering in perovskite solar cells. *Science Bulletin*, *65*(15), 1237-1241. https://doi.org/10.1016/j.scib.2020.04.021

Cheruku, R., Kim, J. H., Krishna, V. M., Periyat, P., & SSSR, S. D. (2023). Photo-electrodes decorated with carbon quantum dots: Efficient dye-sensitized solar cells. *Results in Engineering*, *20*(1), 101611. https://doi.org/10.1016/j.rineng.2023.101611

Chou, C.-S., Chou, F.-C., & Kang, J.-Y. (2012). Preparation of ZnO-coated TiO_2 electrodes using dip coating and their applications in dye-sensitized solar cells. *Powder Technology*, *215*(1), 38-45. https://doi.org/10.1016/j.powtec.2011.09.003

Choudhury, B., Chetri, P., & Choudhury, A. (2013). Oxygen defects and formation of Ce^{3+} affecting the photocatalytic performance of CeO_2 nanoparticles. *Rsc Advances*, *4*(9), 4663-4671. https://doi.org/10.1039/c3ra44603d

Corà, F., Alfredsson, M., Mallia, G., Middlemiss, D. S., Mackrodt, W. C., Dovesi, R., & Orlando, R. (2004). The performance of hybrid density functionals in solid state chemistry. *Principles and Applications of Density Functional Theory in Inorganic Chemistry II*, *1*(1), 171-232. https://doi.org/10.1007/b97944

Crabtree, G. W., & Lewis, N. S. (2007). Solar energy conversion. *Physics today*, *60*(3), 37-42. https://doi.org/10.1063/1.2718755

Cui, Y., Zhu, P., Liao, X., & Chen, Y. (2020). Recent advances of computational chemistry in organic solar cell research. *Journal of Materials Chemistry C*, *8*(45), 15920-15939. https://doi.org/10.1039/d0tc03709e

Cysewski, P. (2019). Application of the Consonance solvent concept for accurate prediction of buckminster solubility in 180 net solvents using COSMO-RS Approach. *Symmetry*, *11*(6), 828. https://doi.org/10.3390/sym11060828

Dalapati, G. K., Sharma, H., Guchhait, A., Chakrabarty, N., Bamola, P., Liu, Q., Saianand, G., Krishna, A. M. S., Mukhopadhyay, S., & Dey, A. (2021). Tin oxide for optoelectronic, photovoltaic and energy storage devices: a review. *Journal of Materials Chemistry A*, *9*(31), 16621-16684. https://doi.org/10.1039/d1ta01291f

Das, S. K., Ganguli, S., Kabir, H., Khandaker, J. I., & Ahmed, F. (2020). Performance of natural dyes in dye-sensitized solar cell as photosensitizer. *Transactions on Electrical and Electronic Materials*, *21*(1), 105-116. https://doi.org/10.1007/s42341-019-00158-y

Dawo, C., & Chaturvedi, H. (2023). Recent advances in the development of flexible dye-sensitized solar cells: fabrication, challenges and applications-a review. *Flexible and Printed Electronics*, *8*(1), 013001. https://doi.org/10.1088/2058-8585/acb660

de Aberasturi, D. J., Serrano-Montes, A. B., & Liz-Marzán, L. M. (2015). Modern applications of plasmonic nanoparticles: from energy to health. *Advanced Optical Materials*, *3*(5), 602-617. https://doi.org/10.1002/adom.201500053

De Angelis, F., Fantacci, S., Selloni, A., Nazeeruddin, M. K., & Grätzel, M. (2007). Time-dependent density functional theory investigations on the excited states of Ru (II)-dye-sensitized TiO_2 nanoparticles: the role of sensitizer protonation. *Journal of the American Chemical Society*, *129*(46), 14156-14157. https://doi.org/10.1021/ja076293e

Decock, K., Zabierowski, P., & Burgelman, M. (2012). Modeling metastabilities in chalcopyrite-based thin film solar cells. *Journal of Applied Physics*, *111*(4), 043703. https://doi.org/10.1063/1.3686651

Devi, N., Parrey, K. A., Aziz, A., & Datta, S. (2018). Numerical simulations of perovskite thin-film solar cells using a CdS hole blocking layer. *Journal of Vacuum Science & Technology B, Nanotechnology and Microelectronics: Materials, Processing, Measurement, and Phenomena*, *36*(4), 04G105. https://doi.org/10.1116/1.5026163

Dhass, A., Beemkumar, N., Harikrishnan, S., & Ali, H. M. (2022). A review on factors influencing the mismatch losses in solar photovoltaic system. *International Journal of Photoenergy*, *2022*(1), 1-27. https://doi.org/10.1155/2022/2986004

Dhass, A., Natarajan, E., & Ponnusamy, L. (2012). Influence of shunt resistance on the performance of solar photovoltaic cell. *2012 International Conference on Emerging Trends in Electrical Engineering and Energy Management (ICETEEEM), 1*(1), 382-386. https://doi.org/10.1109/iceteeem.2012.6494522

Dhonde, M., Bhojane, P., Sahu, K., & Murty, V. (2023). Dye-sensitized photoelectrochemical cells in water splitting. In *Solar-Driven Green Hydrogen Generation and Storage* (pp. 157-191). Elsevier. https://doi.org/10.1016/b978-0-323-99580-1.00005-4

Dhonde, M., Sahu Dhonde, K., Purohit, K., & Murty, V. (2019). Facile synthesis of Cu/N co-doped TiO_2 nanoparticles and their optical and electrical properties. *Indian Journal of Physics*, *93*(1), 27-32. https://doi.org/10.1007/s12648-018-1275-4

Dhonde, M., Sahu, K., Das, M., Yadav, A., Ghosh, P., & Murty, V. V. S. (2022). Recent advancements in dye-sensitized solar cells; from photoelectrode to counter electrode. *Journal of The Electrochemical Society*, *169*(6), 066507. https://10.1149/1945-7111/ac741f

Dhonde, M., Sahu, K., & Murty, V. (2021). Cu-doped TiO_2 nanoparticles/graphene composites for efficient dye-sensitized solar cells. *Solar Energy*, *220*(1), 418-424. https://doi.org/10.1016/j.solener.2021.03.072

Dhonde, M., Sahu, K., Murty, V., Nemala, S. S., & Bhargava, P. (2017). Surface plasmon resonance effect of Cu nanoparticles in a dye sensitized solar cell. *Electrochimica Acta*, *249*(1), 89-95. https://doi.org/10.1016/j.electacta.2017.07.187

Dias, B. V., Tractz, G. T., Viomar, A., Maia, G. A., Da Cunha, M. T., & Rodrigues, P. R. (2018). Photoelectrochemical behavior of the cell FTO/TiO_2/CeO_2/N719 obtained from the Pechini and precipitation of cerium oxide methods. *Journal of Electronic Materials*, *47*(9), 5556-5563. https://doi.org/10.1007/s11664-018-6465-5

Dissanayake, M. L., Senadeera, G., & Bandara, T. (2017). Mixed cation effect and iodide ion conductivity in electrolytes for dye sensitized solar cells. *Ionics*, *23*(10), 2901-2907. https://doi.org/10.1007/s11581-016-1902-z

Dong, Z., Ren, H., Hessel, C. M., Wang, J., Yu, R., Jin, Q., Yang, M., Hu, Z., Chen, Y., & Tang, Z. (2014). Quintuple-shelled SnO_2 hollow microspheres with superior light scattering for high-performance dye-sensitized solar cells. *Advanced Materials*, *26*(6), 905-909. https://doi.org/10.1002/adma.201304010

dos Santos, S. B., Boratto, M. H., Ramos Jr, R. A., & Scalvi, L. V. (2022). Influence of Pb^{2+} doping in the optical and electro-optical properties of SnO_2 thin films. *Materials Chemistry and Physics*, *278*(1), 125571. https://doi.org/10.1016/j.matchemphys.2021.125571

Doumon, N. Y., Yang, L., & Rosei, F. (2022). Ternary Organic Solar Cells: A Review of The Role of the Third Element☆. *Nano Energy*, *1*(1), 106915. https://doi.org/10.1016/j.nanoen.2023.108369

Drygała, A., Starowicz, Z., Gawlińska-Nęcek, K., Karolus, M., Lipiński, M., Jarka, P., Matysiak, W., Tillová, E., Palček, P., & Tański, T. (2023). Hybrid Mesoporous TiO_2/ZnO Electron Transport Layer for Efficient Perovskite Solar Cell. *Molecules*, *28*(15), 5656. https://doi.org/10.3390/molecules28155656

Du, P., Song, L., Xiong, J., Li, N., Xi, Z., Wang, L., Jin, D., Guo, S., & Yuan, Y. (2012). Coaxial electrospun TiO_2/ZnO core–sheath nanofibers film: Novel structure for photoanode of dye-sensitized solar cells. *Electrochimica Acta*, *78*(1), 392-397. https://doi.org/10.1016/j.electacta.2012.06.034

Duarte, A. E., Cruz, A. L., Marquina, A. V., Martínez, J. A., Juárez, A. G., & Islas, C. Z. (2024). One-step method to simultaneously grow TiO_2 compact and porous layers for DSSC photoelectrodes. *Applied Nanoscience*, *14*(5), 819-826. https://doi.org/10.1007/s13204-024-03050-1

Eisenbarth, T., Unold, T., Caballero, R., Kaufmann, C. A., & Schock, H.-W. (2010). Interpretation of admittance, capacitance-voltage, and current-voltage signatures in Cu (In, Ga) Se_2 thin film solar cells. *Journal of Applied Physics*, *107*(3), 034509. https://doi.org/10.1063/1.3277043

Eithiraj, R., & Geethalakshmi, K. (2013). Suitability of amorphous TiO_2 nanoparticles as a photoelectrode in dye sensitized solar cells: A DFT–TDDFT study. *Chemical Physics Letters*, *585*(1), 138-142. https://doi.org/10.1016/j.cplett.2013.08.103

El Mouhi, R., Slimi, A., Fitri, A., Benjelloun, A. T., ElKhattabi, S., Benzakour, M., Mcharfi, M., & Kurban, M. (2022). DFT, DFTB and TD-DFT theoretical investigations of π-conjugated molecules based on thieno [2, 3-b] indole for dye-sensitized solar cell applications. *Physica B: Condensed Matter*, *636*(1), 413850. https://doi.org/10.1016/j.physb.2022.413850

Elroby, S. A., & Jedidi, A. (2020). Density functional theory study on two D-π-A-type organic dyes containing different anchoring groups for dye-sensitized solar cells. *Structural Chemistry*, *31*(3), 1125-1135. https://doi.org/10.1007/s11224-020-01489-w

Elseman, A. M., Xu, C., Yao, Y., Elisabeth, M., Niu, L., Malavasi, L., & Song, Q. L. (2020). Electron Transport Materials: Evolution and Case Study for High-Efficiency Perovskite Solar Cells. *Solar Rrl*, *4*(7), 2000136. https://doi.org/10.1002/solr.202000136

Es-Smairi, A., Fazouan, N., Maskar, E., Bziz, I., Sabil, M., & Rai, D. (2024). The effect of oxygen atom substitution in the sulphur sites of the bulk ZnS: A DFT study. *Chemical Physics*, *578*(1), 112144. https://doi.org/10.1016/j.chemphys.2023.112144

Feng, Y., Chen, J., Huang, X., Liu, W., Zhu, Y., Qin, W., & Mo, X. (2016). A ZnO/TiO_2 composite nanorods photoanode with improved performance for dye-sensitized solar cells. *Crystal Research and Technology*, *51*(10), 548-553. https://doi.org/10.1002/crat.201600012

Filipič, M., Berginc, M., Smole, F., & Topič, M. (2012). Analysis of electron recombination in dye-sensitized solar cell. *Current Applied Physics*, *12*(1), 238-246. https://doi.org/10.1016/j.cap.2011.06.011

Forsberg, C. W. (2009). Sustainability by combining nuclear, fossil, and renewable energy sources. *Progress in Nuclear energy*, *51*(1), 192-200. https://doi.org/10.1016/j.pnucene.2008.04.002

Fujisawa, J.-i., & Hanaya, M. (2018). Light harvesting and direct electron injection by interfacial charge-transfer transitions between TiO_2 and carboxy-anchor dye LEG4 in dye-sensitized

solar cells. *The Journal of Physical Chemistry C*, *122*(1), 8-15. https://doi.org/10.1021/acs.jpcc.7b04749

Gan, Y., Bi, X., Liu, Y., Qin, B., Li, Q., Jiang, Q., & Mo, P. (2020). Numerical Investigation Energy Conversion Performance of Tin-Based Perovskite Solar Cells Using Cell Capacitance Simulator. *Energies*, *13*(22), 5907. https://doi.org/10.3390/en13225907

Garcia, J. M., Heald, L. F., Shaffer, R. E., & Sayres, S. G. (2021). Effect of oxidation on excited state dynamics of neutral Ti_nO_{2n-x} ($n< 10$, $x< 4$) clusters. *The Journal of Chemical Physics*, *155*(21), 211102. https://doi.org/10.1063/5.0071264

Gasso, S., & Mahajan, A. (2022). MXene based 2D-2D heterostructures for Counter Electrode in third generation Dye Sensitized Solar Cells. *Chemical Physics Letters*, *808*(1), 140144. https://doi.org/10.1016/j.cplett.2022.140144

Ge, Z., Wang, C., Chen, Z., Wang, T., Chen, T., Shi, R., Yu, S., & Liu, J. (2021). Investigation of the TiO_2 nanoparticles aggregation with high light harvesting for high-efficiency dye-sensitized solar cells. *Materials Research Bulletin*, *135*(1), 111148. https://doi.org/10.1016/j.materresbull.2020.111148

Gebreslassie, Y. T., & Gebretnsae, H. G. (2021). Green and cost-effective synthesis of tin oxide nanoparticles: a review on the synthesis methodologies, mechanism of formation, and their potential applications. *Nanoscale research letters*, *16*(1), 97. https://doi.org/10.1186/s11671-021-03555-6

Genesio, G., Maynadié, J., Carboni, M., & Meyer, D. (2018). Recent status on MOF thin films on transparent conductive oxides substrates (ITO or FTO). *New Journal of Chemistry*, *42*(4), 2351-2363. https://doi.org/10.1039/c7nj03171h

Gerlich, V., Sulovská, K., & Zálešák, M. (2013). COMSOL Multiphysics validation as simulation software for heat transfer calculation in buildings: Building simulation software validation. *Measurement*, *46*(6), 2003-2012. https://doi.org/10.1016/j.measurement.2013.02.020

Ghosh, P., Sundaram, S., Nixon, T. P., & Krishnamurthy, S. (2022). Influence of nanostructures in perovskite solar cells. *Encyclopedia of Smart Materials*, *2*(1), 646-660. https://doi.org/10.1016/b978-0-12-815732-9.00054-1

Giannouli, M. (2013). Nanostructured ZnO, TiO_2, and composite ZnO/TiO_2 films for application in dye-sensitized solar cells. *International Journal of Photoenergy*, *2013*(1), 1-18. https://doi.org/10.1155/2013/612095

Godin, R., & Durrant, J. R. (2021). Dynamics of photoconversion processes: the energetic cost of lifetime gain in photosynthetic and photovoltaic systems. *Chemical Society Reviews*, *50*(23), 13372-13409. https://doi.org/10.1039/d1cs00577d

Goh, Z., Saidi, N. M., Farhana, N., Bashir, S., Iqbal, J., Ramesh, K., Ramesh, S., Wageh, S., & Kalam, A. (2022). Sonochemically synthesized cobalt oxide nanoparticles as an additive for natural polymer iodide electrolyte based dye-sensitized solar cells. *Sustainable Energy Technologies and Assessments*, *49*(1), 101746. https://doi.org/10.1016/j.seta.2021.101746

Gong, J., Sumathy, K., Qiao, Q., & Zhou, Z. (2017). Review on dye-sensitized solar cells (DSSCs): Advanced techniques and research trends. *Renewable and Sustainable Energy Reviews*, *68*(1), 234-246. https://doi.org/10.1016/j.rser.2016.09.097

Gour, K. S., Parmar, R., Kumar, R., & Singh, V. N. (2020). Cd-free Zn (O,S) as alternative buffer layer for chalcogenide and kesterite based thin films solar cells: a review. *Journal of Nanoscience and Nanotechnology*, *20*(6), 3622-3635. https://doi.org/10.1166/jnn.2020.17537

Grätzel, M. (2005). Solar energy conversion by dye-sensitized photovoltaic cells. *Inorganic chemistry*, *44*(20), 6841-6851. https://doi.org/10.1021/ic0508371

Grifoni, F., Bonomo, M., Naim, W., Barbero, N., Alnasser, T., Dzeba, I., Giordano, M., Tsaturyan, A., Urbani, M., & Torres, T. (2021). Toward Sustainable, Colorless, and Transparent Photovoltaics: State of the Art and Perspectives for the Development of Selective Near-Infrared Dye-Sensitized Solar Cells. *Advanced Energy Materials*, *11*(43), 2101598. https://doi.org/10.1002/aenm.202101598

Gubernatis, J., & Lookman, T. (2018). Machine learning in materials design and discovery: Examples from the present and suggestions for the future. *Physical Review Materials*, *2*(12), 120301. https://doi.org/10.1103/physrevmaterials.2.120301

Guillemoles, J.-F., Kirchartz, T., Cahen, D., & Rau, U. (2019). Guide for the perplexed to the Shockley–Queisser model for solar cells. *Nature photonics*, *13*(8), 501-505. https://doi.org/10.1038/s41566-019-0479-2

Gustavsson, L., Haus, S., Lundblad, M., Lundström, A., Ortiz, C. A., Sathre, R., Le Truong, N., & Wikberg, P.-E. (2017). Climate change effects of forestry and substitution of carbon-intensive materials and fossil fuels. *Renewable and Sustainable Energy Reviews*, *67*(1), 612-624. https://doi.org/10.1016/j.rser.2016.09.056

Hailegnaw, B., Sariciftci, N. S., & Scharber, M. C. (2020). Impedance Spectroscopy of Perovskite Solar Cells: Studying the Dynamics of Charge Carriers Before and After Continuous Operation. *Physica status solidi (a)*, *217*(22), 2000291. https://doi.org/10.1002/pssa.202000291

Halkos, G. E., & Gkampoura, E.-C. (2020). Reviewing usage, potentials, and limitations of renewable energy sources. *Energies*, *13*(11), 2906. https://doi.org/10.3390/en13112906

Hall, R. S., Lamb, D., & Irvine, S. J. C. (2021). Back contacts materials used in thin film CdTe solar cells—A review. *Energy Science & Engineering*, *9*(5), 606-632. https://doi.org/10.1002/ese3.843

Han, J., Fan, F., Xu, C., Lin, S., Wei, M., Duan, X., & Wang, Z. L. (2010). ZnO nanotube-based dye-sensitized solar cell and its application in self-powered devices. *Nanotechnology*, *21*(40), 405203. https://doi.org/10.1088/0957-4484/21/40/405203

Han, X., Ji, Y., & Yang, Y. (2022). Ferroelectric photovoltaic materials and devices. *Advanced Functional Materials*, *32*(14), 2109625. https://doi.org/10.1002/adfm.202109625

Hassanien, R. H. E., Li, M., & Lin, W. D. (2016). Advanced applications of solar energy in agricultural greenhouses. *Renewable and Sustainable Energy Reviews*, *54*(1), 989-1001. https://doi.org/10.1016/j.rser.2015.10.095

Hayat, M. B., Ali, D., Monyake, K. C., Alagha, L., & Ahmed, N. (2019). Solar energy—A look into power generation, challenges, and a solar-powered future. *International Journal of Energy Research*, *43*(3), 1049-1067. https://doi.org/10.1002/er.4252

Heidarzadeh, H., & Tavousi, A. (2019). Performance enhancement methods of an ultra-thin silicon solar cell using different shapes of back grating and angle of incidence light. *Materials Science and Engineering: B*, *240*(1), 1-6. https://doi.org/10.1016/j.mseb.2018.12.025

Hezam, A., Namratha, K., Drmosh, Q., Chandrashekar, B. N., Jayaprakash, G. K., Cheng, C., Swamy, S. S., & Byrappa, K. (2018). Electronically semitransparent ZnO nanorods with superior electron transport ability for DSSCs and solar photocatalysis. *Ceramics International*, *44*(6), 7202-7208. https://doi.org/10.1016/j.ceramint.2018.01.167

Ho, Y.-C., Hoque, M. N. F., Stoneham, E., Warzywoda, J., Dallas, T., & Fan, Z. (2017). Reduction of oxygen vacancy related traps in TiO_2 and the impacts on hybrid perovskite solar cells. *The Journal of Physical Chemistry C*, *121*(43), 23939-23946. https://doi.org/10.1021/acs.jpcc.7b08384

Hoang Huy, V. P., & Bark, C.-W. (2023). Review on Surface Modification of SnO_2 Electron Transport Layer for High-Efficiency Perovskite Solar Cells. *Applied Sciences*, *13*(19), 10715. https://doi.org/10.3390/app131910715

Hossain, M. F., Hossain, S., & Uddin, M. J. (2017). Renewable energy: Prospects and trends in Bangladesh. *Renewable and Sustainable Energy Reviews*, *70*(1), 44-49. https://doi.org/10.1016/j.rser.2016.11.197

Hossain, M. K., Mohammed, M. K., Pandey, R., Arnab, A., Rubel, M., Hossain, K., Ali, M. H., Rahman, M. F., Bencherif, H., & Madan, J. (2023). Numerical analysis in DFT and SCAPS-1D on the influence of different charge transport layers of $CsPbBr_3$ perovskite solar cells. *Energy & Fuels*, *37*(8), 6078-6098. https://doi.org/10.1021/acs.energyfuels.3c00035

Hossain, M. K., Rubel, M. H. K., Toki, G. I., Alam, I., Rahman, M. F., & Bencherif, H. (2022). Effect of various electron and hole transport layers on the performance of $CsPbI_3$-based perovskite solar cells: a numerical investigation in DFT, SCAPS-1D, and wxAMPS frameworks. *ACS omega*, *7*(47), 43210-43230. https://doi.org/10.1021/acsomega.2c05912

Hossen, M. J., Rahman, M. B., Miah, M. H., Hamzah, H. M., Said, S. M., Hatta, S., & Islam, M. A. (2025). Modeling and optimization of high efficiency Pb-free Cs-based halide double

perovskite solar cell using SCAPS-1D. *Journal of Optics*, *1*(1), 1-15. https://doi.org/10.1007/s12596-025-02550-9

Hou, L., Zhang, M., Guan, Z., Li, Q., & Yang, J. (2018). Effect of annealing ambience on the formation of surface/bulk oxygen vacancies in TiO_2 for photocatalytic hydrogen evolution. *Applied Surface Science*, *428*(1), 640-647. https://doi.org/10.1016/j.apsusc.2017.09.144

Hsu, C.-Y., Chen, Y.-C., Lin, R. Y.-Y., Ho, K.-C., & Lin, J. T. (2012). Solid-state dye-sensitized solar cells based on spirofluorene (spiro-OMeTAD) and arylamines as hole transporting materials. *Physical Chemistry Chemical Physics*, *14*(41), 14099-14109. https://doi.org/10.1039/c2cp41326d

Huang, X., Zhang, Y., Sun, H., Li, D., Luo, Y., & Meng, Q. (2009). A new figure of merit for qualifying the fluorine-doped tin oxide glass used in dye-sensitized solar cells. *Journal of Renewable and Sustainable Energy*, *1*(6), 063107. https://doi.org/10.1063/1.3278518

Iqbal, M. A., Malik, M., Shahid, W., Din, S. Z. U., Anwar, N., Ikram, M., & Idrees, F. (2022). Materials for Photovoltaics: Overview, Generations, Recent Advancements and Future Prospects. *Thin Films Photovoltaics*, *1*(1), 5. https://doi.org/10.5772/intechopen.101449

Ishraq, M. H., Kabir, M. R., Tarekuzzaman, M., Rahman, M. F., Rasheduzzaman, M., & Hasan, M. Z. (2024). ETL and HTL Engineering in $CH_3NH_3PbBr_3$ Perovskite for Stable and Efficient Performance Photovoltaic Devices Applications using SCAPS-1D. *Advanced Theory and Simulations*, *7*(9), 2400360. https://doi.org/10.1002/adts.202400360

Izam, N. S. M. N., Itam, Z., Sing, W. L., & Syamsir, A. (2022). Sustainable development perspectives of solar energy technologies with focus on solar Photovoltaic—A review. *Energies*, *15*(8), 2790. https://doi.org/10.3390/en15082790

Jahantigh, F., & Safikhani, M. J. (2019). The effect of HTM on the performance of solid-state dye-sanitized solar cells (SDSSCs): a SCAPS-1D simulation study. *Applied Physics A: Materials Science & Processing*, *125*(4), 276. https://doi.org/10.1007/s00339-019-2582-0

Janani, M., Srikrishnarka, P., Nair, S. V., & Nair, A. S. (2015). An in-depth review on the role of carbon nanostructures in dye-sensitized solar cells. *Journal of Materials Chemistry A*, *3*(35), 17914-17938. https://doi.org/10.1039/c5ta03644e

Jang, Y. J., Thogiti, S., Lee, K.-y., & Kim, J. H. (2019). Long-term stable solid-state dye-sensitized solar cells assembled with solid-state polymerized hole-transporting material. *Crystals*, *9*(9), 452. https://doi.org/10.3390/cryst9090452

Javed, R., Ain, N. u., Gul, A., Arslan Ahmad, M., Guo, W., Ao, Q., & Tian, S. (2022). Diverse biotechnological applications of multifunctional titanium dioxide nanoparticles: An up-to-date review. *IET nanobiotechnology*, *16*(5), 171-189. https://doi.org/10.1049/nbt2.12085

Jeyakumar, R., Bag, A., Nekovei, R., & Radhakrishnan, R. (2020). Influence of Electron Transport Layer (TiO_2) Thickness and Its Doping Density on the Performance of $CH_3NH_3PbI_3$-Based Planar Perovskite Solar Cells. *Journal of Electronic Materials*, *49*(6), 3533-3539. https://doi.org/10.1007/s11664-020-08041-w

Jhuma, F. A., Shaily, M. Z., & Rashid, M. J. (2019). Towards high-efficiency CZTS solar cell through buffer layer optimization. *Materials for Renewable and Sustainable Energy*, *8*(1), 6. https://doi.org/10.1007/s40243-019-0144-1

Ji, C., Zhang, Z., Masuda, T., Kudo, Y., & Guo, L. J. (2019). Vivid-colored silicon solar panels with high efficiency and non-iridescent appearance. *Nanoscale Horizons*, *4*(4), 874-880. https://doi.org/10.1039/c8nh00368h

Jumabaev, A., Khudaykulov, B., Holikulov, U., Norkulov, A., Subbiah, J., Al-Dossary, O. M., Hushvaktov, H., Absanov, A., & Issaoui, N. (2025). Molecular structure, vibrational spectral assignments, MEP, HOMO-LUMO, AIM, NCI, RDG, ELF, LOL properties of acetophenone and for its solutions based on DFT calculations. *Optical Materials*, *159*(1), 116683. https://doi.org/10.1016/j.optmat.2025.116683

Kabir, F., Sakib, S. N., & Matin, N. (2019). Stability study of natural green dye based DSSC. *Optik*, *181*(1), 458-464. https://doi.org/10.1016/j.ijleo.2018.12.077

Kaiser, I., Ernst, K., Fischer, C.-H., Könenkamp, R., Rost, C., Sieber, I., & Lux-Steiner, M. C. (2001). The eta-solar cell with CuInS2: A photovoltaic cell concept using an extremely thin absorber (eta). *Solar energy materials and solar cells*, *67*(1-4), 89-96. https://doi.org/10.1016/s0927-0248(00)00267-1

Karmalawi, A. M., Rayan, D. A., & Rashad, M. M. (2020). Establishment and evaluation of photovoltaic quantum efficiency system at central metallurgical research and development institute. *Optik*, *217*(1), 164931. https://doi.org/10.1016/j.ijleo.2020.164931

Karthick, S., Velumani, S., & Bouclé, J. (2020). Experimental and SCAPS simulated formamidinium perovskite solar cells: a comparison of device performance. *Solar Energy*, *205*(1), 349-357. https://doi.org/10.1016/j.solener.2020.05.041

Kato, N., Moribe, S., Shiozawa, M., Suzuki, R., Higuchi, K., Suzuki, A., Sreenivasu, M., Tsuchimoto, K., Tatematsu, K., & Mizumoto, K. (2018). Improved conversion efficiency of 10% for solid-state dye-sensitized solar cells utilizing P-type semiconducting CuI and multi-dye consisting of novel porphyrin dimer and organic dyes. *Journal of Materials Chemistry A*, *6*(45), 22508-22512. https://doi.org/10.1039/c8ta06418k

Kersten, F., Engelhart, P., Ploigt, H.-C., Stekolnikov, A., Lindner, T., Stenzel, F., Bartzsch, M., Szpeth, A., Petter, K., & Heitmann, J. (2015). Degradation of multicrystalline silicon solar cells and modules after illumination at elevated temperature. *Solar energy materials and solar cells*, *142*(1), 83-86. https://doi.org/10.1016/j.solmat.2015.06.015

Khanmohammadi, K., Sohrabi, B., & Meymian, M. Z. (2018). Effect of electron-donating and-withdrawing substitutions in naphthoquinone sensitizers: the structure engineering of dyes for DSSCs. *Journal of Molecular Structure*, *1167*(1), 274-279. https://doi.org/10.1016/j.molstruc.2018.05.014

Kim, J. H., Moon, K. J., Kim, J. M., Lee, D., & Kim, S. H. (2015). Effects of various light-intensity and temperature environments on the photovoltaic performance of dye-sensitized solar cells. *Solar Energy*, *113*(1), 251-257. https://doi.org/10.1016/j.solener.2015.01.012

Kim, K., Gwak, J., Ahn, S. K., Eo, Y.-J., Park, J. H., Cho, J.-S., Kang, M. G., Song, H.-E., & Yun, J. H. (2017). Simulations of chalcopyrite/c-Si tandem cells using SCAPS-1D. *Solar Energy*, *145*(1), 52-58. https://doi.org/10.1016/j.solener.2017.01.031

Kim, S.-S., Yum, J.-H., & Sung, Y.-E. (2005). Flexible dye-sensitized solar cells using ZnO coated TiO_2 nanoparticles. *Journal of Photochemistry and Photobiology A: Chemistry*, *171*(3), 269-273. https://doi.org/10.1016/j.jphotochem.2004.10.019

Kowsar, A., Billah, M., Dey, S., Debnath, S. C., Yeakin, S., & Farhad, S. F. U. (2019). Comparative Study on Solar Cell Simulators. 2019 2nd International Conference on Innovation in Engineering and Technology (ICIET), *1*(1), 1-6. https://doi.org/10.1109/iciet48527.2019.9290675

Krishnan, S., & Senthilkumar, K. (2021). The influence of the shape and configuration of sensitizer molecules on the efficiency of DSSCs: a theoretical insight. *RSC advances*, *11*(10), 5556-5567. https://doi.org/10.1039/d0ra10613e

Kuciauskas, D., Monat, J. E., Villahermosa, R., Gray, H. B., Lewis, N. S., & McCusker, J. K. (2002). Transient absorption spectroscopy of ruthenium and osmium polypyridyl complexes adsorbed onto nanocrystalline TiO_2 photoelectrodes. *The Journal of Physical Chemistry B*, *106*(36), 9347-9358. https://doi.org/10.1021/jp014589f

Kumar, N., Lee, H. B., Hwang, S., Kim, T.-W., & Kang, J.-W. (2019). Fabrication of plasmonic gold-nanoparticle-transition metal oxides thin films for optoelectronic applications. *Journal of Alloys and Compounds*, *775*(1), 39-50. https://doi.org/10.1016/j.jallcom.2018.10.055

Kumar, S., Kumar, S., Rai, R., Lee, Y., Nguyen, T. H. C., Kim, S. Y., Van Le, Q., & Singh, L. (2023). Recent development in two-dimensional material-based advanced photoanodes for high-performance dye-sensitized solar cells. *Solar Energy*, *249*(1), 606-623. https://doi.org/10.1016/j.solener.2022.12.013

Kumara, G., Okuya, M., Murakami, K., Kaneko, S., Jayaweera, V., & Tennakone, K. (2004). Dye-sensitized solid-state solar cells made from magnesiumoxide-coated nanocrystalline titanium dioxide films: enhancement of the efficiency. *Journal of Photochemistry and Photobiology A: Chemistry*, *164*(1-3), 183-185. https://doi.org/10.1016/j.jphotochem.2003.11.020

Kunzmann, A., Valero, S., Sepúlveda, Á. E., Rico-Santacruz, M., Lalinde, E., Berenguer, J. R., García-Martínez, J., Guldi, D. M., Serrano, E., & Costa, R. D. (2018). Hybrid Dye-Titania Nanoparticles for Superior Low-Temperature Dye-Sensitized Solar Cells. *Advanced Energy Materials*, *8*(12), 1702583. https://doi.org/10.1002/aenm.201702583

Labat, F., Baranek, P., & Adamo, C. (2008). Structural and electronic properties of selected rutile and anatase TiO_2 surfaces: an ab initio investigation. *Journal of Chemical Theory and Computation*, *4*(2), 341-352. https://doi.org/10.1021/ct700221w

Labat, F., Lainé, P. P., Ciofini, I., & Adamo, C. (2006). Spectral properties of bipyridyl ligands by time-dependent density functional theory. *Chemical Physics Letters*, *417*(4-6), 445-451. https://doi.org/10.1016/j.cplett.2005.10.066

Lamiel-Garcia, O., Cuko, A., Calatayud, M., Illas, F., & Bromley, S. T. (2017). Predicting size-dependent emergence of crystallinity in nanomaterials: titania nanoclusters versus nanocrystals. *Nanoscale*, *9*(3), 1049-1058. https://doi.org/10.1039/c6nr05788h

Lancelle-Beltran, E., Prené, P., Boscher, C., Belleville, P., Buvat, P., Lambert, S., Guillet, F., Marcel, C., & Sanchez, C. (2008). Solid-State Organic/Inorganic Hybrid Solar Cells Based on Poly (octylthiophene) and Dye-Sensitized Nanobrookite and Nanoanatase TiO_2 Electrodes. *European Journal of Inorganic Chemistry*, *2008*(6), 903-910. https://doi.org/10.1002/ejic.200701033

Lancelle-Beltran, E., Prené, P., Boscher, C., Belleville, P., Buvat, P., & Sanchez, C. (2006). All-solid-state dye-sensitized nanoporous TiO_2 hybrid solar cells with high energy-conversion efficiency. *Advanced Materials*, *18*(19), 2579-2582. https://doi.org/10.1002/adma.200502023

Law, M., Greene, L. E., Radenovic, A., Kuykendall, T., Liphardt, J., & Yang, P. (2006). ZnO− Al_2O_3 and ZnO− TiO_2 core− shell nanowire dye-sensitized solar cells. *The Journal of Physical Chemistry B*, *110*(45), 22652-22663. https://doi.org/10.1021/jp0648644

Lee, C.-P., Li, C.-T., & Ho, K.-C. (2017). Use of organic materials in dye-sensitized solar cells. *Materials Today*, *20*(5), 267-283. https://doi.org/10.1016/j.mattod.2017.01.012

Lee, K. M., Lee, E. S., Yoo, B., & Shin, D. H. (2013). Synthesis of ZnO-decorated TiO_2 nanotubes for dye-sensitized solar cells. *Electrochimica Acta*, *109*(1), 181-186. https://doi.org/10.1016/j.electacta.2013.07.055

Lenzmann, F., O'Regan, B., Sommeling, P., Slooff, L., Smits, J. J., & Kuipers, H. P. (2005). Dye solar cells without electrolyte or hole-transport layers. A feasibility study of a concept

based on direct regeneration of the dye by metallic conductors. *Progress in Photovoltaics: Research and Applications*, *13*(4), 333-340. https://doi.org/10.1002/pip.631

Li, B., Shang, X., Li, L., Xu, Y., Wang, H., Yang, X., Pei, M., Zhang, R., & Zhang, G. (2020). A fluorescence probe based on 6-phenylimidazo [2, 1-b] thiazole and salicylaldehyde for the relay discerning of In^{3+} and Cr^{3+}. *New Journal of Chemistry*, *44*(3), 951-957. https://doi.org/10.1039/c9nj05722f

Li, F., Jiao, Y., Xie, S., & Li, J. (2015). Sponge-like porous TiO_2/ZnO nanodonuts for high efficiency dye-sensitized solar cells. *Journal of Power Sources*, *280*(1), 373-378. https://doi.org/10.1016/j.jpowsour.2015.01.118

Li, M., Wang, Z. K., Yang, Y. G., Hu, Y., Feng, S. L., Wang, J. M., Gao, X. Y., & Liao, L. S. (2016). Copper salts doped spiro-OMeTAD for high-performance perovskite solar cells. *Advanced Energy Materials*, *6*(21), 1601156. https://doi.org/10.1002/aenm.201601156

Li, Y., Huang, W., Huang, H., Hewitt, C., Chen, Y., Fang, G., & Carroll, D. L. (2013). Evaluation of methods to extract parameters from current–voltage characteristics of solar cells. *Solar Energy*, *90*(1), 51-57. https://doi.org/10.1016/j.solener.2012.12.005

Liang, J.-W., Firdaus, Y., Azmi, R., Faber, H., Kaltsas, D., Kang, C. H., Nugraha, M. I., Yengel, E., Ng, T. K., & De Wolf, S. (2022). Cl_2-doped CuSCN Hole transport layer for organic and perovskite solar cells with improved stability. *ACS Energy Letters*, *7*(9), 3139-3148. https://doi.org/10.1021/acsenergylett.2c01545

Lim, J., Kim, M., Park, H. H., Jung, H., Lim, S., Hao, X., Choi, E., Park, S., Lee, M., & Liu, Z. (2021). Kinetics of light-induced degradation in semi-transparent perovskite solar cells. *Solar energy materials and solar cells*, *219*(1), 110776. https://doi.org/10.1016/j.solmat.2020.110776

Lin, L., Jones, T. W., Yang, T. C. J., Duffy, N. W., Li, J., Zhao, L., Chi, B., Wang, X., & Wilson, G. J. (2021). Inorganic electron transport materials in perovskite solar cells. *Advanced Functional Materials*, *31*(5), 2008300. https://doi.org/10.1002/adfm.202170032

Litvinov, V. G., Ermachikhin, A. V., Kusakin, D. S., Vishnyakov, N. V., Gudzev, V. V., Karabanov, A. S., Karabanov, S. M., & Vikhrov, S. P. (2017). Investigation of Deep-Level

Defects Lateral Distribution in Active Layers of Multicrystalline Silicon Solar Cells. *MRS Advances*, *2*(53), 3141-3146. https://doi.org/10.1557/adv.2017.376

Liu, J., Wei, A., Zhao, Y., Lin, K., & Luo, F. (2014). Dye-sensitized solar cells based on ZnO nanoflowers and TiO_2 nanoparticles composite photoanodes. *Journal of Materials Science: Materials in Electronics*, *25*(2), 1122-1126. https://doi.org/10.1007/s10854-013-1698-9

Liu, R., Yang, W.-D., Qiang, L.-S., & Liu, H.-Y. (2012). Conveniently fabricated heterojunction ZnO/TiO_2 electrodes using TiO_2 nanotube arrays for dye-sensitized solar cells. *Journal of Power Sources*, *220*(1), 153-159. https://doi.org/10.1016/j.jpowsour.2012.07.097

Liu, X., Liu, Z., Ye, H., Tu, Y., Sun, B., Tan, X., Shi, T., Tang, Z., & Liao, G. (2018). Novel efficient C_{60}-based inverted perovskite solar cells with negligible hysteresis. *Electrochimica Acta*, *288*(1), 115-125. https://doi.org/10.1016/j.electacta.2018.09.004

Liu, Y., Sun, Y., & Rockett, A. (2012). A new simulation software of solar cells—wxAMPS. *Solar Energy Materials and Solar Cells*, *98*(1), 124-128. https://doi.org/10.1016/j.solmat.2011.10.010

Lo, C.-F., Hsu, S.-J., Wang, C.-L., Cheng, Y.-H., Lu, H.-P., Diau, E. W.-G., & Lin, C.-Y. (2010). Tuning spectral and electrochemical properties of porphyrin-sensitized solar cells. *The Journal of Physical Chemistry C*, *114*(27), 12018-12023. https://doi.org/10.1021/jp103561c

Lu, T.-F., Li, W., & Zhang, H.-X. (2018). Rational design of metal-free organic D-π-A dyes in dye-sensitized solar cells: Insight from density functional theory (DFT) and time-dependent DFT (TD-DFT) investigations. *Organic Electronics*, *59*(1), 131-139. https://doi.org/10.1016/j.orgel.2018.05.005

Ludin, N. A., Mahmoud, A. A.-A., Mohamad, A. B., Kadhum, A. A. H., Sopian, K., & Karim, N. S. A. (2014). Review on the development of natural dye photosensitizer for dye-sensitized solar cells. *Renewable and Sustainable Energy Reviews*, *31*(1), 386-396. https://doi.org/10.1016/j.rser.2013.12.001

Lunardi, M. M., Dias, P. R., Deng, R., & Corkish, R. (2021). Life Cycle Environmental Assessment of Different Solar Photovoltaic Technologies. *Photovoltaic Sustainability and Management*, *1*(1), 1-34. https://doi.org/10.1063/9780735423152_005

Lunt, R. R., Osedach, T. P., Brown, P. R., Rowehl, J. A., & Bulović, V. (2011). Practical roadmap and limits to nanostructured photovoltaics. *Advanced Materials*, *23*(48), 5712-5727. https://doi.org/10.1002/adma.201103404

Luo, J.-H., Mo, Y.-F., Li, Z.-S., & Du, F.-Y. (2021). Doping effects on catechol functionalized anatase TiO_2 (101) surface for dye-sensitized solar cells. *Materials Research Express*, *8*(1), 015906. https://doi.org/10.1088/2053-1591/abdc3c

Madan, J., Garg, S., Gupta, K., Rana, S., Manocha, A., & Pandey, R. (2020). Numerical simulation of charge transport layer free perovskite solar cell using metal work function shifted contacts. *Optik*, *202*(1), 163646. https://doi.org/10.1016/j.ijleo.2019.163646

Maddah, H. A. (2022). Machine learning analysis on performance of naturally-sensitized solar cells. *Optical Materials*, *128*(1), 112343. https://doi.org/10.1016/j.optmat.2022.112343

Mahmood, K., Sarwar, S., & Mehran, M. T. (2017). Current status of electron transport layers in perovskite solar cells: materials and properties. *Rsc Advances*, *7*(28), 17044-17062. https://doi.org/10.1039/c7ra00002b

Mahmood, K., Swain, B. S., Kirmani, A. R., & Amassian, A. (2015). Highly efficient perovskite solar cells based on a nanostructured WO_3–TiO_2 core–shell electron transporting material. *Journal of Materials Chemistry A*, *3*(17), 9051-9057. https://doi.org/10.1039/c4ta04883k

Maldonado-Valdivia, A. I., Galindo, E. G., Ariza, M. J., & Garcia-Salinas, M. J. (2013). Surfactant influence in the performance of titanium dioxide photoelectrodes for dye-sensitized solar cells. *Solar Energy*, *91*(1), 263-272. https://doi.org/10.1016/j.solener.2013.02.009

Mali, S. S., Patil, J. V., Kim, H., & Hong, C. K. (2018). Synthesis of SnO_2 nanofibers and nanobelts electron transporting layer for efficient perovskite solar cells. *Nanoscale*, *10*(17), 8275-8284. https://doi.org/10.1039/c8nr00695d

Malik, P., Chandel, R., & Chandel, S. S. (2021). A power prediction model and its validation for a roof top photovoltaic power plant considering module degradation. *Solar Energy*, *224*(1), 184-194. https://doi.org/10.1016/j.solener.2021.06.015

Manaa, M. B., Issaoui, N., Al-Ghamdi, Y. O., Belmabrouk, H., & Lamine, A. B. (2020). A microscopic and macroscopic investigation of the adsorption of N719 dye on ZnO nanopowders (ZNP) and ZnO nanorods (ZNR) for dye sensitized solar cells using statistical physics treatment and DFT simulation. *RSC advances*, *10*(46), 27615-27632. https://doi.org/10.1039/D0RA03581E

Manfredi, N., Bianchi, A., Causin, V., Ruffo, R., Simonutti, R., & Abbotto, A. (2014). Electrolytes for quasi solid-state dye-sensitized solar cells based on block copolymers. *Journal of Polymer Science Part A: Polymer Chemistry*, *52*(5), 719-727. https://doi.org/10.1002/pola.27055

MaríSoucase, B., Pradas, I. G., & Adhikari, K. R. (2016). Numerical simulations on perovskite photovoltaic devices. *Perovskite materials: synthesis, characterisation, properties, and applications*, 1(1), 445-486. https://doi.org/10.5772/61751

Markvart, T., & Castañer, L. (2013). Chapter IA-1-Principles of Solar Cell Operation. *Solar Cells, 1*(1), 3-25. https://doi.org/10.1016/b978-0-12-386964-7.00001-9

Mayabadi, A., Waman, V., Kamble, M., Ghosh, S., Gabhale, B., Rondiya, S., Rokade, A., Khadtare, S., Sathe, V., & Pathan, H. (2014). Evolution of structural and optical properties of rutile TiO_2 thin films synthesized at room temperature by chemical bath deposition method. *Journal of Physics and Chemistry of Solids*, *75*(2), 182-187. https://doi.org/10.1016/j.jpcs.2013.09.008

Mazumder, S., Mazumder, P., & Senthilkumar, K. (2022). Device modeling and study of AZO/i-ZnO/ZnS/CZTS-bilayer solar cell for different series and shunt resistances. *Solar Energy*, *245*(1), 46-57. https://doi.org/10.1016/j.solener.2022.08.055

Mehdizadeh-Rad, H., & Singh, J. (2019). Influence of interfacial traps on the operating temperature of perovskite solar cells. *Materials*, *12*(17), 2727. https://doi.org/10.3390/ma12172727

Mehrabian, M., & Dalir, S. (2018). Numerical simulation of highly efficient dye sensitized solar cell by replacing the liquid electrolyte with a semiconductor solid layer. *Optik*, *169*(1), 214-223. https://doi.org/10.1016/j.ijleo.2018.05.059

Mendes, J. O., Della Gaspera, E., & van Embden, J. (2022). High-Resistance Metal Oxide Window Layers for Optimal Front Contact Interfaces in Sb_2Se_3 Solar Cells. *Solar RRL*, *6*(8), 2200265. https://doi.org/10.1002/solr.202200265

Meng, Q.-B., Takahashi, K., Zhang, X.-T., Sutanto, I., Rao, T., Sato, O., Fujishima, A., Watanabe, H., Nakamori, T., & Uragami, M. (2003). Fabrication of an efficient solid-state dye-sensitized solar cell. *Langmuir*, *19*(9), 3572-3574. https://doi.org/10.1021/la026832n

Meng, S., & Kaxiras, E. (2010). Electron and hole dynamics in dye-sensitized solar cells: influencing factors and systematic trends. *Nano letters*, *10*(4), 1238-1247. https://doi.org/10.1021/nl100442e

Merlinsky, L. S., Pistonesi, C., Pronsato, M. E., Baraldo, L., & Williams, F. J. (2024). Electronic structure modulation in ruthenium (II) polypyridine complexes adsorbed on rutile TiO_2 (110) surfaces. *Surface Science*, *742*(1), 122452. https://doi.org/10.1016/j.susc.2024.122452

Messmer, C., Bivour, M., Schön, J., Glunz, S. W., & Hermle, M. (2018). Numerical simulation of silicon heterojunction solar cells featuring metal oxides as carrier-selective contacts. *IEEE Journal of Photovoltaics*, *8*(2), 456-464. https://doi.org/10.1109/jphotov.2018.2793762

Meyer, E. L., Mvokwe, S. A., Oyedeji, O. O., Rono, N., & Agoro, M. A. (2025). Computational Study of Chalcogenide-Based Perovskite Solar Cell Using SCAPS-1D Numerical Simulator. *Materials*, *18*(1), 186. https://doi.org/10.3390/ma18010186

Mills, E. F. E. A., Dong, J., Yiling, L., Baafi, M. A., Li, B., & Zeng, K. (2021). Towards sustainable competitiveness: How does financial development affect dynamic energy efficiency in Belt & Road economies? *Sustainable Production and Consumption*, *27*(1), 587-601. https://doi.org/10.1016/j.spc.2021.01.027

Minbashi, M., Omrani, M. K., Memarian, N., & Kim, D.-H. (2017). Comparison of theoretical and experimental results for band-gap-graded CZTSSe solar cell. *Current Applied Physics*, *17*(10), 1238-1243. https://doi.org/10.1016/j.cap.2017.06.003

Mingsukang, M. A., Buraidah, M. H., Arof, A. K., & Das, N. (2017). Third-generation-sensitized solar cells. *Nanostructured Solar Cells, 1*(1), 1-9. https://doi.org/10.5772/65290

Mirzaei, A., Janghorban, K., Hashemi, B., Hosseini, S. R., Bonyani, M., Leonardi, S. G., Bonavita, A., & Neri, G. (2016). Synthesis and characterization of mesoporous α-Fe_2O_3 nanoparticles and investigation of electrical properties of fabricated thick films. *Processing and Application of Ceramics*, *10*(4), 209-217. https://doi.org/10.2298/pac1604209m

Mohamed, H. (2014). Theoretical study of the efficiency of CdS/PbS thin film solar cells. *Solar Energy*, *108*(1), 360-369. https://doi.org/10.1016/j.solener.2014.07.017

Molapo, K. M., Ndangili, P. M., Ajayi, R. F., Mbambisa, G., Mailu, S. M., Njomo, N., Masikini, M., & Iwuoha, P. B. (2012). Electronics of conjugated polymers (I): Polyaniline. *International Journal of Electrochemical Science*, *7*(12), 11859-11875. https://doi.org/10.1016/s1452-3981(23)16509-6

Momeni, M. M., & Ghayeb, Y. (2015). Visible light-driven photoelectrochemical water splitting on ZnO–TiO_2 heterogeneous nanotube photoanodes. *Journal of Applied Electrochemistry*, *45*, 557-566. https://doi.org/10.1007/s10800-015-0836-x

Morales-Pumarino, D., & Barquera-Lozada, J. E. (2023). Electron density and its reduced density gradient in the study of π–π interactions. *International Journal of Quantum Chemistry*, *123*(18), e27051. https://doi.org/10.1002/qua.27051

Mortadi, A., El Hafidi, E., Nasrellah, H., Monkade, M., & El Moznine, R. (2024). Analysis and optimization of lead-free perovskite solar cells: investigating performance and electrical characteristics. *Materials for Renewable and Sustainable Energy*, *13*(2), 219-232. https://doi.org/10.1007/s40243-024-00260-z

Moses, G., Huang, X., Zhao, Y., Auf der Maur, M., Katz, E. A., & Gordon, J. M. (2020). InGaN/GaN multi-quantum-well solar cells under high solar concentration and elevated temperatures for hybrid solar thermal-photovoltaic power plants. *Progress in*

Photovoltaics: Research and Applications, *28*(11), 1167-1174. https://doi.org/10.1002/pip.3326

Mostefaoui, M., Mazari, H., Khelifi, S., Bouraiou, A., & Dabou, R. (2015). Simulation of high efficiency CIGS solar cells with SCAPS-1D software. *Energy Procedia*, *74*(1), 736-744. https://doi.org/10.1016/j.egypro.2015.07.809

Movla, H. (2014). Optimization of the CIGS based thin film solar cells: Numerical simulation and analysis. *Optik*, *125*(1), 67-70. https://doi.org/10.1016/j.ijleo.2013.06.034

Mujtahid, F., Gareso, P. L., Armynah, B., & Tahir, D. (2022). Review effect of various types of dyes and structures in supporting performance of dye-sensitized solar cell TiO_2-based nanocomposites. *International Journal of Energy Research*, *46*(2), 726-742. https://doi.org/10.1002/er.7310

Muñoz-García, A. B., Benesperi, I., Boschloo, G., Concepcion, J. J., Delcamp, J. H., Gibson, E. A., Meyer, G. J., Pavone, M., Pettersson, H., & Hagfeldt, A. (2021). Dye-sensitized solar cells strike back. *Chemical Society Reviews*, *50*(22), 12450-12550. https://doi.org/10.1039/d0cs01336f

Mustafa, F. M., Abdel Khalek, A. A., Mahboob, A. A., & Abdel-Latif, M. K. (2023). Designing Efficient Metal-Free Dye-Sensitized Solar Cells: A Detailed Computational Study. *Molecules*, *28*(17), 6177. https://doi.org/10.3390/molecules28176177

Nabil, E., Hasanein, A. A., Alnoman, R. B., & Zakaria, M. (2021). Optimizing the Cosensitization Effect of SQ02 Dye on BP-2 Dye-Sensitized Solar Cells: A Computational Quantum Chemical Study. *Journal of Chemical Information and Modeling*, *61*(10), 5098-5116. https://doi.org/10.1021/acs.jcim.1c00739

Nadimi, R., Tokimatsu, K., & Yoshikawa, K. (2017). Sustainable energy policy options in the presence of quality of life, poverty, and CO_2 emission. *Energy Procedia*, *142*(1), 2959-2964. https://doi.org/10.1016/j.egypro.2017.12.314

Naik, P., Babu, D. D., & Jayaprakash, G. K. (2023). A computational approach for screening carbazole based organic dyes as potential photosensitizers for DSSCs application. *Results in Chemistry*, *6*(1), 101000. https://doi.org/10.1016/j.rechem.2023.101000

Nalçakan, H., Kurtay, G., Sarıkavak, K., Şen, N., & Sevin, F. (2023). Computational insights into bis-N, N-dimethylaniline based D-π-A photosensitizers bearing divergent-type of π-linkers for DSSCs. *Journal of Molecular Graphics and Modelling*, *122*(1), 108485. https://doi.org/10.1016/j.jmgm.2023.108485

Nam, S.-H., Lee, K. H., Yu, J.-H., & Boo, J.-H. (2019). Review of the development of dyes for dye-sensitized solar cells. *Applied Science and Convergence Technology*, *28*(6), 194-206. https://doi.org/10.5757/asct.2019.28.6.194

Naqvi, S., & Patra, A. (2021). Hole transport materials for perovskite solar cells: A computational study. *Materials Chemistry and Physics*, *258*(1), 123863. https://doi.org/10.1016/j.matchemphys.2020.123863

Nath, D. C., Kundu, I., Sharma, A., Shivhare, P., Afzal, A., Soudagar, M. E. M., & Park, S. G. (2023). Internet of Things integrated with solar energy applications: a state-of-the-art review. *Environment, Development and Sustainability*, *26*(10), 24597-24652. https://doi.org/10.1007/s10668-023-03691-2

Nath, N. C. D., Choi, S. Y., Jeong, H. W., Lee, J.-J., & Park, H. (2016). Stand-alone photoconversion of carbon dioxide on copper oxide wire arrays powered by tungsten trioxide/dye-sensitized solar cell dual absorbers. *Nano Energy*, *25*(1), 51-59. https://doi.org/10.1016/j.nanoen.2016.04.025

Nazari, M. T., Mazutti, J., Basso, L. G., Colla, L. M., & Brandli, L. (2021). Biofuels and their connections with the sustainable development goals: a bibliometric and systematic review. *Environment, Development and Sustainability*, *23*(8), 11139-11156. https://doi.org/10.1007/s10668-020-01110-4

Nazeeruddin, M. K., Baranoff, E., & Grätzel, M. (2011). Dye-sensitized solar cells: A brief overview. *Solar Energy*, *85*(6), 1172-1178. https://doi.org/10.1016/j.solener.2011.01.018

Nazeeruddin, M. K., Pechy, P., Renouard, T., Zakeeruddin, S. M., Humphry-Baker, R., Comte, P., Liska, P., Cevey, L., Costa, E., & Shklover, V. (2001). Engineering of efficient panchromatic sensitizers for nanocrystalline TiO_2-based solar cells. *Journal of the American Chemical Society*, *123*(8), 1613-1624. https://doi.org/10.1021/ja003299u

Neukom, M., Züfle, S., Jenatsch, S., & Ruhstaller, B. (2018). Opto-electronic characterization of third-generation solar cells. *Science and Technology of advanced MaTerialS*, *19*(1), 291-316. https://doi.org/10.1080/14686996.2018.144209

Nisar, J., Topalian, Z., De Sarkar, A., Österlund, L., & Ahuja, R. (2013). TiO_2-based gas sensor: a possible application to SO_2. *ACS Applied Materials & Interfaces*, *5*(17), 8516-8522. https://doi.org/10.1021/am4018835

Nizamuddin, A., Arith, F., Rong, J., Zaim, M., Rahimi, A. S., & Saat, S. (2021). Investigation of copper (I) thiocyanate (CuSCN) as a hole transporting layer for perovskite solar cells application. *Journal of Advanced Research in Fluid Mechanics and Thermal Sciences*, *78*(2), 153-159. https://doi.org/10.37934/arfmts.78.2.153159

Noman, M., Sherwani, T., Jan, S. T., & Ismail, M. (2023). Exploring the impact of kesterite charge transport layers on the photovoltaic properties of $MAPbI_3$ perovskite solar cells. *Physica Scripta*, *98*(12), 125507. https://doi.org/10.1088/1402-4896/ad07c1

Nowotny, J., Alim, M. A., Bak, T., Idris, M. A., Ionescu, M., Prince, K., Sahdan, M. Z., Sopian, K., Teridi, M. A. M., & Sigmund, W. (2015). Defect chemistry and defect engineering of TiO_2-based semiconductors for solar energy conversion. *Chemical Society Reviews*, *44*(23), 8424-8442. https://doi.org/10.1039/c4cs00469h

O'regan, B., & Grätzel, M. (1991). A low-cost, high-efficiency solar cell based on dye-sensitized colloidal TiO_2 films. *nature*, *353*(6346), 737-740. https://doi.org/10.1038/353737a0

O'Regan, B., Lenzmann, F., Muis, R., & Wienke, J. (2002). A solid-state dye-sensitized solar cell fabricated with pressure-treated P25− TiO_2 and CuSCN: Analysis of pore filling and IV characteristics. *Chemistry of Materials*, *14*(12), 5023-5029. https://doi.org/10.1021/cm020572d

Ojotu, K. A., & Babaji, G. (2020). Simulation of an Optimized Poly 3-Hexylthiophene (P3HT) based solid state Dye Sensitized Solar Cell (ss-DSSC) using SCAPS. *International Journal Modern Research. Engineering Technology*, *5*(2), 1-10. https://ijmret.org/paper/V5I2/05020110.pdf

Olusola, O., Ewetumo, T., Obagade, T., & Adedayo, K. (2018). Electronic Behaviour of Schottky Diodes Fabricated from Electroplated CdSe Semiconductors. *Asian Journal of Research and Reviews in Physics*, *1*(1), 1-8. https://doi.org/10.9734/ajr2p/2018/v1i224603

Omar, A., & Abdullah, H. (2014). Electron transport analysis in zinc oxide-based dye-sensitized solar cells: a review. *Renewable and Sustainable Energy Reviews*, *31*(1), 149-157. https://doi.org/10.1016/j.rser.2013.11.031

Omar, A., Ali, M. S., & Abd Rahim, N. (2020). Electron transport properties analysis of titanium dioxide dye-sensitized solar cells (TiO_2-DSSCs) based natural dyes using electrochemical impedance spectroscopy concept: A review. *Solar Energy*, *207*(1), 1088-1121. https://doi.org/10.1016/j.solener.2020.07.028

Ouslimane, T., Et-Taya, L., Elmaimouni, L., & Benami, A. (2021). Impact of absorber layer thickness, defect density, and operating temperature on the performance of $MAPbI_3$ solar cells based on ZnO electron transporting material. *Heliyon*, *7*(3), e06379. https://doi.org/10.1016/j.heliyon.2021.e06379

Pandit, N. A., & Ahmad, T. (2022). Tin oxide based hybrid nanostructures for efficient gas sensing. *Molecules*, *27*(20), 7038. https://doi.org/10.3390/molecules27207038

Pang, S., Xie, T., Zhang, Y., Wei, X., Yang, M., Wang, D., & Du, Z. (2007). Research on the effect of different sizes of ZnO nanorods on the efficiency of TiO_2-based dye-sensitized solar cells. *The Journal of Physical Chemistry C*, *111*(49), 18417-18422. https://doi.org/10.1021/jp0763073

Pastore, M., & Angelis, F. D. (2013). Modeling materials and processes in dye-sensitized solar cells: understanding the mechanism, improving the efficiency. *Multiscale modelling of organic and hybrid photovoltaics*, *1*(1), 151-236. https://doi.org/10.1007/128_2013_468

Patel, M., Kim, H.-S., Kim, J., Yun, J.-H., Kim, S. J., Choi, E. H., & Park, H.-H. (2017). Excitonic metal oxide heterojunction (NiO/ZnO) solar cells for all-transparent module integration. *Solar Energy Materials and Solar Cells*, *170*(1), 246-253. https://doi.org/10.1016/j.solmat.2017.06.006

Patni, N., Sharma, P., Parikh, M., Joshi, P., & Pillai, S. G. (2018). Cost effective approach of using substrates for electrodes of enhanced efficient dye sensitized solar cell. *Materials Research Express*, *5*(9), 095509. https://doi.org/10.1088/2053-1591/aad952

Perera, V., & Tennakone, K. (2003). Recombination processes in dye-sensitized solid-state solar cells with CuI as the hole collector. *Solar energy materials and solar cells*, *79*(2), 249-255. https://doi.org/10.1016/s0927-0248(03)00103-x

Periyasamy, K., Sakthivel, P., Venkatesh, G., Vennila, P., Mary, Y. S., & Haseena, S. (2023). Structural and Photophysical Studies of Triphenylamine-Based Organic Dyes for Applications in DSSCs: Experimental and DFT Analysis. *Polycyclic Aromatic Compounds*, *44*(8), 5314-5337. https://doi.org/10.1080/10406638.2023.2264450

Peter, L. M. (2007). Characterization and modeling of dye-sensitized solar cells. *The Journal of Physical Chemistry C*, *111*(18), 6601-6612. https://doi.org/10.1021/jp069058b

Pinto, A. H., Nogueira, A. E., Dalmaschio, C. J., Frigini, I. N., de Almeida, J. C., Ferrer, M. M., Berengue, O. M., Gonçalves, R. A., & de Mendonça, V. R. (2022). Doped tin dioxide (d-SnO_2) and its nanostructures: review of the theoretical aspects, photocatalytic and biomedical applications. *Solids*, *3*(2), 327-360. https://doi.org/10.3390/solids3020024

Pockett, A., Spence, M., Thomas, S. K., Raptis, D., Watson, T., & Carnie, M. J. (2021). Beyond the First Quadrant: Origin of the High Frequency Intensity-Modulated Photocurrent/Photovoltage Spectroscopy Response of Perovskite Solar Cells. *Solar Rrl*, *5*(5), 2100159. https://doi.org/10.1002/solr.202100159

Portillo-Cortez, K., Martínez, A., Dutt, A., & Santana, G. (2019). N719 Derivatives for application in a dye-sensitized solar cell (DSSC): a theoretical study. *The Journal of Physical Chemistry A*, *123*(51), 10930-10939. https://doi.org/10.1021/acs.jpca.9b09024

Prabakar, K., Son, M., Kim, W.-Y., & Kim, H. (2011). TiO_2 thin film encapsulated ZnO nanorod and nanoflower dye sensitized solar cells. *Materials Chemistry and Physics*, *125*(1-2), 12-14. https://doi.org/10.1016/j.matchemphys.2010.09.028

Prajapat, K., Dhonde, M., Sahu, K., Bhojane, P., Murty, V., & Shirage, P. M. (2023). The evolution of organic materials for efficient dye-sensitized solar cells. *Journal of Photochemistry and*

Photobiology C: Photochemistry Reviews, *1*(1), 100586. https://doi.org/10.1016/j.jphotochemrev.2023.100586

Prayogi, S., & Marzuki, M. I. (2022). The Effect of addition of SnO_2 doping on the electronic structure of TiO_2 thin film as photo-anode in DSSC applications. *Journal of Emerging Supply Chain, Clean Energy, and Process Engineering*, *1*(1), 1-6. https://doi.org/10.57102/jescee.v1i1.3

Premalal, E., Dematage, N., Kumara, G., Rajapakse, R., Shimomura, M., Murakami, K., & Konno, A. (2012). Preparation of structurally modified, conductivity enhanced-p-CuSCN and its application in dye-sensitized solid-state solar cells. *Journal of Power Sources*, *203*(1), 288-296. https://doi.org/10.1016/j.jpowsour.2011.12.034

Qu, H., & Li, X. (2019). Temperature dependency of the fill factor in PV modules between 6 and 40 °C. *Journal of Mechanical Science & Technology*, *33*(4), 1981-1986. https://doi.org/10.1007/s12206-019-0348-4

Rahman, S., Haleem, A., Siddiq, M., Hussain, M. K., Qamar, S., Hameed, S., & Waris, M. (2023). Research on dye sensitized solar cells: recent advancement toward the various constituents of dye sensitized solar cells for efficiency enhancement and future prospects. *Rsc Advances*, *13*(28), 19508-19529. https://doi.org/10.1039/d3ra00903c

Rahman, S. I., Faisal, S., Ahmed, S., & Dhrubo, T. I. (2017). A comparative study on different HTMs in perovskite solar cell with ZnOS electron transport layer. 2017 IEEE Region 10 Humanitarian Technology Conference (R10-HTC), *1*(1) 546-550. https://doi.org/10.1109/r10-htc.2017.8289019

Rahmatian, M., Sayyaadi, H., & Ameri, M. (2024). Indoor photovoltaics: A numerical model of dye-sensitized solar cells based on indoor illumination for the Internet of Things applications. *Energy Conversion and Management: X*, *1*(1), 100606. https://doi.org/10.1016/j.ecmx.2024.100606

Rai, N., Rai, S., Singh, P. K., Lohia, P., & Dwivedi, D. (2020). Analysis of various ETL materials for an efficient perovskite solar cell by numerical simulation. *Journal of Materials Science: Materials in Electronics*, *1*(1), 1-12. https://doi.org/10.1007/s10854-020-04175-z

Raiford, J. A., Boyd, C. C., Palmstrom, A. F., Wolf, E. J., Fearon, B. A., Berry, J. J., McGehee, M. D., & Bent, S. F. (2019). Enhanced nucleation of atomic layer deposited contacts improves operational stability of perovskite solar cells in air. *Advanced Energy Materials*, *9*(47), 1902353. https://doi.org/10.1002/aenm.201902353

Raj, A., Kumar, M., & Anshul, A. (2021). Recent advancement in inorganic-organic electron transport layers in perovskite solar cell: current status and future outlook. *Materials Today Chemistry*, *22*(1), 100595. https://doi.org/10.1016/j.mtchem.2021.100595

Raj, A., Kumar, M., Singh, P. K., Singh, R. C., Bherwani, H., Gupta, A., & Anshul, A. (2021). A computational approach to investigate the suitable ETL for lead-free $CsGeI_3$ based perovskite solar cell. *Materials Today: Proceedings*, *47*(1), 1564-1569. https://doi.org/10.1016/j.matpr.2021.03.610

Raja, R., Govindaraj, M., Antony, M. D., Krishnan, K., Velusamy, E., Sambandam, A., Subbaiah, M., & Rayar, V. W. (2017). Effect of TiO_2/reduced graphene oxide composite thin film as a blocking layer on the efficiency of dye-sensitized solar cells. *Journal of Solid State Electrochemistry*, *21*(3), 891-903. https://doi.org/10.1007/s10008-016-3437-7

Ramanujam, J., & Singh, U. P. (2017). Copper indium gallium selenide based solar cells–a review. *Energy & Environmental Science*, *10*(6), 1306-1319. https://doi.org/10.1039/c7ee00826k

Ranasinghe, C., Wanninnayake, W., Kumara, G., Rajapakshe, R., & Sirimanne, P. (2014). An enhancement of efficiency of a solid-state dye-sensitized solar cell due to cocktail effect of N719 and black dye. *Optik*, *125*(2), 813-815. https://doi.org/10.1016/j.ijleo.2013.07.068

Rangel-Kuoppa, V.-T., Hérnandez-Vásquez, C., Flores-Márquez, J.-M., González-Trujillo, M.-Á., & Contreras-Puente, G.-S. (2018). Shunt resistance and saturation current determination in CdTe and CIGS solar cells. Part 1: A new theoretical procedure and comparison with other methodologies. *Semiconductor Science and Technology*, *33*(4), 045007. https://doi.org/10.1088/1361-6641/aab017

Ranjusha, R., Lekha, P., Subramanian, K., Shantikumar, V. N., & Balakrishnan, A. (2011). Photoanode activity of ZnO nanotube based dye-sensitized solar cells. *Journal of Materials Science & Technology*, *27*(11), 961-966. https://doi.org/10.1016/s1005-0302(11)60170-9

Raoui, Y., Ez-Zahraouy, H., Kazim, S., & Ahmad, S. (2021). Energy level engineering of charge selective contact and halide perovskite by modulating band offset: Mechanistic insights. *Journal of Energy Chemistry*, *54*(1), 822-829. https://doi.org/10.1016/j.jechem.2020.06.030

Ravidas, B. K., Roy, M. K., & Samajdar, D. P. (2023). Investigation of photovoltaic performance of lead-free $CsSnI_3$-based perovskite solar cell with different hole transport layers: First Principle Calculations and SCAPS-1D Analysis. *Solar Energy*, *249*(1), 163-173. https://doi.org/10.1016/j.solener.2022.11.025

Ravishankar, S., Riquelme, A., Sarkar, S. K., Garcia-Batlle, M., Garcia-Belmonte, G., & Bisquert, J. (2019). Intensity-modulated photocurrent spectroscopy and its application to perovskite solar cells. *The Journal of Physical Chemistry C*, *123*(41), 24995-25014. https://doi.org/10.1021/acs.jpcc.9b07434

Reynaud, C. A., Clerc, R., Lechêne, P. B., Hébert, M., Cazier, A., & Arias, A. C. (2019). Evaluation of indoor photovoltaic power production under directional and diffuse lighting conditions. *Solar energy materials and solar cells*, *200*(1), 110010. https://doi.org/10.1016/j.solmat.2019.110010

Rezaei-Sameti, M., Rahmenai, F., & Satari, M. (2025). Exploring the molecular interactions between Busulfan anticancer drug and DNA/RNA nucleobases: A comprehensive computational analysis utilizing DFT, TD-DFT, AIM, RDG, solvent effect, and docking techniques. *Journal of Molecular Liquids*, *425*(1), 127175. https://doi.org/10.1016/j.molliq.2025.127175

Roghabadi, F. A., Alidaei, M., Mousavi, S. M., Ashjari, T., Tehrani, A. S., Ahmadi, V., & Sadrameli, S. M. (2019). Stability progress of perovskite solar cells dependent on the crystalline structure: From 3D ABX_3 to 2D Ruddlesden–Popper perovskite absorbers. *Journal of Materials Chemistry A*, *7*(11), 5898-5933. https://doi.org/10.1039/c8ta10444a

Rondan-Gómez, Ayala-Mató, F., Seuret-Jiménez, D., Santana-Rodríguez, G., Zamudio-Lara, A., De Los Santos, I. M., & Seuret-Hernández, H. (2020). New architecture in dye sensitized solar cells: A SCAPS-1D simulation study. *Optical and Quantum Electronics*, *52*(6), 1-11. https://doi.org/10.1007/s11082-020-02437-y

Rondán-Gómez, V., Montoya De Los Santos, I., Seuret-Jiménez, D., Ayala-Mató, F., Zamudio-Lara, A., Robles-Bonilla, T., & Courel, M. (2019). Recent advances in dye-sensitized solar cells. *Applied Physics A*, *125*(1), 1-24. https://doi.org/10.1007/s00339-019-3116-5

Rono, N., Merad, A. E., Kibet, J. K., Martincigh, B. S., & Nyamori, V. O. (2021a). Optimization of Hole Transport Layer Materials for a Lead-Free Perovskite Solar Cell Based on Formamidinium Tin Iodide. *Energy Technology*, *9*(12), 2100859. https://doi.org/10.1002/ente.202100859

Rono, N., Merad, A. E., Kibet, J. K., Martincigh, B. S., & Nyamori, V. O. (2021b). A theoretical investigation of the effect of the hole and electron transport materials on the performance of a lead-free perovskite solar cell based on $CH_3NH_3SnI_3$. *Journal of Computational Electronics*, *20*(2), 993-1005. https://doi.org/10.1007/s10825-021-01673-z

Rouway, M., Boulahia, Z., Chakhchaoui, N., Fouzia, F., Omari, L. E. H., Cherkaoui, O., & Van Langenhove, L. (2020). Mathematical and numerical modelling of soiling effects of photovoltaic solar panels on their electrical performance. *IOP Conference Series: Materials Science and Engineering*, *827*(1), 012064. https://doi.org/10.1088/1757-899x/827/1/012064

Rudra, S., Sarker, S., & Kim, D. M. (2019). Review on simulation of current–voltage characteristics of dye-sensitized solar cells. *Journal of Industrial and Engineering Chemistry*, *80*(1), 516-526. https://doi.org/10.1016/j.jiec.2019.08.030

Saeed, M., Marwani, H. M., Shahzad, U., Asiri, A. M., & Rahman, M. M. (2024). Recent advances, challenges, and future perspectives of ZnO nanostructure materials towards energy applications. *The Chemical Record*, *24*(1), e202300106. https://doi.org/10.1002/tcr.202300106

Sahoo, D., & Manik, N. (2023). Study on the effect of temperature on electrical and photovoltaic parameters of lead-free tin-based Perovskite solar cell. *Indian Journal of Physics*, *97*(2), 447-455. https://doi.org/10.1007/s12648-022-02401-4

Saito, Y., Kitamura, T., Wada, Y., & Yanagida, S. (2002). Application of poly (3, 4-ethylenedioxythiophene) to counter electrode in dye-sensitized solar cells. *Chemistry Letters*, *31*(10), 1060-1061. https://doi.org/10.1246/cl.2002.1060

Sakai, N., Miyasaka, T., & Murakami, T. N. (2013). Efficiency enhancement of ZnO-based dye-sensitized solar cells by low-temperature $TiCl_4$ treatment and dye optimization. *The Journal of Physical Chemistry C*, *117*(21), 10949-10956. https://doi.org/10.1021/jp401106u

Sakamoto, H., Igarashi, S., Uchida, M., Niume, K., & Nagai, M. (2012). Highly efficient all solid state dye-sensitized solar cells by the specific interaction of CuI with NCS groups II. Enhancement of the photovoltaic characteristics. Organic Electronics, 13(3), 514-518. https://doi.org/10.1016/j.orgel.2011.11.017

Salas Castillo, M. S., Liu, X., Abd-AlHamid, F., Connelly, K., & Wu, Y. (2022). Intelligent windows for electricity generation: A technologies review. *Building Simulation*, *15*(10), 1747-1773. https://doi.org/10.1007/s12273-022-0895-y

Salmahaminati, Abe, M., Purnama, I., Mulyana, J. Y., & Hada, M. (2020). Density Functional Study of Metal-to-Ligand Charge Transfer and Hole-Hopping in Ruthenium (II) Complexes with Alkyl-Substituted Bipyridine Ligands. *ACS Omega*, *6*(1), 55-64. https://doi.org/10.1021/acsomega.0c01199

Samiul Islam, M., Sobayel, K., Al-Kahtani, A., Islam, M. A., Muhammad, G., Amin, N., Shahiduzzaman, M., & Akhtaruzzaman, M. (2021). Defect Study and Modelling of SnX_3-Based Perovskite Solar Cells with SCAPS-1D. *Nanomaterials (Basel)*, *11*(5), 1218 https://doi.org/10.3390/nano11051218

Samsuri, S., Rahman, M., & Umar, A. (2017). Comparative study of the properties of TiO_2 nanoflower and TiO_2-ZnO composite nanoflower and their application in dye-sensitized solar cells. *Ionics*, *23*(1), 1897-1902. https://doi.org/10.1007/s11581-017-2010-4

Samuel, J. J., & Yam, F. (2020). Photocatalytic degradation of methylene blue under visible light by dye sensitized titania. *Materials Research Express*, *7*(1), 015051. https://doi.org/10.1088/2053-1591/ab6409

Sanda, M. D., Badu, M., Awudza, J., & Boadi, N. (2021). Development of TiO_2-based dye-sensitized solar cells using natural dyes extracted from some plant-based materials. *Chemistry International*, *7*(1), 9-20. https://doi.org/10.31219/osf.io/ybxgd

Sangpongsanont, Y., Chenvidhya, D., Chuangchote, S., & Kirtikara, K. (2020). Corrosion growth of solar cells in modules after 15 years of operation. *Solar Energy*, *205*(1), 409-431. https://doi.org/10.1016/j.solener.2020.05.016

Santika, W. G., Anisuzzaman, M., Bahri, P. A., Shafiullah, G., Rupf, G. V., & Urmee, T. (2019). From goals to joules: A quantitative approach of interlinkages between energy and the Sustainable Development Goals. *Energy Research & Social Science*, *50*(1), 201-214. https://doi.org/10.1016/j.erss.2018.11.016

Sati, M., & Verma, M. (2021). Fundamentals of energy: its potentials and achievements. In *Renewable Energy and Green Technology* (pp. 1-12). CRC Press. https://doi.org/10.1201/9781003175926-1

Seeger, Z. L., & Izgorodina, E. I. (2020). A systematic study of DFT performance for geometry optimizations of ionic liquid clusters. *Journal of Chemical Theory and Computation*, *16*(10), 6735-6753. https://doi.org/10.1021/acs.jctc.0c00549

Sekar, N., & Gehlot, V. Y. (2010). Metal complex dyes for dye-sensitized solar cells: Recent developments. *Resonance*, *15*(9), 819-831. https://doi.org/10.1007/s12045-010-0091-8

Sen, A., Putra, M. H., Biswas, A. K., Behera, A. K., & Groβ, A. (2023). Insight on the choice of sensitizers/dyes for dye sensitized solar cells: A review. *Dyes and Pigments*, *213*(1), 111087. https://doi.org/10.1016/j.dyepig.2023.111087

Shabir, G., Arooj, S., Javed, A. H., Saeed, A., Shahzad, N., Iqbal, N., & Jabeen, E. (2022). The Development of Highly Fluorescent Hemicyanine and Dicyanoisophorone Dyes for Applications in Dye-Sensitized Solar Cells. *Journal of Fluorescence*, *32*(2), 799-815. https://doi.org/10.1007/s10895-021-02873-3

Shahpari, M., Behjat, A., Khajaminian, M., & Torabi, N. (2015). The influence of morphology of hematite (α-Fe_2O_3) counter electrodes on the efficiency of dye-sensitized solar cells. *Solar Energy*, *119*(1), 45-53. https://doi.org/10.1016/j.solener.2015.06.039

Shalini, S., Balasundaraprabhu, R., Kumar, T. S., Prabavathy, N., Senthilarasu, S., & Prasanna, S. (2016). Status and outlook of sensitizers/dyes used in dye sensitized solar cells (DSSC): a review. *International Journal of Energy Research*, *40*(10), 1303-1320. https://doi.org/10.1002/er.3538

Shao, S., & Loi, M. A. (2020). The role of the interfaces in perovskite solar cells. *Advanced Materials Interfaces*, *7*(1), 1901469. https://doi.org/10.1002/admi.201901469

Shariatinia, Z. (2020). Recent progress in development of diverse kinds of hole transport materials for the perovskite solar cells: A review. *Renewable and Sustainable Energy Reviews*, *119*(1), 109608. https://doi.org/10.1016/j.rser.2019.109608

Sharma, G., Singh, S. P., Kurchania, R., & Ball, R. (2013). Cosensitization of dye sensitized solar cells with a thiocyanate free Ru dye and a metal free dye containing thienylfluorene conjugation. *RSC advances*, *3*(17), 6036-6043. https://doi.org/10.1039/c3ra23155k

Sharma, K., Sharma, V., & Sharma, S. S. (2018). Dye-Sensitized Solar Cells: Fundamentals and Current Status. *Nanoscale Research Letters*, *13*(1), 381. https://doi.org/10.1186/s11671-018-2760-6

Sharma, V. (2020). Optical properties of tin oxide nanomaterials. *Tin Oxide Materials*, *1*(1), 61-99. https://doi.org/10.1016/b978-0-12-815924-8.00004-9

Shi, Y., Wang, K., Du, Y., Zhang, H., Gu, J., Zhu, C., Wang, L., Guo, W., Hagfeldt, A., & Wang, N. (2013). Solid-state synthesis of ZnO nanostructures for quasi-solid dye-sensitized solar cells with high efficiencies up to 6.46%. *Advanced Materials*, *25*(32), 4413-4419. https://doi.org/10.1002/adma.201301852

Shin, S. S., Kim, K., Yoo, J., Kim, J. H., Ahn, S., Cho, A., Kim, D., Jo, Y., Jeong, I., & Shin, D. (2021). Heterojunction interface passivation strategy for Cu $(In_{1-x}, Ga_x)Se_2$ solar cell with nano-level engineering of Zn-based buffer structure via atomic layer deposition method. *Solar Energy Materials and Solar Cells*, *224*(1), 111010. https://doi.org/10.1016/j.solmat.2021.111010

Shum, K., Chen, Z., Qureshi, J., Yu, C., Wang, J. J., Pfenninger, W., Vockic, N., Midgley, J., & Kenney, J. T. (2010). Synthesis and characterization of $CsSnI_3$ thin films. *Applied Physics Letters*, *96*(22), 221903. https://doi.org/10.1063/1.3442511

Singh, A., Radicchi, E., Fantacci, S., Nunzi, F., De Angelis, F., & Gagliardi, A. (2019). Interface electrostatics of solid-state dye-sensitized solar cells: A joint drift-diffusion and density functional theory study. *The Journal of Physical Chemistry C*, *123*(24), 14955-14963. https://doi.org/10.1021/acs.jpcc.9b03658

Singh, D., Saini, R. K., & Bhagwan, S. (2018). Recent Developments in Dye-Sensitized Solar Cells and Potential Applications. *Emerging Photovoltaic Materials: Silicon & Beyond*, *1*(1), 443-486. https://doi.org/10.1002/9781119407690.ch12

Singh, N., Agarwal, A., & Agarwal, M. (2021). Performance evaluation of lead–free double-perovskite solar cell. *Optical Materials*, *114*(1), 110964. https://doi.org/10.1016/j.optmat.2021.110964

Singh, P., & Ravindra, N. M. (2012). Temperature dependence of solar cell performance—an analysis. *Solar Energy Materials and Solar Cells*, *101*(1), 36-45. https://doi.org/10.1016/j.solmat.2012.02.019

Singh, R., Sandhu, S., & Lee, J.-J. (2019). Elucidating the effect of shunt losses on the performance of mesoporous perovskite solar cells. *Solar Energy*, *193*(1), 956-961. https://doi.org/10.1016/j.solener.2019.10.018

Singh, S. (2021). Energy Crisis and Climate Change: Global Concerns and Their Solutions. *Energy: Crises, Challenges and Solutions*, *1*(1), 1-17. https://doi.org/10.1002/9781119741503.ch1

Sinha, N. K., Roy, P., Ghosh, D. S., & Khare, A. (2021). Simulation and analysis of schottky junction perovskite solar cells (SJPSCs). IOP Conference Series: Materials Science and Engineering, *1120*(1), 012017. https://doi.org/10.1088/1757-899x/1120/1/012017

Sinsermsuksakul, P., Hartman, K., Bok Kim, S., Heo, J., Sun, L., Hejin Park, H., Chakraborty, R., Buonassisi, T., & Gordon, R. G. (2013). Enhancing the efficiency of SnS solar cells via

band-offset engineering with a zinc oxysulfide buffer layer. *Applied Physics Letters*, *102*(5), 053901. https://doi.org/10.1063/1.4789855

Slami, A., BouchaouR, M., & Merad, L. (2019). Numerical Study of Based Perovskite Solar Cells by SCAPS-1D. *International Journal of Energy and Environment.*, *13*(1), 17-21. https://www.researchgate.net/publication/337797426_Numerical_Study_of_Based_Perovskite_Solar_Cells_by_SCAPS-1D

Smith, H. L., Dull, J. T., Longhi, E., Barlow, S., Rand, B. P., Marder, S. R., & Kahn, A. (2020). n-Doping of a Low-Electron-Affinity Polymer Used as an Electron-Transport Layer in Organic Light-Emitting Diodes. *Advanced Functional Materials*, *30*(17), 2000328. https://doi.org/10.1002/adfm.202000328

Snaith, H. J. (2010). Estimating the maximum attainable efficiency in dye-sensitized solar cells. *Advanced Functional Materials*, *20*(1), 13-19. https://doi.org/10.1002/adfm.200901476

Snaith, H. J., Humphry-Baker, R., Chen, P., Cesar, I., Zakeeruddin, S. M., & Grätzel, M. (2008). Charge collection and pore filling in solid-state dye-sensitized solar cells. *Nanotechnology*, *19*(42), 424003. https://doi.org/10.1088/0957-4484/19/42/424003

Sohag, M. A. Z., Kumari, P., Agrawal, R., Gupta, S., & Jamwal, A. (2020). Renewable Energy in Bangladesh: Current Status and Future Potentials. Proceedings of International Conference in Mechanical and Energy Technology, *1*(1), 353-363. https://doi.org/10.1007/978-981-15-2647-3_32

Stashans, A., Lunell, S., & Grimes, R. (1996). Theoretical study of perfect and defective TiO_2 crystals. *Journal of Physics and Chemistry of Solids*, *57*(9), 1293-1301. https://doi.org/10.1016/0022-3697(95)00321-5

Sun, S., Salim, T., Mathews, N., Duchamp, M., Boothroyd, C., Xing, G., Sum, T. C., & Lam, Y. M. (2014). The origin of high efficiency in low-temperature solution-processable bilayer organometal halide hybrid solar cells. *Energy & Environmental Science*, *7*(1), 399-407. https://doi.org/10.1039/c3ee43161d

Sutherland, B. R. (2017). Thermally decomposing perovskites one layer at a time. *Joule*, *1*(3), 423-424. https://doi.org/10.1016/j.joule.2017.10.019

Syafiq, U., Ataollahi, N., & Scardi, P. (2020). Progress in CZTS as hole transport layer in perovskite solar cell. *Solar Energy*, *196*(1), 399-408. https://doi.org/10.1016/j.solener.2019.12.016

Tahir, M., Din, I. U., Zeb, M., Aziz, F., Wahab, F., Gul, Z., Alamgeer, Sarker, M. R., Ali, S., & Ali, S. H. M. (2022). Thin Films Characterization and Study of N749-Black Dye for Photovoltaic Applications. *Coatings*, *12*(8), 1163. https://doi.org/10.3390/coatings12081163

Takahashi, K., Suzaka, S., Sigeyama, Y., Yamaguchi, T., Nakamura, J.-i., & Murata, K. (2007). Efficiency increase by insertion of electrodeposited CuSCN layer into ITO/organic solid interface in bulk hetero-junction solar cells consisting of polythiophene and fullerene. *Chemistry Letters*, *36*(6), 762-763. https://doi.org/10.1246/cl.2007.762

Tan, V., Dias, P. R., Chang, N., & Deng, R. (2022). Estimating the lifetime of solar photovoltaic modules in Australia. *Sustainability*, *14*(9), 5336. https://doi.org/10.3390/su14095336

Tayeb, A. M., Harfoosh, A. K., & Melegy, T. A. (2022). Investigation of the Effect of Type and Concentration of Dye on the Performance of TiO_2 Based Dye Sensitized Solar Cells. *Port-Said Engineering Research Journal*, *26*(4), 8-15. https://doi.org/10.21608/pserj.2022.94940.1141

Teixeira, C. O., Andrade, L., & Mendes, A. (2019). Novel carbon-based material for perovskite solar cells back-contact. *International Journal of Energy Research*, *43*(13), 7541-7546. https://doi.org/10.1002/er.4695

Temba, E. S., Reis, A. S., Kastner, G. F., Monteiro, R. P., & Moreira, R. M. (2016). Separation and determination of the difficult-to-measure radionuclide ^{99}Tc in radioactive wastes from nuclear power plants by using extraction chromatography and radiometric techniques. *Journal of Radioanalytical and Nuclear Chemistry*, *307*(2), 1453-1458. https://doi.org/10.1007/s10967-015-4359-z

Tennakone, K., Kumara, G., Kottegoda, I., Perera, V., Aponsu, G., & Wijayantha, K. (1998). Deposition of thin conducting films of CuI on glass. *Solar Energy Materials and Solar Cells*, *55*(3), 283-289. https://doi.org/10.1016/s0927-0248(98)00117-2

Tennakone, K., Kumara, G., Kumarasinghe, A., Wijayantha, K., & Sirimanne, P. (1995). A dye-sensitized nano-porous solid-state photovoltaic cell. *Semiconductor Science and Technology*, *10*(12), 1689. https://doi.org/10.1088/0268-1242/10/12/020

Todorov, T., Gunawan, O., & Guha, S. (2016). A road towards 25% efficiency and beyond: perovskite tandem solar cells. *Molecular Systems Design & Engineering*, *1*(4), 370-376. https://doi.org/10.1039/c6me00041j

Tsipis, A. C. (2014). DFT/TDDFT insights into the chemistry, biochemistry and photophysics of copper coordination compounds. *RSC advances*, *4*(61), 32504-32529. https://doi.org/10.1039/c4ra04921g

Ukoba, K., Yoro, K. O., Eterigho-Ikelegbe, O., Ibegbulam, C., & Jen, T.-C. (2024). Adaptation of solar power in the Global south: Prospects, challenges and opportunities. *Heliyon*, *10*(7), e28009. https://doi.org/10.1016/j.heliyon.2024.e28009

Uppal, H., Chawla, S., Joshi, A. G., Haranath, D., Vijayan, N., & Singh, N. (2019). Facile chemical synthesis and novel application of zinc oxysulfide nanomaterial for instant and superior adsorption of arsenic from water. *Journal of cleaner production*, *208*(1), 458-469. https://doi.org/10.1016/j.jclepro.2018.10.023

Veeramachaneni, V. (2025). Optimizing Renewable Energy Integration in AI-Driven Data Centers Using Quantum Algorithms. *Journal of Network Security and Data Mining*, *8*(1), 36-48. https://doi.org/10.5281/zenodo.14168045

Verschraegen, J., & Burgelman, M. (2007). Numerical modeling of intra-band tunneling for heterojunction solar cells in SCAPS. *Thin Solid Films*, *515*(15), 6276-6279. https://doi.org/10.1016/j.tsf.2006.12.049

Vigil-Galán, O., Courel, M., Andrade-Arvizu, J., Sánchez, Y., Espíndola-Rodríguez, M., Saucedo, E., Seuret-Jiménez, D., & Titsworth, M. (2015). Route towards low cost-high efficiency second generation solar cells: current status and perspectives. *Journal of Materials Science: Materials in Electronics*, *26*(8), 5562-5573. https://doi.org/10.1007/s10854-014-2196-4

Vossier, A., Hirsch, B., & Gordon, J. M. (2010). Is Auger recombination the ultimate performance limiter in concentrator solar cells? *Applied Physics Letters*, *97*(19), 193509. https://doi.org/10.1063/1.3510474

Wang, H., Yu, Z., Lai, J., Song, X., Yang, X., Hagfeldt, A., & Sun, L. (2018). One plus one greater than two: high-performance inverted planar perovskite solar cells based on a composite CuI/CuSCN hole-transporting layer. *Journal of Materials Chemistry A*, *6*(43), 21435-21444. https://doi.org/10.1039/c8ta07332e

Wang, J., Feng, L., Tang, X., Bentley, Y., & Höök, M. (2017). The implications of fossil fuel supply constraints on climate change projections: A supply-side analysis. *Futures*, *86*(1), 58-72. https://doi.org/10.1016/j.futures.2016.04.007

Wang, M., Chen, P., Humphry-Baker, R., Zakeeruddin, S. M., & Grätzel, M. (2009). The influence of charge transport and recombination on the performance of dye-sensitized solar cells. *ChemPhysChem*, *10*(1), 290-299. https://doi.org/10.1002/cphc.200800708

Wang, N., Hu, J., Gao, L., & Ma, T. (2020). Current Progress in Solid-State Electrolytes for Dye-Sensitized Solar Cells: A Mini-Review. *Journal of Electronic Materials*, *49*(12), 7085-7097. https://doi.org/10.1007/s11664-020-08483-2

Wang, Y.-F., Feng, H., Deng, Y.-R., Xin, F.-F., Li, D.-J., Hu, Z.-F., Zhang, L., & Liu, R.-P. (2022). Solvothermal growth of Zn2SnO4 for efficient dye-sensitized solar cells. *Rare Metals*, *41*(3), 942-950. https://doi.org/10.1007/s12598-021-01820-2

Wazzan, N., Soliman, K. A., & Jha, P. K. (2023). From molecule to device: DFT and SCAPS-1D simulations on the effect of aromaticity of π-linkers on enhancing the performance of anthanthrene-based dyes with D-π-A configuration in dye-sensitized solar cells. https://doi.org/10.21203/rs.3.rs-2646924/v1

Wei, L., Yang, Y., Zhu, Z., Fan, R., Wang, P., Dong, Y., & Chen, S. (2015). Effect of different donor groups in bis (6-methoxylpyridin-2-yl) substituted co-sensitizer on the performance of N719 sensitized solar cells. *Rsc Advances*, *5*(117), 96934-96944. https://doi.org/10.1039/c5ra19417b

Wei, W., Wang, H., & Hu, Y. H. (2014). A review on PEDOT-based counter electrodes for dye-sensitized solar cells. *International Journal of Energy Research*, *38*(9), 1099-1111. https://doi.org/10.1002/er.3178

Wijeyasinghe, N., Eisner, F., Tsetseris, L., Lin, Y. H., Seitkhan, A., Li, J., Yan, F., Solomeshch, O., Tessler, N., & Patsalas, P. (2018). p-Doping of Copper (I) Thiocyanate (CuSCN) Hole-Transport Layers for High-Performance Transistors and Organic Solar Cells. *Advanced Functional Materials*, *28*(31), 1802055. https://doi.org/10.1002/adfm.201802055

Wu, D., Wang, W., Ng, T. W., Huang, G., Xia, D., Yip, H. Y., Lee, H. K., Li, G., An, T., & Wong, P. K. (2016). Visible-light-driven photocatalytic bacterial inactivation and the mechanism of zinc oxysulfide under LED light irradiation. *Journal of Materials Chemistry A*, *4*(3), 1052-1059. https://doi.org/10.1039/c5ta08044d

Wu, N., Wu, Y., Walter, D., Shen, H., Duong, T., Grant, D., Barugkin, C., Fu, X., Peng, J., & White, T. (2017). Identifying the cause of voltage and fill factor losses in perovskite solar cells by using luminescence measurements. *Energy Technology*, *5*(10), 1827-1835. https://doi.org/10.1002/ente.201700374

Wu, T.-C., Huang, W.-M., Meen, T.-H., & Tsai, J.-K. (2023). Performance improvement of dye-sensitized solar cells with pressed TiO_2 nanoparticles layer. *Coatings*, *13*(5), 907. https://doi.org/10.3390/coatings13050907

Wu, Z., Wei, Y., An, Z., Chen, X., & Chen, P. (2014). Co-sensitization of N719 with an organic dye for dye-sensitized solar cells application. *Bulletin Korean Chemistry Society*, *35*(5), 1449. https://doi.org/10.5012/bkcs.2014.35.5.1449

Xiang, C., Zhao, X., Tan, L., Ye, J., Wu, S., Zhang, S., & Sun, L. (2019). A solar tube: Efficiently converting sunlight into electricity and heat. *Nano Energy*, *55*(1), 269-276. https://doi.org/10.1016/j.nanoen.2018.10.077

Xiang, P., Lv, F., Xiao, T., Jiang, L., Tan, X., & Shu, T. (2018). Improved performance of quasi-solid-state dye-sensitized solar cells based on iodine-doped TiO_2 spheres photoanodes. *Journal of Alloys and Compounds*, *741*(1), 1142-1147. https://doi.org/10.1016/j.jallcom.2018.01.220

Xiang, W., Liu, S., & Tress, W. (2021). Interfaces and interfacial layers in inorganic perovskite solar cells. *Angewandte Chemie International Edition*, *60*(51), 26440-26453. https://doi.org/10.1002/anie.202108800

Xie, Y.-L., Li, Z.-X., Xu, Z.-G., & Zhang, H.-L. (2011). Preparation of coaxial TiO_2/ZnO nanotube arrays for high-efficiency photo-energy conversion applications. *Electrochemistry Communications*, *13*(8), 788-791. https://doi.org/10.1016/j.elecom.2011.05.003

Xin, X., Liu, H.-Y., Ye, M., & Lin, Z. (2013). Semiconductor hierarchically structured flower-like clusters for dye-sensitized solar cells with nearly 100% charge collection efficiency. *Nanoscale*, *5*(22), 11220-11226. https://doi.org/10.1039/c3nr04370c

Xu, C., Wu, J., Desai, U. V., & Gao, D. (2012). High-efficiency solid-state dye-sensitized solar cells based on TiO_2-coated ZnO nanowire arrays. *Nano Letters*, *12*(5), 2420-2424. https://doi.org/10.1021/nl3004144

Xue, G., Guo, Y., Yu, T., Guan, J., Yu, X., Zhang, J., Liu, J., & Zou, Z. (2012). Degradation mechanisms investigation for long-term thermal stability of dye-sensitized solar cells. *International Journal Electrochemical Sci*ence, *7*(1), 1496-1511. https://doi.org/10.1016/s1452-3981(23)13430-4

Yadagiri, B., Kumar Kaliamurthy, A., Yoo, K., Cheol Kang, H., Ryu, J., Kwaku Asiam, F., & Lee, J. J. (2023). Molecular Engineering of Photosensitizers for Solid-State Dye-Sensitized Solar Cells: Recent Developments and Perspectives. *ChemistryOpen*, *12*(12), e202300170. https://doi.org/10.1002/open.202300170

Yadav, S. K., Ravishankar, S., Pescetelli, S., Agresti, A., Fabregat-Santiago, F., & Di Carlo, A. (2017). Stability of dye-sensitized solar cells under extended thermal stress. *Physical Chemistry Chemical Physics*, *19*(33), 22546-22554. https://doi.org/10.1039/c7cp04598k

Yahya, M., Bouziani, A., Ocak, C., Seferoğlu, Z., & Sillanpää, M. (2021). Organic/metal-organic photosensitizers for dye-sensitized solar cells (DSSC): Recent developments, new trends, and future perceptions. *Dyes and Pigments*, *192*(1), 109227. https://doi.org/10.1016/j.dyepig.2021.109227

Yang, K., Dai, Y., & Huang, B. (2020). Review of First-Principles Studies of TiO_2: Nanocluster, Bulk, and Material Interface. *Catalysts*, *10*(9), 972. https://doi.org/10.3390/catal10090972

Yang, Q., Wang, K., Yu, H., Zhu, X., Han, C., Deng, L., Yang, H., Zhao, F., Sun, X., & Zhang, Q. (2018). Surface polarization and recombination in organic-inorganic hybrid perovskite solar cells based on photo-and electrically induced negative capacitance studies. *Organic Electronics*, *62*(1), 203-208. https://doi.org/10.1016/j.orgel.2018.08.015

Yang, S., Kou, H., Wang, J., Xue, H., & Han, H. (2010). Tunability of the band energetics of nanostructured $SrTiO_3$ electrodes for dye-sensitized solar cells. *The Journal of Physical Chemistry C*, *114*(9), 4245-4249. https://doi.org/10.1021/jp9117979

Yang, X., Wang, W., Zhang, Y., & Sun, L. (2018). Improving the power conversion efficiency of solid state dye sensitized solar cells with a N-oxoammonium salt: 2, 2, 6, 6-Tetramethyl-1-oxopiperidinebromide. *Solar Energy*, *170*(1), 1001-1008. https://doi.org/10.1016/j.solener.2018.06.040

Yashwantrao, G., & Saha, S. (2022). Perspective on the rational design strategies of quinoxaline derived organic sensitizers for dye-sensitized solar cells (DSSC). *Dyes and Pigments*, *1*(1), 110093. https://doi.org/10.1016/j.dyepig.2022.110093

Yi, Z., Zeng, Y., Wu, H., Chen, X., Fan, Y., Yang, H., Tang, Y., Yi, Y., Wang, J., & Wu, P. (2019). Synthesis, surface properties, crystal structure and dye-sensitized solar cell performance of TiO_2 nanotube arrays anodized under different parameters. *Results in Physics*, *15*(1), 102609. https://doi.org/10.1016/j.rinp.2019.102609

Yikun, Z., Gul, A., Saleem, S., Shabbir, M. S., Bilal, K., & Abbasi, H. M. (2021). The relationship between renewable energy sources and sustainable economic growth: evidence from SAARC countries. *Environmental Science and Pollution Research*, *28*(25), 33390-33399. https://doi.org/10.1007/s11356-021-12795-z

Yildiz, A., Chouki, T., Atli, A., Harb, M., Verbruggen, S. W., Ninakanti, R., & Emin, S. (2021). Efficient Iron Phosphide Catalyst as a Counter Electrode in Dye-Sensitized Solar Cells. *ACS Applied Energy Materials*, *4*(10), 10618-10626. https://doi.org/10.1021/acsaem.1c01628

York, R., & Bell, S. E. (2019). Energy transitions or additions?: Why a transition from fossil fuels requires more than the growth of renewable energy. *Energy Research & Social Science*, *51*(1), 40-43. https://doi.org/10.1016/j.erss.2019.01.008

Yu, H., Bai, Y., Zong, X., Tang, F., Lu, G. M., & Wang, L. (2012). Cubic CeO_2 nanoparticles as mirror-like scattering layers for efficient light harvesting in dye-sensitized solar cells. *Chemical Communications*, *48*(59), 7386-7388. https://doi.org/10.1039/c2cc32239k

Yu, Z. J., Carpenter, J. V., & Holman, Z. C. (2018). Techno-economic viability of silicon-based tandem photovoltaic modules in the United States. *Nature Energy*, *3*(9), 747-753. https://doi.org/10.1038/s41560-018-0201-5

Yue, G., Wu, J., Xiao, Y., Ye, H., Lin, J., & Huang, M. (2011). Flexible dye-sensitized solar cell based on PCBM/P3HT heterojunction. *Chinese Science Bulletin*, *56*(3), 325-330. https://doi.org/10.1007/s11434-010-3080-0

Zainudin, S., Abdullah, H., & Markom, M. (2019). Electrochemical studies of tin oxide based-dye-sensitized solar cells (DSSC): a review. *Journal of Materials Science: Materials in Electronics*, *30*(6), 5342-5356. https://doi.org/10.1007/s10854-019-00929-6

Zeren, F., & Akkuş, H. T. (2020). The relationship between renewable energy consumption and trade openness: New evidence from emerging economies. *Renewable Energy*, *147*(1), 322-329. https://doi.org/10.1016/j.renene.2019.09.006

Zhang, J., Vlachopoulos, N., Jouini, M., Johansson, M. B., Zhang, X., Nazeeruddin, M. K., Boschloo, G., Johansson, E. M., & Hagfeldt, A. (2016). Efficient solid-state dye sensitized solar cells: the influence of dye molecular structures for the in-situ photoelectrochemically polymerized PEDOT as hole transporting material. *Nano Energy*, *19*(1), 455-470. https://doi.org/10.1016/j.nanoen.2015.09.010

Zhang, J., Yu, C., Wang, L., Li, Y., Ren, Y., & Shum, K. (2014). Energy barrier at the N719-dye/CsSnI 3 interface for photogenerated holes in dye-sensitized solar cells. *Scientific reports*, *4*(1), 1-6. https://doi.org/10.1038/srep06954

Zhang, J., Zhang, W., Cheng, H.-M., & Silva, S. R. P. (2020). Critical review of recent progress of flexible perovskite solar cells. *Materials Today*, *39*(1), 66-88. https://doi.org/10.1016/j.mattod.2020.05.002

Zhang, P., Wu, J., Zhang, T., Wang, Y., Liu, D., Chen, H., Ji, L., Liu, C., Ahmad, W., & Chen, Z. D. (2018). Perovskite solar cells with ZnO electron-transporting materials. *Advanced Materials*, *30*(3), 1703737. https://doi.org/10.1002/adma.201703737

Zhang, S., Yang, X., Numata, Y., & Han, L. (2013). Highly efficient dye-sensitized solar cells: progress and future challenges. *Energy & Environmental Science*, *6*(5), 1443-1464. https://doi.org/10.1039/c3ee24453a

Zhang, X., Xu, Y., Giordano, F., Schreier, M., Pellet, N., Hu, Y., Yi, C., Robertson, N., Hua, J., & Zakeeruddin, S. M. (2016). Molecular engineering of potent sensitizers for very efficient light harvesting in thin-film solid-state dye-sensitized solar cells. *Journal of the American Chemical Society*, *138*(34), 10742-10745. https://doi.org/10.1021/jacs.6b05281

Zhao, Y., Boccard, M., Liu, S., Becker, J., Zhao, X.-H., Campbell, C. M., Suarez, E., Lassise, M. B., Holman, Z., & Zhang, Y.-H. (2016). Monocrystalline CdTe solar cells with open-circuit voltage over 1 V and efficiency of 17%. *Nature Energy*, *1*(6), 1-7. https://doi.org/10.1038/nenergy.2016.67

Zheng, C., Penmetcha, A. R., Cona, B., Spencer, S. D., Zhu, B., Heaphy, P., Cody, J. A., & Collison, C. J. (2015). Contribution of aggregate states and energetic disorder to a squaraine system targeted for organic photovoltaic devices. *Langmuir*, *31*(28), 7717-7726. https://doi.org/10.1021/acs.langmuir.5b01045

Zheng, Z., Xie, W., Lim, Z. S., You, L., & Wang, J. (2014). CdS sensitized 3D hierarchical TiO_2/ZnO heterostructure for efficient solar energy conversion. *Scientific reports*, *4*(1), 5721. https://doi.org/10.1038/srep05721

Zhou, S., Daskeviciene, M., Steponaitis, M., Bubniene, G., Jankauskas, V., Schutt, K., Holzhey, P., Marshall, A. R., Caprioglio, P., & Christoforo, G. (2022). Low-Cost Dopant-Free Carbazole Enamine Hole-Transporting Materials for Thermally Stable Perovskite Solar Cells. *Solar RRL*, *6*(1), 2100984. https://doi.org/10.1002/solr.202100984

Zhu, L., Liu, G., Duan, X., & Zhang, Z. J. (2010). A facile wet chemical route to prepare ZnO/TiO_2 nanotube composites and their photocatalytic activities. *Journal of Materials Research*, *25*(7), 1278-1287. https://doi.org/10.1557/jmr.2010.0172

APPENDICES

Appendix A: Copyright – Journal of Electronic Materials

Article DOI: https://doi.org/10.1007/s11664-021-09250-7

Paper title: Computational Simulation of a Highly Efficient Hole Transport-Free Dye-Sensitized Solar Cell Based on Titanium Oxide (TiO_2) and Zinc Oxysulphide (ZnOS) Electron Transport Layers

Author(s): Benjamin K. Korir, Joshua K. Kibet, Silas M. Ngari

Appendix B: Copyright – Journal of Optical and Quantum Electronics

Article DOI: https://doi.org/10.1007/s11082-021-03013-8

Paper title: Simulated performance of a novel solid-state dye-sensitized solar cell based on phenyl-C_{61}-butyric acid methyl ester ($PC_{61}BM$) electron transport layer

Author(s): Benjamin K. Korir, Joshua K. Kibet, Silas M. Ngari

Appendix C: Abstract of Paper published in Journal of Energy Science & Engineering

Received: 20 February 2024 | Revised: 27 May 2024 | Accepted: 4 June 2024

DOI: 10.1002/ese3.1815

REVIEW

A review on the current status of dye-sensitized solar cells: Toward sustainable energy

Benjamin K. Korir | **Joshua K. Kibet** | **Silas M. Ngari**

Department of Chemistry, Egerton University, Njoro, Kenya

Correspondence
Benjamin K. Korir, Department of Chemistry, Egerton University, P.O Box 536-20115, Njoro, Kenya.
Email: korir.1367419@student.egerton.ac.ke

Abstract

Dye-sensitized solar cells (DSSCs) are among the most attractive third-generation photovoltaic technologies due to their low toxicity, versatility, roll-to-roll compatibility, ultralightness, and attractive power conversion efficiencies (PCEs). However, their transition from the laboratory scale to the industrial scale has been slow due to their inability to compete with silicon-based cells in terms of efficiencies and stabilities. Research activities on DSSCs have been ongoing for several decades to improve the efficiency and cost-effectiveness of photovoltaics but these attempts are still inadequate. Their chemical and physical properties must be refined to increase efficiency and commercialization. This review provides a concise overview of the recent advances taking place in the DSSCs research field, including molecular engineering technologies, the quest for superior carrier transport materials (CTMs), efficient sensitizers, and better electrodes. Also, this review compiles knowledge of the historical development of DSSCs, the current advancements such as control of surface morphologies, doping strategies, modeling and simulation, characterization, and recent cutting-edge research happenings in photovoltaic research. Finally, nanostructured materials that have been used as photoelectrodes and the practical applications of DSSCs in internet of things (IoT) and portable electronics are examined to identify challenges and future advancements. The main aim of this work is to be a pathfinder for scientific researchers in this field exploring various energy harvesting materials and optimization strategies of different components of DSSCs.

KEYWORDS

carrier transport materials, internet of things, molecular engineering, nanostructured materials, photovoltaic technologies, portable electronics

1 | INTRODUCTION

Presently, the world's population is increasing rapidly in tandem with energy consumption, with the possibility of energy demand surpassing population growth.[1–3] Essentially, fossil fuels, nuclear energy, and bioenergy are chiefly used as primary energy sources.[4–6] The constant use of nuclear and fossil fuels such as coal, natural gas, and liquefied petroleum gas (LPG) has resulted in the emission of radioactive wastes, including

Appendix D: Abstract of Paper published in Journal of Electronic Materials

Journal of Electronic Materials
https://doi.org/10.1007/s11664-021-09250-7

ORIGINAL RESEARCH ARTICLE

Computational Simulation of a Highly Efficient Hole Transport-Free Dye-Sensitized Solar Cell Based on Titanium Oxide (TiO_2) and Zinc Oxysulfide (ZnOS) Electron Transport Layers

Benjamin K. Korir[1] · **Joshua K. Kibet**[1] · **Silas M. Ngari**[1]

Received: 5 August 2021 / Accepted: 16 September 2021

Abstract

In order to mitigate the current global energy and environmental challenges associated with the use of fossil fuels, there is a need for better energy alternatives such as the inexhaustible solar energy. Of great interest is the design and fabrication of low-cost photovoltaic devices which are the epitome of efficient solar energy harvesting. Herein, we report inexpensive hole transport layer (HTL)-free dye-sensitized solar cell architecture with robust photovoltaic (PV) performance. In the proposed solar cell model, expensive hole transport layers, CuI, CuSCN, Spiro-OMeTAD, and PEDOT:PSS, are not required, but instead, a metallic layer is used for dye regeneration. A thorough analysis of the effect of series and shunt resistances, conduction band offset, Schottky barriers, working temperature, the metal work function of the back contact, and the electron affinities of the electron transport layers (ETLs) on the performance of the proposed solar cell is presented. The Solar Capacitance Simulator (SCAPS-1D) is used to perform the numerical simulations of the proposed solar cell design. The study focused on modeling HTL-free dye-sensitized solar cells with the configuration: FTO/ETL/N719 dye/Au. The performance of two ETLs—ZnOS and TiO_2 are critically examined. The optimized model cell performance for the FTO/ZnOS/N719 dye/Au architecture gave an optimal power conversion efficiency (PCE) of 11.54%, 62.71% as the fill factor (FF), short circuit current (Jsc) of 18.50 $mAcm^{-2}$, and an open-circuit voltage (Voc) of 0.99 V. On the other hand, the cell architecture FTO/TiO_2/N719 dye/Au gave an optimized performance of 10.22% as the PCE, 63.58% as the FF, a Voc of 0.97 V, and 16.50 $mAcm^{-2}$ as the Jsc. Based on these results, ZnOS is a suitable ETL material that has better PV performance of the solar cell device under consideration. ZnOS is earth-abundant, has a tunable band gap, is less toxic, and is, therefore, a promising candidate to replace TiO_2 ETL in future designs and manufacture of HTL-free DSSCs for commercial production.

Keywords Conduction band offset · dye-sensitized · electron affinity · photovoltaic · SCAPS-1D · Schottky barriers

Appendix E: Abstract of Paper published in Journal of Optical and Quantum Electronics

Optical and Quantum Electronics (2021) 53:368
https://doi.org/10.1007/s11082-021-03013-8

Simulated performance of a novel solid-state dye-sensitized solar cell based on phenyl-C_{61}-butyric acid methyl ester ($PC_{61}BM$) electron transport layer

Benjamin K. Korir[1] · **Joshua K. Kibet**[1] · **Silas M. Ngari**[1]

Received: 3 December 2020 / Accepted: 6 June 2021

Abstract
Climate change has approached a major crisis limit worldwide due to exhaust emissions arising from the use of traditional transport fuels. Solar energy, therefore, appears to be the most promising alternative energy that can mitigate air quality and environmental degradation. Herein, we report numerical simulation of a novel model solid-state dye-sensitized solar cell consisting of solid-state layers with the configuration FTO/PC_{61}BM/N719/CuSCN/Au using 1-dimensional solar cell capacitance simulator software (SCAPS-1D). The motivation underpinning the numerical simulation of the solar cell architecture proposed in this study was to optimize phenyl-C61-butyric acid methyl ester ($PC_{61}BM$) performance as the electron transport layer. In this model, the effects of varying several parameters—temperature, absorber thickness, defect density, and metallic back contact on the overall solar cell performance have been critically examined. After optimizing the input parameters, the optimal conversion efficiency was 5.38% while the optimized open-circuit voltage was 0.885 V. Besides, 70.94% was the optimum fill factor and the peak short-circuit current of 8.563 mA cm^{-2} was achieved. Built-in voltage of ~1.0 V was estimated from the Mott–Schottky curve and the cell band diagram. The power conversion efficiency obtained in this study is robust for this cell configuration, and is toxic-free compared to the lead-based perovskite solar cells. These findings are therefore useful in the advancement and fabrication of high-performance dye-based photovoltaic devices for large-scale industrial production.

Keywords Climate change · Solar energy · SCAPS-1D · Dye-sensitized solar cells · Numerical simulation

Appendix F: N719 dye Iso surface and Non-Covalent Interactions

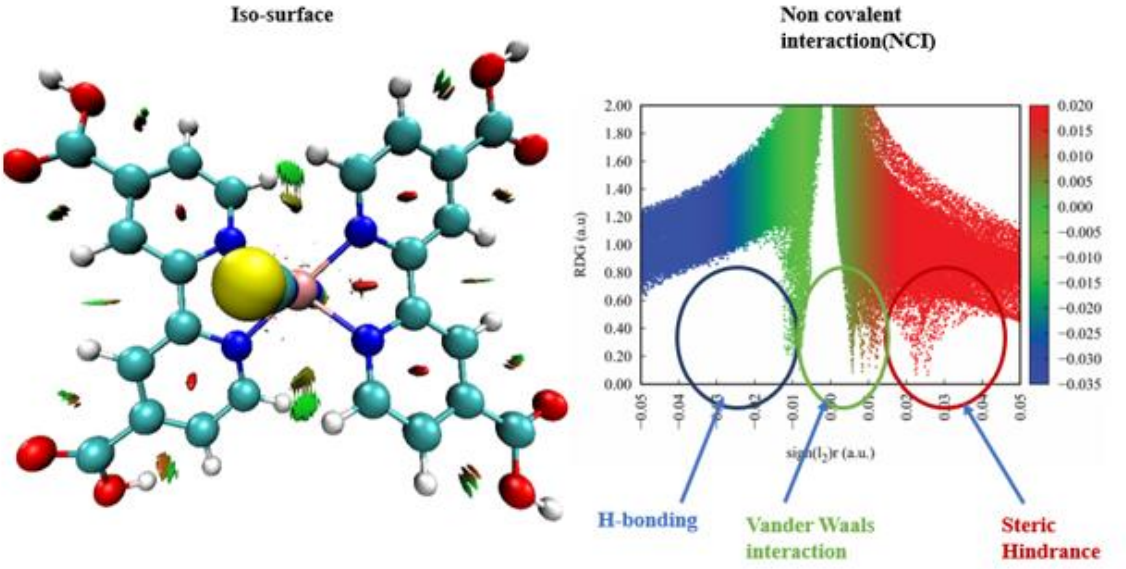

The iso-surace and reduced density gradient (RDG) of N719 help to visualize electronic density distribution, charge transfer paths as well as interactions such as steric effects, van der Waals, and hydrogen bonding behaviour in the dye.

Appendix G: The HOMO-LUMO Energy Gap of the Simulated Materials using TD-DFT

Name of the Molecules	HOMO (eV)	LUMO (eV)	Eg (eV)
Dye	-5.04	-3.91	1.13
CUCSN	-5.85	-3.82	2.03
SnO2	-8.31	-3.89	4.42
TiO2	-4.55	-2.63	1.92
ZnOS	-4.86	-4.43	0.43

Appendix H: Reactivity and Charge Transfer Efficiency of Simulated Materials

Name of the Molecules	η (hardness) (eV)	S (softness) (eV)	μ (chemical potential) (eV)	χ (electronegativity) (eV)	ω (electrophilicity) (eV)	ΔNmax (total charge transfer)
Dye	0.57	1.77	-4.48	4.48	5.66	7.92
CUCSN	1.02	0.98	-4.84	4.84	11.86	4.76
SnO2	2.21	0.45	-6.10	6.10	41.12	2.76
TiO2	0.96	1.04	-3.59	3.59	6.19	3.74
ZnOS	0.26	4.65	-4.65	4.65	2.32	21.60

.

Appendix I: NACOSTI Permit

REPUBLIC OF KENYA

NATIONAL COMMISSION FOR SCIENCE,TECHNOLOGY & INNOVATION

Ref No: 681220

Date of Issue: 18/May/2025

RESEARCH LICENSE

This is to Certify that Mr.. Benjamin KIPCHIRCHIR Korir of Egerton University, has been licensed to conduct research as per the provision of the Science, Technology and Innovation Act, 2013 (Rev.2014) in Nakuru on the topic: THEORETICAL OPTIMIZATION OF OPTOELECTRONIC PROPERTIES OF ELECTRON TRANSPORT MATERIALS FOR DYE-SENSITIZED SOLAR CELLS BASED ON SOLAR CELL CAPACITANCE SIMULATOR for the period ending : 18/May/2026.

License No: NACOSTI/P/25/4173370

681220

Applicant Identification Number

Deputy Director
NATIONAL COMMISSION FOR SCIENCE,TECHNOLOGY & INNOVATION

Verification QR Code

NOTE: This is a computer generated License. To verify the authenticity of this document, Scan the QR Code using QR scanner application.

See overleaf for conditions